SLOT-DIE COATING OF HYBRID PEROVSKITE: MATERIAL STUDY AND INTEGRATION INTO PHOTOVOLTAIC DEVICES.

MATHILDE FIEVEZ

Interdisciplinary graduate school – school of electrical and electronic engineering

A thesis submitted to the Nanyang Technological University in partial fulfilment of the requirement for the degree of Doctor of Philosophy.

2021

Statement of Originality

I hereby certify that the work embodied in this thesis is the result of original research, is free of plagiarised materials, and has not been submitted for a higher degree to any other University or Institution.

12/08/2021

. . . . . .

Date

. . . . . .

Mathilde FIEVEZ

Supervisor Declaration Statement

I have reviewed the content and presentation style of this thesis and declare it is free of plagiarism and of sufficient grammatical clarity to be examined. To the best of my knowledge, the research and writing are those of the candidate except as acknowledged in the Author Attribution Statement. I confirm that the investigations were conducted in accord with the ethics policies and integrity standards of Nanyang Technological University and that the research data are presented honestly and without prejudice.

12/08/2021

. . . . . .

Date

. . . . . .

Ass. Pr. Wei Lin LEONG

Authorship Attribution Statement

This thesis contains material from 1 paper published in the following peer-reviewed journal(s) / from papers accepted at conferences in which I am listed as an author.

Chapter 5 is partially published in Fievez, M. *et al.* Slot-die coated methylammonium-free perovskite solar cells with 18% efficiency. *Sol. Energy Mater. Sol. Cells* **230**, 111189 (2021). DOI:10.1016/j. solmat.2021.111189.

The contributions of the co-authors are as follows:

- Pr. Subodh MHAISALKAR and Dr. Solenn BERSON assisted in the project funding and project administration.
- Ass. Pr. Wei Lin LEONG, Dr. Daymond KOH, Dr. Stéphane CROS and Dr. Matthieu MANCEAU provided the initial project direction.
- I prepared the manuscript drafts with Dr. Prem RANA. The manuscript was revised by Ass. Pr. Wei Lin LEONG, Dr. Daymond KOH, Dr. Fadilah JAMALUDIN, Dr. Biplab GHOSH.
- I co-designed the study with Dr. Prem RANA and performed all the laboratory work at the Create Laboratory and at the Research Technological Plaza (both parts of the Energy research institute @ NTU). I also analyzed the data.
- All microscopy, including sample preparation, was conducted by me and Dr. Prem RANA in the Research Technological Plaza (ERI@N).
- Jia Haur LEW assisted in the training and set up of the slot-die coating machine.

- Dr Biplab GHOSH assisted in the collection of X-ray diffraction spectroscopy data. I carried out the data interpretation.
- Dr Fadilah JAMALUDIN assisted in the collection and provide guidance in the interpretation of the TRPL data. Dr. Annalisa BRUNO assisted in the interpretation of the TRPL data.
- Dr. Prem RANA assisted in the substrate preparation, slot-die coting machine operation, SEM data collection, device fabrication and device performance measurement (JV and MPPT).
- I collected the absorbance and photoluminescence data and did the data analysis.

12/08/2021

. . . . .	. . . . .
Date	Mathilde FIEVEZ

THÈSE

Pour obtenir le grade de

DOCTEURE DE L'UNIVERSITE GRENOBLE ALPES

préparée dans le cadre d'une cotutelle *entre la Communauté Université Grenoble Alpes (UGA) et Nanyang Technological University (NTU)*

Spécialité : **Matériaux, Mécanique, Génie Civil, Electrochimie**

Arrêté ministériel : le 25 mai 2016

Présentée par

Mathilde FIEVEZ

Thèse dirigée par **Stéphane CROS,** Ingénieur de recherche, CEA
co-encadrée par **Matthieu Manceau**, Ingénieur de recherche, CEA
co-dirigée par **Wei Lin LEONG,** Professeure assistante, NTU
co-encadrée par **Daymond KOH**, Chercheur docteur, NTU

préparée au sein du **CEA/LITEN/Laboratoire des Cellules Tandem (LCT)** et au sein du **Energy Research Institute @ NTU (ERIAN)** dans les Écoles Doctorales **IMEP-2** - Ingénierie, Matériau, Mécanique, Environnement, Energétique, Procédés, Production et **Interdisciplinary Graduate school (IGS)**- Sustainable Earth.

Slot-die coating of hybrid perovskite: material study and integration into photovoltaic devices.

Thèse soutenue publiquement le **23 Juin 2021** devant le jury composé de :

Monsieur Bernard RATIER
Professeur, Université de Limoges, Rapporteur
Monsieur Trystan WATSON
Professeur, Swansea University, Rapporteur
Madame Lydia WONG
Professeure associée, NTU, Examinatrice
Monsieur Daniel BELLET
Professeur, UGA/LMGP, Président
Madame Eva UNGER
Chercheuse docteure, Helmholtz Zentrum Berlin, Examinatrice

A scientist in his laboratory is not a mere technician: he is also a child confronting natural phenomena that impress him as though they were fairy tales.

Marie Curie

Résumé

Depuis 2009, les matériaux hybrides pérovskites halogénés ont émergé en tant que technologie photovoltaïque innovante, contrastant avec les technologies existantes à base de silicium par leur mise en œuvre par voie liquide qui réduit significativement l'empreinte carbone de la fabrication des panneaux solaires. En 2021, le rendement de cellules solaires à base de pérovskite atteint 25.5% à l'échelle laboratoire, réduisant l'écart de performance avec la technologie silicium (26.6%). Une des difficultés rencontrées lors du développement de cette technologie à échelle industrielle est l'homogénéité du dépôt de la couche pérovskite sur des grandes surfaces. Malgré l'existence de procédés industriels (impression jet d'encre, enduction slot-die) pour déposer le film liquide précurseur sur des grands substrats, le défi réside dans le contrôle de la cristallisation du matériau pérovskite à l'échelle industrielle. Dans ce travail, nous avons étudié le dépôt par voie humide d'une pérovskite halogénée mixte ($Cs_xFA_{(1-x)}Pb(I_{0.88}Br_{0.12})_3$) par le procédé slot-die combiné à un couteau d'air et une chauffe de substrat pour permettre la cristallisation sur des dimensions de 5 x 5 cm^2 et 10 x 10 cm^2. Nous détaillons l'effet des paramètres du procédé slot-die, de l'encre pérovskite précurseur et du substrat sous-jacent sur la morphologie du film pérovskite et ses qualités opto-électroniques. Nous dévoilons le rôle du précurseur CsI dans cette cristallisation assistée par flux d'air et montrons que son effet diffère vis-à-vis de la cristallisation conventionnelle par anti-solvant. Nous optimisons la combinaison d'un couteau d'air et d'une chauffe de substrat pour permettre la formation d'un film pérovskite $Cs_{0.15}FA_{0.79}Pb(I_{0.88}Br_{0.12})_3$ compacte de façon reproductible et homogène. L'intégration de ces couches dans des dispositifs photovoltaïques a mené à des rendements de conversion de 18% à l'échelle laboratoire (0.09 cm^2) et 11.5% à l'échelle mini-module (52 cm^2). Ce travail ouvre la voie à la compréhension et au contrôle de la cristallisation du matériau pérovskite sur des grandes surfaces, nécessaire pour l'industrialisation de cette technologie.

Mots clés : Pérovskite double cation, Slot-die, Couteau d'air, Larges surfaces.

Abstract

In the last decade, metal halide perovskites have emerged as an innovative thin film photovoltaic technology that contrasts with current technologies due to its solution processability that could significantly reduce its manufacturing environmental footprint. In 2020, perovskite solar cells at laboratory scale reach 25.5% power conversion efficiency, closing the gap to silicon based solar cells performances (26.6%). One of the major bottlenecks of perovskite photovoltaic modules fabrication is the homogeneous deposition of perovskite material over large areas. Whereas scalable processes (inkjet, slot-die coating) can be adapted from the organic photovoltaics industry to deposit the wet precursor film over large areas, the control of the perovskite crystallization remains a challenge at that scale. In this work, we investigate the wet deposition of double cation mixed-halides perovskite ($Cs_xFA_{(1-x)}Pb(I_{0.88}Br_{0.12})_3$) via slot-die coating combined with synergistic gas quenching and substrate heating over 5 x 5 cm^2 and 10 x 10 cm^2 substrates. More specifically, we detail the effect of the process parameters, precursor ink composition and substrate nature (*e.g.* planar vs mesoporous, TiO_2 vs SnO_2) on the perovskite film morphological and opto-electronics properties. We unveil the role of the CsI precursor in the gas-assisted crystallization and show that its effect differs from the conventional anti-solvent assisted crystallization. We show that slot-die coating technique combined with synergistic gas quenching and substrate heating can produce compact, homogenous and reproducible $Cs_{0.15}FA_{0.79}Pb(I_{0.88}Br_{0.12})_3$ perovskite films. We integrate the perovskite slot-die coated layers in planar (n-i-p) photovoltaic device configuration yielding power conversion efficiency (PCE) of 18% over 0.09 cm^2 and 11.5% over 52 cm^2 device active area. This work provides insights into achieving controlled perovskite crystallization of perovskite films over large areas, which is necessary for the industrialization of this technology.

Keywords: Methylammonium-free perovskite, Slot-die coating, Gas-quenching, Large areas.

Acknowledgments

My interest for the perovskite material started in 2016. I want to thank my first mentor, Mei Gao, who showed me how to distinguish a promising from a defective film simply by starring at it. Since that day, I got fascinated by this astonishing and yet so capricious material. I want to thank Doojin Vak who teached me so much about printing and from whom originated the idea of combining gas-quenching with a slot-die coater. Since our 12 meters long perovskite experiment in the Flexible Electronics Lab, I promised myself to demonstrate the applicability and robustness of this crystallization technique for the emerging perovskite photovoltaic industry. Them, and many more discussion with inspiring mentors (Régine, Corinne, Marie-Odile, Daniel, Juliette, Chungho) are the reason why I got here today.

All of this work became a reality thanks to the collaboration between two laboratories: the LMPO (now LCT) group in CEA INES and the ERIAN Perovskite group in NTU university. I want to thank the people who guided my path towards the PhD: Pr. Subodth Mhaisalkar who believed in the slot-die coating from the early stages, Anish, Fritz, Amna and Jia Haur who welcomed me in the team in 2017 and Pr. Wei Lin Leong who later became my PhD supervisor from NTU side. Thanks to Pr. Claude Guet, I had the opportunity to meet the CEA team (Florence Lefevre Lejoud, Frédéric Schuster, Solenn Berson, Stéphane Cros and Matthieu Manceau) who provided me with the funding for this work (Printrose PTC project). This adventure was an extraordinary chance to work with people with various scientific backgrounds, communication styles and cultures.

I want to thank my PhD supervisors, Stéphane and Wei Lin, for having encouraged my project at all times, my mentors Matthieu and Daymond for the daily discussions and the laboratory leaders Solenn Berson and Subodh Mhaisalkar for welcoming me in their teams. For the last 3 years, I felt supported and challenged in this project when I needed most. I am grateful for this chance to have pursued my PhD in such a stimulating and enriching environment. All of you have teached me various skills that will be useful for the rest of my professional life: vision, strategy, collaborative mindset, direct communication, availability, honesty and humility. Furthermore, I want to thank the jury members for accepting to read my work and for the interesting discussions we shared during the PhD defense. I particularly thank Pr. Ratier and Pr. Watson for reviewing this work, Pr. Bellet for his role of jury president and Pr. Wong, Dr. Eva Unger for the relevant discussions they triggered.

Of course, this PhD journey would not have been possible without the presence of numerous people both in France and in Singapore. I want to thank the CEA team who welcomed me in April 2018, Solenn for her strategic views and encouragements, Stéphane for trusting me and helping me to pave my own way, Matthieu for his strong expertise (I will miss our discussions on the caesium heart theory) and his incredibly successful slot-die coating experiments (numerous records but not that many headlines), Pascal who designed the slot-

die box *sur mesure* and who shared my interest in do-it-yourself, Carine who will never stop impressing me with her energy and dedication to do her best and help others in the lab (you are a doctor to me), Muriel for her knowledge in characterization and her trust with the XRD equipment, Noëlla for the OPV discussions and for the literature updates, Florence for her patience with the slot-die and her daily smile, Nathalie for her kindness and efficient help with the orders. To the PhD candidates that are now Dr. Marc-Antoine, Dr. Vincent, Dr. Manon, Dr. Pia and Dr. Thibault, thank you for welcoming me in the PhD family and for supporting me all these years!

Of course, I want to thank the people who joined the team along the way, in particular future Dr. Mathis and Félix, your daily jokes, discussions and feedbacks made my life happier (I am already impressed by you guys, I wish you all the best for the finish line!). I want to particularly thank Emmanuelle for her hard work on the slot-die coater with me in 2019. Thanks to her energy, we probably coated way too many samples (~ 500) in 2 months, but I really enjoyed to share my world with such an enthusiastic person (we will write that song one day!). I want to thank Daniel for the long discussions we had on perovskite in the lab and on life outside the lab, Van Son for his happiness and motivation, Caroline for her positive attitude and the fun moments shared together, Elise for the bike rides to work, pizza evenings and for being an inspiration every day, Axel for his joy of life, Marina for the numerous discussions on science or on other topics, Olzhas for his advices and open-mindedness, Andrii for our optical discussions and his kindness to explain physical concepts to me, Nikoletta for her dynamism and the Greek food delivery, Grégoire for bringing up my coach 7 floors in the stairs…, Sénami and Pia for learning how to ski with me, Emmanuel for making me read more books in 3 months than in the past 5 years, Chloé and José for starting up the wine club with me and Catherine and Guillaume for pursuing this project after my departure. To all my friends in Chambéry, Arika, Arnaud, Juanma, Laurène, Joël-Louis, Jean, Roumej, Victor, Lise-Marie, Antonino, Maribel, Hasan, Lauriane, Joséphine, Pia, Consuelo, Charles, Baptiste, thank you for sharing a hike, a dance, a run, a beer, a flat, or just some of your time with me.

From Singapore, I want to thank Wei Lin for her supervision, the group leader Daymond for organizing the monthly meetings and providing insights and suggestions on my work, Pr. Claude for his lessons in communication and his support to get the cotutelle agreement signed, the laboratory manager, Heryani Ahmad, for making our life safer and easier (you will be missed), and Dr. Prem Rana for sharing my life 24-7 for the first 6 months. You teached me so much: resilience, friendship, joy, humility. Thank you for your patience. It was an honour to work with you on this tricky project (you definitely have a lucky hand). I want to thank Fritz for helping me out with the airknife, you were not here when I came back but I am very grateful for the time we worked together (enjoy your cranberries for the next thanksgiving), Jia Haur for his everlasting energy (when are you sleeping man?) and free advices on many topics, Amna for teaching me how to slot-die on the n-Rad, Rahul for his

astonishing drive (I wish you well for your PhD), Li Jia for his daily practical help and valuable scientific inputs (your evolution is so inspiring since 2017), Xie Lin for the fun times and teaching me blade coating at her lost hours, Li Xin and Benny for the lunches at Kansama (Benny, danke schön für mein Deutsch Praktikum), Kudi for her serenity, kindness and the inspiration she was for me, Enke for the Mongolian songs between two evaporation batches, Sudhansu for the numerous discussions on triple cations and his calm and listening attitude, Monika for the quick chats in Create, Xin Yu for his energy and curiosity (your French is amazing), Anna for her Swiss German dynamism and open mindedness, Sjoed for introducing me to the design of experiment, Biplab for telling me so much about (PhD) life and pushing me back up from time to time, Bhumika for setting an example for me (yes, you are!) and for the introduction to the toastmaster program, Fadilah for her help with the TRPL measurement and the paper writing (thank you for your time), Yan Fong for the efficient Monday literature meetings and for the numerous discussions we shared, Anil for his friendship and honesty, Herlina for helping out when I needed most, Raihanna for her help with the PL and our discussion in the lab, Riyas for the discussions on crystallization, Bening for being in the same boat (I wish you well for the future), Maldhav for the discussions during the lab demo, Abijidth for his dynamism and humour and for opening for me the door to Pr. Wei Lin lab! Thanks to you, I felt at home in Singapore.

I also want to thank Singapore for welcoming me. I lived in Clementi during the circuit breaker period in 2020. Even far from my family, I felt supported (I am thankful to Ash and Dash, my flatmates). This period enabled me to start public speaking online with NTU toastmaster club. I also took some of my time to volunteer at the riding for the disabled association in 2019 to connect with the local society. Besides a working experience, this cultural immersion opened new horizons to me. I want to thank my SG friends Dewi (you're my oldest friend there) and Gabriel, Florence, Chloé, Fey, Danny, Adele, Kieran, Aurore, Matthieu, Suraj, Junior, Miguel, Hubert, Will, Geoffrey, Etienne, Ange, Antonia, Grace, Wing and Pierre for having shared parts of my life along the way.

J'aimerai remercier mes amis proches qui n'ont pas eu l'occasion de me voir souvent ces 5 dernières années : Mélanie, Alice W., Hélène, Alice D., Anouk, Alexandra, Yasmine, Ilham, Marine, Arthur, Alice L., Fanny, Jeanne, Khadidja, Mathilde B., Mathilde D., Tiphaine, Claire, Camille, Adrien, Maxime, Madeleine, Lise, Léonid, Yacine, Hu Hien, Juan et Taese, Guillaume et Christophe. Merci d'avoir été là à chacun de mes retours.

Enfin, je veux remercier ma famille: mes deux grand mères qui ont toujours été là (l'une m'a confié de ne jamais compter le nombre de chutes mais le nombre de fois où l'on se relève), mes cousins, en particulier mes deux cousines qui m'ont inspiré en faisant des études aussi longues que moi mais dans d'autres domaines, mon frère Adrien, et surtout mes parents pour leur investissement dans mon éducation. Merci à vous de m'avoir permis d'aller au bout de ce projet!

Table of contents

Table of abbreviations and acronyms

(n-i-p)	Device structure ETL/Perovskite/HTL
(p-i-n)	Device structure HTL/Perovskite/ETL
2-ME	2-methoxyethanol
ACN	Acetonitrile
ALD	Atomic layer deposition
Au	Gold
CBD	Chemical bath deposition
CBZ	Chlorobenzene
CdTe	Cadmium telluride
CB	Conduction band
CHP	N-Cyclohexyl-2-pyrrolidone
CIGS	Copper Indium Gallium Sulfide
CO_2	Carbon dioxide
c-Si	Crystalline silicon
CsI	Caesium iodide
Cr	Chromium
DFT	Density functional theory
DLS	Dynamic light scattering
D_N	Donor number
DMSO	Dimethylsulfoxide
DMF	Dimethylformamide
DSSC	Dye sensitized solar cells
EDTA	ethylenediamine tetraacetic acid
EDX	Energy dispersive X-Ray
Eg	Band gap energy
ETL	Electron transporting layer
FA	Formamidinium ($NH_2CH = NH_2^+$)
FAI	Formamidinium iodide
FDC	Fast crystallization-deposition
FE-SEM	Field emission scanning electron microscopy
FF	Fill factor
FTO	Fluorine doped tin oxide
GFF	Geometrical fill factor

GHG	Greenhouse gas
GIWAXS	Grazing incidence wide angle X-Ray scattering
GMF	Glass microfiber
hPa	Hectopascal
HTL	Hole transporting layer
IQE	Internal quantum efficiency
ITO	Indium doped tin oxide
IPCE	Incident photon-to-current conversion efficiency
ISO	Image sensor optimization
J_{sc}	Current density
KBr	Potassium bromide
LASER	Light amplification by stimulated emission of radiation
LiTFSI	bis(trifluoromethane) sulfonimide lithium salt
MA	Methylammonium ($CH_3NH_3^+$)
MACl	Methylammonium chloride
MAI	Methylammonium iodide
MABr	Methylammonium bromide
NMP	N-methyl-2-pyrrolidone
NVCS	Non-volatile coordinative solvent
Nd:YAG	Neodymium-doped yttrium aluminium garnet
o-DCB	Ortho-dichlorobenzene
PCBM	phenyl-C61-butyricacid methyl ester
PCE	Power conversion efficiency
PEAI	Phenethylammonium
PbI_2	Lead iodide
$PbBr_2$	Lead bromide
PbS	Lead sulfide
PL	Photoluminescence
Psi	Pound per square inch
PTAA	Poly[bis(4-phenyl)(2,4,6-trimethylphenyl)amine]
PTFE	Polytetrafluoroethylene
PV	Photovoltaic
QFLS	Quasi-Fermi level splitting
R_a	Average surface roughness
rh	Relative humidity

rpm	Revolutions per minute
SEM	Scanning Electron Microscopy
Spiro-OMeTAD	2,2′,7,7′-tetrakis [N, N -di- p -methoxyphenyl-amine]9,9′-spirobifluorene (synonym: Spiro-MeOTAD)
tBP	4-tert-butyl pyridine
TEM	Transmission electron microscopy
TCO	Transparent conductive oxide
TOF-SIMS	Time-of-flight secondary-ion mass spectrometry
TRPL	Time-resolved photoluminescence
$Ti(OBu)_4$ or TBT	Titanium butoxide or tetrabutyl titanate
UV	Ultraviolet
VB	Valence band
V_{oc}	Open-circuit voltage
VNCS	Volatile non-coordinative solvent
XRD	X-Ray diffraction

General Introduction

- **Broader context**

Today, newly industrialized and developing countries are facing a fast demographic and economic growth. The human development in these regions requires an increase of the energy production. In the meantime, the extreme events caused by the climate change have raised awareness on the importance to limit our greenhouse gas (GHG) emissions. Industrialized countries started to shift their energy production model from fossil-based to low-carbon energy sources. Developing countries install more renewable energy sources than non-renewables ones since 2018 [1]. Nuclear, hydropower, wind power and solar energy (concentrated and photovoltaic) are current technologies to produce decarbonized electricity. They represented 29% of the world electricity production in 2020 [2] and could reduce the GHS emissions by 100 times compared to electricity production relying on fossil energy sources (**Figure 1**). Notably, solar photovoltaic (PV) levelized cost of electricity has become lower than coal [3], which makes it a cost-effective solution to produce low-carbon electricity in newly industrialized and developing countries.

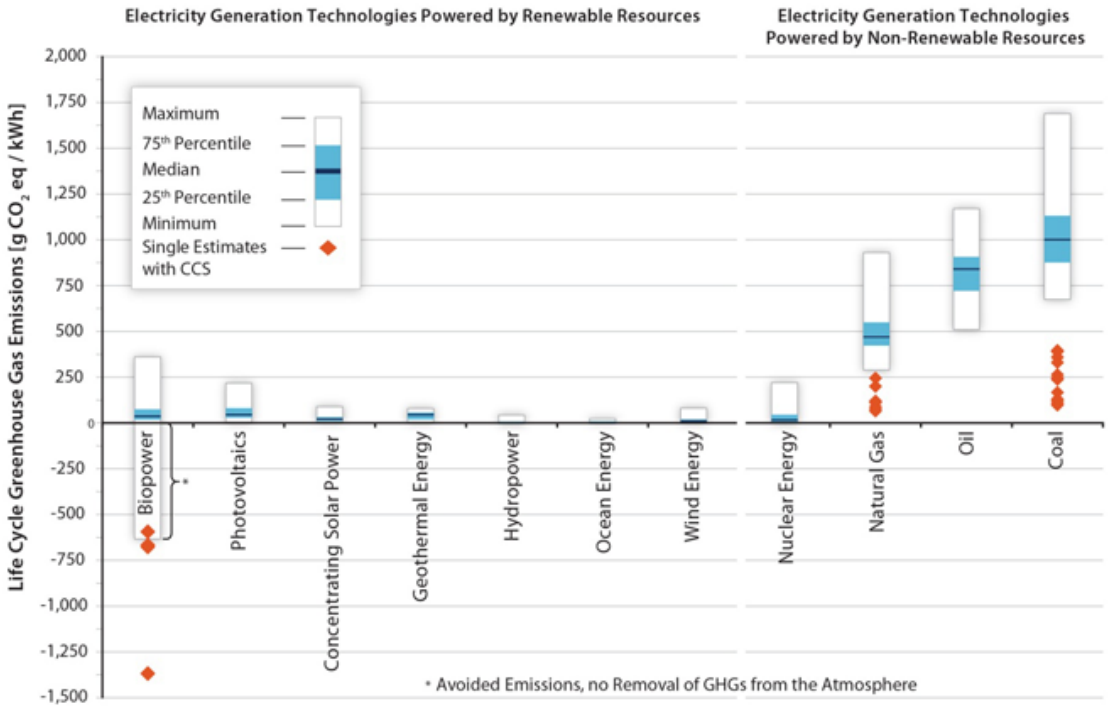

***Figure 1**: Life cycle greenhouse gas emissions for various electricity production technologies [4].*

Despite their reduced (or null) GHG emissions during operation, these low-carbon technologies still produce GHG during their manufacturing phase. To further reduce the environmental footprint of those technologies, manufacturing approaches minimizing the material, energy and water usage are desirable. In the case of solar photovoltaics, thin film technologies have emerged to address those challenges by using more absorbent semiconductors (*e.g.* CdTe, CIGS) that can reduce the material use (100 times thinner absorber layers), by using less energy intensive processes to deposit those materials (lower temperatures compared to silicon crystallization) and by limiting the use of water [5].

As a result, cadmium telluride (CdTe) technology has a lower carbon footprint (15.83 gCO_2eq/kWh) compared to crystalline silicon (c-Si, 27.20 gCO_2eq/kWh) while retaining relatively high power conversion efficiency (22.1% and 26.6% and respectively [6]). Consequently, the time needed for thin film solar panels to produce back the energy used for their fabrication (energy payback time) is shorter compared to c-Si technology. Typically, the energy payback time of CdTe solar panels is less than one year (**Table 1**).

Inherited from the dye sensitized solar cells (DSSC), metal halide perovskites have emerged as a new absorber material class for thin film photovoltaics in the past decade. Today, the perovskite solar cells performance (25.5% record power conversion efficiency) is closing the gap at laboratory scale with the crystalline silicon (c-Si) solar cells performance (26.6%). Metal halide perovskites have the advantage to retain good opto-electronic properties when solution-processed, in contrasts to other thin film technologies employing sputtering or thermal evaporation processes [7]. This ease of implementation is responsible for the booming research in this field. It also conveys this technology the shorter energy payback time among c-Si and thin films photovoltaics technologies [8].

	c-Si	**CdTe**	**CIGS**	**Perovskite**
Absorption coefficient (cm^{-1})	10^3 - 10^4	10^4 - 10^5		
Band gap (eV) (indirect/direct)	1.1 (indirect)	1.44 (direct)	1 - 1.6 (direct)	1.56 - 1.75* (direct)
Typical absorber thickness (µm)	170 - 200	3 - 5	1 - 2	0.4 – 1
Record cell efficiency (%)	26.6	22.1	23.4	25.5
Carbon footprint (gCO_2eq/kWh)	27.20	15.83	21.44	-
Energy payback time (years)	1.23	0.68	1.01	0.2 – 0.3

***Table 1**: Comparison of the main thin film technologies properties [9] and performances [10]. *This range concerns the lead halide perovskites and can be further extended by allowing tin with lead.*

One of the main bottlenecks for the perovskite technology industrialization is the difficulty to achieve high performances over large-area devices. More specifically, the perovskite crystallization requires to be carefully controlled during the solution process by triggering the nucleation and growth in the initial wet precursor film. While wet film coating processes such as slot-die coating are already available at industrial scale (as exemplified in the organics photovoltaics industry), the adaptation of the method used to trigger the perovskite crystallization in the laboratory (anti-solvent quenching) to large-area samples (anti-solvent bathing) is not as efficient [11]. Consequently, alternative crystallization methods are needed to control the perovskite deposition in scalable processes.

In the literature, the control of the perovskite crystallization was widely studied at laboratory scale using the spin-coating process. The conventional crystallization method consists in dropping an anti-solvent on the precursor wet film to trigger the perovskite nucleation. Alternative crystallization methods include thermal annealing [12], gas-quenching [13], plasma curing [14] or vacuum-pumping [15]. When adapted to large-area processing, such as slot-die coating, those solutions are not optimal as they complexify the experimental flow (addition of 1 step) and usually separate temporally the perovskite wet film formation from its crystallization (~ seconds to minutes). Therefore, embedded crystallization tools are desired to trigger the perovskite crystallization while coating the precursor wet film.

Current crystallization methods that can be embedded directly on the coating process are gas-quenching [13] and plasma curing [14]. At the time this work started, such methods had already been well-documented for $MAPbI_3$ perovskite, the parent material of metal halide perovskites. Yet this material has shown limitations in terms of thermal stability, in line with the high volatility of the methyl ammonium cation [16]. In this study, we focused on a methylammonium-free perovskite formulation, $Cs_xFA_{1-x}Pb(I_{1-y}Br_y)_3$, that had not been employed in the combination of gas-quenching and the slot-die coating process at the beginning of this work (see **Chapter I – Table 3**).

- **Objectives of the study**

This work focused on the formation of mixed-halides mixed-cations perovskite via gas-quenching assisted slot-die coating process. It focused on understanding the influence of the perovskite coating parameters, the precursor ink composition and the underlying substrate nature on the slot-die coated layers as well as their impact on perovskite solar cells performances. The final aim of this work is to improve the homogeneity of the perovskite layers over large-area substrates (5 x 5 cm^2 and 10 x 10 cm^2) for good compatibility with photovoltaic modules fabrication.

- **Outline of this manuscript**

In this dissertation, we will introduce the context of perovskite photovoltaics and large-area deposition processes (**Chapter I**) and present the experimental methods used in this work to characterize the perovskite layer properties and resulting device performances (**Chapter II**). Then, we will detail the results of the studies, in three different parts:

- First, we compared the properties of perovskite films deposited by spin-coating and crystallized by the anti-solvent (conventional) method with those of perovskite films deposited by slot-die coating and crystallized by gas-quenching. We integrated those two layers of interest into photovoltaic devices to study the impact of the crystallization on the device performance. This will set an initial diagnosis of the quality of the slot-die coated layers compared to the state-of-the-art spin-coated layers (**Chapter III**).

- Secondly, the effects of ink precursors stoichiometry on the slot-die coated film properties were studied with specific focus on the caesium and formamidinium contents in the precursor ink. We studied the effect of post-annealing on the slot-die coated layers properties. We also integrated the slot-die coated layer with optimal stoichiometry into photovoltaic devices (**Chapter IV**) to unveil the impact of the perovskite material quality on device performance.

- Thirdly, we studied the properties of the slot-die coated films deposited on three state-of-the-art electron transporting layers (planar SnO_2, planar TiO_2 and mesoporous TiO_2) to assess the compatibility of the slot-die coating process with various substrates and its device integration into various state-of-the-art device structures. We also studied the performance distribution of devices fabricated at various locations of a 10 x 10 cm^2 substrate and eventually demonstrated a proof-of-concept photovoltaic module (**Chapter V**).

Finally, we conclude the dissertation by providing insights on the relevance of these results to the field, followed by proposing future perspectives of this work.

- **Work undergone**

This work started in CEA INES laboratory in April 2018. The first research direction consisted in identifying the process window (see **Chapter III**) and the perovskite ink formulation (see **Chapter IV**) to permit the deposition of compact slot-die coated films. In February 2019, the optimized ink was transferred on a second slot-die coating equipment in NTU laboratory. The entire workflow presented in this thesis was performed in both laboratories from 1) ink preparation, 2) substrates preparation, 3) slot-die coating of the absorber, 4) material characterization, 5) device completion and 6) device measurement. The notable differences between both workplaces were the substrate size, slot-die coating equipment and device structure employed (see **Chapter II**). In total, two periods of 6 months have been spent in the NTU laboratory (Feb-Aug 2019 and 2020) in the frame of this work.

Chapter I: State of the art

This chapter introduces metal halide perovskites and their utilization as semiconductors for photovoltaic applications. It describes the solution processing methods available to deposit perovskite wet precursor films over large areas. It presents the existing strategies to control the perovskite crystallization and discuss their applicability to large-area films. Finally, it reports the influence of the perovskite precursor ink composition, substrate temperature and nature on the perovskite film morphology and perovskite solar cells performance.

I.1. Metal halide perovskites for PV applications

The organic-inorganic metal halide perovskites have recently emerged as a promising light-absorber family for photovoltaic applications with power conversion efficiencies reaching 25.5% in 2020 [10]. Here, we present the main material properties of the metal halide perovskite thin films and introduce the fabrication and operation of perovskite photovoltaic devices. This promising technology, yielding high performance at laboratory scale (**Figure 1**), faces challenges towards industrialization as the deposition processes of the metal halide perovskite layer and other device stack layers lack of technological maturity.

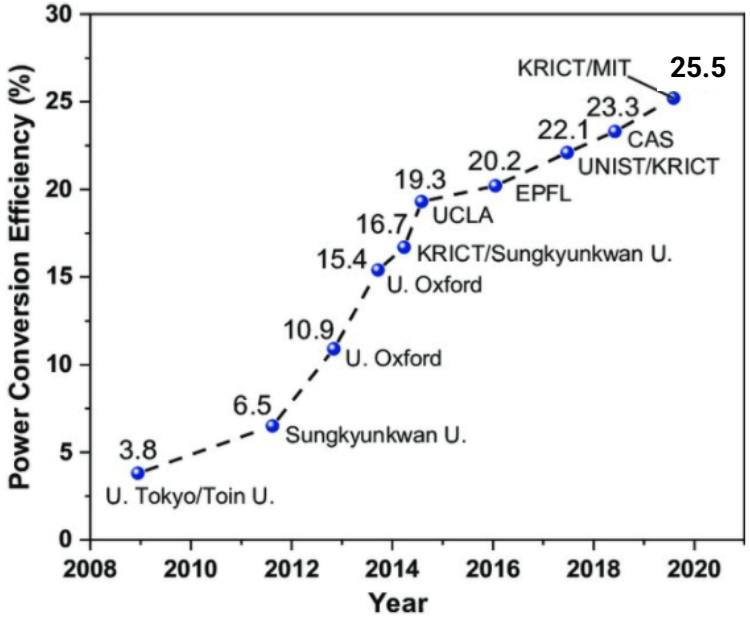

***Figure 1**: Evolution of the perovskite solar cells performances since 2009 [17–25,10].*

I.1.1. Inorganic-organic metal halide perovskites

- **Perovskite crystalline structure**

Perovskite is the name of the crystalline structure originally describing calcium titanate ($CaTiO_3$) mineral and with a more general formula ABX_3. The German crystallographer Gustav Rose identified this crystalline structure and named it after the Russian mineralogist Lev Perovski in 1839. Metal halide perovskites have emerged in 2009 [17] and correspond to materials where the oxygen is replaced by an halogen in the X site (**Figure 2**). Metal halide perovskites are typically composed of an organic cation (*e.g.* methylammonium, MA^+) in the A site, a divalent metal cation (*e.g.* Pb^{2+}) in the B site and halides anions (*e.g.* I^-) in the X site to form a metal halide perovskite material (*e.g.* $MAPbI_3$).

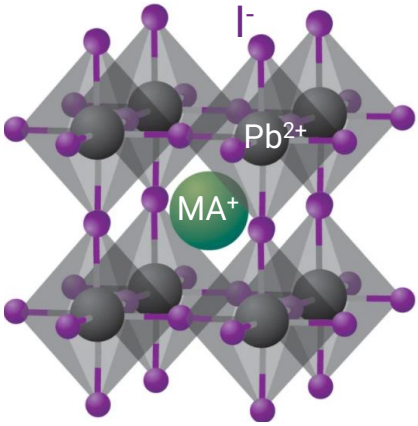

***Figure 2**: Crystalline structure of the $MAPbI_3$ perovskite. Schematics adapted from reference [26]. MA^+ is the methylammonium cation, Pb^{2+} the lead cation and I^- the iodide anion.*

A particularity of ABX_3 perovskites is that the A, B and X sites can be occupied by a range of chemical elements or even combinations of them under certain conditions. Goldschmidt described in 1926 an indicator, named tolerance factor, that express the ability to form a cubic or pseudo cubic ABX_3 structure from the candidate ions radius ratios [27]. The tolerance factor was described by the formula:

$$\alpha = \frac{rA+rX}{\sqrt{2}(rB+rX)} \qquad (E_1)$$

where r_i are the ionic radii of the ions (A, B and X) constituting the ABX_3 lattice. Their values can be estimated from ionic radius values or using steric sizes estimated by Density Functional Theory (DFT) calculations [28,29]. Goldschmidt describes that a cubic or pseudo cubic structure can form for a tolerance factor $0.8 \leq \alpha \leq 1$ for perovskite oxides. This formula is also valid for metal halide perovskites, confirmed by the observation of pseudo cubic structures for $0.8 \leq \alpha \leq 0.9$ [28] and cubic structures for $0.9 \leq \alpha \leq 1$ [28] in the literature. For tolerance factors exceeding 1, the presence of polymorphs has been reported in metal halide perovskites [28] similarly to perovskite oxides.

Metal halide perovskites differentiate themselves from oxide perovskites by their semi-conducting properties [17]. They usually exhibit a direct band gap [30,31] and both valence and conduction band levels can be adjusted by tuning the perovskite ABX_3 composition (**Figure 3**). In particular, the substitution of the methylammonium cation (MA^+) by the formamidinium cation (FA^+) can reduce the band gap energy from E_g = 1.57 eV ($MAPbI_3$) to E_g = 1.48 eV ($FAPbI_3$), closing the gap to the single junction photovoltaics optimum band gap of 1.4 eV [32]. Similarly, the methylammonium cation (MA^+) can be substituted by the caesium cation (Cs^+) to form full inorganic $CsPbI_3$ metal halide perovskite with a larger band gap (E_g = 1.73 eV [33]). In the X site, the substitution of the iodide anion (I^-) by the bromide anion (Br^-) can progressively increase the metal halide perovskite band gap from 1.57 to 2.29 eV [34].

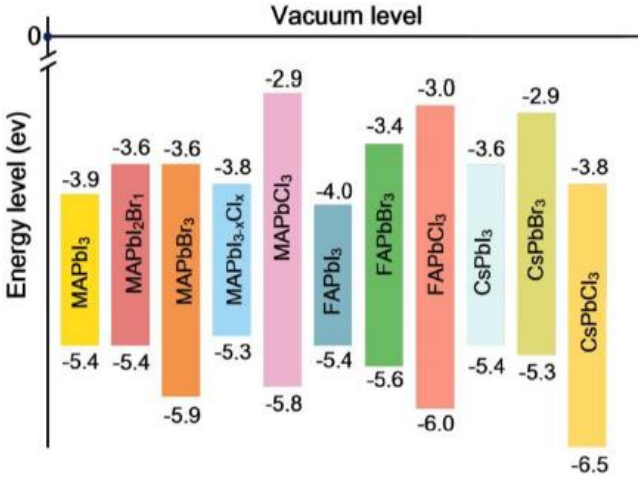

***Figure 3**: Metal halide perovskites energy levels for various compositions. Schematics reproduced from reference [35].*

The modification of A cation size (Cs^+ 188 pm ≤ MA^+ 217 pm [28] ≤ FA^+ 253 pm [28]) can modify the structure tolerance factor (0.81 ≤ 0.92 ≤ 0.98 respectively) (**Figure 4**). According to Goldschmidt theory, the $FAPbI_3$ and $MAPbI_3$ perovskite (tolerance factor ≥ 0.9) are more likely to form a cubic structure compared to the $CsPbI_3$ perovskite (tolerance factors ≤ 0.9).

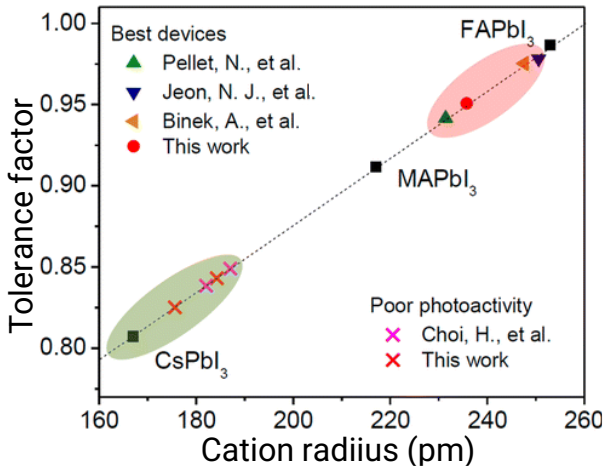

***Figure 4**: Tolerance factor of ABX_3 metal halide perovskites depending on the A cation size [36].*

In fact, the formation of polymorphs has been observed even for metal halide perovskites with tolerance factors above 0.9. More specifically, at ambient temperature, the crystallization of $MAPbI_3$ perovskite can result in the formation of tetragonal and cubic structures [37] and the crystallization of $FAPbI_3$ in the formation of a cubic structure (α-phase) and a hexagonal structure (δ-phase or yellow phase).

The $FAPbI_3$ perovskite under the cubic structure exhibits the most suitable band gap for simple junction perovskite devices (E_g = 1.47 eV). The $FAPbI_3$ cubic structure is composed of a network of corner-sharing [PbI_6^{4-}] octahedra. However, the cubic polymorph coexists with the hexagonal polymorph, composed of face-sharing [PbI_6^{4-}] octahedra (**Figure 5**) [32,38,39] and exhibiting a band gap of 2.36 eV [40], which is not suitable to photovoltaic application.

In brief, the selective formation of $FAPbI_3$ perovskite under the cubic structure is required to obtain a performant photovoltaic absorber.

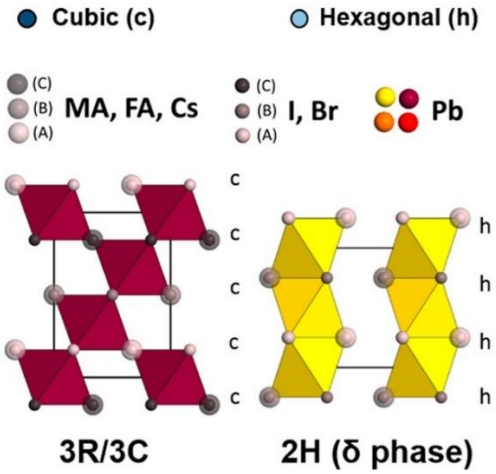

***Figure 5**: $FAPbI_3$ perovskite cubic and hexagonal (or delta phase) structures. Schematics reproduced from reference [41].*

The cubic $FAPbI_3$ structure is thermodynamically stable for temperatures over 185 °C [38,42]. To thermodynamically favour its formation at lower processing temperatures (T ≤ 100 °C), cations and/or anions mixing strategies have been developed [36]. In 2016, the mixture of formamidinium cation (FA^+), methylammonium cation (MA^+), caesium cation (Cs^+) in the A site and of iodide anion (I^-) and the bromide anion (Br) in the X site enabled the selective formation of the 'triple cation mixed halides' perovskite ($MA_{1-x-y}FA_xCs_yPb(I_{1-y}Br_y)_3$) under a cubic structure [40,16,43]. In the literature, the perovskite composition engineering resulted into significant enhancement of the device power conversion efficiency from 2013 to 2017 (**Figure 6**). Today, state-of-the-art $FAPbI_3$-based perovskites contain usually two or more cations and two or more anions to facilitate the $FAPbI_3$ cubic structure formation via low-temperature solution processing. The mechanism of the caesium cation substitution with be detailed in the section **I.3.2**.

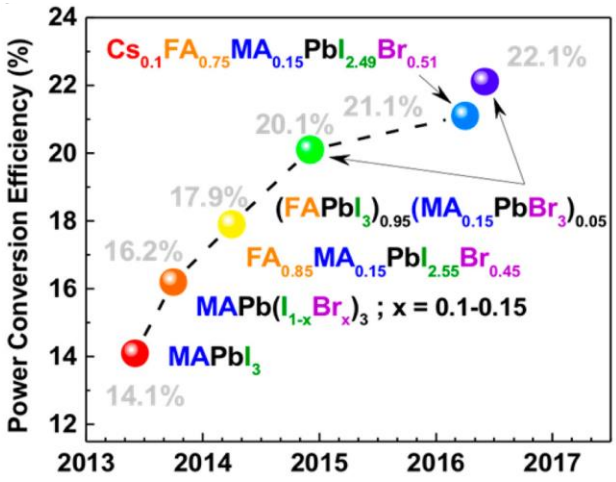

***Figure 6**: Role of perovskite composition engineering in the power conversion efficiency trend. Schematics reproduced from reference [44].*

- **Perovskite opto-electronic properties**

A good photovoltaic (PV) material should combine efficient light absorption and charge transport abilities. Metal halide perovskites exhibit a high absorption coefficient (10^4 – 10^5 cm^{-1} for $MAPbI_3$ [45]), which is comparable to other thin films technologies (CdTe, CIGS) and one order of magnitude higher than crystalline silicon. The electrons and holes have a long charge carrier diffusion length (up to 1 μm [46]), making a perovskite layer of few hundreds nanometres suitable for integration in photovoltaic devices [19,47]. These properties are remarkable for a solution-processable semiconductor and explain the growing interest of the PV community.

In semiconductors, the charge extraction and transport can be limited by charge recombination when a defect is present in the material lattice or between grains in multi-crystalline films [48,49]. When a charge carrier (*e.g.* an electron) encounters a defect, it is energetically stabilized and 'trapped' into this defect (or trap state). The defects density and nature (energy level) will influence the charge transport and impact the photovoltaic performance.

The steepness of the absorption curve can inform on the level of energetical disorder in the material. The absorption curve can be fitted with an exponential decay in the region below the band gap energy to extract the characteristic energy called Urbach energy [50]. The higher the Urbach energy, the more energetic disorder in the material. Metal halide perovskites exhibit lower Urbach energy (15 meV) compared to CIGS (25 meV) but higher than CdTe (10 meV) and GaAs (7 meV). Similarly, the measurements of trap state density in metal halide perovskites (10^{16} – 10^{17} cm^{-3} in poly-crystalline films and 10^9 – 10^{11} cm^{-3} in single crystals), concluded to similar defect density compared to other semiconductors (CdTe 10^{13} – 10^{16} cm^{-3}; CIGS 10^{11} – 10^{15} cm^{-3}; GaAs 10^{13} – 10^{15} cm^{-3}) [51,52].

Despite the similar level of defects in the film, metal halide perovskites exhibit significantly higher photoluminescence efficiency, with predominant radiative recombination pathways which is desirable for performant photovoltaic devices. This difference in photoluminescence has been explained by the energy level distribution of trap states in metal halide perovskites [53]. Generally, defects can be energetically located close to the conduction and valence band (shallow traps) or in the middle of the band gap (deep traps) (**Figure 7**).

For semiconductors materials such as CIGS, CdTe or GaAs, deep trap states are predominant (located in the middle of the band gap), and lead to non-radiative charge recombination [53]. In metal halide perovskites, the trap states are rather located close to the conduction and valence band levels which limits the non-radiative recombination pathways. In this sense, metal halide perovskites are said to be defect-tolerant [53]. This 'defect tolerance' of metal halide perovskites could explain the high charge carriers lifetimes and photovoltaic devices performances [54,55] obtained using this solution-processed multi-crystalline semiconductor.

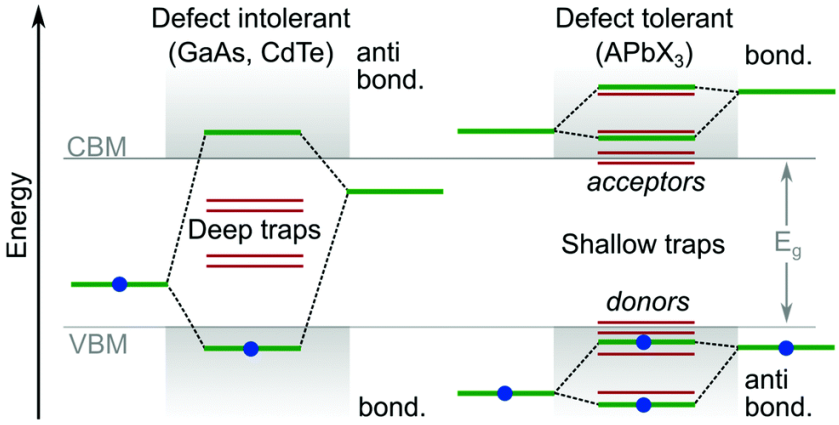

***Figure 7**: Defects states energy level in defect-intolerant and defect tolerant (perovskite) semiconductors [56].*

I.1.2. Perovskite solar cells

- **Device operation**

A photovoltaic device is composed of a semiconductor material that absorbs a photon, transforms it into an electron-hole pair [57] and allows charge carriers transport until their collection. This semiconductor material can be implemented in a p-n junction (c-Si, CdTe, CIGS) or in a p-i-n junction (Perovskite) to extract the charge carriers. In a p-n junction, both sides of a semiconductor layer are doped (p or n-type respectively), which generates an electric field in the material. Under this electrical field, the charge carriers are drifted until they get extracted at the device interfaces.

In a p-i-n (or n-i-p) junction, there is an intrinsic (i) area between the n-type and p-type areas. Metal halide perovskites are considered intrinsic semiconductors as they do not require to be doped to conduct the electrons and holes. In a (p-i-n) structure, the charge carriers generated into the absorber (i) move by diffusion until their selective extraction by an electron transporting material (n-type) and a hole transporting material (p-type). The name of the device configuration depends on the side of illumination: from the hole transporting material (p-type) in (p-i-n) structure or from the electron-transporting material (n-type) for (n-i-p

structure). We note that n-type (or p-type) materials are not necessary n-doped (p-doped) but are designed as such as a convention.

In perovskite solar cells (n-i-p or p-i-n configurations), the final structure is composed of the perovskite absorber sandwiched by an electron-transporting layer (ETL) and a hole-transporting layer (HTL), themselves sandwiched between two electrodes. Under illumination, a voltage is generated at the device terminal (**Figure 8b**).

Historically, the electron-transporting material (ETL) was mesoporous TiO_2, derived from the dye sensitized solar cell structure [17,18]. Miyasaka *et al.* demonstrated the first metal halide perovskite solar cell was using the perovskite material as a dye coated on mesoporous TiO_2 ETL [17]. Over the past decade, planar structures have emerged [47] (**Figure 8b**) thanks to the increasing understanding of the metal halide properties, such as its ambipolar behaviour and charge carriers diffusion length. High device performance has been achieved for a range of various device architectures, including (n-i-p) planar and mesoporous and (p-i-n) planar structures [58]. The specific role of the ETL material in (n-i-p) device configuration will be detailed in section **I.4**.

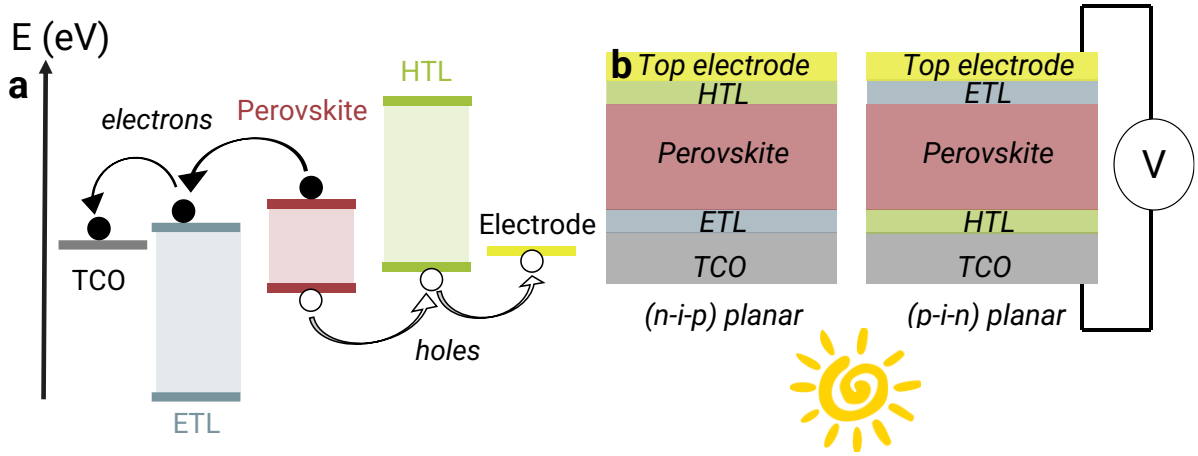

***Figure 8**: **a)** Perovskite solar cell operation. **b)** The two main device structures studied in the literature for perovskite solar cells [59].*

- **Power conversion efficiency**

The performance of a photovoltaic device is measured by its power conversion efficiency, defined by the ratio between converted electricity and the incident photon energy. Depending on the incoming photon energy, the absorber band gap will determine if the photon is absorbed or not. Photon with energy lower than the band gap cannot be absorbed and do not contribute to the charge generation in the absorber. If the incoming photon has an energy superior to the band gap, it will be absorbed into the absorber and generate charges. The energy difference between the photon energy and the absorber band gap will be loss by thermalization.

Shockley and Queisser [60] defined the maximum theoretical power conversion efficiency ('power out') for a single junction by calculating those various losses in function of the absorber band gap (**Figure 9a**). A maximum theoretical power conversion efficiency of 33.7% could be achieved at a band gap of 1.34 eV for a single junction solar cell, relatively close to the formamidinium based metal halide perovskite band gap (1.47 eV). Experimentally, other parameters limit this theoretical efficiency, such charge carrier recombination and light parasitic absorption [61]. The theoretical efficiency limit has been estimated to 27% [31] for $MAPbI_3$ material (with 1.6 eV band gap). The experimental record efficiency of 25.5% was obtained using mixed perovskite (band gap 1.56 eV) in 2020 [62] (**Figure 9b**).

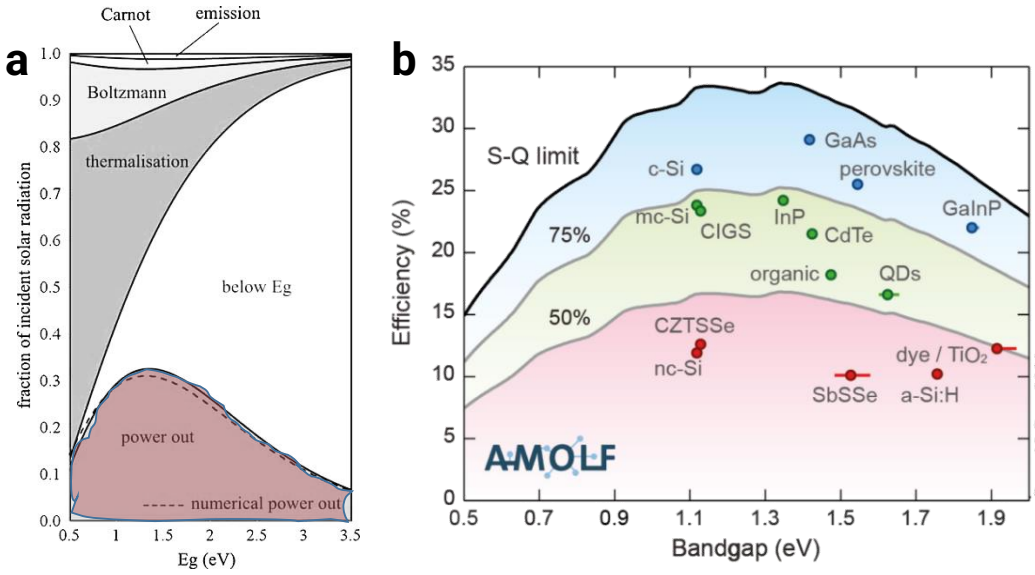

***Figure 9**: **a)** Intrinsic losses in single junction solar cells [63]. **b)** Shockley-Queisser (SQ) limit for a single junction: maximum power conversion efficiency in function of the absorber band gap. [64,65].*

I.2. Large-area perovskite processing: wet film deposition and control of perovskite crystallization

The last years have witnessed rapid development of scalable deposition techniques to address the challenge of fabricating large-area perovskite photovoltaic modules. This section introduces the various processes to deposit metal halide perovskites from the non-scalable to scalable methods and aims to introduce the perovskite crystallization bottleneck faced by the scalable deposition techniques. In the literature, both dry (thermal evaporation) and wet (solution-processed) deposition method exist [66,67]. Here, we decided to focus only on the wet deposition processes, which are particularly attractive for their simplicity of implementation and cost-effectivity.

I.2.1. Precursor solution composition

In a wet deposition process, a precursor wet film is deposited onto the substrate and subsequently crystallized by various means. For $MAPbI_3$ perovskite, the precursor solution is typically composed of methylammonium iodide (MAI) and lead iodide (PbI_2) powders dissolved in a mixture of dimethylformamide (DMF) and dimethylsulfoxide (DMSO). For mixed-cations perovskites, the methylammonium iodide (MAI) can be totally or partially replaced by formamidinium iodide (FAI) or caesium iodide (CsI) respectively. For anions substitutions, the bromide element can be induced by lead bromide ($PbBr_2$) and/or methylammonium bromide (MABr) addition [58,68]. Numerous other precursors type and combinations are available, but we will focus on these six precursors that lead to the highest device performances [58].

I.2.2. Scalable methods to deposit the wet precursor film

Spin-coating is a conventional process to deposit metal halide perovskites. A wet drop of the precursor ink, containing the cations and anions salts dissolved in organic solvents, is deposited onto the substrate that is subsequently driven into rotation to eject the solution by centrifuge effect and form a wet precursor thin film. The precursor wet film thickness depends on the spinning speed and precursor ink viscosity [69]. This method is accessible and easy to implement in a research laboratory. It is, however, not material efficient (99% of the precursor solution is ejected during the spinning step) and does not lead to homogeneous film thicknesses over large areas due to the centrifuge effect. Consequently, scalable processes are needed to deposit the wet perovskite precursor film without relying on the centrifuge effect. Alternative technologies to deposit the precursor wet film over large areas are based on the ejection of ink droplets (spray coating and inkjet coating), on meniscus-assisted coating (slot-die coating and blade coating) or on patterned deposition (screen-printing or gravure printing) (**Figure 10**).

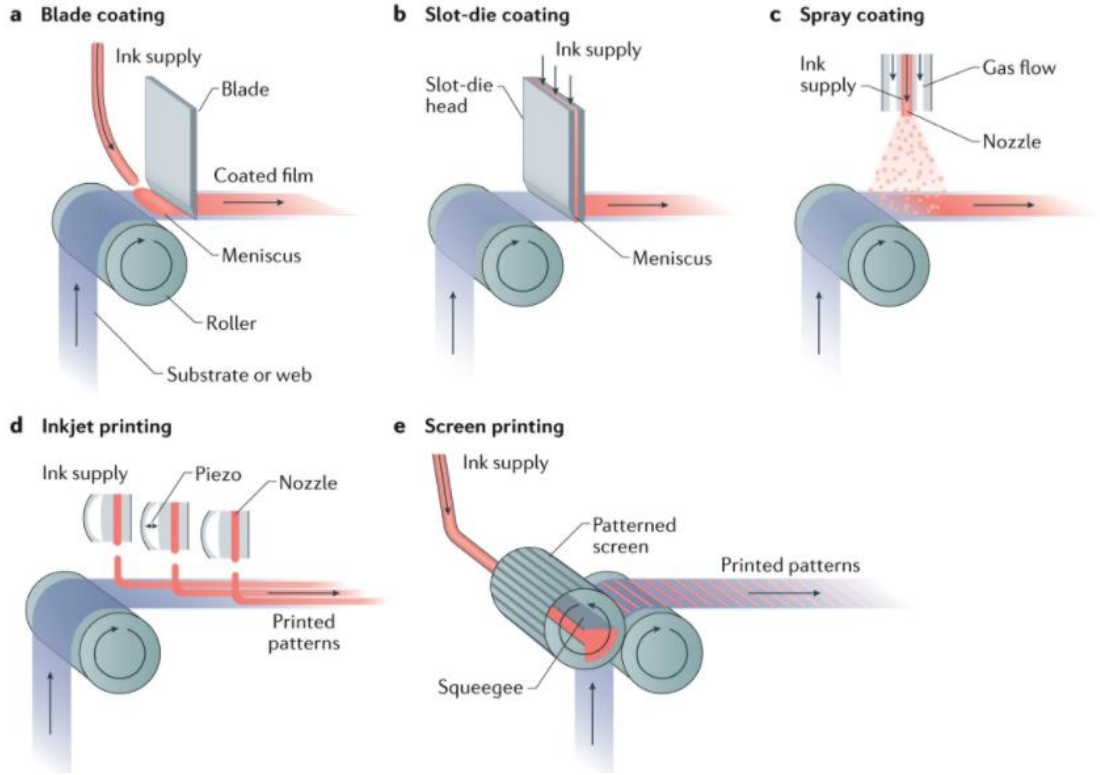

***Figure 10**: Scalable deposition processes for the deposition of large-area thin films. Schematics reproduced from reference [70].*

These deposition techniques have various characteristics (**Table 1**). Spray-coating, slot-die coating and screen-printing have high throughputs (~ 0.1 $m^2.min^{-1}$). Screen-printing or inkjet-printing provides a higher customization level as they can form 2D patterns. Slot-die coating achieves the highest film thickness control (± 5%). Inkjet-printing requires narrower ink viscosities range, compared to spray-coating, meniscus-assisted coating or screen-printing. The screen-printing method is the only method where a physical contact with the substrate is necessary. Slot-die (and blade-coating) require a proximity with the substrate (~ µm) but no direct contact except from the fluid meniscus. Inkjet- and spray-printing are non-contact methods that are performed further away from the substrate (~ cm).

Process	Pattern control	Throughput ($m^2.min^{-1}$)	Thickness control	Ink complexity	Contact/non-contact
Spray	1D	0.12 [14]	average	average	non-contact
Inkjet	2D	0.000025 [71]		high	
Screen-printing		~ 0.1 [72]		low	contact
Slot-die/Blade-coating	1D	0.18 [73]	high		non-contact

***Table 1**: Comparison of the scalable deposition techniques with their characteristics.*

Currently, the most popular precursor wet film deposition methods are blade-coating and slot-die coating due to their good thickness homogeneity over large-area substrates [74,75] and to their compatibility with a wide variety of perovskite precursor inks [76–79].

I.2.3. Methods to control the perovskite crystallization

Once the wet precursor film deposited by a scalable method, it needs to be crystallized. The most common mean to control the perovskite nucleation in the spin-coating process is to add an 'anti-solvent quenching' step [80] (**Figure 11**), in which the wet precursor film is washed with a solvent that reduces the solubility of perovskite crystals, triggering a fast and dense nucleation [80]. The growth of the crystals is then induced by a subsequent thermal annealing step on a hotplate. This is the crystallization mean employed to fabricated most of the perovskite solar cells today, in particular those achieving the highest device performances [62].

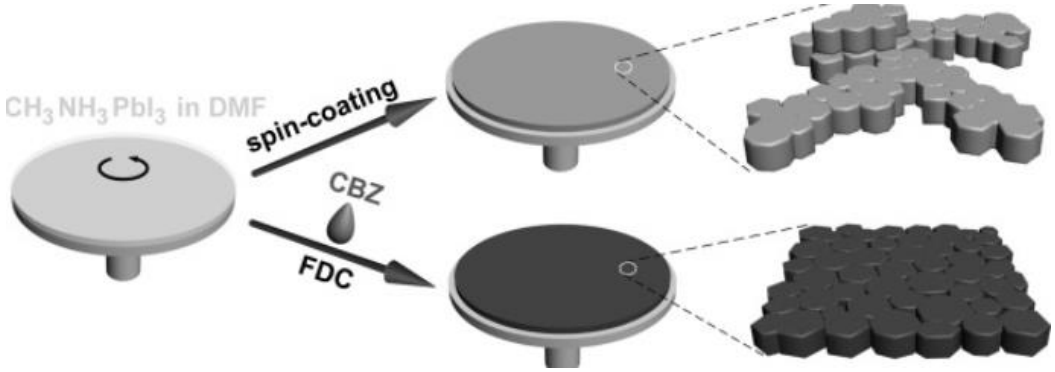

***Figure 11**: Comparison of perovskite film morphology with and without anti-solvent (chlorobenzene) quenching. Schematics reproduced from reference [80]. CBZ stands for chlorobenzene, FDC for fast crystallization-deposition and DMF for dimethylformamide.*

For scalable deposition techniques, this anti-solvent quenching technique cannot be directly transferred as it relies on the centrifuge effect and should be performed immediately after the wet film precursor deposition (challenging batch to batch processing). In the industry, no obvious solution stands out, in contrast to the scalable wet film deposition techniques. The lack of scalable way to control the crystallization is explained by the fact that the parent organic photovoltaic and DSSC technologies did not require this degree of control during the absorber layer deposition (**Figure 12**).

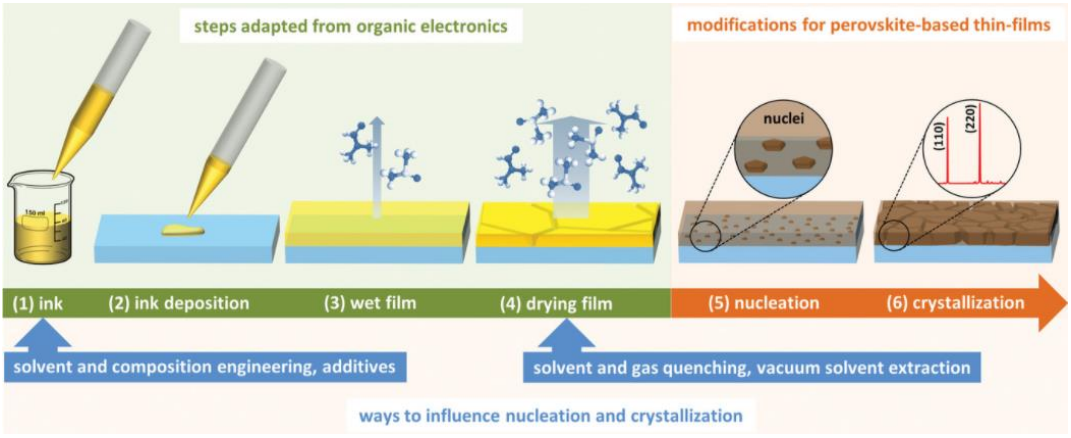

***Figure 12**: Description of a precursor wet film deposition and crystallization. Scheme reproduced from Howard et al [81].*

Therefore, new solutions must be developed to trigger the perovskite crystallization in the wet precursor film deposited *via* scalable processes. Galagan *et al.* [12] applied in-line thermal annealing to roll-to-roll slot-die coated precursor films, yielding a compact morphology with dendritic grain structure (**Figure 13a**). Besides thermal annealing, anti-solvent bathing has been applied to bladed-coated [82], spray-coated [83], slot-die coated [72] or screen-printed [72] precursor wet films to enhance the film morphology. Vacuum pumping combined with thermal annealing has been applied to meniscus-printed films [84] to effectively remove the solvent and obtain a compact morphology. Furthermore, Cotella *et al.* [85] and Hwang *et al.* [86] used a gas-knife to immediately dry the slot-die coated wet film via gas-quenching (**Figure 13b**). With the same embedded approach, Rolston *et al.* [14] applied plasma curing to spray-coated precursor wet films (**Figure 13c**). Besides plasma radiation, Troughton *et al.* [87] used flash Infrared (IR) radiations to crystallize spin-coated precursor films (**Figure 13d**) [88].

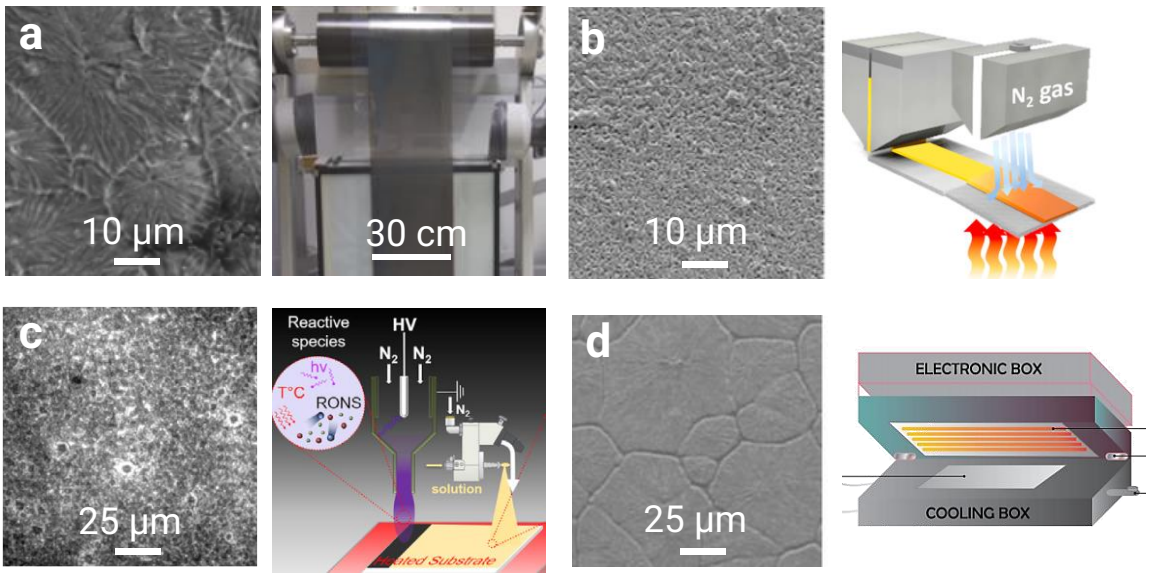

***Figure 13**: Large-area crystallization methods and resulting perovskite film morphologies (SEM pictures): **a)** Roll-to-roll slot-die coating with thermal annealing post treatment [12]. **b)** Sheet-to-sheet slot-die coating with gas quenching [86]. **c)** Spray-coating with plasma assisted crystallization [14]. **d)** Spin-coating with flash infrared annealing [88].*

Among those approaches, the gas-quenching technology stands out due to its simplicity of implementation. Indeed, it does require neither energy nor chemicals to be implemented, in contrast with the other methods (**Table 2**). Regarding the perovskite morphology, the gas-quenching enabled a fast solvent evaporation and resulted in dense and granular morphology (**Figure 13b**), in contrast to the slow solvent evaporation induced by a thermal annealing that results in dendritic grains (**Figure 13a**).

Crystallization method	Energy	Waste	Perovskite morphology
Thermal annealing	Yes	No	dendritic
Solvent bathing	No	Yes (solvents)	granular
Gas-quenching	No	No	granular
Infrared curing	Yes	No	granular
Plasma curing	Yes	No	-

Table 2: *Comparison of the embedded crystallization approaches.*

I.2.4. Gas-knife quenching method

In the gas-quenching assisted crystallization, a gas (air or nitrogen) is blown on top of the wet precursor film to fasten the solvent evaporation, until the precursor solution reaches the super saturation and starts to nucleate. Conings *et al.* introduced the gas-quenching for spin-coated films of $MAPbI_3$ and mixed compositions in 2016 [13] (**Figure 14a**). From a practical point of view, a variety of systems have been implemented to perform the gas-quenching step [77,89–91]. For instance, Li Li Gao *et al.* [92] developed an air blading system with multiple air flows to adapt this technique to blade-coated precursor films (**Figure 14b**). Finally, in 2018, Vak *et al.* [86] applied this technique to slot-die coating, by embedding a gas-knife behind the slot-die coating head (**Figure 14c**).

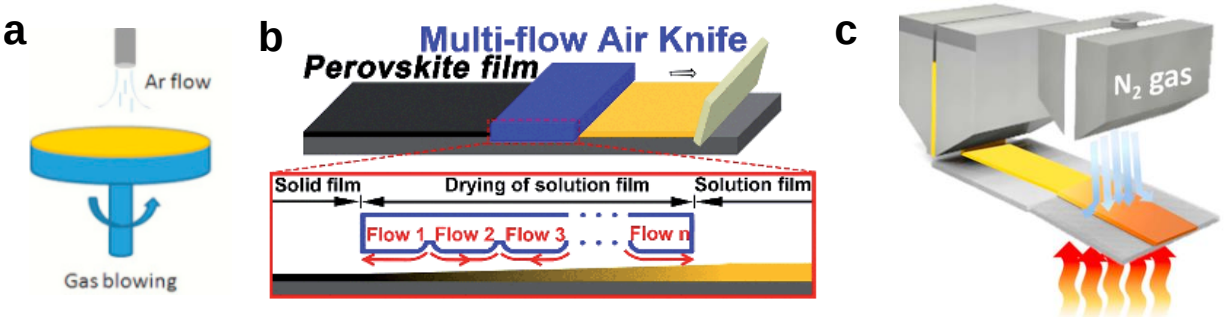

Figure 14*: Evolution of gas-quenching methods from 2014 to 2018.* ***a)*** *(2014) Nitrogen gun on spin-coated films [89].* ***b)*** *(2016) Complex air knife system for blade coated precursor films [92].* ***c)*** *(2018) First report of a simple gas-quenching tool used for slot-die coated precursors films [86].*

To understand the gas-quenching mechanism, diverse approaches are present in the literature. First, a fluid mechanics approach in which the solvent evaporation is fasten by the solvent molecule diffusion in a boundary layer close to the wet precursor film [93] (**Figure 15a**). Furthermore, the perovskite nucleation could be assimilated to a homogeneous nucleation, and described by the LaMer burst nucleation model [94] in which nucleation depends on the degree of super saturation of the solute in the precursor film (C*). More specifically, Hu *et al.* [95] described the gas-quenching as a trigger of fast numerous nucleation

(Figure 15b), reaching the solution super saturation in few seconds which results in compact granular morphology in the resulting perovskite films.

Finally, Nogueira *et al.* [96] studied the gas-quenching phenomenon from a solution chemistry perspective, by in-situ monitoring of the species forming during the gas-quenching step (**Figure 15c**). Their study show that the gas-assisted crystallization has a different kinetic and form different intermediate species in solution, compared to the conventional anti-solvent assisted crystallization. All those approaches are supplementary to grasp the physical and chemical mechanisms behind the gas-assisted perovskite crystallization.

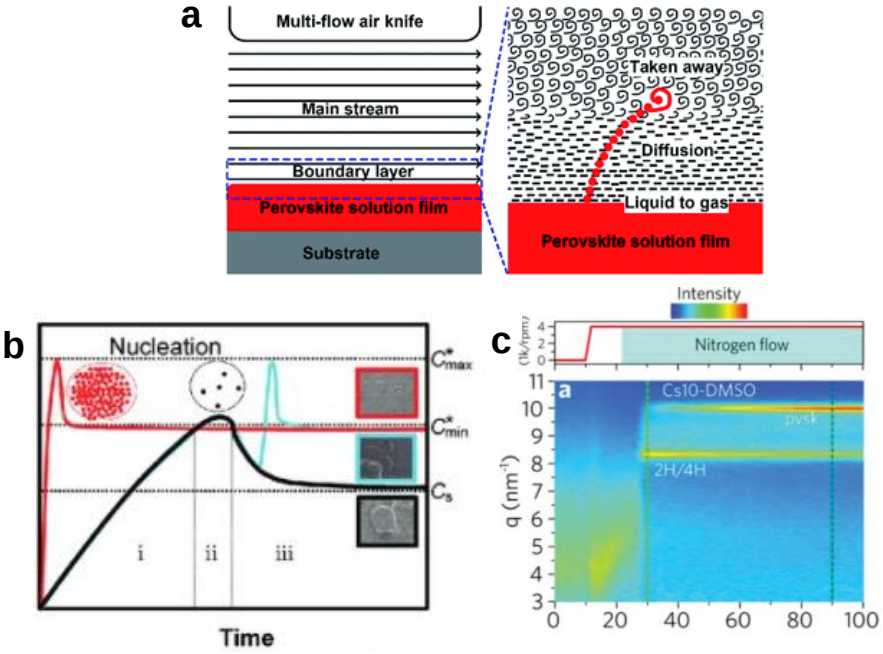

***Figure 15**: Understanding of the gas-quenching crystallization in terms of: **a)** Solvent diffusion [93], **b)** LaMer nucleation and growth model [95] and **c)** Crystalline species formation in the precursor film monitored by GIWAXS [96].*

Beside of the process employed, other factors such as the precursor ink composition and the underlying substrate properties can affect the perovskite film quality (morphology, band gap and crystallinity), hence the performance of perovskite solar cells. The main relationships between the precursor ink composition and perovskite layer properties will be introduced now.

I.3. Influence of the precursor ink on the perovskite film properties and device performances

In the wet precursor film, the concentration of the species in solution and the properties of the solvents (boiling point, solute interaction) will determine the rate of solvent evaporation and the kinetics and thermodynamics of the perovskite nucleation. We will see here how the precursor ink concentration, stoichiometry and solvent system affect the resulting perovskite film properties.

I.3.1. Impact of the precursor ink concentration

For a given wet film thickness, the higher the precursor ink concentration, the more concentrated the perovskite precursors in the wet film, and hence the thicker the dried perovskite film after solvent removal. In the literature, Rai *et al.* tuned the precursor concentration from 0.4 M to 1.4 M to adjust the $Cs_{0.2}FA_{0.8}Pb(I_{0.85}Br_{0.15})_3$ perovskite film thickness from 70 nm to 630 nm respectively (**Figure 16a inset**) [97]. The concentration range upper limit depends on the solubility of the perovskite precursors in solution, which is comprised between 1 and 1.8 M (for $MAPbI_3$) and depends on the DMF:DMSO ratio [98]. Besides the precursor concentration, process parameters such as the rotation speed [99] in the spin-coating process, the coating speed [59] in the blade-coating process or the substrate temperature and number of passes [100] in the spray-coating process can influence the perovskite film thickness.

When implemented into a photovoltaic device, a too thin perovskite film will absorb a limited part of the incident light, and lead to a reduced current density (**Figure 16b,** concentrations from 0.4 to 0.8 M). A thicker perovskite film would absorb more incoming light, which can result in higher current density. However, as the thickness increases, the perovskite material quality might not be maintained if the deposition conditions are not adjusted. Hence, thicker absorbers can exhibit lower performances (**Figure 16a**, concentration 1.4 M). Overall, the optimal perovskite thickness maximizing the device performances depends on the perovskite composition or deposition process employed.

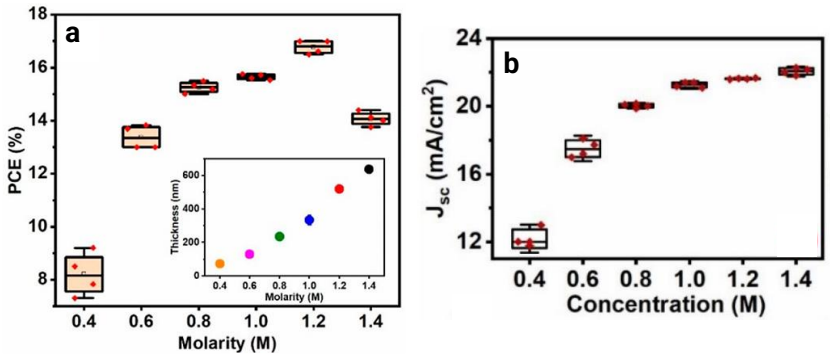

***Figure 16**: Evolution of **a)** the device performances (inset: perovskite thickness) and of **b)** the device current density for precursor ink concentrations ranging from 0.4 to 1.4 M [97].*

I.3.2. Impact of the stoichiometry: Cs^+ cation

Besides the film thickness, the perovskite crystalline quality will influence the device performances. As introduced earlier, the challenge in the crystallization of $FAPbI_3$ material is the selective formation of the $FAPbI_3$ cubic structure (also named α-phase). In spin-coating process with anti-solvent [16] or gas-quenching [96] crystallization, and more recently in slot-die coating processes [12], the addition of the caesium cation (Cs^+) *via* the CsI precursor facilitated the perovskite cubic structure formation. With its small size, the caesium cation can be inserted into the perovskite lattice [16]. This is to contrast with other cations that can be used for stabilization purposes such as rubidium (Rb^+) and are not inserted into the perovskite crystalline structure [101]. At first, the perovskite formation was described by Hu *et al.* [102] as organized [PbI_6^{4-}] cages in solution that could assemble to form MAI-PbI_2-DMF intermediates for $MAPbI_3$ perovskite fabricated using the DMF solvent. Similarly, Xu *et al.* [103] reported the formation of the FAI-CsI-PbI_2 intermediate for caesium containing $FAPbI_3$ perovskite, reinforcing the role of caesium in the solution chemistry of the wet precursor film.

Thanks to recent in-situ monitoring studies, the intermediate species in solution have been identified as polytype structures made of [PbI_6^{4-}] octahedra. Gratia *et al.* [41] defined those polytypes with the Ramsdell notation [104] ('2H', '4H', '6H', '3R'), commonly used to classify oxide perovskite polytypes, and classified here according to the connection between the [PbI_6^{4-}] octahedra *via* either face or corner sharing (**Figure 5**). The 2H polytype corresponds to the hexagonal perovskite phase (or δ phase). Usually, hexagonal polytypes structures have tolerance factors superior to 1 and their appear in sequence: '2H - 4H - 6H' before converting into the cubic 3C structure (**Figure 17a**). Interestingly, Gratia *et al.* found that 3% caesium enables the direct formation of the cubic 3C structure from the '2H' polytype. Another study by Nogueira *et al.* [96] has confirmed the effect of caesium in suppressing the '2H' and '4H' polytypes when 40% caesium was added (**Figure 17b**).

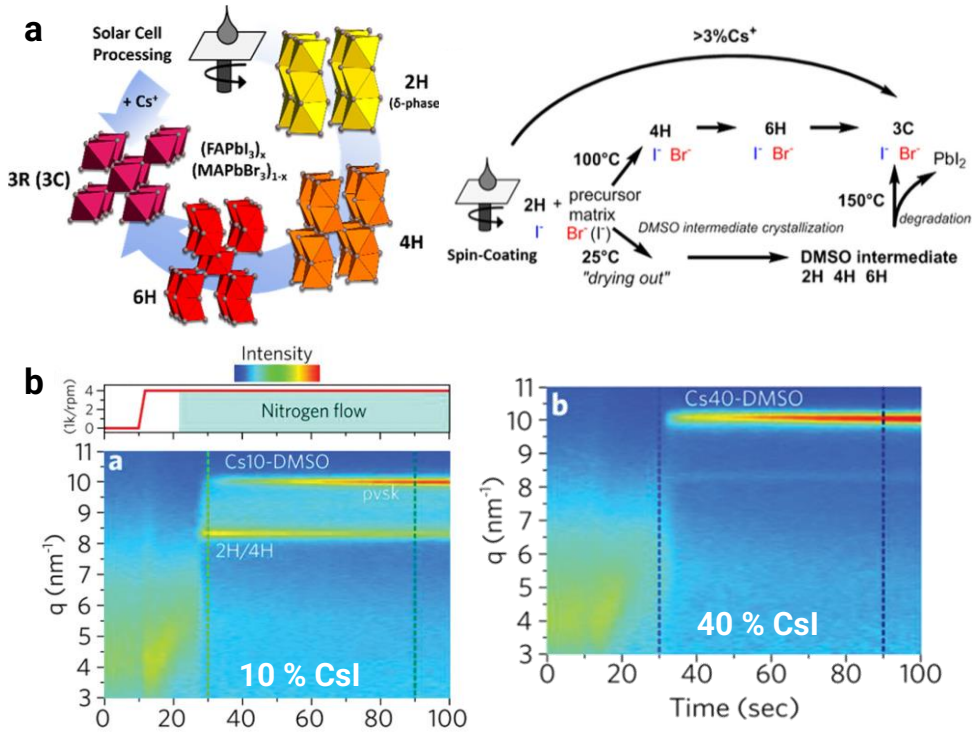

***Figure 17**: Role of caesium during the perovskite crystallization: **a)** Effect on the solution intermediate formation, the caesium presence inhibits the formation of some polytypes from 3% caesium [41]. **b)** Monitoring of the intermediate formation by grazing-incidence wide-angle X-Ray scattering (GIWAXS) for 10 and 40% of caesium [96].*

The effect of caesium on the perovskite structure formation is visible on the performances of photovoltaic device fabricated from precursor solutions containing various caesium contents. Even if the caesium stabilization effect has been observed from 3% caesium (Gratia *et al.*, 2017), the caesium content leading to maximum power conversion can vary from 5% caesium (**Figure 18a**) to 17% (**Figure 18b**), depending on the bromide content in the perovskite formula (20 to 40% respectively). For alternative crystallization means (*e.g.* gas-quenching), the caesium content leading to the best performance may differ (30% in **Figure 18c**). In summary, the caesium content in the precursor ink plays an important role in the precursor chemistry during the wet precursor film evaporation. The caesium content maximizing device performance depends on the perovskite formula (bromide content), the solvent system and the quenching mean employed.

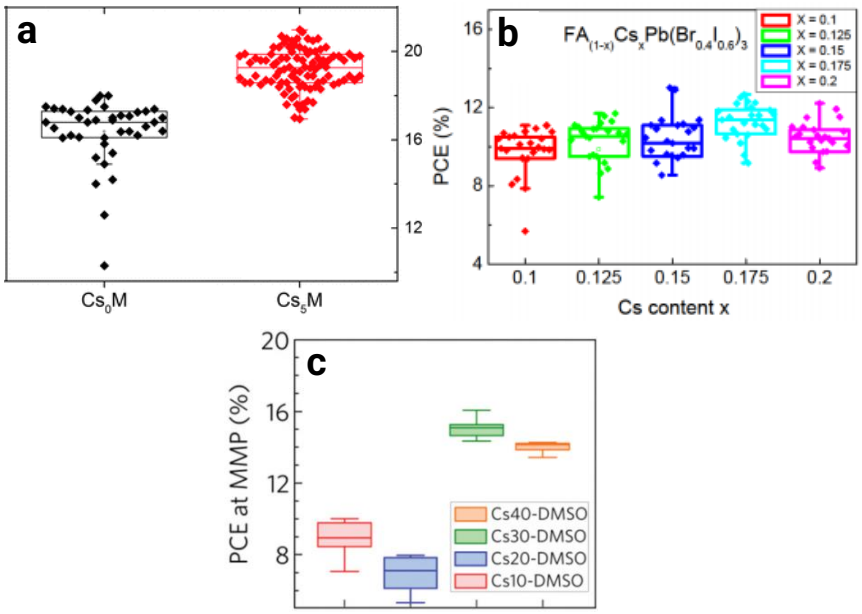

Figure 18**: Influence of the caesium content on the device performances.* ***a) *Optimum at 5% caesium [16].* ***b)*** *Optimum at 17.5% caesium [43].* ***c)*** *Optimum at 30% caesium [96].*

I.3.3. Influence of the stoichiometry: PbI_2 excess

Another strategy to facilitate the perovskite formation is to introduce a precursor in excess. This technique has been used for $MAPbI_3$ material, by introducing excess MAI [105] in the precursor solution to facilitate the crystallization. In the case of mixed-cations $FAPbI_3$-based formulations, the PbI_2 precursor is usually introduced in excess [58].

Beyond its excess reagent role during the perovskite formation, the presence of residual PbI_2 in perovskite films has been found beneficial for the device performance. In particular, Roose *et al.* introduced 6% PbI_2 excess to achieve the highest device performances [106] (**Figure 19a**). Similar effect has been reported for mixed perovskite compositions [107]. This effect was explained by the presence of a thin PbI_2 layer on the perovskite surface and grain boundaries (**Figure 19b**). A thin layer of PbI_2 can act as a passivation agent for the perovskite grain boundaries defects while permitting the charge carriers tunnelling through the layer. If the PbI_2 layer is too thick, however, the wide band gap of PbI_2 can impede the charge transport from grain to grain within the perovskite or from the perovskite to the charge extracting layers (**Figure 19b**). This passivation mechanism explains the existence of a PbI_2 excess optima in respects to the device performance.

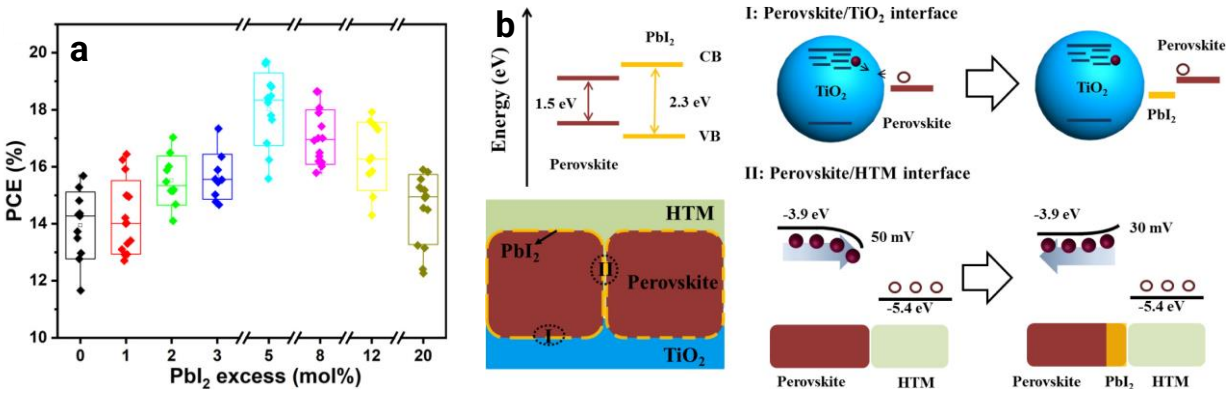

***Figure 19**: **a)** Influence of the PbI_2 excess on device performances [106]. **b)** Passivation mechanism at the grain boundaries and device interfaces [108]. Both examples are using $MAPbI_3$ perovskite.*

I.3.4. Influence of the solvent system

The precursor ink solvents play a major role in controlling the morphology of perovskite films [109]. In particular, DMF-based precursor inks have be found to form dendritic perovskite crystals, whereas dimethylsulfoxide (DMSO) or N-Cyclohexyl-2-pyrrolidone (CHP) based precursor inks lead to more round crystals domains [110]. This difference is explained by the level of coordination between the $[PbI_6^{4-}]$ octahedra and the solvent [102]. Indeed, the more polar the solvent (DMSO > DMF), the stronger the bound with the ionic intermediate species which can affect the resulting perovskite crystal growth. As an example, coordinating solvents, such as DMSO (**Figure 20a-b**) [111], can retard the crystal growth which results in the suppression of dendritic structures. This is applicable to a range of perovskite compositions ($MAPbI_3$ and $FAPbI_3$ for instance), as long as PbI_2 precursor is employed.

Besides their interaction with the precursors in solution, the solvent properties (*e.g.* volatility) can affect the perovskite morphology. To form compact perovskite films, fast solvent evaporation is desirable. This can be achieved by heating high boiling point mixtures (DMF, DMSO) at ~100°C or by increasing the volatility of the solvent mixture. To limit the thermal budget applied to the film, For volatile solvent such as acetonitrile (ACN) and 2-methoxyethanol (2-ME) have been investigated in the literature. The most common solvents have been classified by Deng *et al.* [112] using the donor number (D_N) as a metric of their coordinative power and the vapour pressure as a metric of their volatility (**Figure 20c**).

Due to the lack of solubility of the perovskite precursors in the most volatile solvents, there is a balance to find between fast solvent evaporation and precursors solubilisation. Deng *et al.* [112] used the volatile solvents as co-solvents to maintain appropriate precursors solubility while reducing the vapour pressure of the solvent mixture. Similarly, Arein *et al.* used a mixed solvents system with DMSO, N-methyl-2-pyrrolidone (NMP) and 2-ME to balance fast crystallization and precursor coordination [113]. Nakita et *al.* improved the PbI_2 solubility in

ACN solvent by bubbling methylamine gas inside the solvent prior to precursor addition [114]. This method has not been transferred yet to formamidinium based perovskite.

For scalable deposition processes, Burkit *et al.* demonstrated the use of low boiling point inks containing ACN solvents and their compatibility for slot-die coating of $MAPbI_3$ perovskite films in a roll-to-roll configuration [76,115]. In that case, developing a route to remove the toxic solvents has resulted in decreasing the thermal budget applied to the film and in increasing the processing speed, which are both advantages for the industrial manufacturer.

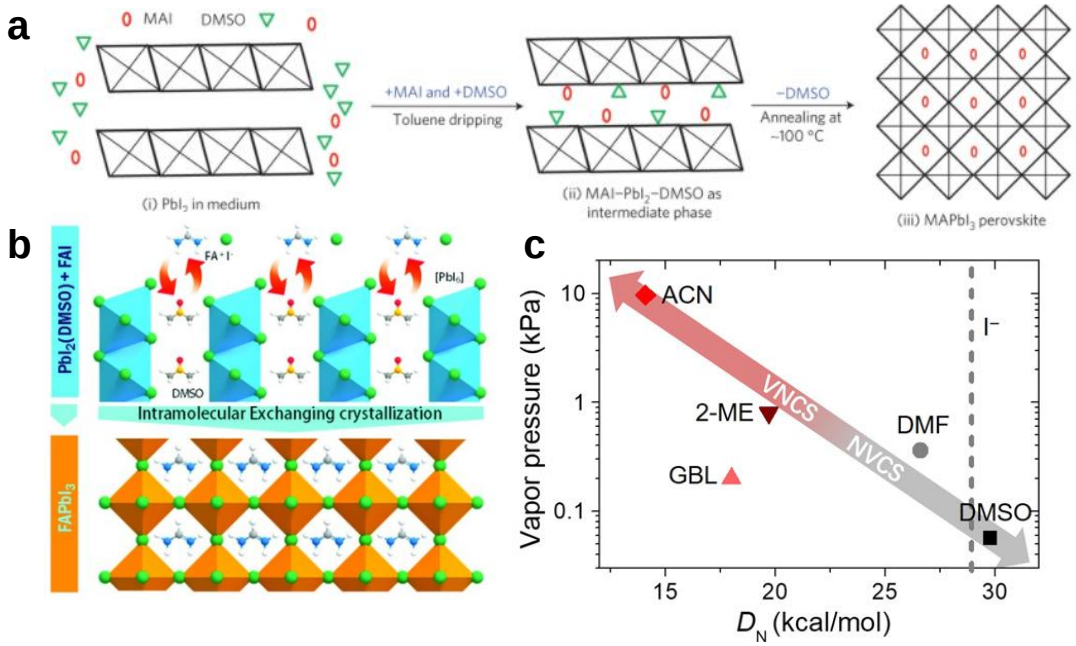

***Figure 20**: Solvent coordinative role during the precursor film crystallization: **a)** DMSO intercalation during $MAPbI_3$ perovskite formation [111,116]. **b)** DMSO intramolecular exchange during $FAPbI_3$ perovskite formation [117]. **c)** Solvents classification by their coordinative power (D_N) and volatility [112]. VNCS stands for volatile non-coordinative solvent and NVCS for non-volatile coordinative solvent.*

I.3.5. Influence of additives

Besides the solvent system or precursors stoichiometry, the morphology of perovskite layers can be tuned by the introduction of additives in the precursor solution. Those additives could affect either the perovskite crystals nucleation or growth.

Without additives, the nucleation of perovskite crystals starts when the supersaturation concentration is reached in the precursor solution. To initiate the perovskite nucleation outside the supersaturation regime, seed particles can be introduced in the solution. The seeds can serve as nucleation site and reduce the free energy barrier for nucleation. In the literature, Zhao *et al.* introduced PbI_2 seed particles [118] to control the nucleation density and form large $FAPbI_3$ grains (**Figure 21a**). Besides PbI_2, Stranks *et al.* noticed the potassium bromide (KBr) seeding effect when introduced in the precursor solution [119]. Beyond precursors-related seed

materials, Lin *et al.* used external seeding agents, lead sulfide (PbS) nanoparticles capped with perovskite precursors (**Figure 21b**) to control the perovskite nucleation and form larger grains [120].

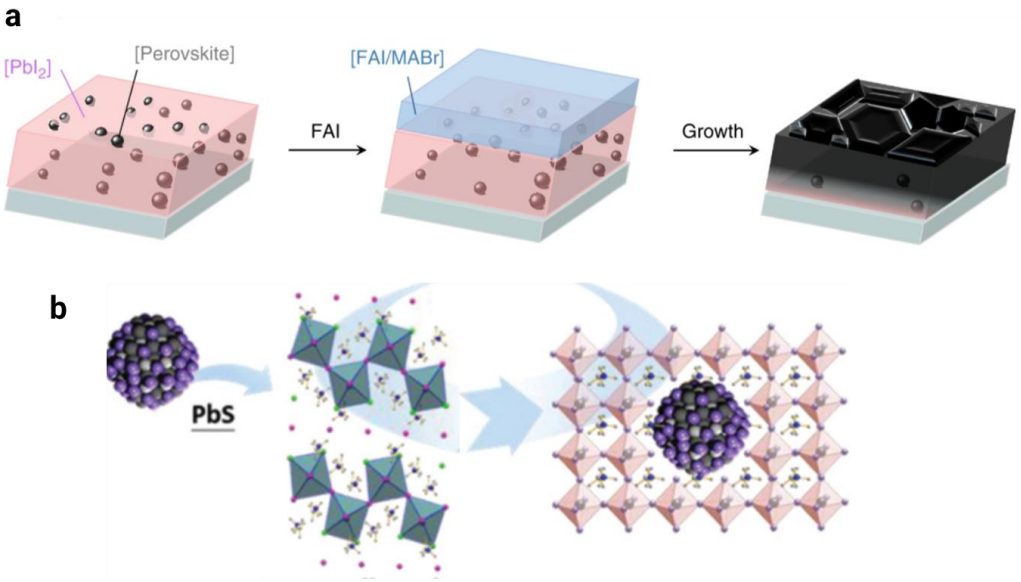

Figure 21**: Seeding strategies to control the nucleation during the perovskite crystallization.* ***a) *PbI_2 seeds in solution [118].* ***b)*** *Functionalized lead sulfide (PbS) nanoparticles [120].*

Furthermore, the morphology of the perovskite layer can be influenced during the growth step. A first category of additives are small molecules that interact with the species in solution (*e.g.* colloids, $[PbI_6^{4-}]$ octahedra) during the crystal growth. Typical examples are methylammonium chloride (MACl) [121], ammonium chloride (NH_4Cl) [122], methylammonium thiocyanate (MeSCN) [123] and methylammonium acetate (MeAc) [124]. These additives are located at the grain boundaries once the perovskite crystal growth completed (**Figure 22a-c**). They can passivate the surface defects or permit the perovskite grain growth upon annealing (Ostwald ripening phenomenon). Notably, the MACl additive can increase the perovskite grain size of $MAPbI_3$ [125] and $FAPbI_3$ [126] perovskites upon annealing.

The second family of additives contains both a chemical function and long alkyl chains with a hydrophobic behaviour such as phenethylammonium (PEAI) [24] and guanidinium iodide (GAI) [127] or functionalized surfactants (L-α-phosphatidylcholine [73]). They can both interact with the species in solution (cross-linking function) and affect the precursor ink viscosity. They behave as templating agents for the formation of larger grains during the crystallization [128] (**Figure 22 b-d**). They are located at the grain boundaries once the perovskite growth completed, which can be beneficial for grain boundaries defects passivation.

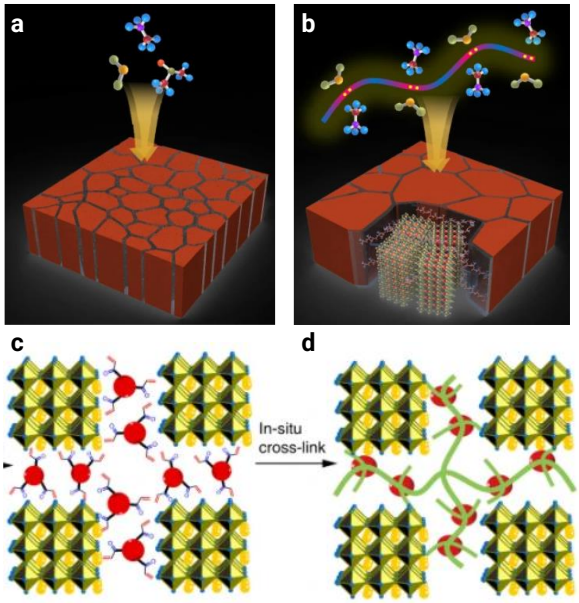

***Figure 22**: Morphology obtained when **a)** small molecules or **b)** macromolecules are added into the precursor ink [129]. **c)** Schematics of cross linking between a ligand and perovskite [128].*

To complete the introduction of parameters that affect the perovskite crystallization, the next section will focus on the role of the underlying substrate temperature and chemical nature.

I.4. Substrate temperature and nature influence on the perovskite film properties and device performances

The substrate underneath the perovskite precursor film influences the perovskite crystallization, as a potential starting point of homogeneous nucleation. In this section, we will introduce strategies to take advantage of the temperature gradient from the substrate to trigger the perovskite crystallization.

I.4.1. Influence of substrate temperature

Substrate heating during the precursor wet film formation (or hot-casting) has been introduced to fasten the perovskite crystallization and form large perovskite domains [130,131] (**Figure 23c**). Nie *et al.* showed that a heated substrate impacted the perovskite crystallization more directly compared to a conventional post-annealing treatment [132]. On a heated surface, the solvent evaporation is accelerated, resulting in a faster crystal growth. This technique favours the crystal growth over the nucleation and results in relatively low nucleation densities. The morphology of the films fabricated by this method exhibits large dentritic domains where crystal growth originated from a central nucleation point (**Figure 23d**).

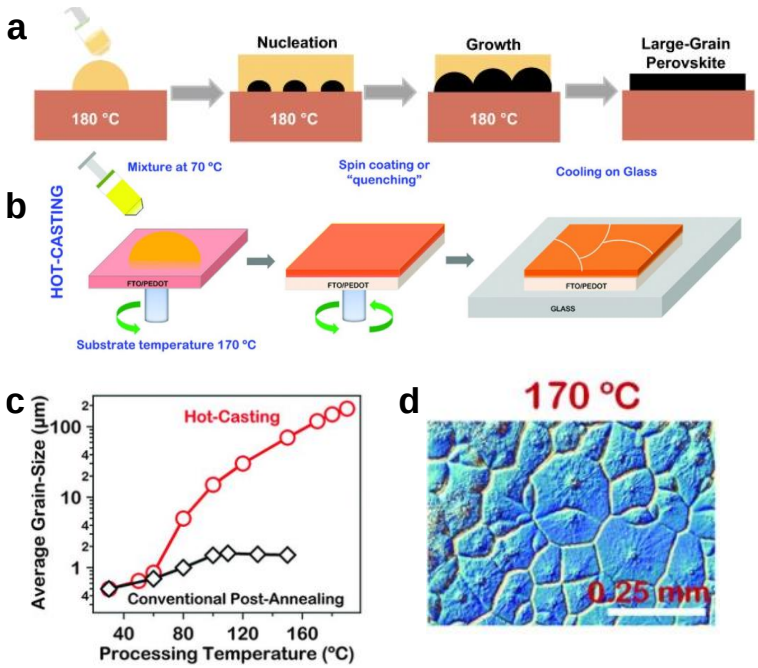

***Figure 23**: Hot-casting method to crystallize spin-coated perovskite precursors films. **a)** With substrate heating at 180 °C [130,131]. **b)** With heated solution and heated substrate at 170 °C [132].*

The substrate heating method (or hot casting) initially developed for spin-coated $MAPbI_3$ perovskite films has been applied to scalable deposition processes (blade coating, slot-die coating) and to mixed-cation perovskite formulations [12,85,133]. Tang *et al.* demonstrated the blade coating of mixed-cations formulations by blade coating on a substrate heated at 120 °C (**Figure 24a**). Furthermore, Cotella *et al.* demonstrated the use of substrate heating at 60°C combined with gas-quenching on slot-die coated precursors films (**Figure 24b**) [85]. The morphologies of perovskite films obtained by this method is similar than the one observed for spin-coated films earlier. Finally, this technique was applied to slot-die coated mixed-cations perovskite in a roll-to-roll configuration by Galagan *et al.* using a belt oven (**Figure 24c**) [12].

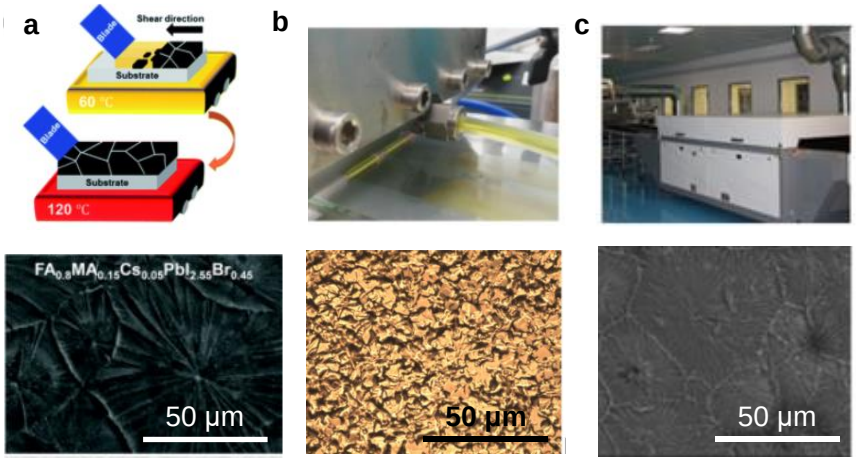

***Figure 24**: Use of substrate temperature in scalable processes. **a)** Blade coating with heated substrate at 120 °C ($FA_{0.8}MA_{0.15}Cs_{0.05}PbI_{2.55}Br_{0.45}$) [133]. **b)** Slot-die coating on a heated substrate at 60 °C ($MAPbI_3$, Cl) [85]. **c)** Slot-die coating (roll-to-roll) on a heated substrate at 140 °C with fast temperature ramping ($Cs_{0.15}FA_{0.85}PbI_{2.85}Br_{0.15}$) [12].*

I.4.2. Influence of substrate nature

In other photovoltaic technologies, the quality of the absorber depends on the underlying substrate. As such, GaAs or CdTe absorbers are grown epitaxially, they are 'lattice matched' with the substrate [134]. This technique is necessary to obtain low defects density in the absorber material and single crystal-like properties [135]. Probably because of their defect tolerance, metal halide perovskites do not require an epitaxial growth to exhibit good semiconducting properties. Consequently, they are compatible with numerous substrates (planar, mesoporous, with various chemical nature) which lead to a high variety of device architectures [136].

Here, we will focus on the planar (n-i-p) device configuration, as the highest photovoltaic performances are obtained with this structure for single junction devices [62]. In an (n-i-p) configuration, the perovskite is coated on the electron transporting layer (ETL), itself coated on a transparent conductive oxide layer (TCO, transparent bottom electrode).

- **Mesoporous and planar TiO_2**

Inherited from the dye-sensitized solar cell (DSSC) architecture [18,137], the historical ETL material is mesoporous TiO_2. In a DSSC device, a thin layer of perovskite (sensitizer) is coated onto the TiO_2 scaffold to maximize the TiO_2/Perovskite contact surface and increase the extraction of electrons (**Figure 25a**). Similarly, mesoporous perovskite solar cells take advantage of the TiO_2 scaffold to improve the m-TiO_2/Perovskite contact (**Figure 25b**). During the perovskite deposition on mesoporous substrates, part of the precursor ink is infiltrated inside the pores of the TiO_2 scaffold or the oversupply of the precursor solution crystallizes on top of it, forming a so called 'capping layer' [138] (**Figure 25b**). Further studies by Snaith *et al.* showed that a planar TiO_2 layer (**Figure 25c**) [20] can work as efficiently as a mesoporous TiO_2 scaffold, suggesting that the contact area between the TiO_2 and perovskite does not limit the charge extraction.

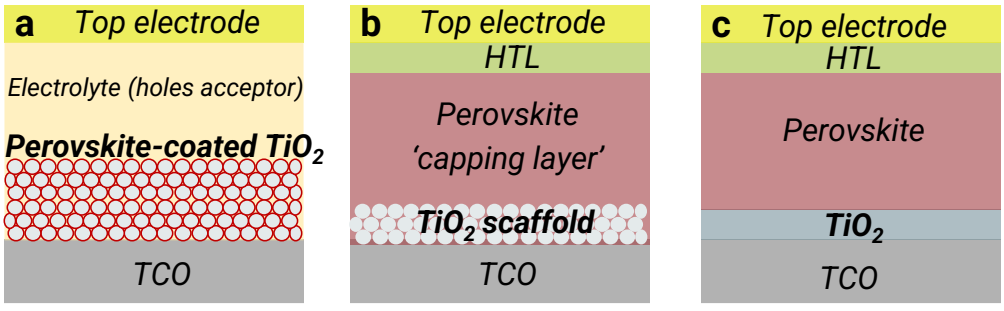

Figure 25**: Schematics of devices using TiO_2 as electron extractor:* ***a) *Dye Sensitized Solar cell.* ***b)*** *Mesoporous perovskite solar cell (n-i-p configuration)* ***c)*** *Planar perovskite solar cell.*

The planar TiO_2 ETLs are usually thinner (≤ 100 nm) than the mesoporous TiO_2 scaffolds (400 - 800 nm [137,139]). The conformal coating of ETL thin films on the transparent conductive oxide (TCO) substrate can be a challenge [140]. In the final device, the ETL layer thickness variations can result in charge carriers recombination at the TCO/ETL/Perovskite interface (**Figure 26**). In the literature, mitigation strategies such as surface treatment [141] ($TiCl_4$, UVO_3) or conformal deposition process such as spray-coating [142], anodization [140] and atomic layer deposition [143,144] can ensure conformal coating of the ETL on the TCO.

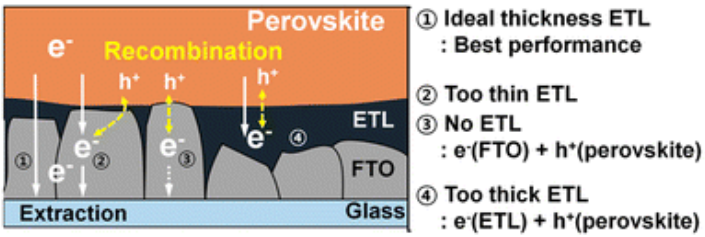

***Figure 26**: General representation of ETL coated on top of rough FTO substrate [140].*

In terms of device performances, mesoporous TiO_2 layers have initially led to higher device performance compared to planar TiO_2 layers due to the lack of conformity of the latter causing device shortage [139,145] (**Figure 26**). In some cases, the planar TiO_2 layer led to performances of 12.9% while the addition of a mesoporous layer increased the device power conversion efficiency to 15% [145]. By using alternative ways such as spray pyrolysis that enable a better conformity of the ETL layer, planar TiO_2 based perovskite solar cells achieve state-of-the-art power conversion efficiency over 20% [58].

- **Planar SnO_2**

Besides TiO_2, other materials, such as SnO_2, have been widely used as electron transporting layers [58,146]. Low-temperature deposition routes such as sol-gel method, nanoparticles, spray-coating or atomic layer deposition (ALD) [146] were developed to deposit planar SnO_2 films. One of the most promising uses the sol-gel reaction of $SnCl_2.2H_20$ precursor at 180 °C and yields a power conversion efficiency of 17.21% [147].

Later, Hagfeld *et al.* reported the use of chemical bath deposition (CBD) post-treatment to improve the quality of spin-coated SnO_2 layers, yielding a power conversion efficiency of 20.7% [148]. **Figure 27a** presents the SnO_2 layer fabrication steps including conventional spin-coating followed by a chemical bath deposition (CBD). The CBD could be responsible to a better surface coverage pf the ETL layer. They compared this method to another conformal deposition process (ALD) and obtained higher device performance using the SnO_2 film treated by CBD compared to the one deposited by atomic layer deposition (ALD). This result suggested a second effect of the CBD treatment besides the enhanced film conformity.

This observation was confirmed by Yoo *et al.*, who tuned the SnO_2 surface chemistry carefully to achieve the record device power conversion efficiency of 24.5% [62]. More specifically, they fabricated SnO_2 layers by sol-gel method using various deposition times. The deposition time increases the SnO_2 quantity deposited on the TCO substrate (**Figure 27b**). Short deposition time resulted in partially covered ETL films, hence in poorer device performances. Long deposition times resulted in thicker SnO_2 films with a modification of the SnO_2 surface chemistry (*e.g.* apparition of oxygen vacancies) that was detrimental to device performance. Besides ETL conformity, the SnO_2 surface chemistry is a main factor to achieve high device performances.

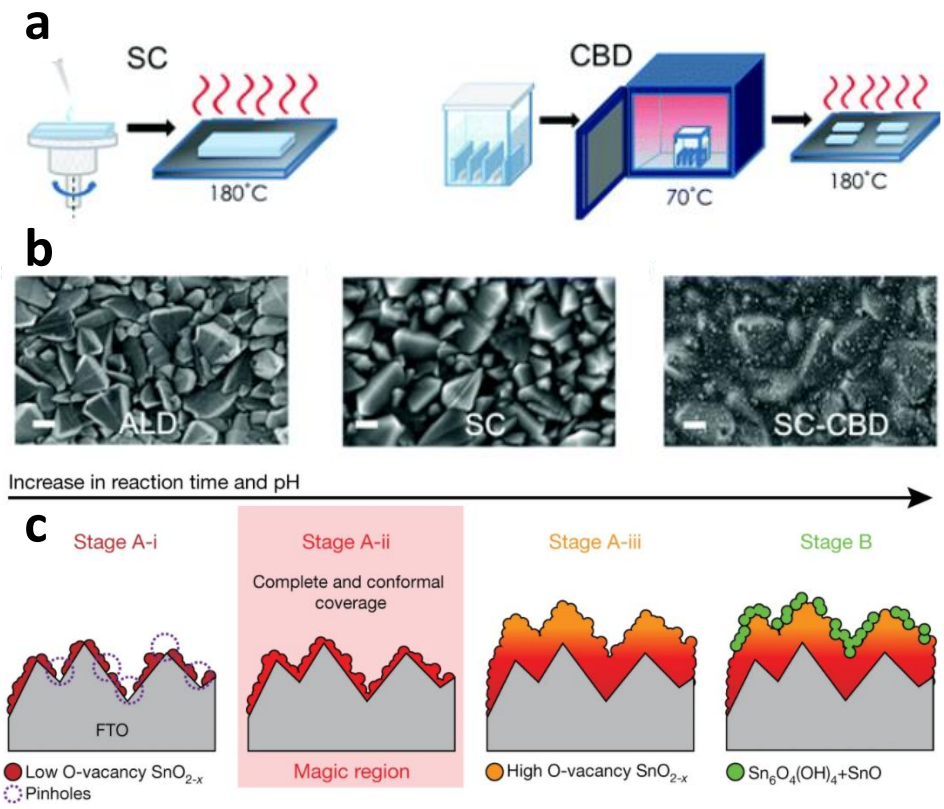

***Figure 27**: Importance of SnO_2 conformal coating and surface chemistry. **a)** Sequential SnO_2 formation via spin-coating and chemical bath deposition (CBD). **b)** Corresponding scanning electron microscopy top images of the FTO/SnO_2 films for SnO_2 deposited by atomic layer deposition (ALD), spin-coating (SC) or spin-coating + CBD (SC-CBD) [148]. **c)** Evolution of the SnO_2 layer morphology and surface chemistry with the deposition time in sol-gel process [62].*

- **Comparison of TiO_2 and SnO_2**

Regarding its opto-electronic properties, SnO_2 has a higher electron mobility (10^{-3} $cm^2.V^{-1}.s^{-1}$) compared to TiO_2 (10^{-4} - 10^{-5} $cm^2.V^{-1}.s^{-1}$) [149]. In a comparative study, Baena *et al.* found that perovskite solar cells in (n-i-p) device structure with SnO_2 ETL performed better compared to the ones using TiO_2 ETL [150] (**Figure 28a**). They explain this increase in performance to the better energy alignment of the SnO_2 conduction band level, for both $MAPbI_3$ and mixed perovskite (**Figure 28b**). Furthermore, the lower valence energy level of SnO_2 provides enhanced hole blocking properties to SnO_2, reinforcing its superior extraction selectivity towards electrons.

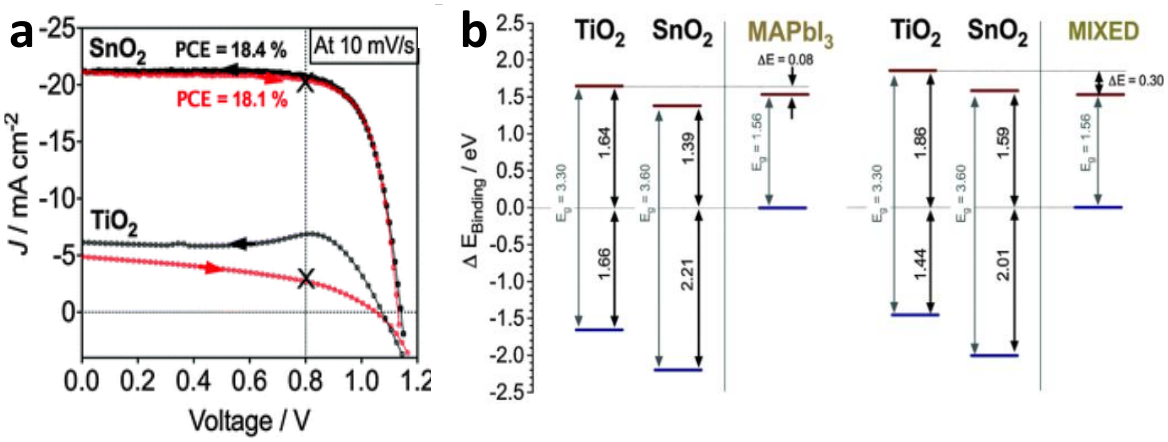

***Figure 28**: Comparison between planar SnO_2 and planar TiO_2 ETLs* [150].

Process	Perovskite	Substrate	device structure	Quenching mean	Active area (cm^2)	PCE_{max} (%)
Spin-coating	FAMAPbIBr	FTO/SnO_2	n-i-p	anti-solvent	0.09	25.4 [62]
	$MAPbI_3$	FTO/TiO_2	n-i-p	gas-quenching	0.1	17.9 [93]
	$FA_{0.81}MA_{0.15}PbI_{2.51}Br_{0.45}$	FTO/TiO_2	n-i-p	vacuum-flash	0.16	20.5 [15]
	FACsPbIBr	FTO/TiO_2	n-i-p	vacuum-flash	0.16	~ 18 [15]
Slot-die coating (≤ 2018)	$Cs_{0.15}FA_{0.85}PbI_{2.85}Br_{0.15}$	PET/ITO/SnO_2	n-i-p	thermal annealing	0.09	15.2 [12]
	$MAPbI_3$(Cl)	ITO/SnO_2	n-i-p	solvent bathing + annealing	0.06	18 [11]
	$MAPbI_3$(Cl)	ITO/PEDOT:PSS	p-i-n	gas-quenching	0.09	19.7 [151]
	$MA_{0.6}FA_{0.38}Cs_{0.02}PbI_{2.975}Br_{0.025}$	ITO/PEDOT:PSS	p-i-n	hot substrate	0.01	14.7 [152]
Slot-die coating (2021)	$MAPbI_3$	ITO/PTAA	p-i-n	hot substrate	0.1	21.8 [153]
	$MAPbI_3$	ITO/SAM (2PACz)	n-i-p	gas quenching	0.16	20.8 [77]
	$FA_{0.83}Cs_{0.17}PbI_{2.83}Br_{0.17}$	FTO/NiMgLiO	n-i-p	gas-quenching	1	18.2 [91]

Table 3: *State-of-the-art perovskite solar cells performances (active area ≤1 cm^2).*

Conclusion

While scalable deposition techniques, such as slot-die coating, were readily available to coat the perovskite precursor wet film over large areas, crystallization tools still had to be developed at that scale. In this review, we identified the gas-quenching as a scalable and environment-friendly solution to trigger the precursor wet film crystallization. By discussing the mechanisms influencing the perovskite film formation, we identified the substrate temperature and perovskite ink composition (stoichiometry, solvents) as parameters influencing the perovskite film morphology. The substrate temperature affects the kinetics of the perovskite crystal growth. The precursor ink composition affects both the organization of the species in solution and the final crystalline structure of metal halide perovskites. By reviewing the various substrates employed to fabricate perovskite solar cells with an (n-i-p) structure, we identified three state-of-the-art electron transporting layers (ETLs) leading to high device performances (≥ 20%): mesoporous TiO_2, planar TiO_2 and planar SnO_2. In this work, we propose to apply the gas-quenching method to crystallize slot-die coated precursor wet films over large areas. We aim to systematically study the influence of substrate temperature, precursor ink composition and underlying substrate nature on the slot-die coated films properties and perovskite solar cells performances.

Chapter II: Experimental methods

This chapter introduces the experimental methods used for the photovoltaic device fabrication. We particularly focus on the perovskite layer deposition and detail the experimental conditions for both spin-coting and slot-die coating processes. Then, we introduce the tools for the multi-characterization approach used in this work to assess the perovskite layer morphological, opto-electronic and crystalline properties. Finally, we present the parameters describing the performance of a photovoltaic device.

II.1. Photovoltaic device fabrication

In this section, we introduce the device fabrication steps including the substrate preparation, the formulation of the perovskite precursor ink, the deposition of the perovskite and interface layers and the evaporation of the top electrode.

II.1.1. Transparent Conductive Oxide (TCO) substrate

- **ITO-coated glass substrates**

The substrates used for the 5 x 5 cm² samples are glass substrates from Visionteck (United Kingdom) coated with indium-doped tin oxide (ITO, sheet resistance 7 Ω/sq). Their thickness is 1.1 mm, comprising 250 nm of ITO and initial area of 5 x 5 cm². We used a green LASER (Nd:YAG, picosecond, λ = 532 nm) to etch 6 separate areas of 8 mm width (**Figure 1a**), defining the boundaries of the future 6 cells of the device. This etching step is also called "P1 scribing" step.

After the scribing step, the ITO-coated glass substrates are cleaned with subsequent sonication baths in acetone (2 x 5 min), isopropanol (2 x 5 min) and deionized water (3 x 5 min) and dried in an oven at 100 °C overnight to remove any traces of water. Chromium (Cr, 10 nm) and gold (Au, 40 nm) contacts are subsequently evaporated using metal masks to get the desired patterns (**Figure 1b**). The Cr/Au contact will facilitate the probing during the measurement of each cell. Prior to the ETL deposition, a UV-ozone cleaning of 30 minutes is performed to enhance the surface wettability.

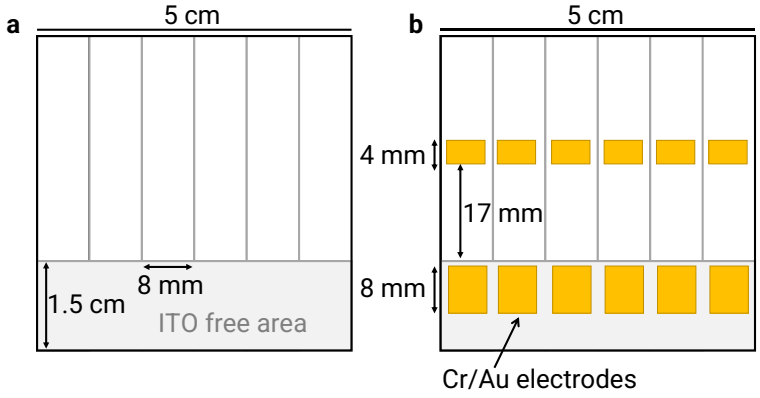

***Figure 1**: ITO-coated glass substrate used for laboratory device fabrication after **a)** Laser patterning and **b)** Cr/Au electrodes evaporation.*

- **FTO-coated glass substrates**

The substrates used for the 10 x 10 cm² samples are glass substrates from Jinge Solar (China) coated with fluorine-doped tin oxide (FTO, sheet resistance 15 Ω/sq). The substrates have a total thickness of 2.2 mm, including 450 nm of FTO and initial area of 30 x 30 cm². The as-received 30 x 30 cm² substrates are etched using a carbon dioxide LASER (CO_2, picosecond,

λ = 10.2 μm) to form the desired pattern which differs between small scale devices (**Figure 2a**) or modules (**Figure 2b**).

After laser scribing, the 30 x 30 cm^2 glass substrates were cut into nine 10 x 10 cm^2 substrates and cleaned by three subsequent ultrasonication baths for 30 minutes in soap (DECON 90) in deionized water, in deionized water and in ethanol (Aldrich). A UV-ozone treatment (Novascan PSD Pro Series) of 30 minutes at room temperature was performed prior to the deposition of the electron transporting layer (ETL) to enhance the surface wettability.

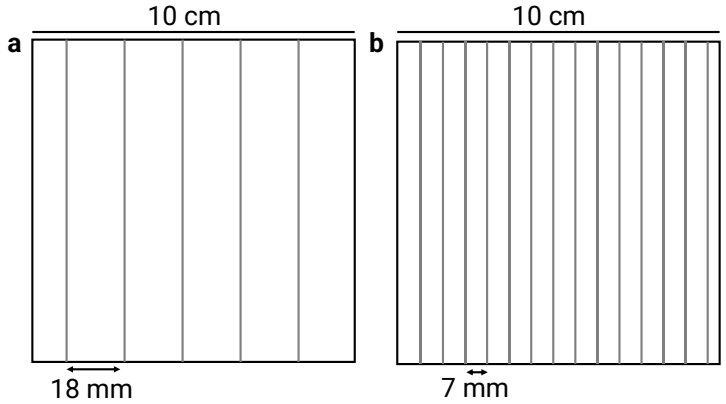

***Figure 2**: FTO-coated glass substrate after laser scribing with designs to fabricate **a)** laboratory-scale devices or **b)** modules.*

II.1.2. ETL layer deposition

- **np-SnO_2 solution preparation and spin-coating**

The np-SnO_2 electron transport layer is deposited from a commercial SnO_2 nanoparticles solution (nanoparticles size 10 - 15 nm, pH of the solution 9 - 10.5) in deionized water at a concentration of 3.75 wt%. It was filtered using a Glass MicroFiber filter (GMF - GMF pore size of 0.45 μm) before use. The deposition method is the sequential spin-coating process: 1) 1200 revolutions per minute (rpm) – 600 $rpm.s^{-1}$ – 2 s, 2) 2400 rpm – 1200 $rpm.s^{-1}$- 1 s, 3) 4000 rpm- 1600 $rpm.s^{-1}$ – 40 s. The spin-coating is carried out under a fume hood. The spin-coated layer (thickness ca 40 nm) is annealed at 80 °C for 1 min under ambient air.

- **sg-SnO_2 solution preparation and spin-coating**

The sg-SnO_2 electron transport layer is prepared by dissolving 0.05 M of $SnCl_2.2H_2O$ (≤ 99.99% trace metal basis, Aldrich) in anhydrous ethanol (Aldrich) as reported earlier in the literature [147]. The solution is mechanically stirred for 5 min and used for spin-coating right after preparation. To form the SnO_2 layer, 1 mL of solution is deposited per 10 x 10 cm^2 substrate by sequential spin-coating process with a puddling step 1) 500 ms – 90° amplitude – 3 s, followed by two spreading steps 2) 500 rpm – 500 $rpm.s^{-1}$ – 5 s and 3) 1000 rpm – 500 $rpm.s^{-1}$ – 10 s. The substrates are preheated at 80 °C until all substrates are spin-coated (~ 10 min), and then further annealed at 180 °C for 1 h to convert the $SnCl_2$ into planar SnO_2 layer (thickness ca 30 nm).

For some samples, a chemical bath deposition (CBD) is performed as reported in the literature [148]. $SnCl_2.2H_2O$ (1 g, Aldrich) is dissolved in 4 L of deionized water in an slightly acidic environment (1 mL of HCl). The substrates are fully immersed into the solution and kept in a heat chamber at 70 °C for 4 h. After cooling down, the substrates are removed from the CBD bath, rinsed with deionized water and annealed at 180 °C for 1h. The substrates are transferred immediately after cooling down to the perovskite slot-die coating process.

- **sg-TiO_2 solution preparation and spin-coating**

The sg-TiO_2 precursor solution is prepared by adding 22.7 g of tetrabutyl-titanate ($Ti(OBu)_4$, Aldrich), 89.1 g of absolute ethanol (Aldrich), 2.8 g of deionized water and 7 g of di-ethanol amine (Aldrich) as reported earlier in the literature [154]. We use a sequential spin-coating process with a puddling step 1) 500 ms - 90° amplitude – 3 s, followed by two spreading steps 2) 500 rpm – 500 rpm.s^{-1} – 5 s and 3) 3000 rpm – 500 rpm.s^{-1} - 40 s to deposit the TiO_2 precursor film. The latter is manually removed using ethanol to form the patterns presented in **Figure 3.** The sg-TiO_2 layer removal is necessary to facilitate device fabrication. Indeed, the TiO_2 layer is more resistive than the SnO_2 layer and requires to be fully removed from the future FTO contact areas. To form the planar TiO_2 layer (thickness ca 40 nm), the substrates are sintered at 500 °C for 1 h with a temperature ramping time of 40 min and cooled down before transfer to the slot-die coating process.

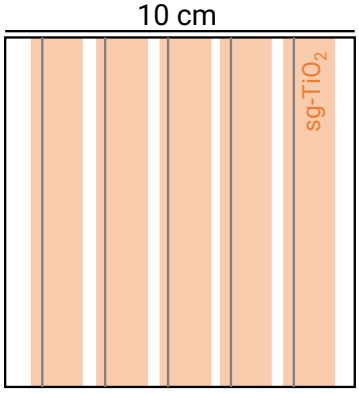

***Figure 3**: sg-TiO_2 coating pattern after the manual removal of stripes to permit the direct contact between the top electrode and FTO during the device fabrication.*

- **c-TiO_2 and m-TiO_2 screen-printing**

For c-TiO_2 layer, a TiO_2 paste (Dyesol BL-1, now GreatCell Solar) is used as received. For the m-TiO_2 layer, a TiO_2 paste (Dyesol 30 NR-D, average nanoparticles size 30 nm) is diluted with terpineol (Aldrich) in weight ratio ranging from 1:3.5 to 1:5.5 to deposit m-TiO_2 thicknesses from 250 to 100 nm respectively. A MT320TV [155] screen-printer (MicroTec, **Figure 4a**) is used with two different screen masks to deposit the compact (c-TiO_2) and mesoporous (m-TiO_2) layers. The c-TiO_2 is deposited with a stripe design (**Figure 4b**), similarly to the sg-TiO_2 pattern (**Figure 3** above).

m-TiO_2 with rectangle pattern is deposited on top of the c-TiO_2 stripes to form 25 pixels over the 10 x 10 cm^2 substrate (**Figure 4b**). The printed films are dried for 20 mins at 100 °C prior to sintering at 500 °C for 1 h.

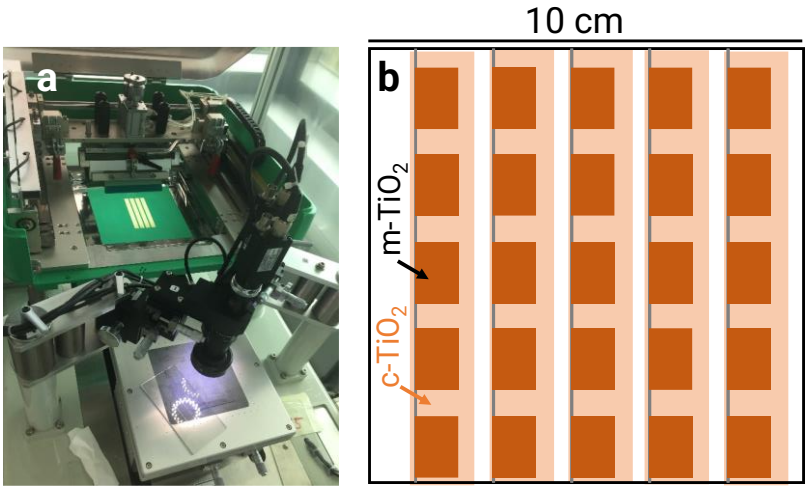

***Figure 4**: **a)** MT320TV Screen-printer used to deposit the c-TiO_2 and m-TiO_2 layers. **b)** Substrate coated with c-TiO_2 and m-TiO_2 layers. The m-TiO_2 mask has a pixel design for laboratory scale device fabrication.*

II.1.3. Perovskite layer deposition

- **Chemicals**

PbI_2 (99.99%, trace metal basis) is purchased from Tokyo Chemical Industry (TCI). FAI is purchased from Dyesol (now Greatcell Solar). $PbBr_2$ (99.999% trace metal basis), CsI (99.999% trace metal basis), N,N Dimethylformamide (DMF, anhydrous, 98.8%) and Dimethyl sulfoxide (DMSO, anhydrous, ≥ 99.9%) are purchased from Aldrich. The precursors are used without further purification.

- **Perovskite precursor solutions**

The perovskite precursor ink is prepared in a nitrogen filled glovebox by mixing (in this order) PbI_2, $PbBr_2$, FAI, and CsI in a DMF : DMSO (4:1 volume ratio) to obtain a 1.2 M solution. The 'reference spin-coating' perovskite ink is prepared in a nitrogen-filled glovebox by mixing 2.296 g of PbI_2, 0.375 g of $PbBr_2$, 0.816 g of FAI and 0.078 g of CsI in 4 mL of DMF and 1 mL of DMSO to form the theoretical $Cs_{0.05}FA_{0.79}Pb(I_{0.88}/Br_{0.12})_{2.84}$ perovskite formula.

For the CsI studies, the quantities of CsI added to the precursor ink are 0, 0.078, 0.156, 0.284 and 0.312 g to prepare the 0, 5, 10, 15 and 20% Cs/Pb solutions, respectively. For the FAI study, the FAI quantity is tuned from 0.816 g to 0.919 g to increase the ratio from 74 to 84%. The CsI quantities remain the ones stated above.

All solutions are kept at 40 °C under stirring overnight in inert atmosphere and used for either spin-coating or slot-die coating the next day.

- **Perovskite layer deposition by spin-coating**

The perovskite precursor solution is deposited using a 3-steps spin-coating process: 1) 200 rpm – 200 rpm.s^{-1} – 5 s, 2) 1000 rpm – 1000 rpm.s^{-1} – 10 s and 3) 6000 rpm – 4000 rpm.s^{-1} – 20 s. During the third step, 700 µL of chlorobenzene is dropped on the substrate 8 s prior to the end of the protocol (after 12 s in step 3). The crystallization is completed by a post-annealing step at 100 °C for 1 h in a nitrogen atmosphere.

- **Perovskite layer deposition by slot-die coating**

The slot-die coating process is a meniscus-assisted deposition of a wet precursor film onto the substrate at a given coating speed (C_s), coating flow rate (C_f) and coating gap (C_g), defining a theoretical wet film thickness (thickness ~ 4 µm) on the rigid substrate. In this configuration, the substrate is fixed and the slot-die head is in movement. The coating speed (C_s) can be adjusted from 1 to 50 mm.s^{-1}, the coating flow rate (C_f) from 10 to 1000 µL.min^{-1} and the coating gap (C_g) from 50 to 300 µm.

The wet precursor film coating is followed by gas-quenching step (nitrogen gas) at a given speed (Q_s), quenching flow rate (Q_f) and quenching gap (Q_g). The gas-knife is fixed to the slot-die coating head, such as the coating and the quenching speeds are equal: $C_s = Q_s = CQ_s$. The gas-knife is connected to a nitrogen line (pressure 6 bar, ~87 psi) or to a nitrogen cylinder (pressure ~ 8.3 bar, 120 psi). The gas flow rate (Q_f) can be adjusted from 25 to 140 L.min^{-1} depending on the set-up employed. The substrate temperature is controlled by a hotplate (range: 25 °C to 100 °C) and is the same in both coating and quenching steps ($C_T = Q_T = CQ_T$).

In CEA laboratory, a TC300 slot-die coater (Automatic Research) is used to coat the perovskite layers onto ETL-coated 5 x 5 cm^2 substrates (**Figure 5a**). The slot-die coating process is conducted in an enclosed environment (purpose-made set up, **Figure 5a**) to maintain between 10 and 20% relative humidity (rh) during coating at T = 21 ± 1 °C. After coating, the perovskite films are annealed for 5 min at 100 °C under nitrogen atmosphere (HP150 hotplate, Sawatec) and stored in a nitrogen-filled glovebox prior to material characterization or device fabrication.

In NTU laboratory, a N-Rad slot-die coater (N-Takt) is used to coat the perovskite layers onto the ETL-coated 10 x 10 cm^2 substrates (**Figure 5b**). A purpose-made enclosure was added to isolate the slot-die coater from ambient environment (**Figure 5b**), maintaining a relative humidity between 20 and 40% during coating at T = 25 ± 1 °C. After coating, the samples were annealed in ambient air for 5 min at 100 °C and stored in a nitrogen-filled glovebox prior to material characterization or device fabrication.

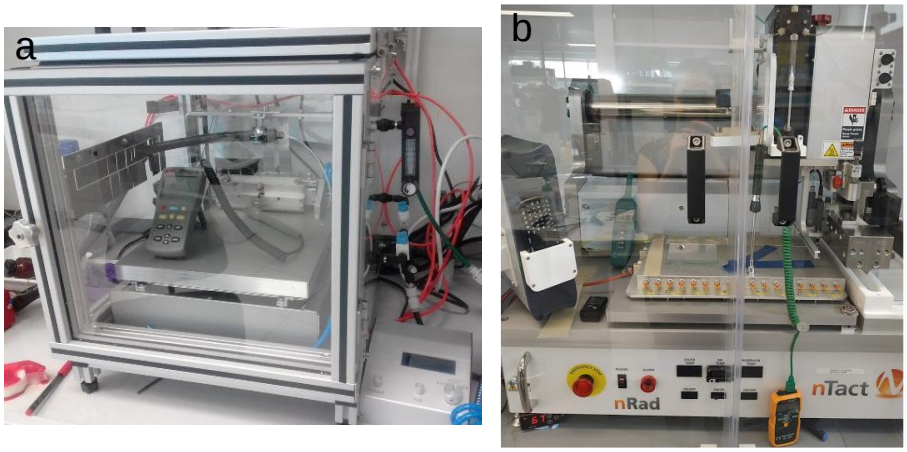

***Figure 5**: Slot-die coaters used in this work: **a)** Automatic research slot-die in enclosed box with controlled humidity. **b)** n-Rad slot-die coater with enclosure to control humidity during coating.*

Prior to device processing, the homogeneity of the slot-die coated layers was assessed. The fabrication of laboratory devices required a homogeneous perovskite film over ~ 5 cm^2 (5 x 5 cm^2 substrate) or ~ 15 cm^2 (10 x 10 cm^2 substrate). The module fabrication required a homogeneous area of ~ 22 cm^2.

II.1.4. HTL and top electrode deposition

- **Spiro-OMeTAD layer**

The solution is prepared by dissolving 72 $g.L^{-1}$ of 2,2′,7,7′-tetrakis [N, N -di- p - methoxyphenyl-amine]9,9′-spirobifluorene (Spiro-OMeTAD, Lumtech) in anhydrous chlorobenzene (Aldrich) with 4-tert-butyl pyridine (tBP, Aldrich, 28.5 µL per mL of stock solution) and lithium salt stock solution (17.5 µL per mL of solution). The lithium salt stock solution is prepared by dissolving 520 mg of bis(trifluoromethane) sulfonimide lithium salt (LiTFSI, 99.95%, Aldrich) in 1 mL of acetonitrile (99.8%, Aldrich). 250 µL of solution is dynamically spin-coated on 10 x 10 cm^2 substrates with a single step at 4000 rpm – 1000 $rpm.s^{-1}$ – 40 s) to form the Spiro-OMeTAD layer (thickness ca 150 nm). Both solution preparation and film coating are performed in the glovebox to limit the air exposure of the perovskite layer.

- **PTAA layer**

The poly[bis(4-phenyl)(2,4,6-trimethylphenyl)amine] layer (PTAA, EM Index, Mw ~ 18000 g/mol) is dissolved at 12 $g.L^{-1}$ in anhydrous toluene (Aldrich) with 4-tert-butyl pyridine (tBP, Aldrich) and lithium bis(trifluoromethylsulfonyl) imide (LiTFSI, Aldrich). The PTAA solution is spin-coated in the glovebox in two steps to form a 70 – 80 nm thick layer : 1) 1500 rpm - 375 $rpm.s^{-1}$ - 40 s, followed by 2) 2000 rpm - 500 $rpm.s^{-1}$ - 30 s.

- **Contact area cleaning**

The 5 x 5 cm² substrates are cleaned first by removing the HTL layer using ortho-dichlorobenzene (o-DCB, Aldrich), then by removing the perovskite layer using dimethyl sulfoxide (DMSO, Aldrich) according to the design presented in **Figure 6a**.

The 10 x 10 cm² substates are then cut into ~ 1 cm² substrates prior to similar cleaning steps that include the HTL layer removal using ortho-dichlorobenzene (o-DCB, Aldrich) and the perovskite layer removal using anhydrous acetonitrile (ACN, Aldrich), according to the design presented in **Figure 6b**.

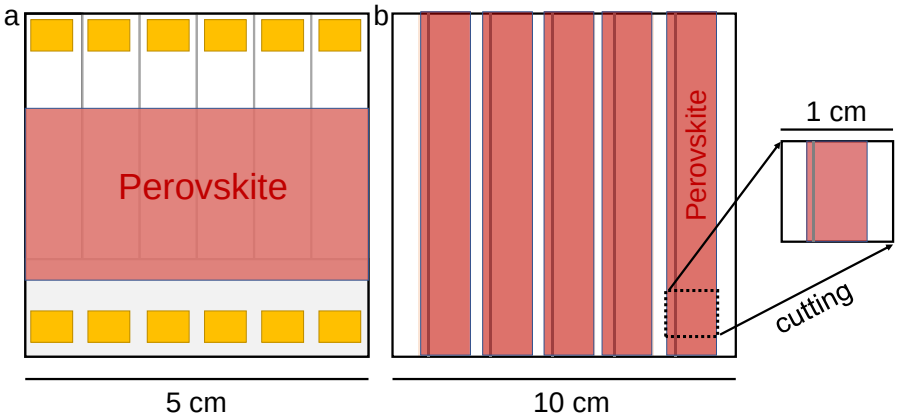

***Figure 6**: Substrates after the perovskite and HTL layers manual cleaning.*

- **Au electrode deposition**

Finally, a 100 nm gold (Au) electrode is thermally evaporated using evaporation rates ranging from 0.1 to 0.5 nm.s^{-1} and chamber pressure of 10^{-6} bar. On the 5 x 5 cm² samples, the evaporation mask enables the deposition of six spherical 0.33 cm² electrodes without cutting the substrate (**Figure 7a**). For the 10 x 10 cm² samples, the evaporation mask results in the deposition of two 0.16 cm² square electrodes (**Figure 7b**). For the 1 cm² samples, an additional soldering is added on both sides of the devices to facilitate the probing during J-V measurement (**Figure 7b**).

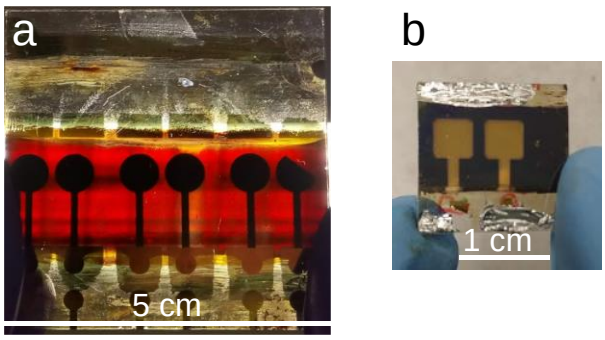

***Figure 7**: Typical laboratory scale devices fabricated with both device structures. **a)** Six electrodes with 0.33 cm³ active area evaporated on the 5 x 5 cm² substrate after cleaning of the contacts. **b)** 1 cm² sample cut from the 10 x 10 cm² substrate and with two 0.16 cm² gold electrodes and soldering to facilitate the J-V measurements.*

II.1.5. Reference processes and device structures

Using the fabrication steps detailed earlier, we defined two fabrication reference processes, using the (n-i-p) device configuration:

- the spin-coating reference process, in which the ETL, HTL and perovskite layers were spin-coated (**Figure 8a**).
- the slot-die coating reference process, in which the ETL and HTL are spin-coated and the perovskite layer is slot-die coated (**Figure 8b**).

The slot-die coating reference process has been developed using two device stacks, corresponding to the standard (n-i-p) device structures used in both laboratories (**Figure 8b**).

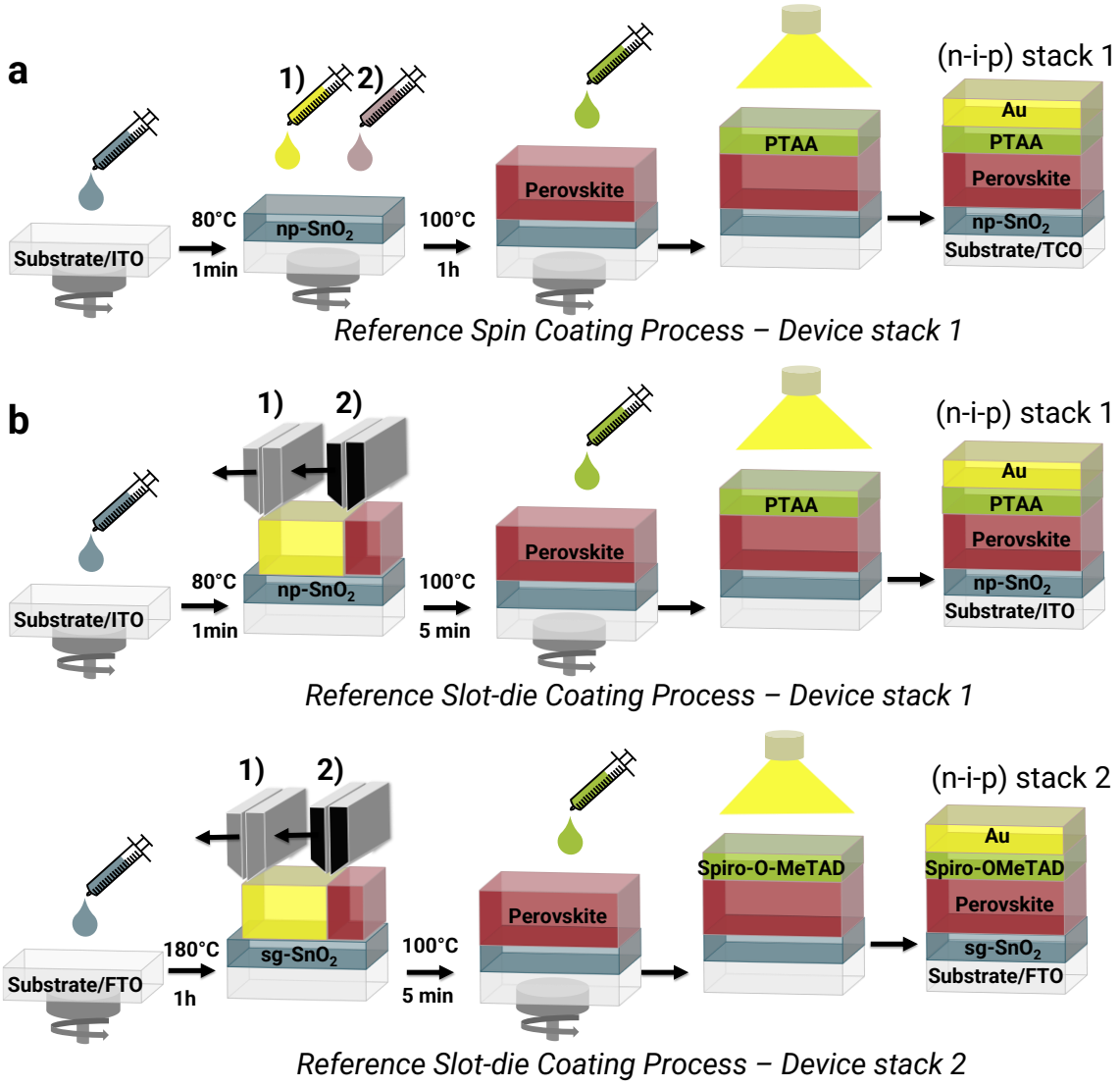

***Figure 8**: Summary of the deposition processes using **a)** spin-coating and **b)** slot-die coating for the perovskite layer, and the final device architectures employed in this work.*

II.1.6. Photovoltaic modules fabrication

The perovskite modules are fabricated following the similar workflow as the 10 x 10 cm^2 laboratory devices (**Figure 9**). First, the laser scribing is performed (P_1) to separate the FTO electrode in cells with a stripe design (stripe width 7 mm, **Figure 2**). Then, the SnO_2 electron transporting layer (ETL) is deposited on the entire substrate by spin-coating with the same protocol as small devices. The perovskite layer is slot-die coated on the SnO_2-coated FTO substrate, and the Spiro-OMeTAD hole transporting layer (HTL) is spin-coated on the perovskite film.

Prior to the top electrode deposition, a CO_2 LASER (λ = 1024 nm) is used to etch the perovskite and Spiro-OMeTAD layers (P_2 scribing). Finally, a "P_3 scribing" step is performed manually by masking the area where the gold is not deposited with Kapton tape (3M, 0.5 mm width). The cross-section views of the P_1 - P_2 - P_3 scribing process can be seen in **Figure 9**. This scribing process aims at connecting the various module stripes in series, by contacting the top gold electrode of one cell (left side on picture) with the bottom FTO electrode of the next cell (right side on picture).

From an initial 100 cm^2 substrate, the final device area varies between 50 and 70 cm^2, due to the masking of the substrate edges by taping during Au evaporation. In the central zone, the device active area corresponds to the central area minus the interconnection area between the stripes, also called 'dead area'. In this process, the width of the dead area between two cells is estimated to 1 mm (distance between P_1 and P_3 etch lines), with a main contribution of the manual taping width in the P_3 step (0.5 mm). The ratio between the device active area and the central area is the geometrical fill factor (GFF). In our case, the GFF in the central area is ~ 70%.

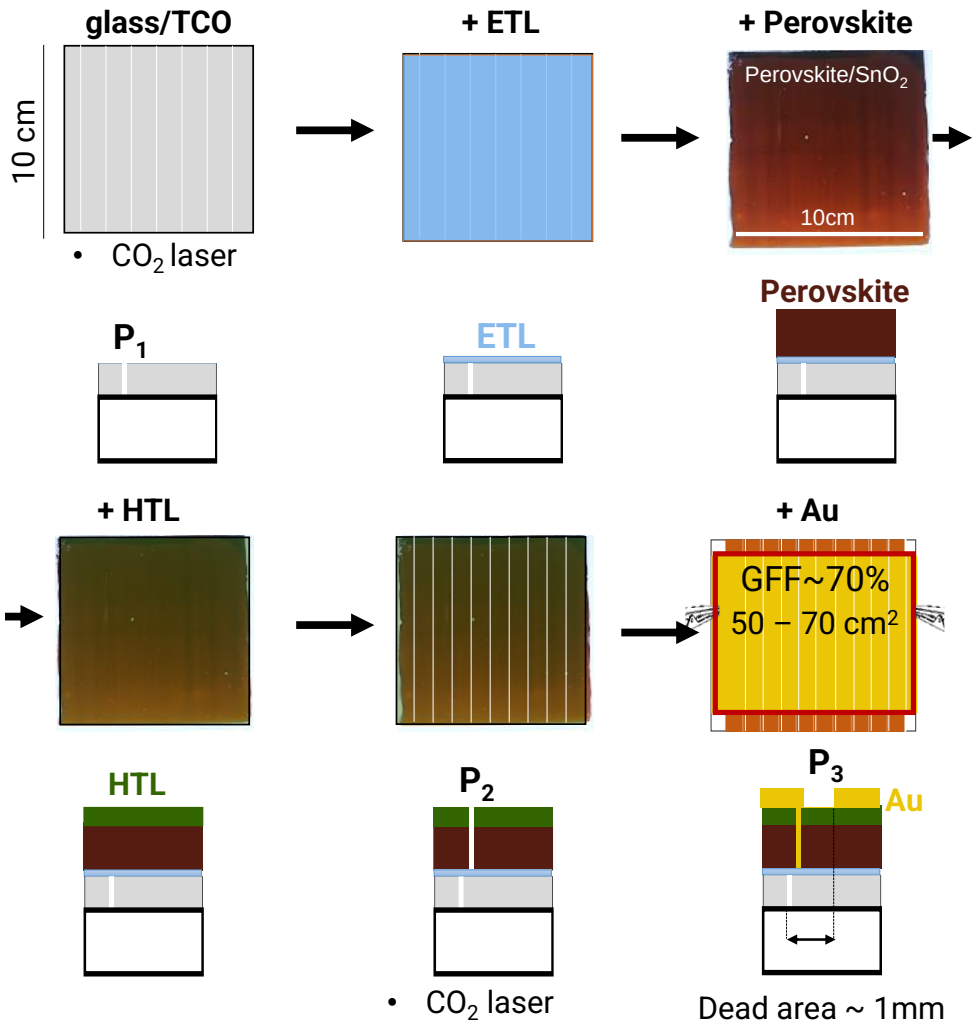

***Figure 9**: Steps of the fabrication of perovskite photovoltaic modules: top and cross-section views. The final device structure is Glass/TCO/ETL/Perovskite/HTL/Au.*

II.2. Characterization of the perovskite layers properties

The characterization of the layer of interest (the perovskite layer) combines complementary techniques to assess the perovskite film morphology, opto-electronic and crystalline properties. All measurements are performed on Glass/TCO/ETL/Perovskite samples, which were cut from 5 x 5 cm^2 into 10 x 10 cm^2 into ~ 1 cm^2 pieces to fit in the various sample holders. We note that this work took place in two distinct laboratories with different characterization equipment. Further discussion is provided in the dedicated sections to introduce the potential variations of measurement methods and how they may affect the interpretation of the data.

II.2.1. Characterization of the perovskite layer morphology

- **Optical imaging**

When working on large-area substrates, a first-level information is provided by the visual inspection of the perovskite films. To save information on the perovskite visual aspect, we record the picture of the perovskite films coated on the 5 x 5 cm^2 and on the 10 x 10 cm^2 substrates using optical imaging *via* white backlit light.

For the 5 x 5 cm^2 samples, we use an existing purpose-built imaging system (Olympus DP70 microscope digital camera connected to DP controller and DP manager software) to take bright field photographs (Coherent Inc lamp ML-0405, cold cathode fluorescent lamp) of the samples on a luminous background with the following settings: size 4080 pixels × 3072 pixels, exposure time of 1 s, image sensor optimization (ISO) of 200 and × 40 magnification (**Figure 10a**). For the 10 x 10 cm^2 samples, a simpler system is built containing a LED backlit pad tablet (Skill) placed in a dark environment (cardboard box). A phone camera (resolution 32 MP) is used to take the picture from the sample at a fixed height ~ 50 cm (**Figure 10b**).

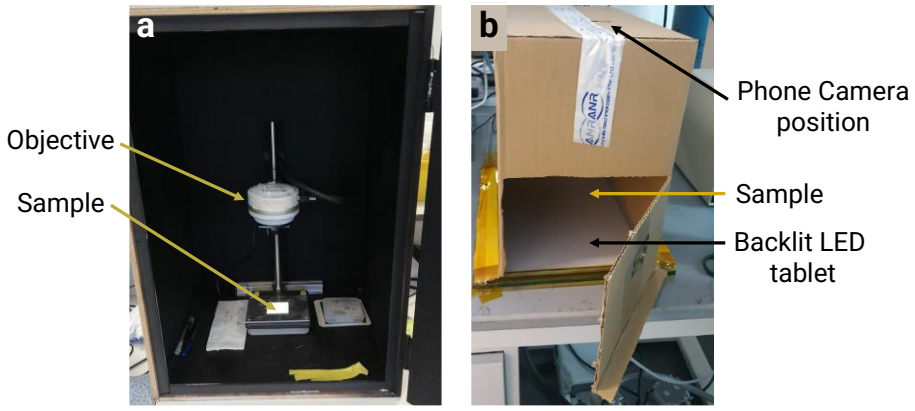

***Figure 10**: Imaging equipment used for the perovskite film visual inspection. **a)** Olympus DP70 set-up. **b)** Home-made equipment.*

- **Extraction of quantitative information from the sample images**

The perovskite film images (**Figure 11a**) are first used to build a sample library and facilitate the batch-to-batch comparison of samples. Later, we have developed a machine vision-based algorithm, "PerovskiteVision", to detect the area of full substrate coverage (**Figure 11b**) and extract quantitative information, such as film thickness, from the images. We calibrate the correlation between the image colour and the perovskite film thickness using the pictures of spin-coated samples with known thicknesses. This enables the conversion of perovskite films imaged into non-destructive film thickness maps (**Figure 11c**). The "Perovskite Vision" algorithm was developed with the university of British Columbia (Pr. Berlinguette group) during the PhD and a paper had been submitted.

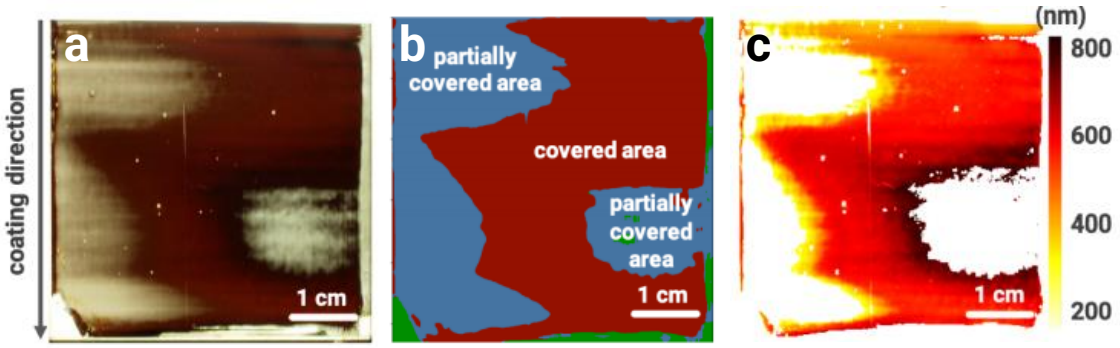

***Figure 11**: Extraction of quantitative information from the perovskite sample image over a 5 x 5 cm² substrate. **a)** Picture of the perovskite film. **b)** Visualization of the perovskite covered area, partially covered and non-covered area using "PerovskiteVision" algorithm. **c)** Contactless film thickness mapping in the covered area obtained using the colour-thickness calibration.*

- **Optical microscopy**

To assess the substrate coverage at micrometric scale, we record the optical images with a microscope Leica DMLM, connected to a Leica DFC420 camera with a magnification ranging from x 10 to x 100. The optical microscopy pictures reported in the manuscript are taken using the x 100 magnification. Those images are treated using ImageJ software to extract the film coverage from the optical images. From the raw image, a binary image is fabricated, then the threshold adjusted, and the outline of the film determined the "Find particles" function of ImageJ software. An example is presented in **Figure 12b**.

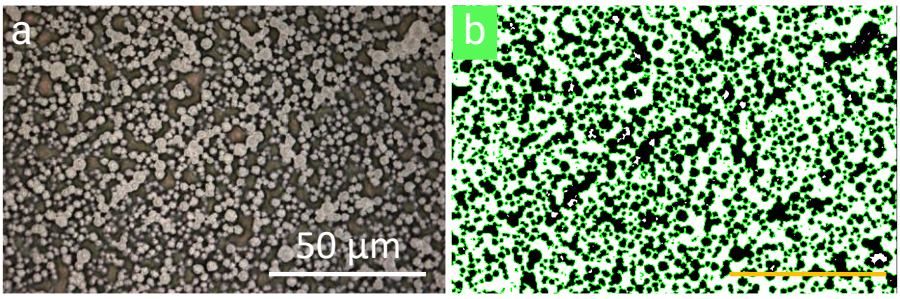

***Figure 12**: Calculation of the film coverage using ImageJ software on the optical microscopy image. **a)** Initial optical microscopy image (magnification x 100): the perovskite film is in light grey and the substrate in dark grey. **b)** Area detected as the perovskite film area by ImageJ software (the contours are highlighted in green).*

- **Profilometry**

To determine the perovskite film thickness and roughness, we use either a Dektak XT (Bruker, diamond stylus, resolution 0.1 nm) or a NanoMap 500 LS (AEP Technologies, resolution 0.1 nm) profilometer. Prior to the measurement, a step is created in the perovskite film by manually etching the film with a tweezer. Nine profiles are performed on three different etched lines per sample. The scan of the perovskite surface in a non-etched location provides an estimation of the average surface roughness (R_a) [156]. The measurement parameters are a stylus force ~ 1 mg, scanning speed of 30 µm.s^{-1} and a scanning length of 1000 µm. A height calibration is performed on the first sample in a batch measurement and repeated between two samples if necessary.

- **Scanning Electron Microscopy**

The Scanning Electron Microscopy (SEM) images (top and cross-sections) are obtained from a Jeol JSM-7600F Field Emission Scanning Electron Microscope (FE-SEM) using an electron accelerating voltage of 5 kV and working distance of 8 mm or by using a Nova NanoSEM 630 (FEI, now Thermo Fischer Scientific) with an accelerating voltage of 10 kV and a working distance of 6.5 mm. No metallization was performed on the samples for the top images. For the cross-section images, the samples are cleaved using a diamond scraper and running pliers. After the cutting, the cross-section area is blown with compressed air to remove any glass particles and platinum is sputtered using a plasma sputterer (Jeol). We used ImageJ software for the grain size determination.

Energy dispersive X-Ray (EDX) analyses were performed using the Nova NanoSEM 630 (FEI, now Thermo Fischer Scientific) with an accelerating voltage of 10 kV, a working distance of 6.5 mm and a scanning time of 30 s.

II.2.2. Characterization of the opto-electronic properties

- **UV-visible spectrophotometry**

In the first configuration, the absorption spectra is derived from the transmission measurement using a UV-2600 or UV-2501PC spectrophotometer (Shimadzu), with a monochromator and an integrating sphere (ISR-2600Plus). The measurement is performed for wavelengths ranging from 300 to 850 nm with a 1 nm step. A deuterium lamp is used from 300 to 323 and an iodine tungsten lamp from 323 to 850 nm. Prior to the sample measurement, the background spectra is measured in air (**Figure 13a**). For the thin film sample spectra, the perovskite film is facing the incident light beam (**Figure 13a**) and the transmitted light is trapped in the integrating sphere and collected by a photodetector. In this configuration, the absorption of the thin film sample is calculated from the sample transmission alone, neglecting the sample reflection (A = 1- T).

The limitation of this set up is that it does not consider the light reflected at the air/sample interface in the thin film absorption calculation. To correct the effect of reflection on our absorption spectra, we have used a combined transmission and reflection measurement approach (**Figure 13b-c**) on another spectrophotometer (Perkin Elmer) with integrating sphere and monochromator for wavelengths ranging from 200 to 1200 nm with a 10 nm step. During the transmission measurement, the sample is placed facing the incident light source, similarly to the previous method. During the reflection measurement, the sample is placed facing the incident light and an obturator is placed behind it to minimize transmission losses. In this configuration, the sample total reflection (including specular and diffuse reflections) is collected in the integrating sphere.

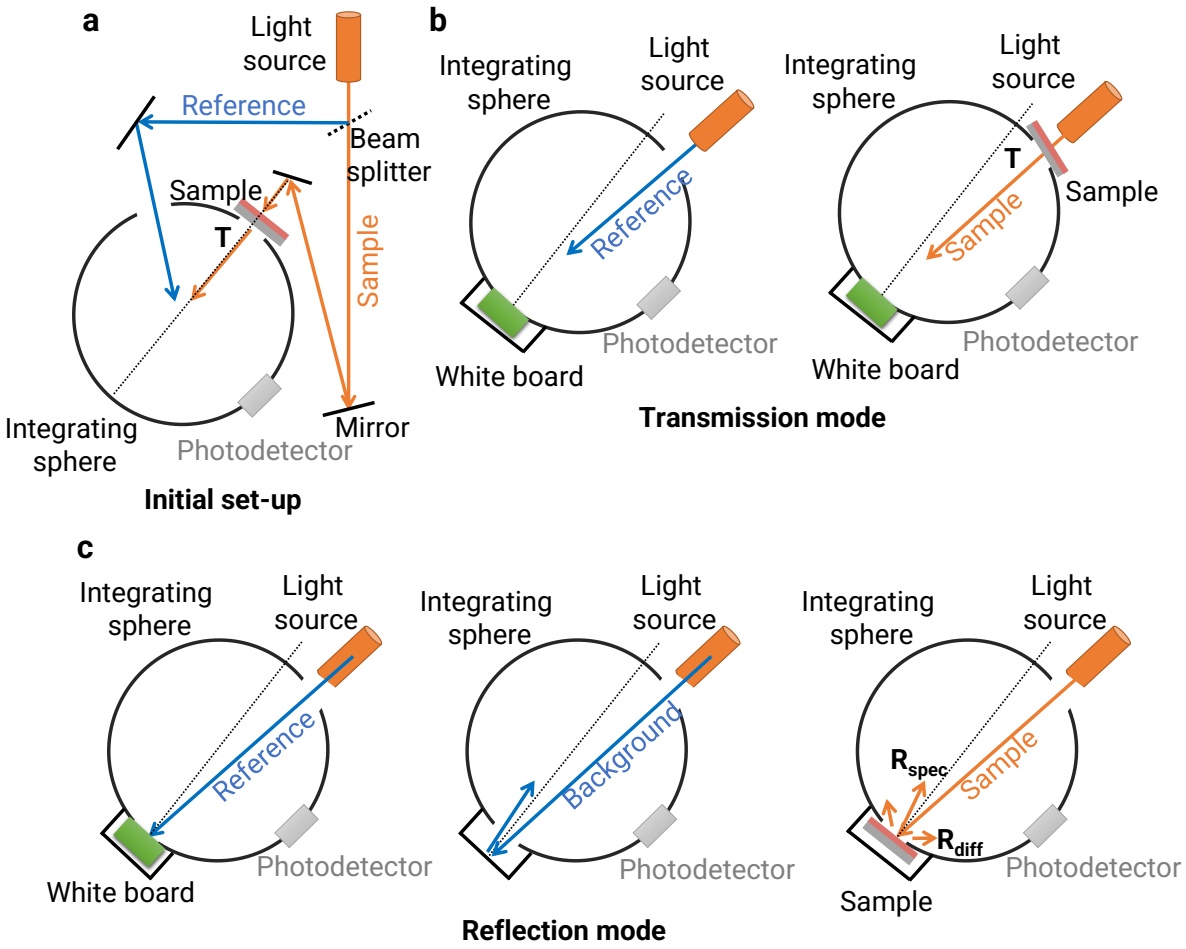

***Figure 13**: Configurations used for the transmission and reflection measurements.*

To calculate the absorbance from the transmission and reflection measurements, we use the following formula: $A = 1 - T - R$ (E_1)

where A is the thin film sample absorption, T the sample transmission and R the sample reflection. The measured transmission can be assimilated to the sample transmission. The measured reflection, however, was the sum of the sample reflection and from the parasitic reflection R' (**Figure 14**). Therefore, we correct it using the following formula: $R = R_{mes} - R'$ with $R' = T^2 * R_O$ where T is the transmission of the thin film and R_O the reflectance of the obturator, assimilated of the background reflectance.

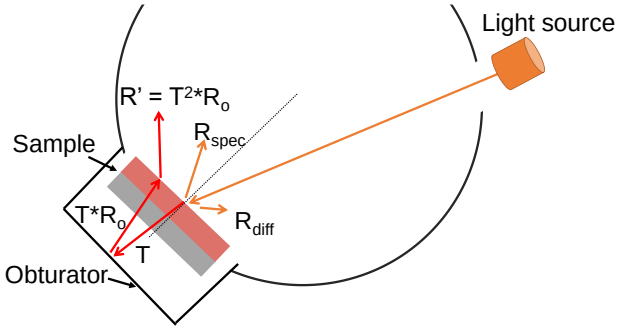

***Figure 14**: Correction of the reflectance due to parasitic effect of the obturator which is not behaving like a light trap.*

- **Determination of the material band gap via the Tauc plot method**

From the absorption spectra, we can extract the band gap of the perovskite material, using the Tauc plot method [157]. This method consists in using the relationship between the absorption coefficient and the band gap energy of light absorber materials:

$$(\alpha h\nu)^{1/n} = \beta\,(h\nu - E_g) \qquad (E_2)$$

Where α is the absorption coefficient of the thin film (m^{-1}), h the Planck constant ($6.663.10^{-34}$ $m^2.kg.s^{-1}$), ν the photon frequency ($\nu = c/\lambda$, with c the speed of light and λ the photon wavelength, in s^{-1}), n is an index that varies with the nature of the band gap of the absorber material (n = 1/2 for direct band gap and 2 for indirect band gaps), and E_g (eV) the band gap of the absorber material. In the case of perovskite materials, n = 1/2 (direct band gap) is generally assumed in the Tauc plot method, while the possible indirect band gap behaviour for halide perovskite remains in discussion in the literature [158].

First, the absorption coefficient (α) is calculated from the sample absorption (A) and perovskite film thickness (t), following this equation: $\alpha = \ln(10)^* A/t$. To determine the band gap of the thin film absorbers, we calculate $(\alpha h\nu)^2$ values from the absorption spectra, film thickness and photon wavelength ($\nu = c/\lambda$). We plot this quantity in function of the photon energy hν. By linear regression, we obtain the intercept of the curve with the X axis, where $h\nu = E_g$ and deducted the band gap of the perovskite material.

- **Photoluminescence spectrophotometry**

The photoluminescence spectra are obtained using a F-4500 FL spectrophotometer (Hitachi), with a Xenon lamp. Optical filters (Edmund Optics) are added to limit the measurement artefacts caused by the 2 λ harmonics presence: a low pass at 575 nm to filter the excitation signal and a high pass at 600 nm to filter the emission signal before the detector (**Figure 15**). The spectra are acquired using a speed of 240 $nm.min^{-1}$ for an emission wavelength range of 600 to 900 nm (1 nm resolution).

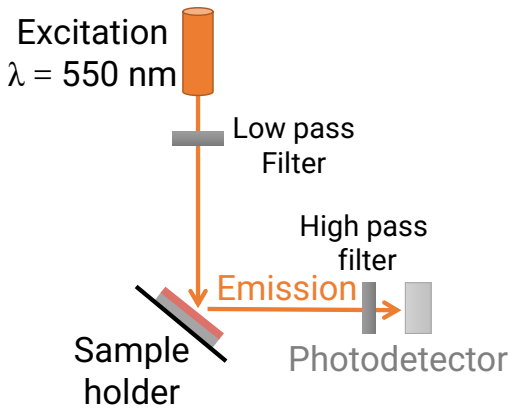

Figure 15: *Configuration used for the photoluminescence measurement.*

- **Time-resolved photoluminescence**

The photoluminescence can be probed in a steady-state configuration or in a time-resolved configuration. The evolution of the PL intensity over time provides additional insights on the recombination rate of the charge carriers in the perovskite film. This recombination kinetics is interesting to quantify the charge carriers lifetime and compare various recombination kinetics in the absorber or at the perovskite/extracting layers interfaces.

The Time-Resolved Photoluminescence (TRPL) measurement are performed using a Picoquant PicoHarp300 time correlated single photon counting system coupled with a micro-PL system. The excitation is performed by a pico-second pulsed LASER diode of 405 nm wavelength and 40 MHz frequency. The signal is observed at 540 nm (Acton SP-2300i monochromator, 300 mm focal, 15 nm slit). The TRPL signals were normalized and fitted using the Origin software 'Normalize' and 'Fit' functions. For the fit, a mathematical bi-exponential exponential model was used.

II.2.3. Characterization of the crystalline structure

- **X-Ray diffraction**

Diffraction is used to extract information about this crystalline motive, such as the crystalline structure (cubic, tetragonal, hexagonal) and the lattice parameters (unit length along each crystallographic axis). X-Ray incident light has wavelength in the angstrom range, which is in the range of the distances between atoms. Therefore, X-Ray light can be diffracted by atomic arrangement if they verify the condition for constructive interferences defined by the Bragg law:

$$2d*\sin(\theta) = p*\lambda \qquad (E_3)$$

with d the distance between 2 parallel plans of atoms (**Figure 16**), θ the incident angle of X-Ray light to the crystalline plan probed and λ the wavelength of the incident X-Ray light. To meet this criterion, the optical path difference between 2 parallel light beams (2d*sin(θ)) should be a multiple of the incident light wavelength. This multiple, p, is a integer also called order.

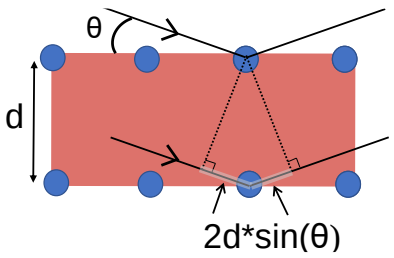

***Figure 16**: Reflexion of X-Ray by a family of planes spaced by a distance d.*

To probe the perovskite crystal by X-Ray Diffraction (XRD), we used two measurement configurations (**Figure 17**): the Bragg-Brentano geometry, in which both the XRD beam and the X-Ray detector are always in movement as such as θ = 2θ; and the grazing incidence X-Ray diffraction (GIXRD) in which the incident angle of the X-Ray beam is fixed to a low angle (ω = 3°) and the detector moves at a 2θ angle.

The grazing incident measurement provides insight on the surface of the thin film while the Bragg-Brentano measurement probes the entire thickness of the thin film. Here, the penetration depth in grazing incidence was in the order of magnitude of the perovskite layer thickness (incident angle θ = 3°, penetration depth estimation of 2 µm [159]). We concluded that both configurations were probing the entire depth of the perovskite film, confirmed by the detection of the substrate diffraction peaks (ITO and FTO) in both diffraction patterns.

For the Bragg-Brentano configuration, we use an Aeris (Malvern PANalytical) X-Ray diffractometer with a cobalt source ($\lambda_{K\alpha}$ = 1.789 Å) and a detector (PIXcel1D-Medipix3) with 2θ values ranging from 10 to 60°. The optics include a divergence slit of ½°, a mask of 23 mm and Soller slits of 0.04° (**Figure 17a**). The sample is spinning at a speed of 60 rpm during the measurement. For the grazing incidence configuration, we use a Bruker D8 Advance X-Ray diffractometer with a copper source ($\lambda_{K\alpha}$ = 1.541 Å) and a detector with 2θ range from 5 to 60°. The optics include an exit slit, anti-scattering slits and Soller slits (**Figure 17b**).

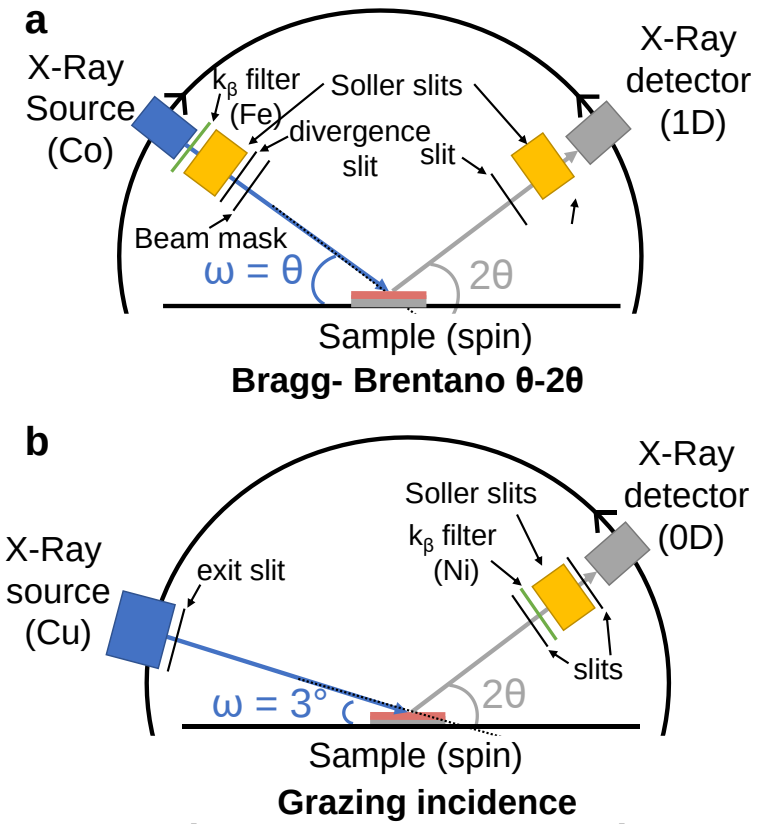

***Figure 17**: XRD measurement configurations used in this work.*

- **Semi-quantitative extraction of information from XRD patterns**

The X-Ray diffraction peaks inform on the presence of crystalline products in the thin films, such as crystalline PbI_2, cubic perovskite structure and undesirable hexagonal perovskite structure (or delta phase). However, it does not necessary lead to a quantitative fraction of PbI_2 or perovskite in the thin film as the amorphous materials are not detected. Yet, the presence of PbI_2 under an amorphous form in perovskite thin films has been reported in the literature [107]. Furthermore, for crystalline products, the more rigorous approach in the literature is to integrate the XRD peak areas (perovskite and PbI_2) with a structure factor correction to quantify their fraction in the perovskite thin film [160]. Here, the presence of multi-oriented perovskite (cubic structure) along various diffraction plans ((001), (011) and (111)) requires more complex calculations to determine the structure factors.

Therefore, we have used a semi-quantitative approach based on the XRD peak areas integration. The areas of the crystalline PbI_2 peak at $2\theta = 12.7°$, of the three perovskite peaks (plans (001), (011) and (111)) and the δ-$FAPbI_3$ at $2\theta = 11.24°$ are integrated using the 'multiple peak fit' function in OriginPro9 software. The baseline is manually adjusted and the diffraction peaks manually annotated on each XRD pattern analysed. All integrated areas are summed and the peak area ratio is calculated as the ratio between the peak area of the peak of interest and the total integrated area. If a low angle peak is detected ($2\theta \sim 9°$), the peak area is considered in this calculation and its peak area ratio extracted. This method is not strictly quantitative but has been useful to compare the samples studied in this work.

II.3. Characterization of the photovoltaic device performance

Once the devices completed, we characterize their performance by current-voltage measurement. We measure the device performance both initially (after device fabrication) and after storage in the dark in controlled atmosphere (~30-40% relative humidity) to study the performance shelf life.

II.3.1. Device electrical measurement: J-V Curves

The ITO-based devices current-voltage (J-V) curves are recorded by a solar simulator Oriel 92190 (Newport) connected to a multimeter SMU 2602A (Keithley) and under standard AM 1.5 G illumination (1600 W, Xenon lamp, Ushio) in ambient condition (~ 30% relative humidity, clean room environment). The power of the lamp is calibrated with a reference silicon cell (certified at Fraunhofer ISE) every time the solar simulator was turned on. The scans are performed in the following conditions: Reverse scan 1.2 to - 0.2 V, on a device active area of 0.33 cm^2 without masking.

The FTO-based devices J-V curves are obtained by using a solar simulator XEC-301S (San-EI Electric) connected to a Keithley 2612A and under standard AM 1.5 G illumination (Xenon lamp). The measurements are carried in the ambient atmosphere at an initial temperature of 25 °C and room humidity of 50%. The system is calibrated with a silicon cell as reference (Fraunhofer ISE). The scans are performed in the following conditions: Forward scan -0.1 to 1.2 V; reverse scan 1.2 to -0.1 V; dwell time of 3.2 ms and a scan rate of 3.4 V/s. We use a metallic mask with aperture of 0.09 cm^2 and no anti reflection coating layer for the measurements. No external bias is applied before measurement.

The Incident Photon-to-Current Conversion Efficiency (IPCE) measurements are recorded using PVE300 (Bentham), containing a dual xenon/quartz halogen light source. The measure is carried in DC mode, (Newport Oriel Sol3A solar simulator with a 450-W Xenon lamp) with a wavelength from 300 to 850 nm. The maximum power output tracking are measured by an Autolabmachine (PGSTAT302N, Software version- NOVA 1.11).

The modules re measured with the solar simulator XEC-301S mentioned above. The module active area is calculated by measuring the length and width of each cell. The module is connected to the solar simulator using alligator clips connected to soldered lines on the side of the module. The illumination area is 10 x 10 cm^2 (no masking of the active area).

II.3.2. Parameters extracted from the J-V curves

From the J-V characteristics measured, we can extract four figures of merit: the open-circuit voltage (V_{oc}), the short-circuit current density (J_{sc}), the fill factor (FF) (**Figure 17**) and the power conversion efficiency (PCE).

The short-circuit current (J_{sc}) is defined as the current flowing in the device when no external voltage is applied (V = 0 V). It is expressed as a density measured on the device 'active area'. The J_{sc} depends on both generation and extraction of charge carriers formed in the absorber. In most cases, the higher the absorption, the larger the electron-hole pairs generated and the higher the current density. The J_{sc} can be expressed using the incident solar spectra (typically AM1.5, with a photon flux $\Phi_{AM1.5}$) and the ability to convert an incident photon into an electron-hole pair (defined by the external quantum efficiency, EQE) through the following equation: $$Jsc = q * \int_{\lambda ini}^{\lambda end} EQE(\lambda) * \Phi * d\lambda \qquad (E_4)$$

Where q is the elementary charge ($1.602.10^{-19}$ C) and λ_{ini} and λ_{end} the wavelength delimiting the absorption domain of the material. The ability to convert a photon into electrons (EQE) depends on the ability to absorb the incoming photon (absorption) and to convert the photon energy into an electrical current (defined as internal quantum efficiency or IQE). Besides the photon-assisted charge generation, the J_{sc} depends on the charge carriers extraction, which can be limited by charge recombination in the absorber or at the device interfaces.

The open-circuit voltage is reached when no current flows into the device. The maximum achievable V_{oc} depends on the material band gap energy (E_g). Under illumination, electron-hole pairs are generated into the absorber, modifying the thermodynamic equilibrium of the charge carriers. At equilibrium, two quasi-Fermi levels form (one for the electrons and one for the holes) and the energy difference between them is called quasi-Fermi level splitting (QFLS). The formation of those energy levels in the absorber results in an electrical voltage at the device terminal. In theory, the V_{oc} can be estimated from the quasi-Fermi level splitting. Practically, the V_{oc} value is limited by charge recombination in the absorber and at the absorber interfaces [161] and is usually lower than the QFLS. As function of the thermodynamics of the charge carriers, the V_{oc} varies with the temperature and illumination intensity.

The fill factor (FF) is defined as the ratio between the maximum power reached by the experimental device (at maximum power point, or MPP) and the power achievable for an ideal device. The power of the device is defined as P = V * J ($W.m^{-2}$) where V is the device voltage (V) and J the device current density ($mA.cm^{-2}$). The maximum power point corresponds to the (J, V) combination yielding a maximum power output (**Figure 18b**).

The FF is expressed as: $FF = \frac{VMPP*JMPP}{Voc*Jsc}$ (E_5)

where V_{MPP} and J_{MPP} are the voltage and current reached at the maximum power point. The FF corresponds to the ratio between the area of a square defined by V_{MPP} and J_{MPP} divided by the area of the square defined by V_{oc} and J_{sc} (**Figure 18a**).

The power conversion efficiency (PCE) is defined as the ratio between the power delivered by the photovoltaic device and the incident power reaching the device (P_{in}) under standard 1000 W.m^{-2} illumination (1 sun), for a solar spectra AM1.5 and a temperature of the cell of 25 °C. It is expressed: $PCE = \frac{PMPP}{Pin} = \frac{FF*Voc*Jsc}{Pin}$ (E_6)

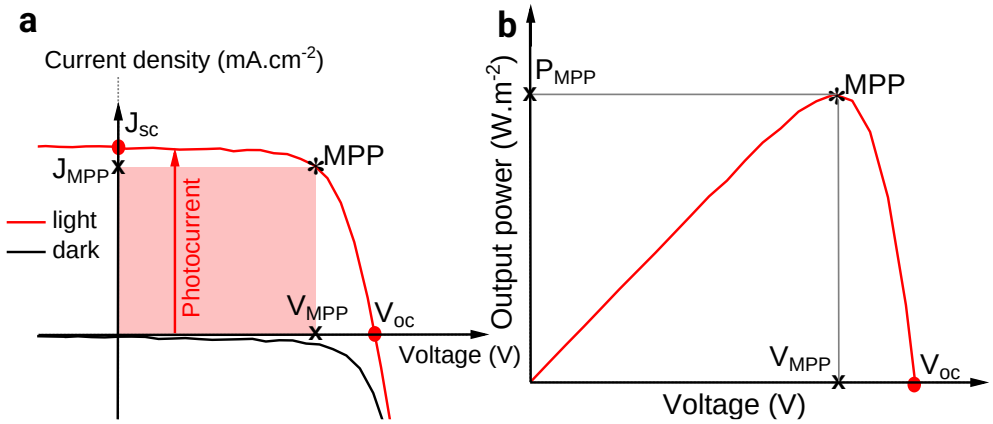

***Figure 18**: **a)** J-V curves parameters description. **b)** Power output in function of the device voltage highlighting the maximum power point (MPP) position.*

II.3.3. J_{sc} optical model

Optical simulations are performed using the TransferMatrix_VaryThickness software provided for free by Stanford University [162,163] using Matlab software. This software computes the current density using the transfer matrix formalism [164,165]. The perovskite layer is modelled by a triple amorphous dispersion law, so as to represent the three oscillators at the origin of each absorption peak in the UV-visible spectra [164,165]. To extract optical indices which are representative of the layers within the solar cell, variable angle spectroscopic ellipsometry measurements are carried out at three different incident angles (50°, 60° and 70°) with an energy range from 0.6 to 4 eV on the following stacks: glass/ITO, glass/ITO/SnO_2, glass/ITO/SnO_2/perovskite and glass/ITO/SnO_2/perovskite/PTAA. Spectra were then fitted using common optical dispersion models for interface layers and electrodes.

The output of the optical simulations is a curve of the current density as a function of the perovskite film thickness. In this work, we compared the experimental J_{sc} values for the corresponding perovskite layer thicknesses with the J_{sc} simulated values (see **Chapters III and IV**). As this optical model depends to the device stack, it was developed for the device stack ITO/np-SnO_2/Perovskite/PTAA/Au architecture. It could be extended to the device structures explored in **Chapter V**.

Chapter III: Perovskite material formation in spin-coating and slot-die coating processes

Here, we introduce two wet processes to deposit the perovskite layer: the laboratory-based spin-coating process and the scalable slot-die coating process. We compare the various perovskite material properties in terms of morphology, optical properties and crystallinity when deposited by those two processes with the same precursor ink. Then, we investigate the impact of precursor ink concentration and post-annealing time on the resulting perovskite layer properties. Finally, we integrated the slot-die coated and spin-coated layers into photovoltaic devices to compare their performances.

III.1. Spin-coating Reference process

Metal halide perovskites are promising photovoltaic materials thanks to their opto-electronic qualities and solution processability. In the laboratory, state-of-the-art perovskite layers are to a large extent processed by spin-coating. We therefore consider spin-coating as a reference process in this work. In this section, we introduce the spin-coating process and the antisolvent assisted crystallization from a practical perspective and characterize the resulting perovskite layers properties (morphology, absorbance, crystallinity). We will use this perovskite thin film characterization methodology for the rest of this work.

III.1.1. Precursor ink formulation and process description

- **Precursor ink: formulation and stoichiometry**

In all wet deposition processes, the chemical precursors are dissolved in a solvent mixture to form the perovskite 'precursor ink'. More precisely, four salts (PbI_2, $PbBr_2$, FAI and CsI) were dissolved in two solvents (DMF and DMSO) for the mixed-cations mixed-halides $Cs_xFA_{1-x}Pb(I_{1-y}Br_y)_3$ perovskite formulation used in this work (FA is the formamidinium cation). The perovskite material will be abbreviated CsFAPbIBr in the rest of the work.

The formulation used was the reference formulation in the laboratory and was not further modified in this section. The precursor ink parameters are summarized in the **Table 1** below. The molarity of the formulation was 1.2 M in respect to [Pb^{2+}]. In the literature, a lack of quantitative tools to measure thin films stoichiometry is often faced and it is usually assumed that the precursor ink stoichiometry is preserved in the resulting thin film [166,167]. It is therefore important to thoroughly prepare the precursor ink as minor stoichiometry variation (1%) may affect the resulting material properties [16].

PbI_2 precursor is widely used in the literature as excess reagent in respect to FAI and CsI precursors to shift the reaction equilibrium towards higher conversion of those precursor into perovskite, yielding high-quality perovskite crystal formation [58,106,107]. However, it has been noticed that PbI_2 presence under a crystalline state in too large proportions can hinder the charge transport and extraction at grain boundaries and/or interfaces and consequently be detrimental to device performances [107,168]. A balance between both phenomena has been demonstrated around 6% lead iodide excess [58]. In this work, we used a similar PbI_2 excess of 6% in the formulation.

Lastly, the addition of secondary cation (Cs^+) and halide (Br^-) to the formulation is known to facilitate the formation of the perovskite cubic structure [40,36,169] and to limit the formation of non-photovoltaic δ-$FAPbI_3$ phase [40,36], also reported as yellow phase in the literature. This topic will be discussed in detail when the crystalline properties of perovskite films will be introduced (**III.1.2.**).

Lead concentration (M)	1.2
PbI_2 excess (%)	6
Cs/Pb molar ratio (%)	5
FA/Pb molar ratio (%)	79
Br:I molar ratio (%)	12 : 88
DMF :DMSO volume ratio	4 : 1

***Table 1**: Composition of the reference precursor ink.*

- **Precursor ink: coatability**

In a wet deposition process, the physico-chemical properties of the ink will influence the wet film coating. In practice, parameters such as the ink density, viscosity and wettability define the substrate/ink interaction. In some systems, the physico-chemical properties of an ink could be approximated with the properties of the solvent mixture. Here, given the relatively high precursor concentration, the precursor ink density is as expected significantly higher (1.51 ± 0.05 $g.mL^{-1}$) than DMF (0.94 $g.mL^{-1}$) and DMSO (1.10 $g.mL^{-1}$) solvent densities. We concluded that the presence of precursors in the ink (under a solute form) affected the solution properties such as density, and from now on, we considered the precursor solution as one system comprised of the precursor solute and the solvent mixture.

Despite the relatively large process window of spin-coating compared to other coating methods such as inkjet printing [170], dewetting phenomena of perovskite inks have been reported, leading to inhomogeneous crystallization and formation of pinholes [171] in the resulting films. In this work, perovskite was spin-coated onto a glass/ITO/SnO_2 substrate. To assess the ink/substrate affinity, we measured the sessile drop angle from the precursor ink onto the SnO_2-coated ITO substrate. As a contact angle close to 0° was obtained (**Figure 1a**), we confirmed that the perovskite ink was fully wetting the substrate.

We extracted the SnO_2-coated ITO substrate wettability envelope (**Figure 1b**) from the sessile drop method with 4 solvents (deionized water, ethylene glycol, diiodomethane and α-bromonaphthalene). The total surface tension of the reference perovskite ink by pendant drop method was 42.5 ± 1 $mN.m^{-1}$. This value is higher than the one of a DMF:DMSO mixture (38.2 ± 1 $mN.m^{-1}$), confirming the influence of precursors on the ink properties. The contact angle between an ink droplet and a non-polar surface (polytetrafluoroethylene) was 76°, consequently the perovskite ink polar and disperse surface tension component were 3.9 and 38.6 $mN.m^{-1}$ respectively (**Figure 1b**). The perovskite ink coordinates were located inside the wettability envelope of the substrate, in line with the full wettability observed on **Figure 1a**. We concluded from those observations that the perovskite ink was compatible with direct coating on SnO_2-coated ITO substrate, without pre-treatment step (such as UVO_3).

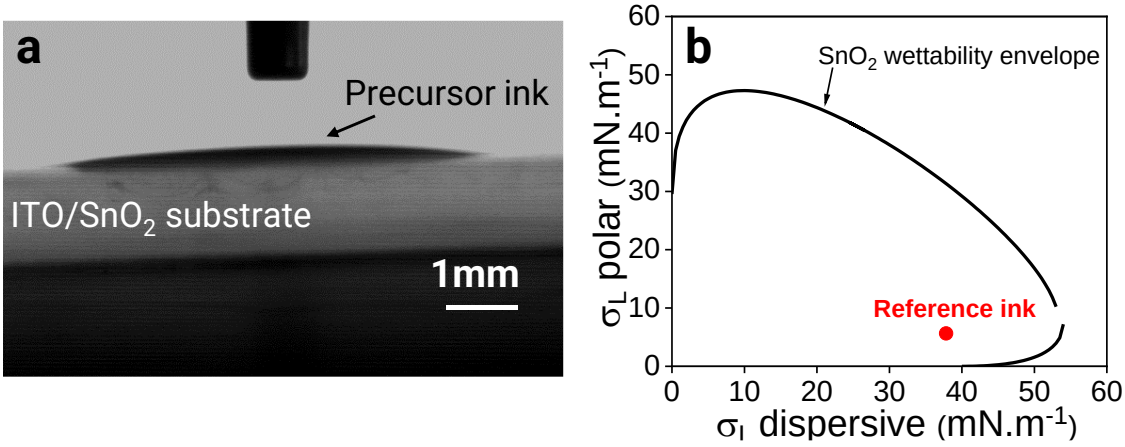

***Figure 1**: Precursor ink properties. **a)** Sessile drop image on SnO_2 substrate. **b)** Wettability envelope of SnO_2 substrate and position of the reference precursor ink.*

- **Perovskite layer formation**

As previously explained in Chapter I, to form a perovskite thin film via wet deposition, two steps are necessary. First, a coating step where the precursor ink is deposited onto a substrate to form a wet precursor film. Then, a crystallization step where the crystal nucleation and growth are triggered by external forces. The control of perovskite crystallization is key to obtain crystalline, absorbent and compact films and the means of control may vary with the deposition technique used [172].

In the case of spin-coating reference process, first, the precursor ink was generously dispensed to cover the entire substrate (~1 mL on 25 cm²). Then, the glass substrate was driven in rotation and most of the ink ejected by centrifugal effect (99%). To describe the wet film thickness during spreading, we used the Emslie, Bonner and Peck model which considers a spun-coated fluid on an infinite disk subject to centrifugal effect [69]. The wet film thickness evolution with time can be described with the following formula:

$$h(t) = \frac{h_0}{\sqrt{1 + \frac{4\rho\omega^2}{3\eta} h_0^2 \, t}} \quad (E_1)$$

with the perovskite ink density ρ = 1.51 g.mL^{-1} (experimental value), viscosity η = 8 mPa.s (literature value [170]), h_0 = 400 µm (1 mL on 25 cm²) and ω the spinning speed that vary with the spin-coating program step. **Figure 2c** presents the evolution of wet film thickness during the spin-coating program (see **Methods**). Overall, the spreading step reduced the wet precursor thickness from 400 µm to 1 µm in few seconds. In recent years, some groups have studied the nucleation and growth kinetics *in-situ* via reflection measurement [173,174] during spin-coating processes. We observed a good correlation between their experimental reflectance measurements results and our physical model estimation of the wet film thickness of 0.9 µm.

After 30 seconds, an "anti-solvent" (600 µL of chlorobenzene) was dropped onto the ~ 1 µm wet precursor film to trigger nucleation [175]. The chlorobenzene was miscible with DMF:DMSO but did not dissolve perovskite precursors. The chlorobenzene addition decreased the solubility of precursors in the solution and induced the formation of nuclei in the wet precursor film [80] (I.2.3). Finally, a thermal post-annealing step at 100 °C for 1 h completed the perovskite crystal growth. This process was performed under a nitrogen-filled glovebox to limit humidity and oxygen exposure (< 1 ppm). The next section presents the properties of the perovskite layers obtained by spin-coating process with the reference precursor ink.

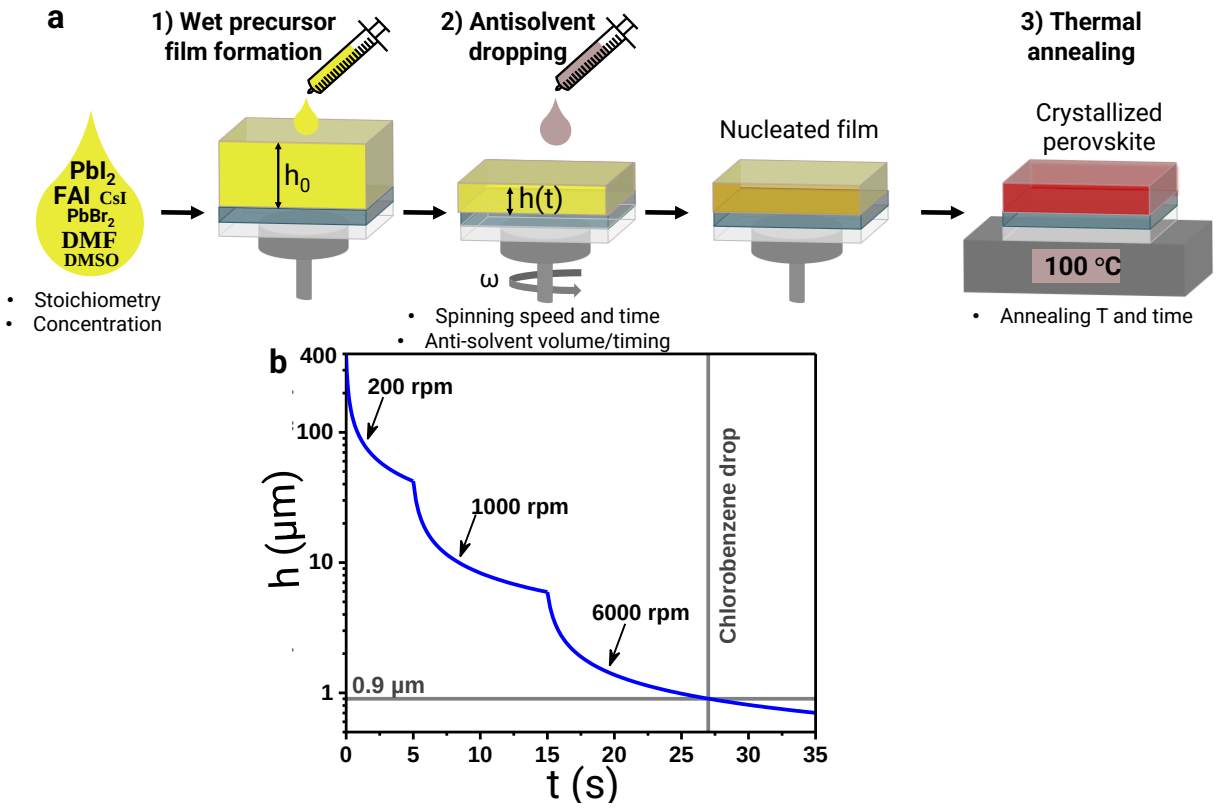

***Figure 2**: Description of spin-coating process. **a)** Spin-coating of perovskite layer: wet film deposition, perovskite crystallization via antisolvent dropping and post-annealing step. **b)** Evolution of the wet film thickness during the spin-coating process calculated from (E_1).*

III.1.2. Material properties of spin-coated perovskite layers

To assess the quality of the perovskite layer, *in-situ* and *ex-situ* characterization approaches exist. Since *in-situ* characterization equipment (reflectance or GIWACS) were not easily accessible, a methodology was developed to characterize *a posteriori* the quality of the perovskite layers. This process development methodology is popular in perovskite research [176–179] as it can be performed using readily accessible equipment (Spectrophotometry, Microscopy, X-Ray diffraction). Once this *ex-situ* approach chosen, we defined the relevant parameters to assess the quality of the perovskite film (**Table 2**).

As large-area coating was performed, we introduced morphological metrics. We measured the perovskite-coated area (A) *via* sample imaging, extracted the film macroscopic coverage (c) from optical microscope images and used profilometry to extract the perovskite film thickness (t) and average surface roughness (R_a). To get closer insights, we used scanning electron microscopy to assess the presence of pinholes (c') and the perovskite grain size (g). As the perovskite material was the absorber material, we assess its band gap using spectrophotometry coupled with Tauc plot extraction method. Lastly, since the perovskite crystallization may result in various crystalline structures, we monitored by X-Ray diffraction the presence of the CsFAPbIBr cubic structure (or α phase) and of the hexagonal structure (δ or yellow phase) in the resulting thin film. We also monitored the residual crystalline PbI_2 quantity as it could affect device performances.

Morphology	coated area (cm^2)	A
	film coverage (%)	c
	perovskite thickness (nm)	t
	film roughness (nm)	R_a
Zoom in	film compacity (%)	c'
	grain size (nm)	g
	white particles	-
Optical	band gap (eV)	E_g
Crystallization	α-CsFAPbIBr	-
	δ-$FAPbI_3$	-
	crystalline PbI_2	-

***Table 2**: Characterization matrix to assess the perovskite layers quality with key indicators and their abbreviations.*

- **Morphology of spin-coated perovskite layer**

The morphology of the perovskite layer will influence the charge generation and transport during the solar cell operation. To reach a maximum device efficiency, the perovskite absorber thickness and roughness should be optimized and the presence of grain boundaries or pinholes minimized. The perovskite film thickness has to be balanced between too thin absorbers limiting the current generation as fewer photons can be absorbed and too thick absorbers that may not retain good opto-electronic properties [180]. The surface roughness influences the coating of additional layers on top of the perovskite layer, therefore a minimal surface roughness is desirable [181]. The perovskite grain boundaries should be minimized as they can act as recombination centre for charge carriers [182,183]. Similarly, macroscopic or microscopic (pin-) holes should be avoided as they create device shorting by forming a direct contact of the electron transport layer (ETL) and the hole transport layer (HTL).

We can see on the sample picture (**Figure 3a**) that the perovskite layer deposited *via* spin-coating reference process was homogeneous over the substrate (coated area A = 25 cm²). To assess the film coverage, profilometry provided a coarse morphological mapping (**Figure 3b**). On the optical microscopy image (**Figure 3c**), the perovskite layer was continuous. We did not observe any pinholes, and therefore considered that the film coverage c was 100% at the micrometric scale. We measured *via* profilometry a perovskite average thickness t = 450 nm and average roughness R_a = 10 nm (**Figure 3d**). The thickness value was within the state of the art thickness range from 300 to 1000 nm [184] within which they can be compatible with device integration.

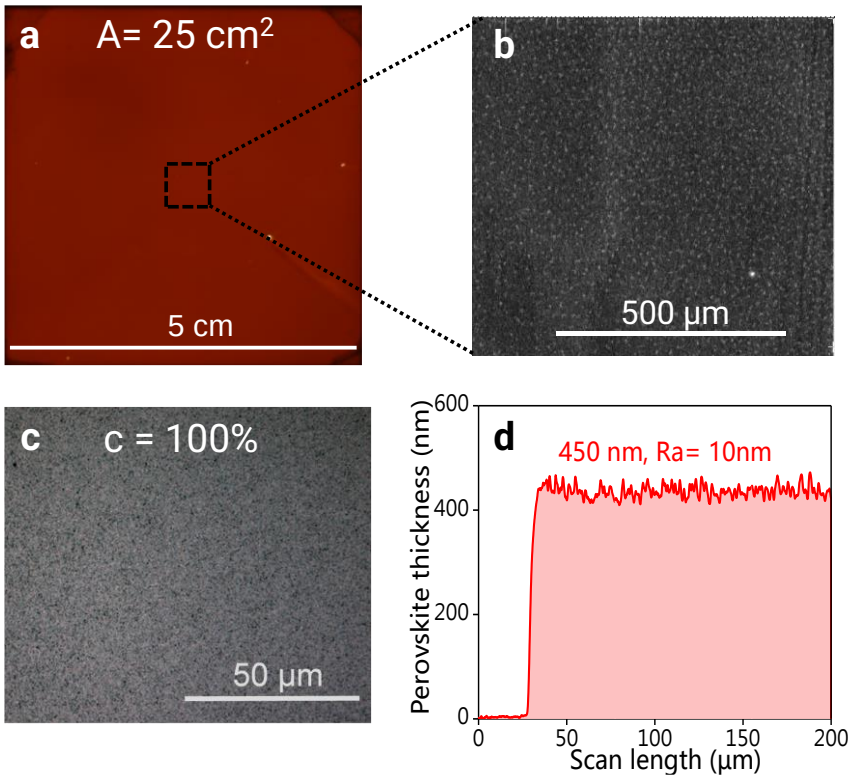

***Figure 3**: Morphology characterization of the spin-coated perovskite layer. **a)** Picture of the spin-coated perovskite layer on a 5 x 5 cm² substrate. **b)** Image reconstructed from profilometry mapping, **c)** Optical microscopy image and **d)** Profilometry scan of the perovskite layer.*

- **"Zoom in" on the perovskite layer morphology**

Since full film coverage was detected at the micrometric scale, we performed scanning electron microscopy (SEM) to assess the film quality at a nanometric scale. On the SEM picture (**Figure 4a**), the perovskite film exhibited a compact granular morphology without pinholes. We defined the film compacity (c') as the film coverage at the SEM scale. The film compacity was 100% in this case. The average grain size was 273 nm (**Figure 4b**). The grain size was within the range (100 – 1000 nm) observed in the literature [185]. The smaller grain size compared to perovskite film thickness suggested that the perovskite layer (t = 450 nm) could be composed of at least two superposed grains (~ 225 nm each).

In the literature, both monolithic (one grain) and multi-layered (multiple superposed grains) morphologies have been reported [186]. The cross-section SEM image confirmed the presence of several superposed grains in the perovskite layer (**Figure 4c**). The cross-section estimated a perovskite thickness of 507 nm, in rather good accordance with the 450 nm average obtained by profilometry. Some white particles were visible at the surface of the perovskite layer (**Figure 4a**). We will discuss their chemical nature further in the crystalline properties characterization section.

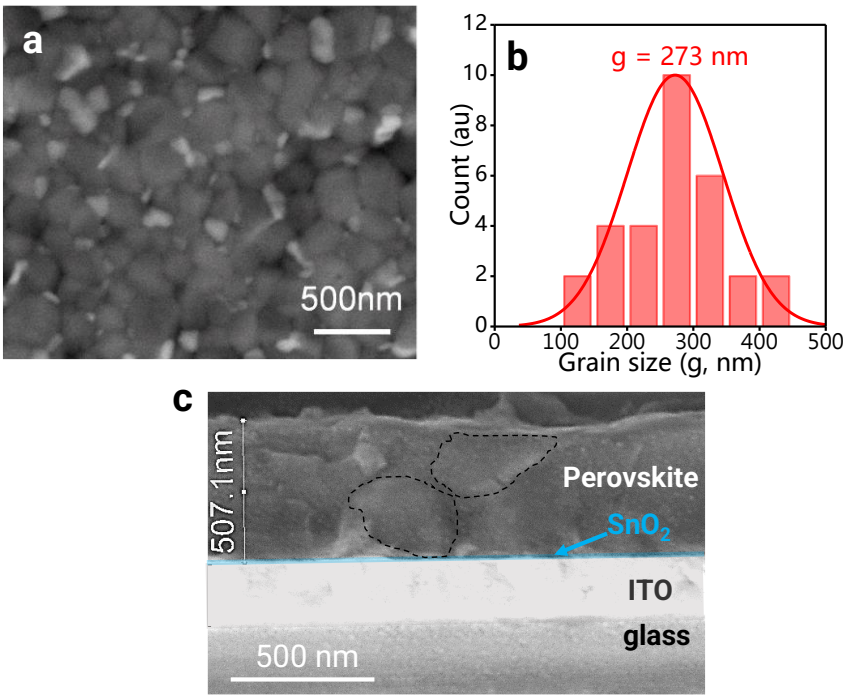

***Figure 4**: Morphology "zoom-in" characterization of the spin-coated perovskite layer. **a)** Scanning Electron Microscopy (SEM) image of the reference perovskite layer on glass/ITO/SnO_2 substrate. **b)** Corresponding grain size distribution. **c)** Cross-section SEM image of the reference spin-coated layer. Two grains contours were highlighted with the dashed lines.*

- **Optical properties**

The absorption spectra (**Figure 5**) of CsFAPbIBr perovskite thin film presented an absorption onset at a wavelength ~ 775 nm and a sharp increase from 700 nm to 400 nm, similarly to what was observed in the literature [187] for high coverage and shiny perovskite films. This result was in accordance with the compact smooth morphology observed earlier. We extracted the optical band gap of the perovskite *via* the Tauc plot method assuming a direct band gap (**Chapter II**). The extracted perovskite optical band gap was E_g = 1.60 ± 0.05 eV, value comprised as expected between the pure $FAPbI_3$ (1.48 eV) and pure $CsPbI_3$ (1.73 eV) materials. The photoluminescence spectra (**Figure 5**) presented a maximum intensity at 765 nm (E_g = 1.62 eV). The bang gap value obtained from PL measurement was in the same range as the optical band gap.

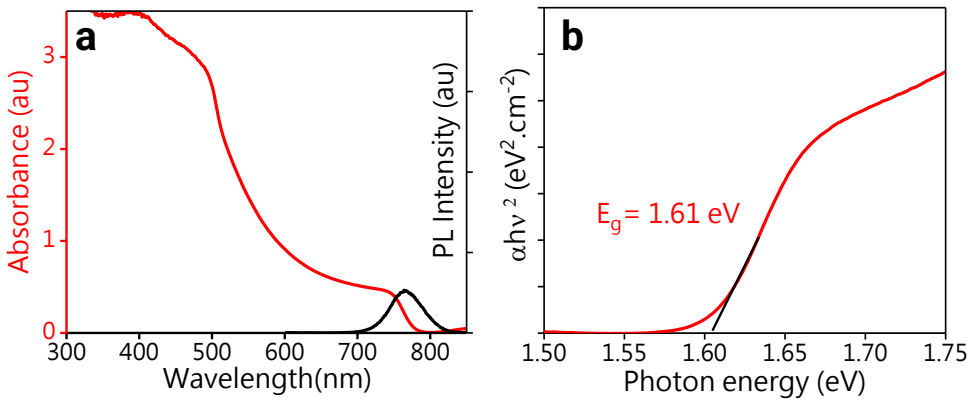

***Figure 5**: Optical characterization of the perovskite layer. **a)** Absorbance and superposed photoluminescence spectra (excitation wavelength: 550 nm) and **b)** Tauc plot band gap extraction for the reference spin-coated perovskite layer.*

- **Crystallographic properties**

The crystallization of $FAPbI_3$ perovskite at room temperature can result in the formation of both the α-CsFAPbIBr (cubic) and δ-$FAPbI_3$ (hexagonal) crystalline structures [16,39,32,117,188]. The presence of δ-$FAPbI_3$ phase is not desirable, as its large band gap (2.36 eV [40]) does not contribute to the photovoltaic effect. The addition of Cs^+ cation (*via* CsI precursor) in $FAPbI_3$ facilitates the formation of the cubic structure for mixed-cations $Cs_{1-x}FA_xPbI_3$ perovskites (x = 0.05 to 0.17) [188]. Similarly, the introduction of the bromide anion (*via* $PbBr_2$ precursor) facilitates the formation of the cubic structure [189]. As commonly used in literature [16], we incorporated 5% Cs/Pb molar ratio in respect to PbI_2 and 17% Br/I molar ratio in the precursor ink formulation (**Table 1** in **III.1.1**).

To assess the perovskite film crystalline structure, we recorded the X-Ray diffraction (XRD) patterns of the perovskite thin films (**Figure 6a)**. The reference perovskite layer has undergone the conversion into the CsFAPbIBr perovskite cubic structure (or α-CsFAPbIBr), evidenced by the signature peaks at 13.81°, 19.70°, 24.28°, 28.16°, 31.64°, 40.45° and 43.00° attributed to the (001), (011), (111), (002), (012), (022) and (003) plans [190], respectively. We noticed that the perovskite crystals had a preferred orientation along the (001) plan. This preferential orientation has been reported in the literature [40], and is possibly related to the precursor solution formulation and to the substrate affinity. Further considerations on this topic are provided in **Chapter IV** (precursor solution) and **V** (substrate affinity). We observed a reduced lattice parameter of a= 6.303 Å (α-CsFAPbIBr [191]) compared to state of the art a= 6.362 Å (α-$FAPbI_3$ [192]). This is in accordance with the literature where the addition of caesium cation and bromide anion is known to reduce the lattice parameter [188].

Beside the α-CsFAPbIBr, we observed the presence of the δ-$FAPbI_3$ tetragonal phase at 11.24°. The negligible peak intensity confirmed that the δ-phase formation was limited in this system. Furthermore, we observed the presence of PbI_2 at 12.40° that can be explained by the introduction of excess PbI_2 precursor (6%). In the literature, PbI_2 has been found to form white particles on top of the perovskite layer [193]. We thus propose that the crystalline PbI_2 detected by XRD could explain the observation of white particles on SEM images (**Figure 4**). Lastly, a CsI diffraction peak was detected at 2θ = 30.50°. It can correspond to the presence of remaining CsI precursor that did not react.

Beyond phase identification, XRD peak area integration can support a semi-quantitative extraction of information on the relative composition of the perovskite thin films [160,194]. The more rigorous approach in the literature is to integrate the XRD peak areas (perovskite and PbI_2) with a structure factor correction to quantify their fraction in the perovskite thin film [160]. In our case, the multiple orientations in CsFAPbIBr perovskite film made the direct application of this method complex. We used a semi-quantitative alternative, where the three α-CsFAPbIBr perovskite ((001), (011) and (111) plans), the δ-$FAPbI_3$ (11.24°) and the crystalline PbI_2 (12.40°) peak areas are measured and their relative values extracted (**Figure 6b-c).** This method will be later used for comparative studies (III.1.3).

In the reference spin-coated sample, the large proportion of perovskite (001) peak (relative peak area ratio of 55%) was in agreement with the (001) preferential orientation in the perovskite film. While the δ-$FAPbI_3$ peak area ratio was negligible (< 0.4%), the crystalline PbI_2 peak area ratio was 27% in average (values from 20 to 40% on **Figure 6c**). The calculated crystalline PbI_2 ratio was much larger that the excess quantity introduced (6%). This could be due to the fact that this method is not strictly quantitative but could also indicate that the sample exhibits a limited conversion into perovskite (PbI_2 which did not react) and/or a perovskite deconversion (PbI_2 as degradation product [195]).

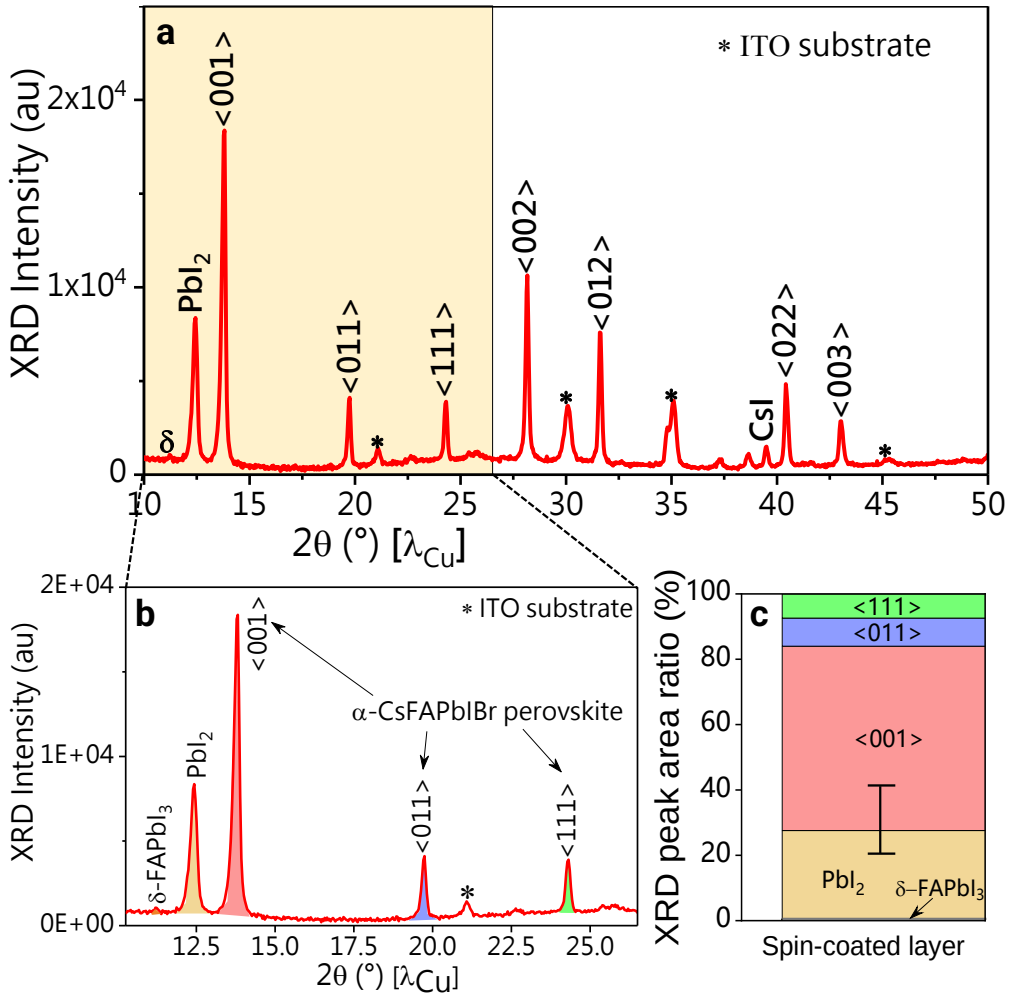

***Figure 6**: Composition characterization of the spin-coated perovskite film. **a)** X-Ray diffractometer of the perovskite reference layer. **b)** Zoom in the interest area. **c)** Extracted Relative Peak Areas from δ-FAPbI₃, PbI₂, (001), (011) and (111) α-CsFAPbIBr perovskite plans.*

Once all the characterizations performed, we can summarize the key metrics of the perovskite layer, using the characterization matrix, as shown in **Table 3**.

Morphology	coated area	A = 25 cm²
	film coverage	c = 100%
	perovskite thickness	t = 450 nm
	film roughness	R_a = 10 nm
Zoom in	film compacity	c' = 100%
	grain size	225 nm
	white particles	Yes
Optical	band gap	E_g = 1.61 eV
Crystallization	α-CsFAPbIBr	Yes
	δ-$FAPbI_3$	Yes (< 0.4%)
	crystalline PbI_2	Yes (27%)

***Table 3**: Characterization matrix of the reference spin-coated layer.*

III.2. Slot-die coating process

In this section, we introduce the slot-die coating process, define the main process parameters and present an iterative process parameter optimization to achieve compact CsFAPbIBr slot-die coated perovskite layers.

III.2.1. Process description and first slot-die coated layer

For a direct comparison to spin-coating process, we used the reference precursor ink formulation in this section. As a reminder, the composition of the reference precursor ink is described in the **Table 1** (**III.1.1**.).

While some parameters such as the precursor ink formulation can easily be transferred from one process to the other, the "anti-solvent" crystallization step cannot be used on a fixed substrate (without centrifuge effect) and is therefore not transferable from spin-coating to slot-die coating process. As seen in **Chapter I**, Conings *et al.* developed the gas-quenching method in spin-coating process as substitute to anti-solvent method for various perovskite formulations including CsFAPbIBr material [13,196]. A first application of gas-quenching to slot-die coated $MAPbI_3$ films was performed in 2018 by Vak *et al.* [86,196]. Gas quenching was combined with limited substrate heating (< 100 °C) for better results. In this work, we decided to apply the gas-quenching nucleation strategy to CsFAPbIBr perovskite in slot-die coating process.

- **Gas-knife assisted slot-die coating description**

Similarly to the spin-coating process, the slot-die coating process was composed of two steps: a coating step and a crystallization step (**Figure 7**). The coating step was controlled by the distance of the die to substrate (coating gap, C_g), the precursor ink coating flow rate (C_f) and the slot-die coating speed (C_s) (**Figure 7b**). Then, the gas-knife quenching step, combined with substrate heating, triggered the nucleation and crystallization of perovskite material (**Figure 7c**). More precisely, the substrate heating (CQ_t) permitted the solvent evaporation (DMF:DMSO, 4:1) and the gas-quenching triggered the nucleation of the precursor wet film though a cooling effect (nitrogen temperature was 20 °C) and by fast solvent evacuation driven by convection [197]. The gas-knife 'power' was tuned by adjusting the gas flow rate (Q_f), the speed of the gas-knife (Q_s) and the distance between gas-knife and substrate (Q_g). In our case, the gas-knife speed was identical to the coating speed ($C_s = Q_s = CQ_s$) because the gas-knife was fixed to the slot-die head. After the gas quenching, a post-annealing step could be performed, similarly to the spin-coating process. The post-annealing parameters were the annealing time (A_t) and temperature (A_T). The list of the parameters is summarized in **Table 4** below.

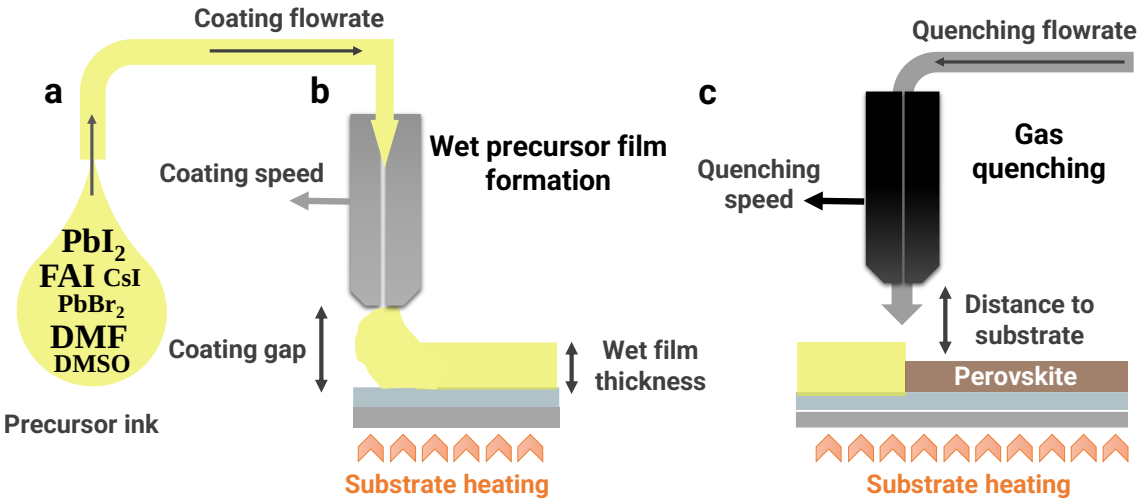

***Figure 7**: Overview of the slot-die coating process with the key process parameters involved.*

Coating		**Quenching**		**Post-Annealing**	
Coating gap	**C_g**	Quenching gap	**Q_g**	Annealing Temperature	**A_T**
Coating speed	**CQ_s**	Quenching speed	**CQ_s**		
Coating flow rate	**C_f**	Quenching flow rate	**Q_f**	Annealing time	**A_t**
Substrate temperature	**CQ_T**	Substrate temperature	**CQ_T**		

***Table 4**: Main process parameters list and abbreviations.*

During the coating step, a major difference with spin-coating process is the efficient material use: there is no ejection of matter in the slot-die coating process. Based on the hypothesis that the quantity of ink deposited on the substrate is conserved in the precursor wet film, we can estimate the theoretical wet film thickness from the coating speed (C_s), coating width and coating ink dispense flowrate (C_f):

$$C_t\,[m] = \frac{C_f[m^3/s]}{coating\ width\ [m]\ x\ C_s\ [m/s]} \qquad (E_2)$$

In the literature, Di Giacomo *et al.* used a 3-4 µm thick precursor wet film for $MAPbI_3$ perovskite slot-die coating at a precursor concentration of 0.6 M to target a 350 nm dried perovskite film thickness [75]. In our system, we used coating parameters from the literature : a coating gap (C_g) of 100 µm, a coating flow rate (C_f) of 100 µL.min^{-1} and a coating speed (CQ_s) of 8 mm.s^{-1} (**Table 5**). With these parameters, we estimated (using equation E_2) a precursor wet film thickness of 4 µm, which was comparable to the wet thickness range used by Di Giacomo *et al.* . We note that the estimated slot-die coated precursor wet film thickness was higher than the estimated spin-coated wet film thickness (0.9 µm). Additional discussion on the wet film thickness and comparison between the spin-coating and the slot-die coating processes is available in **Appendix 1**.

The second main difference between the two processes was the way to control the perovskite nucleation. In the slot-die coating process, we chose a combined approach of substrate heating and gas quenching (**Figure 7c**). We used nitrogen gas with a gas flow rate of 25 L.min^{-1} and a distance to substrate ~ 3 mm as reported earlier in the literature [198]. The quenching speed and temperature were the same as in the coating step.

Since the nucleation mean differed, the post-annealing step differed too. After quenching, slot-die coated layers are generally annealed at 100 °C for shorter times (1-10 minutes [86,199]). Based on those observations, we performed a thermal annealing at 100 °C for 5 min under nitrogen atmosphere after the gas-quenching step.

For the first slot-die coating experiment, the slot-die coating process parameters are summarized in **Table 5**.

Coating		**Quenching**		**Post-Annealing**	
C_g	100 µm	**Q_g**	3 mm	**A_T**	100 °C
CQ_s	8 mm.s^{-1}	**CQ_s**	8 mm.s^{-1}		
C_f	100 µL.min^{-1}	**Q_f**	25 L.min^{-1}	**A_t**	5 min
CQ_T	100 °C	**CQ_T**	100 °C		

***Table 5**: Process parameters used for the first slot-die coating experiment.*

- **First slot-die coated perovskite layer**

The properties of the resulting perovskite layer will be presented following the same characterization matrix developed earlier for the spin-coated layers: 1) morphology, 2) optical properties and 3) perovskite conversion.

In the slot-die coating process, we deposited the meniscus on the substrate at a certain distance from the substrate edge (0.5 – 1 cm), which resulted in a slightly lower coated area (A = 20 cm^2, **Figure 8a**) compared to the spin-coated substrate (A = 25 cm^2) where the entire substrate was covered by the perovskite film. We observed a poor micrometric coverage by optical microscopy (**Figure 8b)** and extracted a film coverage c = 40%. from this image. By profilometry (**Figure 8c**), we measured film thickness variations between t = 0 to 8 µm and observed the formation of aggregates of 20 µm diameter which may correspond to the grey craters observed in the optical image (**Figure 8b**). During the coating, we observed that the precursor wet film started to dry when in contact with the 100 °C substrate and prior to the gas quenching step. This could explain the disruptive morphology obtained [12].

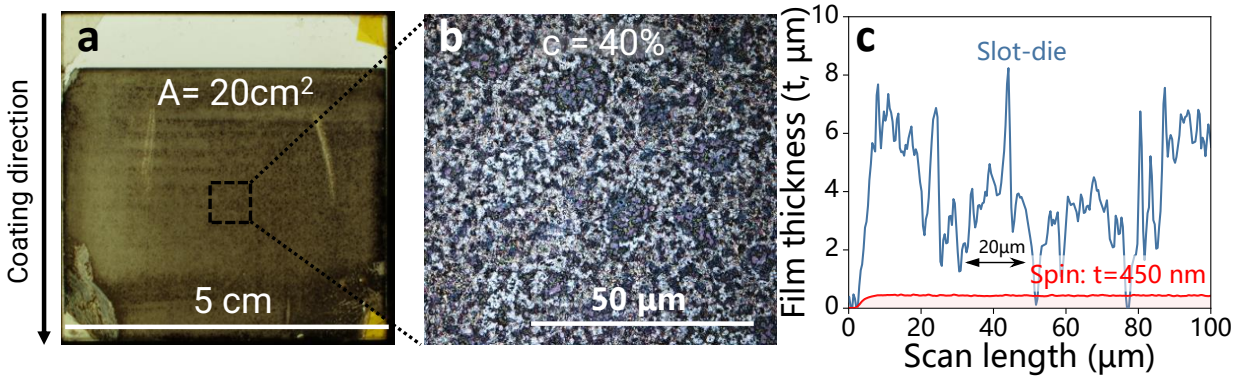

***Figure 8**: First slot-die coated perovskite layer characterization. **a)** Picture of the slot-die coated sample on a 5 x 5 cm² substrate. **b)** Optical image of the slot-die coated sample. **c)** Profilometry mapping of the slot-die coated layer (blue) and of the reference spin-coated layer (red).*

In the absorbance spectra (**Figure 9a**), the slot-die coated layer exhibited a reduced absorption onset at 780 nm, which corresponds to α-CsFAPbIBr material band gap. However, due to the rough morphology, the absorbance curve remained flat in the wavelength range 780 - 500 nm [187]. We noticed a secondary wave around 450 nm that may correspond to the presence of reaction intermediates in the film [41,200] that did not convert to perovskite. X-Ray diffraction results (**Figure 9b**) confirmed the presence of α-CsFAPbIBr perovskite material with its signature peaks at 2θ = 13.81°, 19.70°, 24.28°. Yet, they all exhibit very low intensity in accordance with the low absorbance detected at absorption onset. The absence of peak at 2θ = 12.4° suggests that crystalline PbI_2 was not detectable in this sample. However, low angles peaks (2θ ~ 9°) unveils the presence of unreacted intermediates in the film.

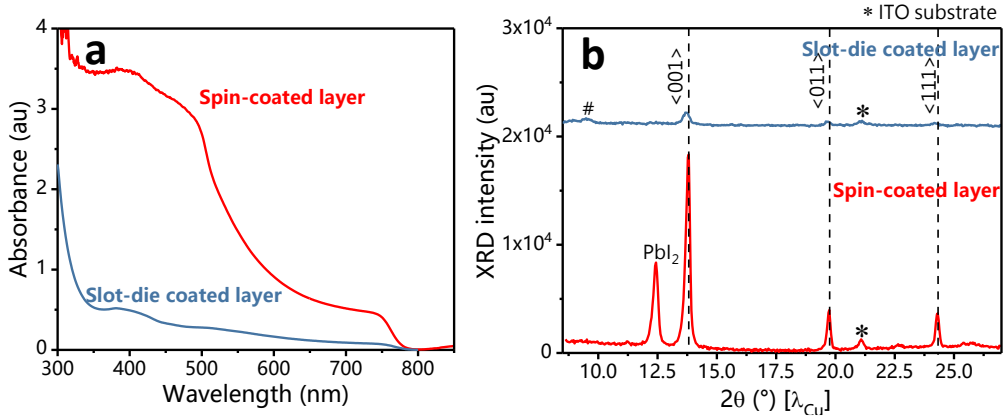

***Figure 9**: Optical properties and perovskite conversion.* **a)** *Absorbance spectra and* **b)** *XRD patterns of reference spin-coated layer (red) and first slot-die coated layer (blue).*

III.2.2. Towards a compact slot-die coated layer

In this section, we investigated strategies to enhance the slot-die coated film morphology, starting with the substrate temperature tuning, motivated by the experimental observation that the solvent evaporation was too strong at a substrate temperature of 100 °C.

- **Substrate temperature (CQ_T) optimization**

First, we studied the influence of the substrate temperature on the perovskite film morphology and crystallinity. As previously used, the nitrogen gas flow rate was fixed to 25 L.min^{-1}. Similarly, the perovskite precursor wet film was slot-die coated using the same coating conditions as the previous experiment (**Table 6**). Here, we investigated the following substrate temperature (CQ_T) values: 35 °C, 40 °C, 50 °C, 60 °C, 70 °C, 80 °C, 90 °C and 100 °C. The process parameters are summarized in **Table 6**.

Coating		Quenching		Post-Annealing	
C_g	100 µm	**Q_g**	3 mm	**A_T**	100 °C
CQ_s	8 mm.s^{-1}	**CQ_s**	8 mm.s^{-1}		
C_f	100 µL.min^{-1}	**Q_f**	25 L.min^{-1}	**A_t**	5 min
CQ_T	35 - 100 °C	**CQ_T**	35 - 100 °C		

***Table 6**: Process parameters used for the substrate temperature optimization. The modified parameter is highlighted in green colour.*

All slot-die coated perovskite films exhibited a rough appearance, similar to the first slot-die coated film (**Figure 8a**). The coated area was A = 20 cm² for all samples. The optical microscopy images of the resulting films morphologies are presented in **Figure 10**. At low temperature, we observed needles shapes (35 °C) and round patches (35 - 40 °C). When the temperature increased (50 - 70 °C), the number of domains increased and their size decreased. At 70 and 80 °C, needles shape crystals were observed. Over 80°C, round domain with large dimensions and various contrasts were observed, most likely due to different typologies.

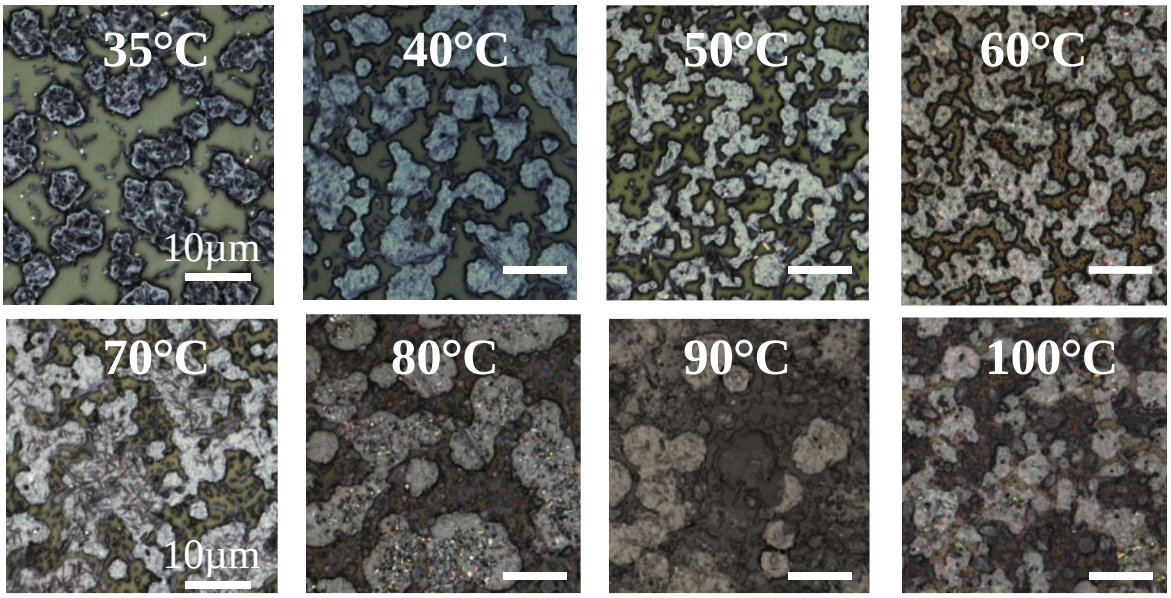

***Figure 10**: Optical images of slot-die coated perovskite layers obtained with substrate temperatures (CQ_T) ranging from 35 °C to 100 °C.*

On all slot-die coated samples, the film was only partially covering the substrate (c ≪ 100%). **Figure 11a** provides the profilometry scans of the samples fabricated at CQ_T = 35, 60 and 80 °C. We observed a similar behaviour to the previous experiment at 100 °C, with micrometric film thickness variations. Interestingly, the film coverage (**Figure 11b**), varied with the substrate temperature (CQ_T), linked to the change of morphology. From 35 to 50 °C, it increased linearly with the temperature, to reach a maximum value of c = 60% at 50 °C and remained constant around 55% at higher substrate temperatures. In the optical images, one can see an evolution of the film coverage, but also an evolution of the domain size. To take the latter into account, we extracted a secondary parameter from those images: the domain density defined as the number of domains observed per unit of surface (see **Appendix 2**). The evolution of the domain density showed a maximum value at CQ_T = 60 °C (**Appendix 2**). We concluded that the substrate temperature of 60 °C was the more appropriate value as it maximizes the domain density on the substrate. At this stage, the film coverage was still limited (c = 55%), underlying the need for further optimization beyond the substrate temperature.

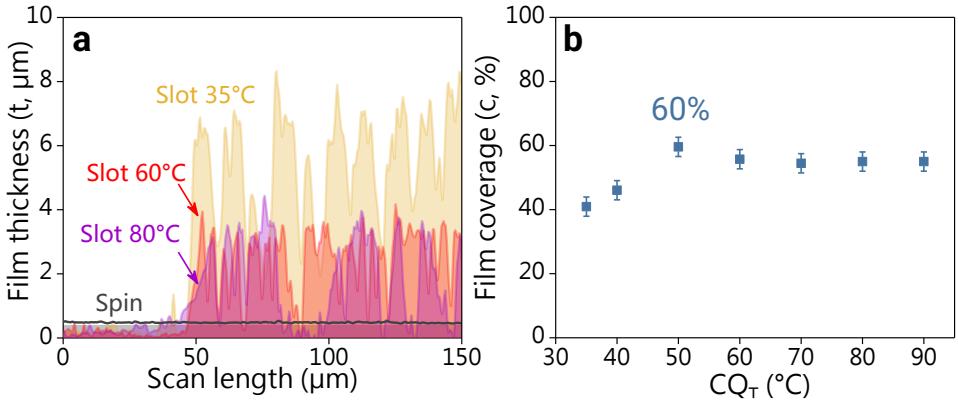

***Figure 11**: **a)** Profilometry scans of slot-die coated layers fabricated at CQ_T = 35, 60 and 80 °C. **b)** Evolution of the film coverage with the substrate temperature (CQ_T).*

On the absorbance spectra (**Figure 12a)**, the slot-die coated samples exhibited a small onset at 780 nm, corresponding to the presence of α-CsFAPbIBr material. However, due to the poor substrate coverage, the absorbance curves remained flat in the wavelength range 400 - 700 nm (**Figure 12a, Appendix 3).**

At low temperature (CQ_T = 35 °C), X-Ray diffraction (**Figure 12b**) revealed the presence of the low angle intermediate phase (2θ = 9-10°), δ-$FAPbI_3$ (2θ = 11.2°) and crystalline PbI_2 (2θ = 12.4°). The corresponding film morphologies contained needles and round domains. In the literature, PbI_2 crystals deriving from a DMF:PbI_2 solution intermediate [193] or fabricated in humid environment [201] have been reported with a similar needle structure. We therefore suggest that the needles could be attributed to PbI_2 crystals and the round domains (see 35 °C sample) to δ-$FAPbI_3$ material.

At CQ_T = 60 °C, the low angle peak was not present and we observed a significant diminution of crystalline PbI_2 and δ-$FAPbI_3$ peaks intensity. On the other hand, the α-CsFAPbIBr peak intensity increased. This increase was correlated with a denser morphology at 60 °C (**Appendix 2**). At CQ_T = 80 °C, no new phases were detected besides the intermediates low angle peaks (2θ = 9-10°) and the α-CsFAPbIBr perovskite peak. We discuss the link to the perovskite precursors solubility behaviours in function of the temperature in the **Appendix 2**.

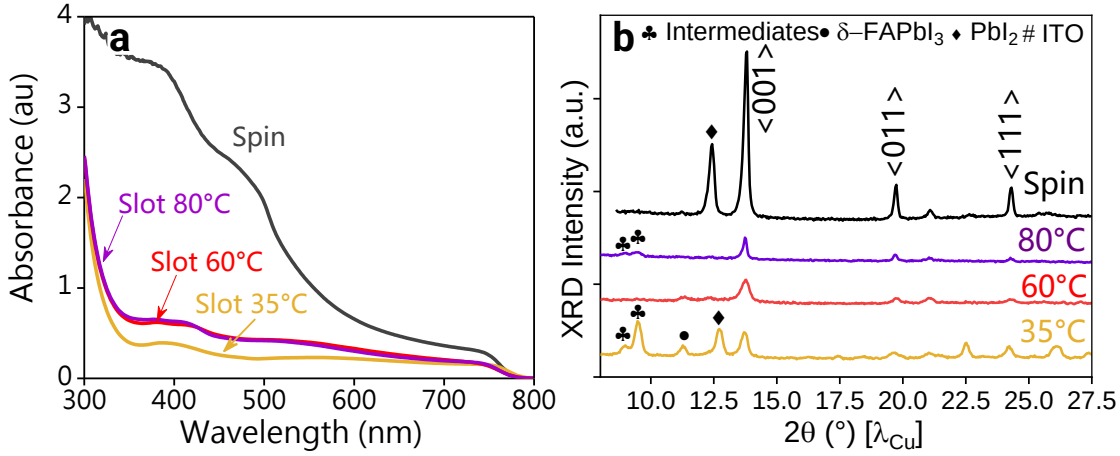

***Figure 12**: **a)** Absorbance spectra and **b)** XRD patterns of the slot-die coated films for substrate temperature values CQ_T = 35, 60 and 80 °C. The spin-coated curves is added in black for comparison.*

- **Quenching flow rate (Q_f) optimization**

The best conditions from the previous experiment did not yield a fully covered film. To reach full film coverage (c = 100%), other process parameters such as the quenching flow rate Q_f could be optimized. In this paragraph, we investigated nitrogen quenching flow rate values ranging from 25 to 100 $L.min^{-1}$ at the fixed substrate temperature CQ_T = 60 °C identified earlier. The process parameters are summarized in **Table 7**.

Coating		Quenching		Post-Annealing	
C_g	100 µm	Q_g	3 mm	A_T	100°C
CQ_s	8 mm.s^{-1}	CQ_s	8 mm.s^{-1}		
C_f	100 µL.min^{-1}	Q_f	25-100 L.min^{-1}	A_t	5 min
CQ_T	60 °C	CQ_T	60 °C		

***Table 7**: Process parameters used for the quenching flow rate optimization. The modified parameter is highlighted in green colour.*

When we increased the gas flow rate (Q_f), we observed the formation of a brown on a limited surface of the substrate (A' ~ 1 x 5 cm²) for Q_f = 75 and 100 L.min^{-1} (**Figure 13e-f**). On those samples, we took the optical microscopy images in the brown areas. These pictures revealed that much higher coverage were achieved when increasing quenching flow rate.

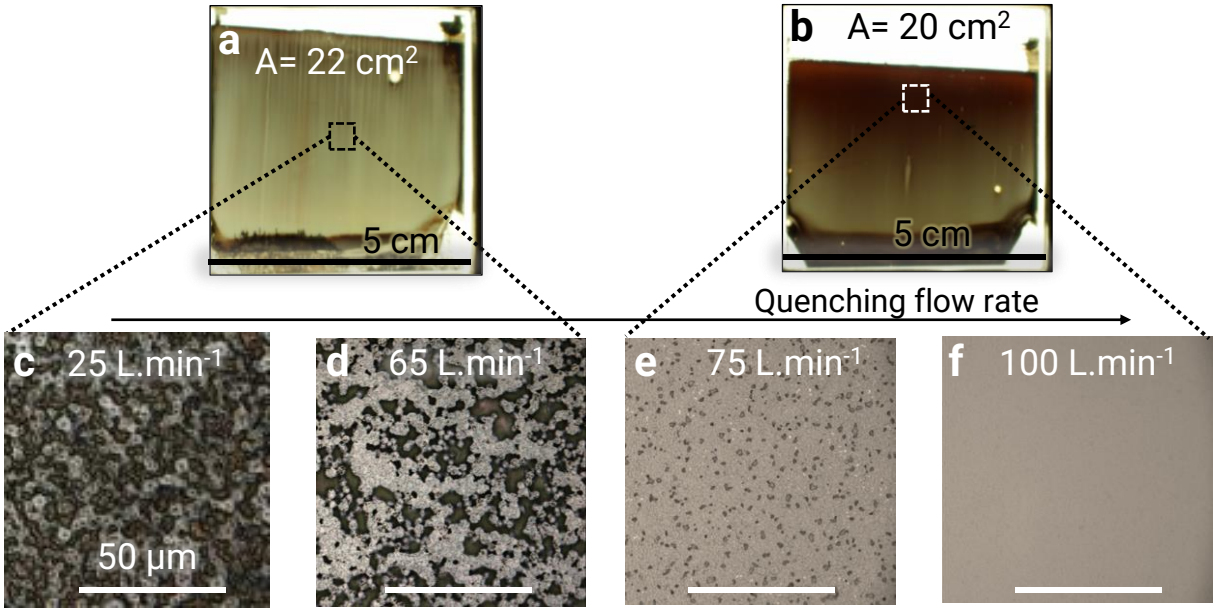

***Figure 13**: Pictures of the slot-die coated sample with **a)** Q_f = 25 L.min^{-1} and **b)** Q_f =100 L.min^{-1}. **c-f)** Optical images of the slot-die coated samples with Q_f = 25, 50, 75 and 100 L.min^{-1} respectively. The perovskite film is in light grey colour and the substrate in dark grey colour.*

To complete the morphological observations, we monitored the profilometry scan of the slot-die coated layers for Q_f = 25 and 100 L.min^{-1} (**Figure 14a)**. The compact slot-die coated layer (Q_f = 100 L.min^{-1}, c = 100%) showed a perovskite layer thickness around 550 nm (**Figure 14a**), slightly higher than the reference spin-coated layer (450 nm). This thickness variation could be due to a difference in the wet film thickness, as we estimated the slot-die coated precursor wet film to be thicker (4 µm) than the spin-coated one (1 µm).

However, at the fixed precursor ink concentration (1.2 M), we would expect a linear relationship between the wet and dried film thicknesses. This result challenged our wet precursor film thickness estimation of 4 µm in the slot-die coating process, suggesting an initially lower experimental wet film thickness or a mechanical contraction of the wet film during the gas-quenching step (**Appendix 4)**.

The substrate coverage c, extracted from the optical images, increased from 55 to 100% (full film coverage) as we increased the gas flow rate Q_f from 25 to 100 L.min^{-1} (**Figure 14b**). For practical reasons, we did not investigate higher quenching flow rates, as they could not be achieved on the experimental setup. In conclusion, increasing the gas flow rate Q_f until 100 L.min^{-1} enabled us to reach the full film coverage target in a limited compact area (A' = 1 x 5 cm²) of the 5 x 5 cm² substrate.

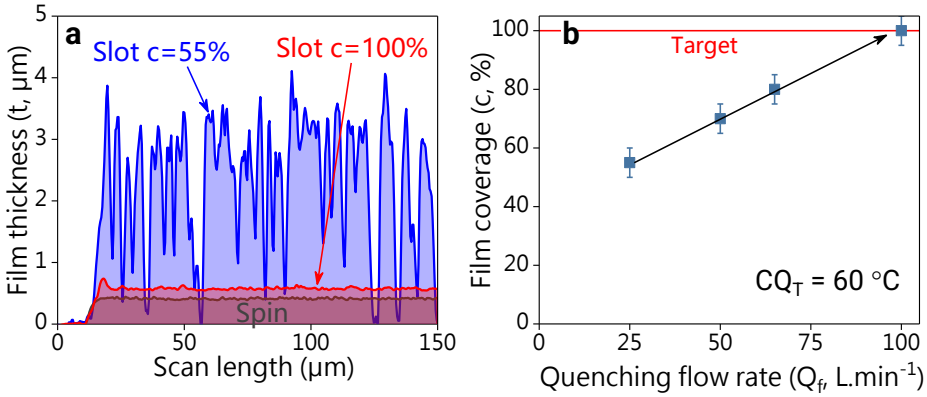

Figure 14: a) *Profilometry scans of slot-die coated layers with Q_f = 25 (red) and 100 L.min^{-1}(blue). The spin-coated layer scan is added in grey for comparison.* ***b)*** *Evolution of the film coverage with Q_f. The films coverage values were extracted from the optical microscopy images using Image J.*

We recorded the absorbance curves of the slot-die coated films (**Figure 15a**). Interestingly, the film coverage increase contributed to the increase of the slope in the wavelength range 400 - 700 nm. This change of slope can be explained by a reduced scattering effect in the samples with higher film coverage. In the literature, scattering effects are known as an artefact during the UV-visible spectroscopy measurement [187]. We used the equations developed by Tian and Scheblykin [187] to simulate the effect of light scattering on the absorbance curves (**Appendix 4**) and found a good correlation with the experimental data for wavelengths between 500 and 780 nm. Other additional contributions may lead to changes for wavelengths below 500 nm. Finally, we recorded the XRD patterns from the same samples (**Figure 15b**) and observed an increase of the perovskite peak intensities with the increase of the surface coverage. More perovskite material was present on the samples with high film coverage, confirming that the material forming was the α-CsFAPbIBr perovskite. We noticed the presence of crystalline PbI_2 as a crystallization by-product in all slot-die coated samples.

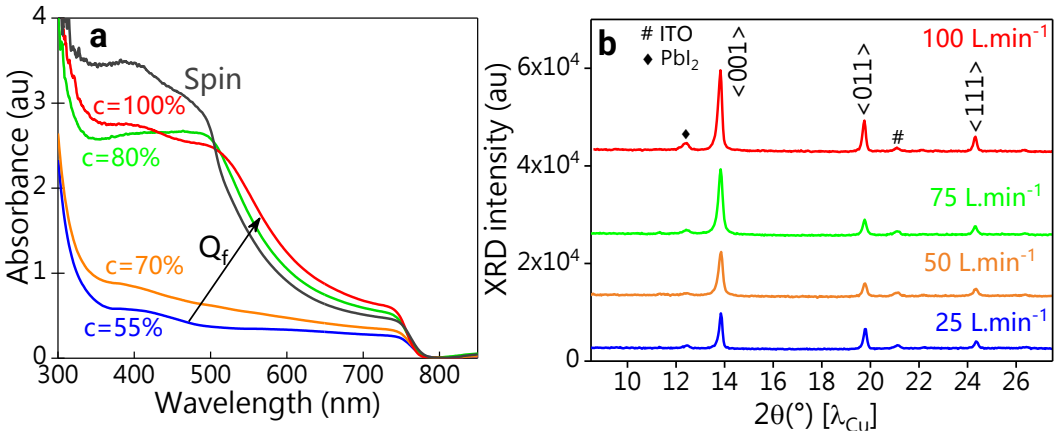

***Figure 15**: **a)** Absorbance spectra of the slot-die coated layers fabricated at Q_f = 25, 50, 75 and 100 L.min^{-1}, yielding film coverage of 55, 70, 80 and 100% respectively. The spin-coated layer curve is added in grey for comparison. **b)** XRD patterns of the corresponding samples.*

- **Discussion on the crystallization mechanism**

These results confirmed the direct effect of gas-quenching on the film formation. The stronger the quenching flow rate, the higher the nucleation density and perovskite film coverage. This nucleation effect could be attributed to a combination of a cooling effect (nitrogen temperature ~ 20 °C / precursor wet film temperature ~ 60 °C) impacting the precursor's solubility at the liquid/air surface; and of a fast solvent removal (by convection) at this liquid/air interface.

On the one hand, Cotella *et al.* [85] proposed that the cooling effect of gas-quenching (at 25 °C) may retard the perovskite nucleation in the cold areas (on the top of the wet precursor film), which could result in a levelling effect of perovskite crystals that preferentially grow along the hot substrate to form compact layers. However, the temperature gradient effect in our system may be more complex than usually described in the literature as some perovskite precursors may have inverse solubility behaviours [202] and may preferentially nucleate in those cold areas.

On the other hand, the fast solvent removal effect due to gas-quenching has been observed at room temperature in the literature. Conings *et al.* used the gas-quenching method without substrate heating to successful form spin-coated perovskite layers [196]. According to this work, the high solvent evaporation rate at the surface of the perovskite film could control the perovskite nucleation alone. In short, gas-quenching could contribute to both cooling effect and fast solvent removal in our system.

When we increased the quenching flowrate Q_f from 25 to 100 L.min^{-1} to obtain a compact morphology (c = 100%), we noticed that the compact area (A') was limited on the substrate (**Figure 13b**). Prior to perform the rest of the perovskite films characterizations, we

decided to investigate the role of the coating/quenching speed (CQ_s) on the macroscopic film homogeneity.

- **Process speed (CQ_s) optimization**

During the slot-die coating, we noticed that the diffuse part of the film dried prior to the arrival of the gas-knife. As the coating and quenching heads were both in movement, the spatial film homogeneity (in particular along the coating direction) did depend on the time at which the quenching head hit the wet precursor film. We decided to study the impact of another process parameter: the process speed (CQ_s). This speed could affect both the wet precursor film thickness (if considered as C_s) and the homogeneity of the gas flow rate reaching the substrate (if considered as Q_s). In this paragraph, we studied the impact of the process speed (CQ_s) on the perovskite film homogeneity (A' area) by varying its value from 8 to 33 mm.s^{-1}. The experimental process parameters are reported in **Table 8**.

Coating		**Quenching**		**Post-Annealing**	
C_g	100 µm	**Q_g**	3 mm	**A_T**	100 °C
CQ_s	8 - 33 mm.s^{-1}	**CQ_s**	8 - 33 mm.s^{-1}		
C_f	100 µL.min^{-1}	**Q_f**	100 L.min^{-1}	**A_t**	5 min
CQ_T	60 °C	**CQ_T**	60 °C		

***Table 8**: Process parameters used for the coating/quenching speed (CQ_s) optimization. The modified parameter is highlighted in green colour.*

We monitored the perovskite layer homogeneity *via* sample imaging (**Figure 16 a-d**). The homogeneity metric was the covered area A' corresponding to the brown area on the pictures. The sample at 8 mm.s^{-1} (reproduction of the previous batch, Q_f = 100L.min^{-1}) gave a similar pattern compared to the previous batch with a covered area A'= 8 cm^2. We observed that the precursor wet film on the bottom part was dried prior to the gas-knife arrival. By increasing the process speed from CQ_s = 8 to 28 mm.s^{-1}, the gas-knife could extend its operation window along the coating direction, resulting in the covered area increased from 8 to 15 cm^2 (**Figure 16e**). The maximum covered area of A' = 20.5 cm^2 was reached at a process speed of 28 mm.s^{-1}. At higher process speeds (CQ_s = 33 mm.s^{-1}), the gas-knife did not have the time to properly quench the precursor wet film that did not dried homogeneously (**Figure 16d**).

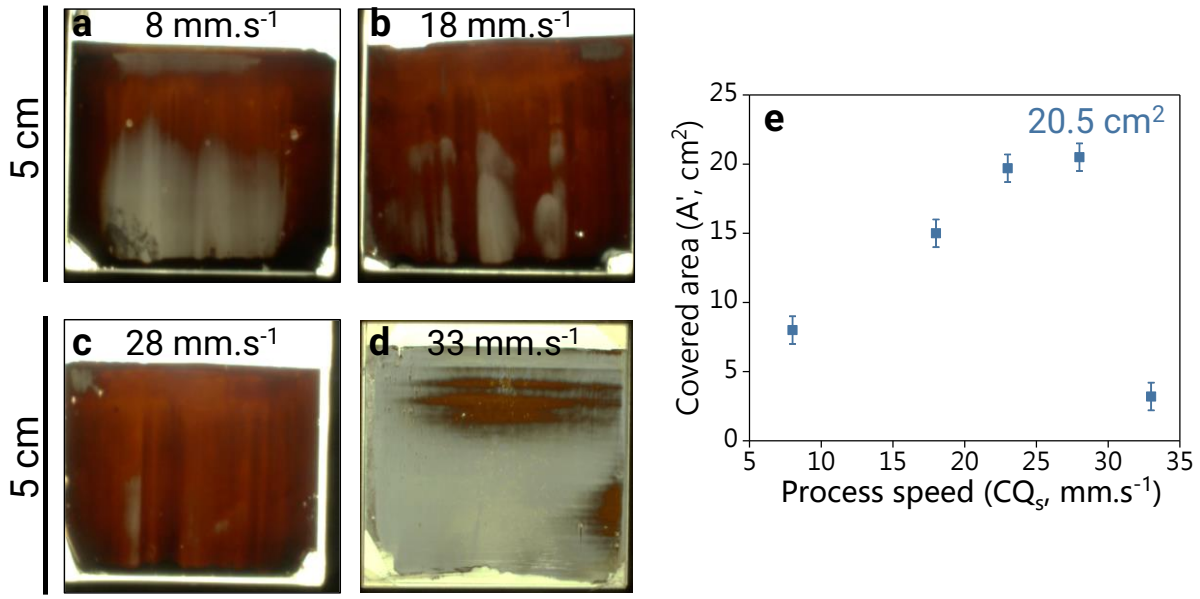

***Figure 16**: **a-d)** Pictures of the slot-die coated samples fabricated at CQ_s = 8, 18, 28 and 33 mm.s^{-1}. **e)** Covered area A' extracted from the images for various process speeds.*

According to this study, the process speed to maximize the covered area was CQ_s = 28 mm.s^{-1}. The strong dependence of the macroscopic homogeneity with the process speed (CQ_s) unveiled that gas-quenching had an impact on the crystallization homogeneity at macroscopic scale. We suggest that the gas-knife induced mechanical wet film deformation (**Appendix 4**) could be responsible for the local modification of the film thickness. Those irregularities were even more complex during coating as the gas-knife was in movement. Perspectives to understand this gas-induced wet film deformation could be to simulate the gas flow going out of a fixed gas-knife and its interaction with the precursor wet film, in both static and dynamic configurations.

In the next section, the exhaustive material characterization of the slot-die coated layer fabricated at CQ_s = 28 mm.s^{-1} will be presented and compared to the spin-coated layer properties.

III.3. Comparison of spin-coated and slot-die coated perovskite films and device performances

At a given perovskite precursor ink (reference solution), the use of a different quenching mean (anti-solvent in spin-coating process or gas-quenching in slot-die coating process) can lead to variations in the resulting perovskite layer properties and device performances. Here, we compared the compact slot-die coated properties in term of morphology, optical properties and crystallinity to the reference spin-coated layer properties.

III.3.1. Compact slot-die coated layers properties

- **Zoom-in on slot-die coated layer morphology**

In both processes, compact and pinholes free films were obtained (**Figure 17**). The slot-die coated films are slightly thicker (t = 575 nm) than spin-coated layers (t = 450 nm) (**Figure 17c**), possibly due to the variation of the precursor wet film thickness from 0.9 to 4 µm. The grain size (g = 240 nm) of slot-die coated sample was smaller in average than the spin-coated counterpart (g = 273 nm), unveiling a possible higher density of nucleation [203] from gas-quenching compared to anti-solvent quenching [13]. Both layers exhibited the presence of white particles at the surface. We suggest that the white particles were linked to the presence of crystalline PbI_2 as observed earlier (**III.1.2**).

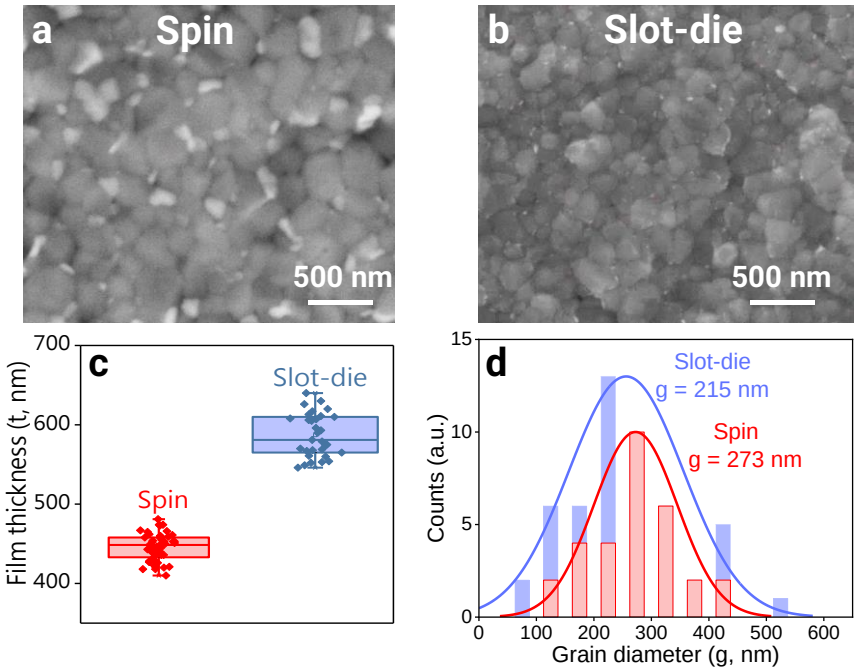

Figure 17: a-b) *SEM images* ***c)*** *Perovskite films thickness and* ***d)*** *grain distribution of spin-coated reference (red) and slot-die coated (blue) perovskite layers fabricated from 1.2 M reference precursor solution.*

- **Optical properties**

The absorption curves of slot-die coated and spin-coated layers were showing similar shape and a similar absorption onset around 780 nm, corresponding to the perovskite material absorption (**Figure 18a**). The optical band gap E_g = 1.60 eV was similar to the spin-coated layer band gap (1.61 eV) (**Figure 18b**). The absorption onset of the slot-die coated layer was slightly higher (~ 20%) than the spin-coated counterpart, in good accordance with the perovskite film thickness variation (+ 22%) (**Figure 17c**). This supports the hypothesis than the deposition and crystallization methods do not significantly affect the resulting absorption properties.

Photoluminescence spectra (PL, **Figure 18c**) of slot-die coated films showed a peak at a similar position than spin-coated layer (~ 765 nm) but with a reduced intensity. A PL intensity reduction can be observed in a defective material, where defects lead to non-radiative recombination of the charge carriers [204]. In the slot-die coated perovskite film, those defects could originate from the numerous grain boundaries (due to smaller grain size observed in **Figure 17b**) and/or to the presence of by-products of the crystallization. To evaluate the second hypothesis, we performed X-Ray Diffraction (XRD) measurements in the next paragraph.

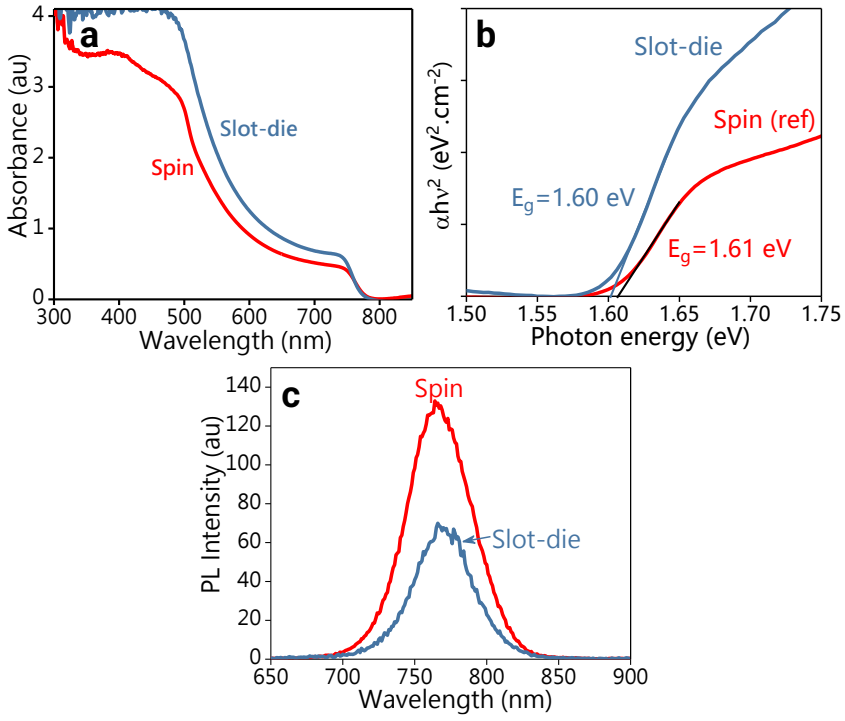

***Figure 18**: **a)** Absorbance spectra of spin-coated reference and slot-die coated perovskite layers fabricated from 1.2 M precursor solution concentration. **b)** Extraction of corresponding optical band gaps via Tauc plot method. **c)** Photoluminescence spectra with an excitation wavelength of 550 nm for both spin-coated and slot-die coated layers.*

- **Crystallinity and conversion into perovskite material**

We confirmed the presence of α-CsFAPbIBr perovskite in the X-Ray diffraction pattern with a similar (001) preferred orientation (2θ = 13.81°) in the slot-die coated layer (**Figure 19a**). The perovskite (001) peak intensity was lower than spin-coated one (I_{Slot} = 0.67* I_{Spin}) which suggests a less efficient formation of perovskite crystals in the slot-die coated layer.

Regarding the by-products formation, we observed the δ-$FAPbI_3$ phase presence (2θ = 11.4°) in higher proportions (XRD peak area ratio) in the slot-die coated film (5%) compared to the spin-coating reference (< 0.4%). This difference showed that the crystallization mean used (at a fixed precursor ink solution) affects the conversion of CsFAPbIBr material into the cubic structure. In addition, a higher crystalline PbI_2 peak area ratio was observed in the slot-die coated film (38%) compared to the spin-coated film (27%) (**Figure 19b**). Both δ-$FAPbI_3$ and crystalline PbI_2 presence in the thin film could explain the lower PL intensity observed for slot-die coated material (**Figure 19c**).

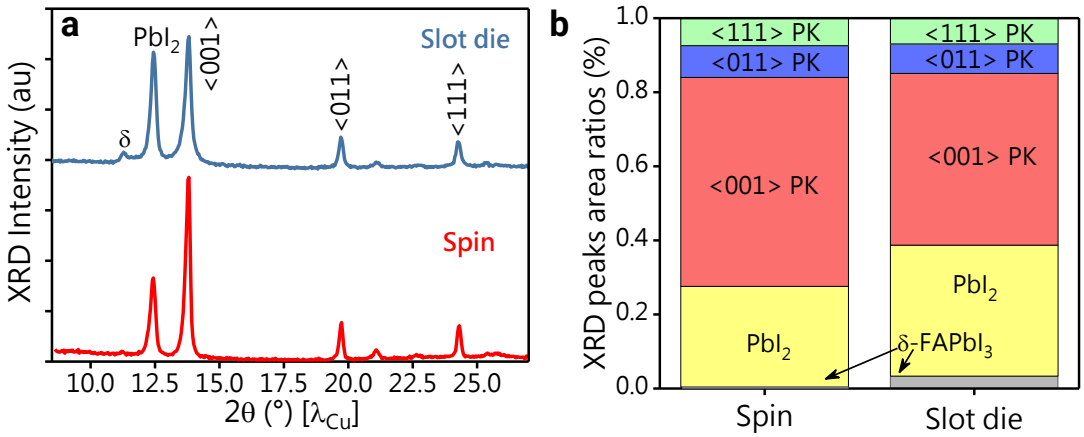

Figure 19: a) *X-Ray diffractometers of spin-coated (1h annealing – 100 °C) and slot-die coated perovskite layers (5 min annealing – 100 °C).* ***b)*** *XRD peaks area ratios compared for both samples.*

The XRD results showed that the perovskite conversion into cubic structure via gas-knife quenching was less efficient than the one by anti-solvent quenching (spin-coated layers). A possible hypothesis to explain the limited perovskite conversion could be the lower thermal budget applied to the film during the post-annealing step (5 min at 100 °C) compared to the spin-coated layer (60 min at 100 °C). The impact of the post-annealing step (5 min at 100 °C) on the slot-die coated perovskite layer conversion will be investigated in the next section.

III.3.2. Effect of thermal post-annealing on the slot-die coated layers properties

In contrary to spin-coating process where the perovskite brown films forms during the post-annealing step, we observed the formation of a brown film already after the quenching step in the slot- die coating process. This observation suggests that perovskite was formed prior to post-annealing. Here, we investigated the material properties of this "as-quenched" perovskite film and compare it to the reference slot-die coated layer after post-annealing (5 min at 100 °C). Besides the characterization of the intermediate film properties, this study aims at understanding if the slot-die coated layer conversion into α-CsFAPbIBr evolved during the post-annealing step. The slot-die coating process parameters used in this study are summarized in **Table 9** below.

Coating		**Quenching**		**Post-Annealing**	
$\mathbf{C_g}$	100 µm	$\mathbf{Q_g}$	3 mm	$\mathbf{A_T}$	100 °C/NA
$\mathbf{CQ_s}$	28 mm.s^{-1}	$\mathbf{CQ_s}$	28 mm.s^{-1}		
$\mathbf{C_f}$	100 µL.min^{-1}	$\mathbf{Q_f}$	100 L.min^{-1}	$\mathbf{A_t}$	5 min/0 min
$\mathbf{CQ_T}$	60 °C	$\mathbf{CQ_T}$	60 °C		

***Table 9**: Process parameters used for the post-annealing study. The modified parameters are highlighted in green colour.*

Prior to annealing, the "as-quenched" slot-die coated film exhibited a compact morphology with comparable grain size as the annealed slot-die coated samples (**Figure 20a**). The X-Ray diffraction results confirmed the presence of the perovskite material, under a mixture of δ-$FAPbI_3$ and α-CsFAPbIBr phases (**Figure 20d**) even without post-annealing. The evidence of perovskite formation prior to annealing in the slot-die coating process reinforced the difference between antisolvent and gas-quenching assisted crystallization mechanisms.

Regarding the perovskite material, we observed the increase of the α-CsFAPbIBr peak intensity after annealing, correlated with a photoluminescence intensity increase **(Figure 20c**). As the perovskite layer thickness and absorbance were not modified, it showed that post-annealing could enhance the perovskite quality by decreasing the non-radiative recombination losses. It reinforced the utility of such post-annealing steps to fabricate high quality perovskite films. Moreover, the grain size did not vary upon annealing, showing that the slot-die coated layer did not undergo any grain growth mechanism upon annealing.

Furthermore, the δ-$FAPbI_3$ XRD peak intensity did not change prior and after annealing the slot-die coated layer. We concluded that, as expected, the energy applied during thermal annealing (100 °C) could not trigger the conversion of the δ-$FAPbI_3$ phase into the α-CsFAPbIBr phase. This result was in accordance to the higher $FAPbI_3$ phase transition temperature of 185 °C, reported in the literature [42]. As a conclusion, the formation of δ-$FAPbI_3$ phase seemed rather to originate from the different quenching method employed in slot-die coating process.

Finally, a major difference between the "as-quenched" and the annealed slot-die coated films was the absence of the crystalline PbI_2 peak before annealing. We suggest that the excess PbI_2 was present under an amorphous form in the "as-quenched" sample. Upon annealing (5 min at 100 °C), we observed the formation of white particles on top of the film (**Figure 20a-b**), correlated with the appearance of a crystalline PbI_2 peak in the X-Ray diffraction patterns (**Figure 20d**). Similarly, the crystalline PbI_2 peak area ratio increased upon annealing to reach 38%, which is a higher ratio than in the spin-coated film (27%). As annealing seems to favour the crystalline PbI_2 formation, the kinetic of this formation appeared faster in the slot-die coated layers (5 min) compared to the spin-coated ones (60 min). This difference could be related to the difference of film morphology and in particular to the smaller grain size of slot-die coated layers, where the numerous grain boundaries can serve as nucleation sites for crystalline PbI_2. To keep a limited PbI_2 formation in the slot-die coated films, we did not investigate longer post-annealing times.

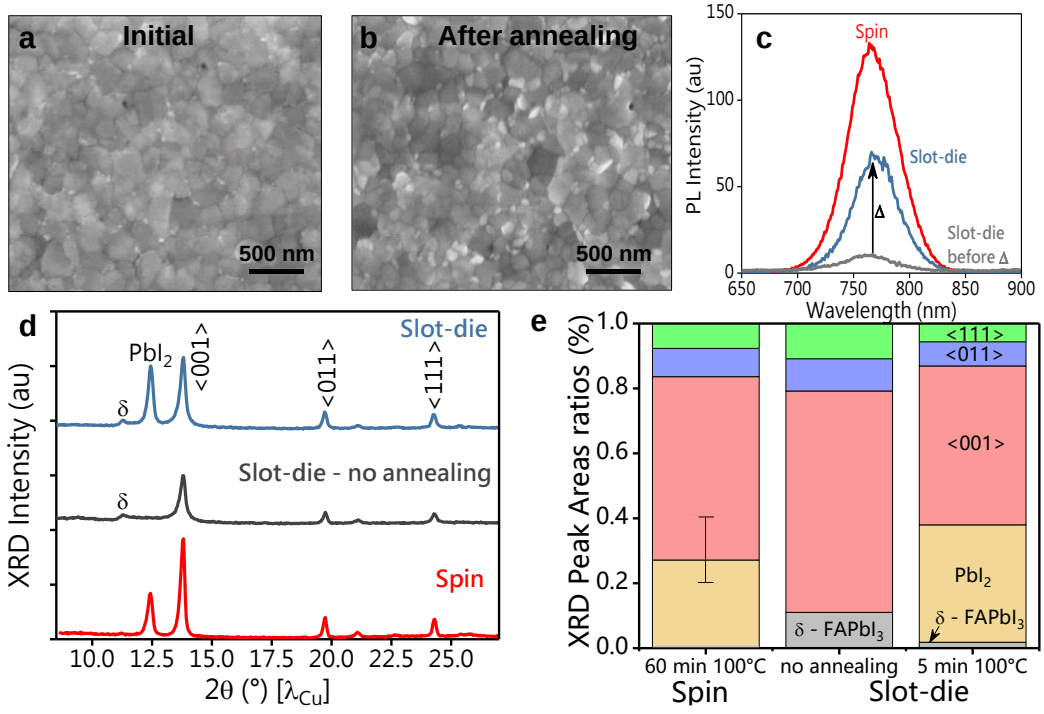

***Figure 20**: **a-b)** SEM top images of slot-die coated layers "as-quenched" and after 5 min at 100 °C. **c)** Photoluminescence spectra, **d)** X-Ray diffraction patterns, and **e)** Corresponding XRD peak area ratio extraction of the layers shown in a) and b). The reference spin-coated layer is added for comparison.*

- **Optimized slot-die coating process parameters**

During the process optimization, the process parameters (CQ_T, Q_f and CQ_s) modification did affect either the microscopic film coverage (c) or the macroscopic covered area (A'). In the rest of this chapter, the process parameters of slot-die coated layer will be set to the reference process conditions in **Table 10**.

Coating		Quenching		Post-Annealing	
C_g	100 µm	**Q_g**	3 mm	**A_T**	100 °C
CQ_s	28 mm.s^{-1}	**CQ_s**	28 mm.s^{-1}		
C_f	100 µL.min^{-1}	**Q_f**	100 L.min^{-1}	**A_t**	5 min
CQ_T	60 °C	**CQ_T**	60 °C		

***Table 10**: Optimized process parameters used in slot-die coating process. The parameters highlighted in grey have been optimized.*

III.3.3. Integration of spin-coated and slot-die layers into photovoltaic devices

Once the perovskite layer deposited either by spin-coating or slot-die coating process, the aim was to implement it as an absorber layer into photovoltaic devices. We chose the (n-i-p) structure because it was the state-of-the-art solar cell architecture in both laboratories. In this section, we will first present the global methodology for device fabrication and measurement. Then, the spin-coated reference device results and slot-die coated device results will be reported.

- **Device structure and device fabrication**

The reference device architecture was glass/ITO/SnO_2/Perovskite (spin-coated or slot-die coated)/PTAA/Au (**Figure 21a**). Practically, the electron transport layer was a very thin (t = 40 nm) nanoparticulate SnO_2 layer deposited on an ITO-coated glass substrate. The perovskite layer thickness was in the t = 350 - 550 nm range. On top of perovskite, the hole transporting layer material, PTAA, was spin-coated to form a 150 nm thick layer. Finally, a back contact gold electrode of 100 nm was evaporated to complete the stack. We started the device integration with the perovskite layers fabricated from the reference precursor ink (1.2 M).

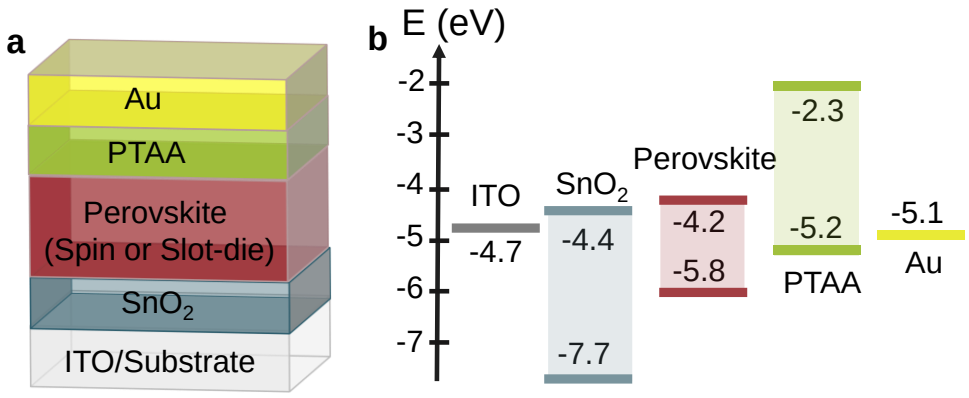

***Figure 21**: **a)** Device architecture of a (n-i-p) perovskite solar cell used in this section. **b)** Energy band diagram of the various materials composing the solar device extracted from the literature [205–207].*

- **J-V measurement method**

Once the device stack completed, we assessed the device performances by measuring the Current-Voltage (J-V) characteristics (See **Methods**). An important source of discussion in the literature is how to measure and report the J-V characteristics of perovskite based devices [208]. Therefore, the measurement protocol definition was important to acquire reliable and comparable data. In this section, we used the common reverse bias sweep to measure the J-V curves over a device active area of 0.33 cm^2. The devices were unencapsulated. For a quick reproducibility assessment, we averaged the device performances over at least five devices for each condition. When lower than 100%, we communicated the device fabrication yield, corresponding to the percentage of functioning devices out of all devices fabricated. Regarding the shelf life (defined as the repeated measurement of devices stored in the dark in ambient air, following ISOS-D1 guidelines [208]), we studied it from 0 to 4 days for the reference spin-coated devices (**see Appendix 5**), but presented only the initial measurements for slot-die coated devices.

Once the methodology was set for device integration, (J-V) measurement and reporting, we can present the integration results of the slot-die coated layers into photovoltaic devices and compare their performances to the spin-coated devices performances.

- **Photovoltaic devices performances**

Figure 22 reports the J-V characteristics of champion devices fabricated from both spin-coated and slot-die coated perovskite layers (1.2 M reference precursor ink). The champion slot-die coated device exhibited a power conversion efficiency of 13.31% (See **Appendix 6** for the entire device dataset). In average, we observed that the slot-die coated devices performed less (PCE ~ 12%) than their spin-coating counterpart did (PCE ~ 16%). All device parameters were affected (**Figure 22c**).

Despite a higher absorbance onset (**Figure 18a**), the slot-die coated layer implemented in a photovoltaic device led to lower current density (ΔJ_{sc} = - 0.8 mA.cm^{-2}) compared to its spin-coated counterpart, indicating a limited current generation or extraction in the device. The V_{oc} deficit (ΔV_{oc} = - 65 mV) observed in the slot-die coated devices cannot be due to the perovskite energy alignment modifications (**Figure 22b**) as both perovskite layers shown similar band gap. Hence, we suggest that a modification of the device interface properties could have limited the V_{oc} in the slot-die coated devices.

Lastly, the fill factor (FF) values of slot-die coated device were also lower (ΔFF = - 10 points). Since slot-die coated devices did not show higher current densities, the fill factor loss cannot be due to larger current dissipation in the device [209]. The series resistance was similar in both cases, but we observed a lower parallel resistance, that can result from recombination centres or leakage at one interface. In conclusion, the slot-die coated devices seemed limited be the presence of charge recombination in the perovskite absorber or at the device interfaces. This hypothesis was supported by the lower PL intensity observed in the slot-die coated layers (**Figure 18c**).

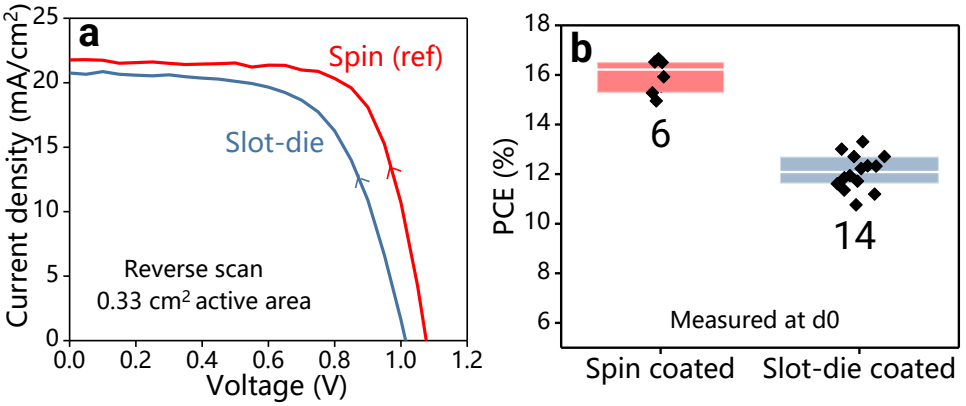

c	V_{oc} (V)	J_{sc} (mA/cm^2)	FF (%)	PCE (%)
Spin (ref-day 0)	1.075± 0.024	21.5 ± 0.4	69.1 ± 5.5	15.9 ± 1.0
Slot-die (day 0)	0.995 ± 0.028	20.4 ± 0.8	59.5 ± 4.8	12.1 ± 1.2

***Figure 22**: **a)** J-V characteristics of spin- and slot-die coated based devices fabricated from 1.2M reference precursor solution. **b)** Performance statistics of the two conditions. **c)** Device performances average measure initially (day 0).*

III.4. Influence of the precursor ink concentration

Once the slot-die coating process parameters optimized to maximize the film coverage (microscopic scale) and homogeneity (macroscopic scale), a thickness variation of 125 nm between the slot-die coated (575 nm) and the reference spin-coated layer (450 nm) fabricated from the reference precursor ink was observed. This variation could be due to the difference in precursor wet film thickness in both processes. Another way to adjust the perovskite thickness is to tune the precursor ink concentration. This motivated us to study the impact of the precursor ink concentration in both processes to compare the perovskite thickness evolution and eventually link it to the estimated precursor wet film values.

III.4.1. Spin-coated layers from various precursor ink concentrations

First, we investigated the effect of the precursor ink concentration on the spin-coated perovskite layer properties to use them as a comparison point. We used precursor ink concentrations of 0.9, 1.2 and 1.5 M (**Table 11**). We report the characterization of the perovskite layer by following the same characterization matrix as used in III.1.2, starting with the morphological inspection of the perovskite layer.

concentration (M)	0.9 - 1.2 - 1.5 M
Pb^{2+} excess (%)	6
Cs/FA molar ratio	5 : 95
Br/I molar ratio	12 : 88
DMF :DMSO volume ratio	4 : 1

***Table 11**: Composition of the precursor ink used in the section.*

- **Morphology**

The precursor concentration will determine the solute reservoir that can be crystallized from a given volume of solution. If matter were conserved from the solution to the dried film, we would expect the dried film thickness evolution to be proportional to the precursor concentration for a given wet precursor film thickness. In the reference spin-coating process, after the ejection step (~99% of initial volume) by centrifuge effect (**Figure 3**), the volume of the semi-dried film (0.9 µm thick) could be considered as constant, as we neglected the ink viscosity effects in our model. Consequently, one would expect a linear increase of the film thickness with the increase of precursor solution concentration.

Figure 23d confirmed the expected linear thickness increase from 350 nm to 550 nm with the precursor ink concentration. Interestingly, similar grain size (g = 300 nm) was observed for all concentrations, highlighting that precursor ink concentration did not influence the nucleation density in the anti-solvent crystallization process. On the SEM pictures (**Figure 23a-c**), we observed the presence of white particles, most likely PbI_2 particles [193] for all concentrations (see XRD section below).

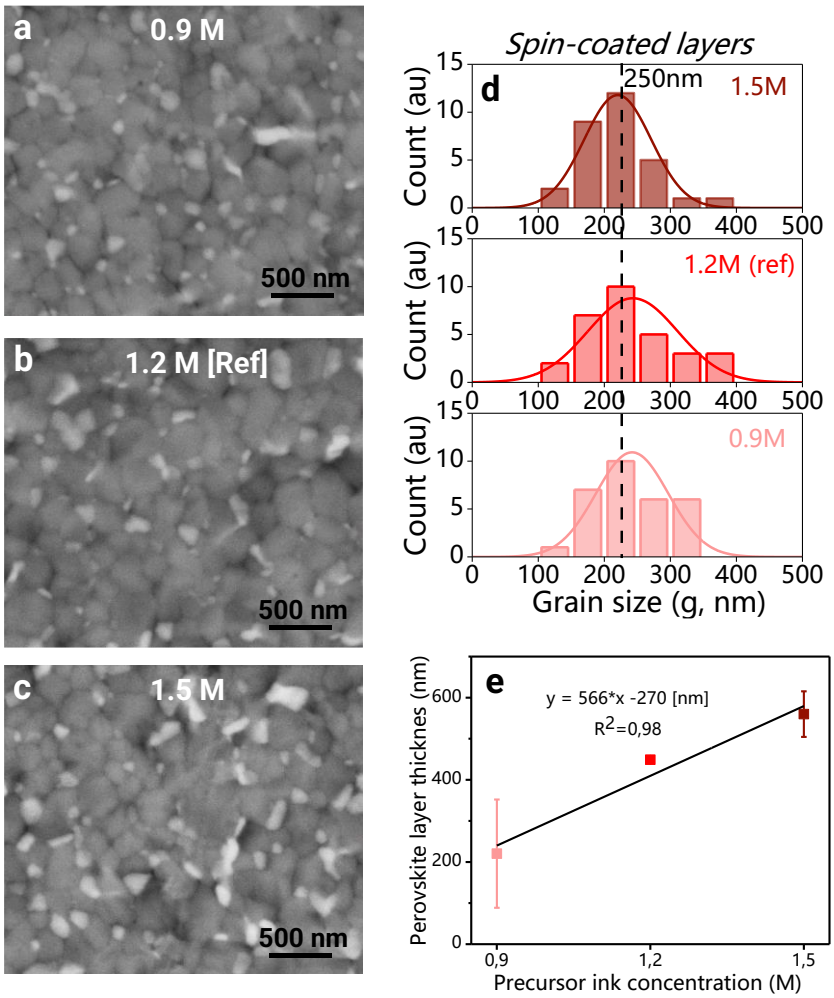

***Figure 23**: Impact of precursor ink concentration on spin-coated films morphology. **a-c)** SEM top images, **d)** Grain size distribution and **e)** Thicknesses of spin-coated layers fabricated from 0.9, 1.2 and 1.5 M precursor concentrations respectively.*

- **Optical properties**

As expected, we observed that the absorbance onset increased linearly with the concentration, following the perovskite thickness increase (**Figure 24a**). The band gap of the perovskite material remained constant E_g ~ 1.61 eV (**Figure 24b**).

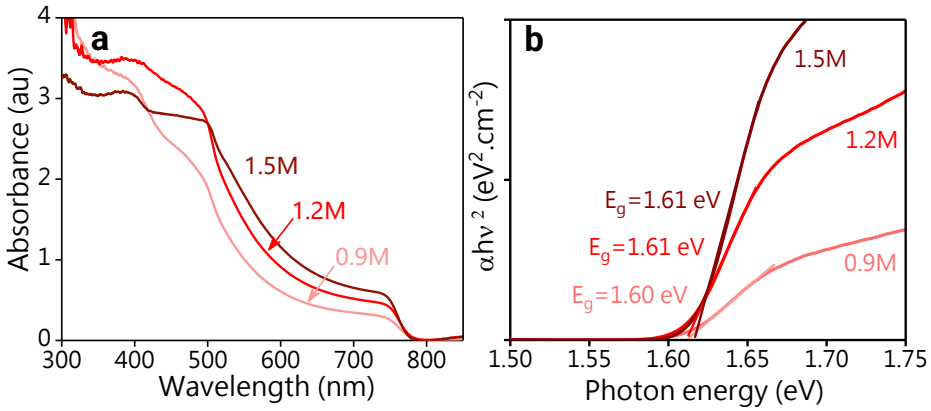

***Figure 24**: Impact of precursor ink concentration on the film optical properties. **a)** Absorption spectra and **b)** Tauc plot of spin coated layers fabricated at 0.9, 1.2 and 1.5 M respectively.*

- **Crystallinity and conversion into perovskite material**

We recorded the X-Ray diffraction patterns to compare the crystallinity of the films fabricated from the 0.9 M, 1.2 M and 1.5 M precursor concentrations (**Figure 25a**). We observed that the intensity of α-CsFAPbIBr diffraction peaks increased with the concentration, in particular for the (001) plan which was the preferential orientation at all concentrations (**Figure 25a**). This XRD peak intensity increase, in line with the perovskite thickness increase, was not linear with the concentration. From 0.9 M to 1.2 M, the XRD peak intensity was multiplied by 2.5; while from 1.2 M to 1.5 M, it was only multiplied by 1.26. The increase of the perovskite XRD peaks intensity seemed to slow down at higher concentration, highlighting, as expected, the difficulty to maintain good crystallinity in thicker perovskite films.

The presence of the δ-$FAPbI_3$ in the spin-coated films remained very limited even at the highest concentration (1.5 M), reinforcing the fact that the anti-solvent quenching was efficient to convert the film into α-CsFAPbIBr independently of the solute quantity available in the precursor ink. This strengthens the fact that the formation of δ-$FAPbI_3$ in the slot-die coated film was probably due to the different quenching method used.

Regarding by-products formation, the crystalline PbI_2 peak intensity (2θ = 12.3°) increased with the concentration, in line with the increased film thickness. Interestingly, this increase was faster than the perovskite (001) peak intensity increase from 0.9 M to 1.5 M (**Figure 23a**). The extracted XRD peak area ratio increased from 18.5% to 43%, reaching the peak area ratio of the perovskite (001) peak at 1.5 M. However, as the film absorption gradually increases from 0.9 to 1.5 M (**Figure 22a**), suggesting a gradual increase of the perovskite fraction in the film, we attributed the faster evolution of the crystalline PbI_2 XRD peak areas to a difference in the structure factors of those materials [160]. This observation reinforced the semi-quantitative character of the ratios extracted from the XRD patterns and the importance to couple them with other characterization methods.

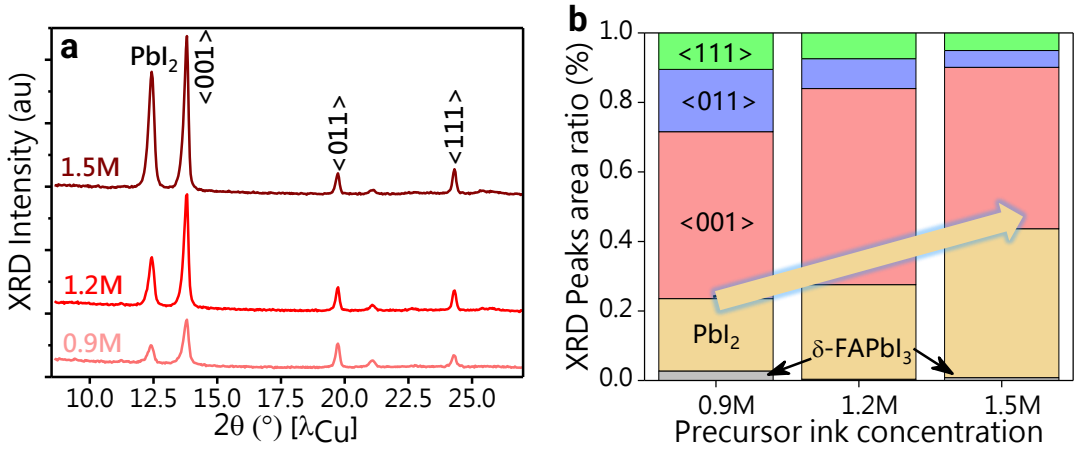

***Figure 25**: Impact of precursor ink concentration on spin-coated films properties: **a)** XRD diffraction patterns and **b)** XRD Peak area ratios.*

III.4.2. Influence of precursor ink concentration on spin-coated device performances

In this section, we implemented the spin-coated layers from 0.9 M and 1.5 M precursor solutions into photovoltaic devices and compared their performances to the reference spin-coated devices fabricated at 1.2 M.

- **Device performances at various concentrations**

Figure 26a reports the J-V characteristics (J-V curves and extracted PCE and J_{sc}) of spin-coated devices fabricated from the three precursor inks concentrations. The more diluted concentration (0.9 M) led to significantly lower performance, due to lower J_{sc} and V_{oc}. The current density loss (19.3 mA.cm^{-2} in average compared to 21.9 mA.cm^{-2} at 1.2 M) could be explained by the lower film thickness and absorption at 0.9 M. The slight V_{oc} decrease (1.064 V compared to 1.090 V at 1.2 M) and FF loss (67.7% compared to 71.7%) suggest that other factors, possibly interfacial, limit the 0.9 M device performances.

When using the higher precursor concentration (1.5 M), the device performance was comparable with the reference (1.2 M) devices, with a slight increase of current density (22.2 mA.cm^{-2} compared to 21.9 mA.cm^{-2} in average), in line with the higher absorption observed at that concentration.

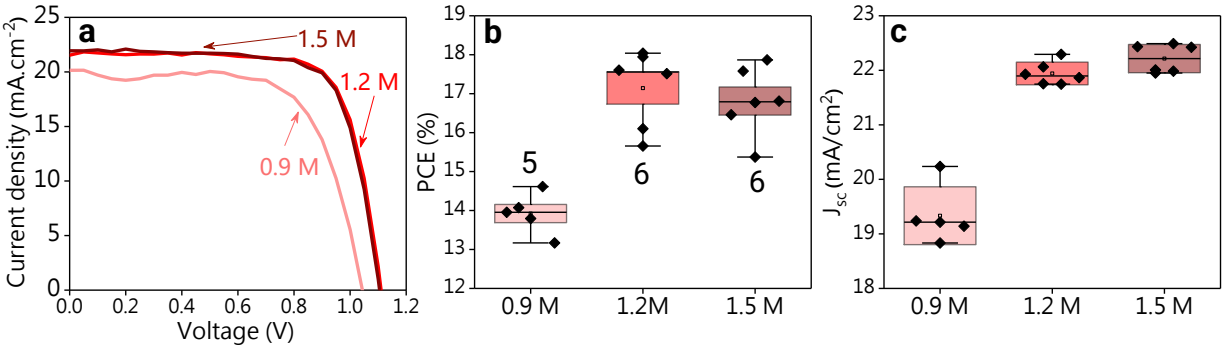

d	V_{oc} (V)	J_{sc} (mA.cm^{-2})	FF (%)	PCE (%)
0.9M	1.064± 0.022	19.3 ± 0.9	67.7 ± 5.5	13.9 ± 0.7
1.2M (ref)	1.090 ± 0.033	21.9 ± 0.8	71.7 ± 5.9	17.1 ± 2.1
1.5M	1.080 ± 0.038	22.2 ± 0.3	70.2 ± 4.9	16.8 ± 1.4

***Figure 26**: Impact of precursor ink concentration on **a)** J-V characteristics, **b)** power conversion efficiency (number of devices are provided for each condition) and **c)** J_{sc} of spin-coated based photovoltaic devices. **d)** Summary of average J-V parameters.*

Despite the slightly higher current density at 1.5 M (**Figure 27**), we observed similar performances compared to 1.2 M reference (**Figure 27**), with a slight V_{oc} and FF decrease. As the more concentrated precursor solution led to a thicker perovskite film, one could possibly expect a slight voltage decrease and higher resistive losses in the device due to the thickness increase, hence a lower fill factor value as observed.

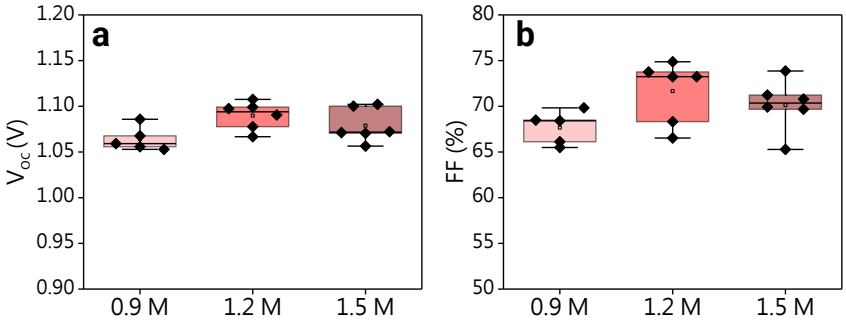

***Figure 27**: Impact of precursor ink concentration on other performance parameters: **a)** Open-circuit voltage (V_{oc}) and **b)** Fill factor (FF).*

- **Current density loss attributed to perovskite thickness variations**

We used a current density simulation tool to quantify the current loss that could be attributed to the thickness variation. This simulation is based on optical indices and thicknesses of materials present in the device stack (glass/ITO/Perovskite/PTAA/Au) and on the assumption that the light coming into the stack can either be absorbed, reflected or transmitted at every interface. We used a comprehensive optical model [162–165] to simulate the light path in the stack and to deduct the theoretical value of current density (see **Chapter II).**

A particularly interesting outcome of this model was the ability to plot the current density in function of the perovskite layer thickness. **Figure 28a** presents the position of experimental current densities on this simulated curve that shows local optima at 150 nm, 280 nm and 460 nm. We observed a good agreement of 1.2 M and 1.5 M experimental points with the model, whereas the 0.9 M J_{sc} values were significantly lower than those expected by the model.

The lower current density at 0.9 M was correlated with a change of perovskite material quality, clearly visible by the reduced photoluminescence peak intensity (**Figure 28b**) and the presence of δ-$FAPbI_3$ in a larger peak area ratio (2.7%) than the reference (0.3%) (III.3.1). It suggests that higher charge carrier recombination into the absorber limited the current extraction and the resulting power conversion efficiency of the device fabricated at 0.9 M. Regarding the deviation from the optical model, we noticed that this model considered that the device internal quantum efficiency (IQE) is equal to 1. Yet, if the perovskite material quality is reduced (at 0.9 M), one could suggest that this model hypothesis was not fulfilled.

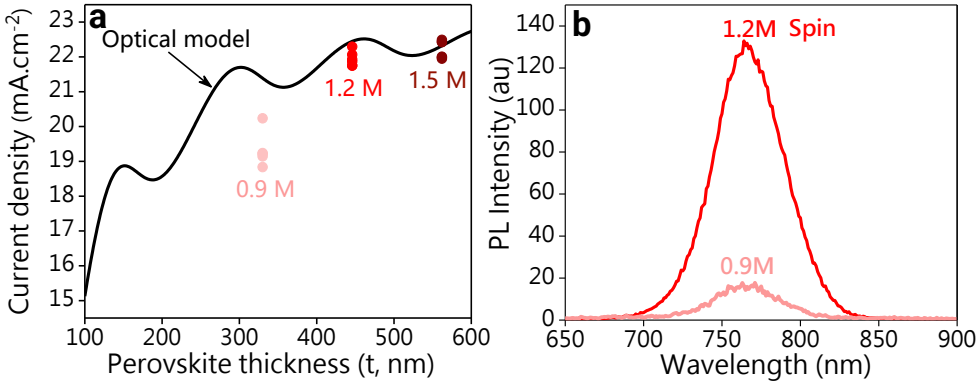

***Figure 28**: **a)** Evolution of current density (J_{sc}) in function of the perovskite layer thickness (t). The black line represents the simulation and the colour points the experimental values for each precursor ink concentration. **b)** Photoluminescence of spin-coated layers fabricated from the 0.9 M and 1.2 M (reference) precursor ink solutions.*

III.4.3. Slot-die coated layers from various ink concentrations

- **Morphology and optical properties**

As studied in the spin-coating process, we investigate here how the precursor ink concentration affect the film thickness, absorption and crystalline properties of slot-die coated layers. To tune the perovskite thickness towards the spin-coated standard (t = 450 nm), in a similar fashion to what was done for spin-coating, we decreased the precursor concentration from 1.2 M (reference) to 0.9 M. The thickness and absorbance of 0.9 M based slot-die coated layer were reported in **Figure 29,** along with the 1.2 M (reference) based slot-die coated layer. The spin-coated layer data from 0.9 and 1.2 (reference) solutions were added for process comparison.

We observed **(Figure 29a)** that the 0.9 M slot-die coated layer was 350 nm thick, which was comparable to the spin-coated layer thickness fabricated from the same concentration. From 0.9 to 1.2 M (+ 33% increase), the spin-coated layer thickness increased from 350 nm to 450 nm (+ 30%) while the slot-die coated film thickness increased from 350 nm to 550 nm (+ 57%). The absorbance onset followed the film thickness trend (**Figure 29b**): the onset was the same for both processes at 0.9 M and increased significantly at 1.2 M with a different magnitude for both processes. Tauc plots (**Figure 29c**) show that the 0.9 M slot-die coated film had a more significant Urbach tail (780 - 800 nm) compared to the spin-coated film. It can result from the presence of more defects in the film. The next paragraph will investigate the film crystallinity.

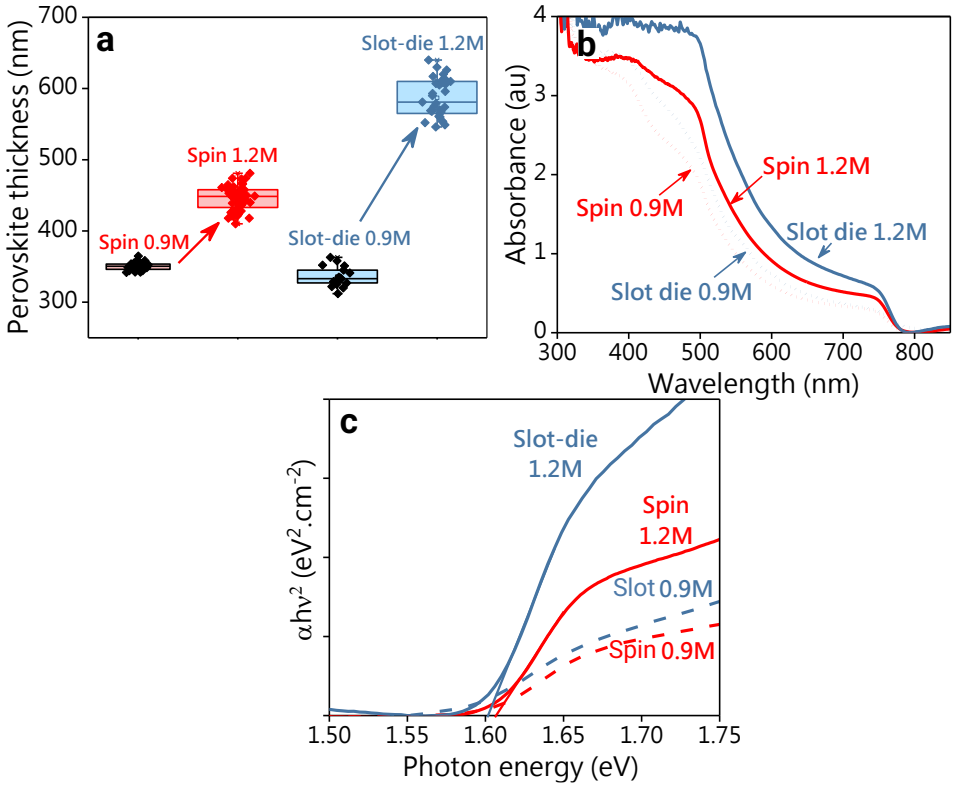

***Figure 29**: **a)** Thicknesses of spin-coated reference and slot-die coated films from 0.9 and 1.2 M precursor solution concentrations measured by surface profilometry. **b)** Corresponding absorbance curves. **c)** Band gap extraction via Tauc plot method from the absorbance curves.*

- **Crystallinity and conversion into perovskite material**

To assess how the precursor concentration affected the crystallinity of the perovskite material, the XRD patterns were recorded (**Figure 30a**). For both processes, we observed an increase of the α-CsFAPbIBr ((001) orientation) peak intensity when the precursor ink concentration increased from 0.9 M to 1.2 M, in accordance with the increased perovskite thickness. Surprisingly, this peak intensity increase was more pronounced for spin-coated layers than slot-die coated ones, despite the latter more pronounced thickness increase. This would indicate a lower crystallinity of the slot-die coated samples.

A notable difference between both processes was the more significant presence of δ-$FAPbI_3$ ($2\theta = 11.7°$) in the slot-die coated films (8 and 5% respectively) for both 0.9 and 1.2 M concentrations. Despite the higher XRD peak intensities at 0.9 M compared to the spin-coated films, the presence of δ-$FAPbI_3$ by-product in the slot-die coated film showed that gas-quenching was limiting the perovskite conversion into the cubic structure compared to the anti-solvent quenching method.

Similarly to the (001) perovskite peak intensity, the crystalline PbI_2 peak intensity (**Figure 30b**) increased with the concentration in both processes, in line with the film thickness increase. This increase appeared to be independent of the conversion mean used (anti-solvent or gas-quenching). Indeed, crystalline PbI_2 crystallization rather relied on the PbI_2 excess precursor available in the precursor ink (excess PbI_2 [107]) and on the thermal budget applied to the film (**III.3.2**). We propose that the higher the concentration, the larger the PbI_2 excess, and the more crystallized PbI_2 upon annealing, independently from the quenching mean used.

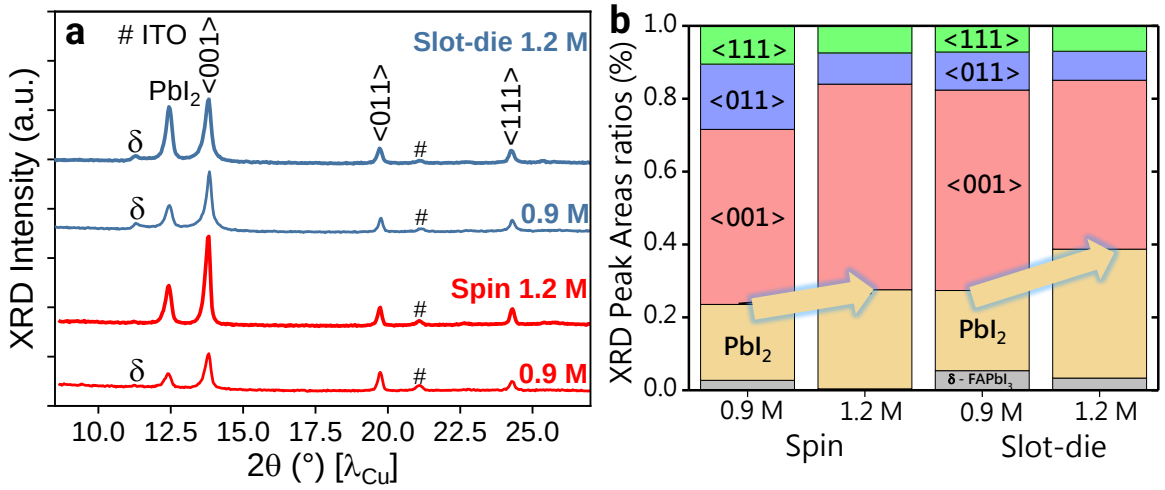

***Figure 30**: **a)** X-Ray diffraction patterns from the slot-die coated and spin-coated films from 0.9 and 1.2 M precursor concentrations. **b)** Corresponding XRD peak area ratios.*

III.4.4. Influence of precursor ink concentration on slot-die coated device performances

Similarly to spin-coated devices, slot-die coated devices fabricated from 0.9 M solution exhibited lower performances, mainly due to a lower current density (**Figure 31**). In the material study (**III-2-3**), we have seen that the precursor ink concentration controlled the perovskite layer thickness. Here, the device J_{sc} decreases from 20.4 to 19.8 $mA.cm^{-2}$ (- 0.6 $mA.cm^{-2}$, averaged values), following the perovskite thickness decrease from t = 450 nm to 350 nm.

To decorrelate the effect of a perovskite thickness variation from a change of perovskite material quality to the J_{sc} decrease, we used the same optical model as developed earlier (**Figure 28a**). We added the slot-die coated 0.9 M point for a direct comparison (**Figure 31b**). The J_{sc} values of both slot-die coated devices were below the optical model and in similar proportions (grey arrows on the graph). The current density deviation to the optical model (- .35 and 1.79 $mA.cm^{-2}$ respectively) could be explained by the presence of defects in the slot-die coated layers (**III.3.2**). Interestingly, both slot-die coated layer exhibited a similar deviation, indicating that they both suffer from significant extraction losses.

Interestingly, the thickness variation of slot-die coated layers (350 *vs* 450 nm) did not significantly affect the other electrical parameters. The device fill factor (FF) remained stable for both perovskite thicknesses (**Figure 31d**). Series resistance were comparable, indicating that the charge mobility inside the perovskite material was not limiting the device operation. Furthermore, the shunt resistance was not modified with the thickness and remained lower than in spin-coated devices. Reduced shunt resistance in slot-die coated device can originate from defects in the absorber material or at the device interfaces. As the perovskite thickness (absorber material) modification did not have a significant impact on the shunt resistance, we propose that the defects limiting our device operation could be mainly located at the device interfaces. In addition, the open-circuit voltage (V_{oc}) remained constant for the champion devices (**Figure 31a**), where in theory it should have increased at a lower perovskite thickness. The defective interfaces could be the factor limiting the V_{oc} increase.

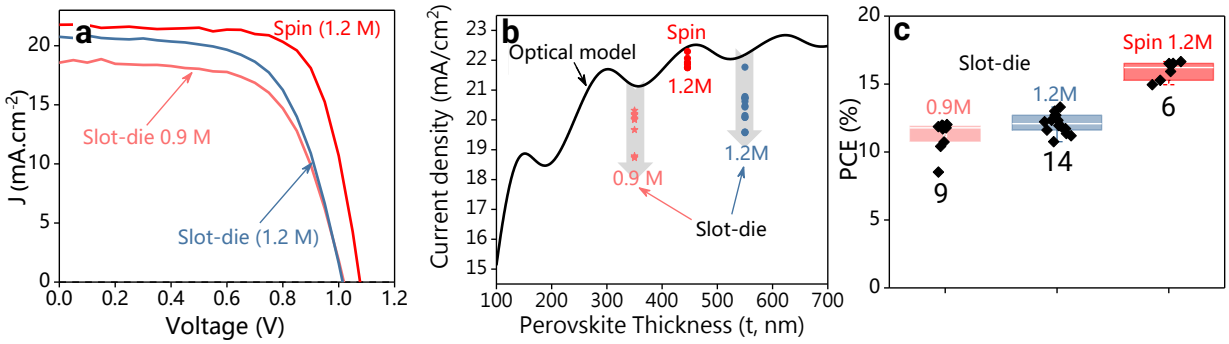

d	V_{oc} (V)	J_{sc} (mA/cm^2)	FF (%)	PCE (%)
Spin (ref - day 0)	1.075± 0.024	21.5 ± 0.4	69.1 ± 5.5	15.9 ± 1.0
Slot-die	0.995 ± 0.028	20.4 ± 0.8	59.5 ± 4.8	12.1 ± 1.2
Slot-die 0.9 M	0.961 ± 0.091	19.8 ± 1.0	59.0 ± 10	11.2 ± 2.7

Figure 31: a) *JV curves of champion device of each condition.* ***b)*** *Current densities of experimental devices in respect to the theoretical line calculated from optical simulation.* ***c)*** *Statistics of device parameters.* ***d)*** *Summary of averages performances for all three conditions.*

Conclusion

In this chapter, we introduced the spin-coating and slot-die coating processes to deposit the perovskite layer and combined them with two quenching methods. In the spin-coating process, the nucleation was triggered by an antisolvent quenching whereas in slot-die coating process, simultaneous substrate heating and gas-quenching were employed. We tuned the slot-die coating process parameters with an incremental approach to obtain a compact perovskite layer over the 5 x 5 cm^2 substrate. We then compared the optical, morphological and crystalline properties of the perovskite layers fabricated *via* both processes using the same precursor ink. Besides the similar band gap and slightly smaller grains, we observed that the slot-die coated layers present incomplete conversion into perovskite cubic structure, unveiling a lower 'conversion power' of the gas-knife assisted crystallization.

When integrated into devices, the slot-die coated layer underperformed (~ 13%) the spin-coated ones (~ 16.5%) because of lower V_{oc} (- 60 mV), FF (- 8 points) and J_{sc} (- 2 $mA.cm^{-2}$). The first limitation in slot-die coated devices was the fill factor, most likely impeded by the incomplete perovskite conversion and lower quality of the slot-die coated device interfaces. The device interface quality appeared more critical in the slot-die coating process, in particular at the SnO_2/Perovskite where heterogeneous nucleation can take place in the slot-die coating process. Further investigations on the substrate role will be reported in **Chapter V**.

We then varied the precursor ink concentration in both processes and studied the resulting films properties. The slot-die coated layers exhibited an incomplete perovskite conversion, independently of the precursor concentration employed, reinforcing the fact that the change of quenching mean limited this conversion. Mitigation strategies to favour the formation of CsFAPbIBr cubic structure in slot-die coated layers will be reported in **Chapter IV**.

Appendixes

Appendix 1: Evolution of the precursor wet film thickness with the coating speed (C_s).

In the slot-die coating process, we used *(E_3)* to link the process parameters (C_s, C_f and the coating width) to an estimation of the precursor wet film thickness. In order to verify the wet film equation, we slot-die coated perovskite layers for various coating speeds C_s = 8 mm.s^{-1} to 33 mm.s^{-1}. We monitored the dried film thickness and calculated the predicted wet film thickness by *(E_3)* equation. In **Figure A1**, we observed an increase of the dried perovskite film thickness (in orange) with the increased coating speed (C_s), which contradicts the trend derived from *(E_3)* equation (in gray).

$$C_t\,[m] = \frac{C_f[m^3/s]}{coating\ width\ [m]\ x\ C_s\ [m/s]} \qquad (E_2)$$

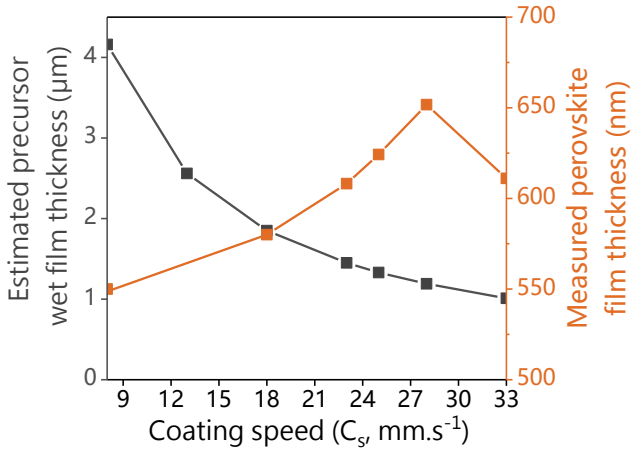

***Figure A1**: Estimation of precursor wet film thickness after (E_3) (black) and experimental measures of resulting perovskite film thickness for coating speeds from 8 to 33 mm.s^{-1} (orange).*

In the literature, a film thickness increase with the coating speed has been attributed to the Landau-Levitch coating mode [210]. This regime has been observed previously in the literature for slot-die coated perovskite layers [211–214]. In this regime, fluid capillarity is the driving phenomena responsible for the dynamic meniscus formation on the substrate. To improve our physical wet film definition, parameters such a as the speed range [210,73], the ink viscosity [215], surface tension and boiling point [112] need to be taken into consideration.

In addition, if capillarity influenced the coating regime, it is important to assess its influence on the operation window. Usually, the coating gap is a key parameter to avoid capillarity issue. In our case, because of the low viscosity of the precursor ink and its good wettability on the substrate (**III-1-1**), we were always within the operation window of slot-die coating (coating range 8-33 mm.s^{-1}) with a coating gap of 100 µm. To explore the impact of the gap on the coatability, we tested gaps from 50 µm to 500 µm. At reduced coating gap, we observed that parallelism was limiting the coating homogeneity perpendicularly to the coating

direction. At larger coating gap, the meniscus formation at start was longer and resulted in solution oversupply that was lost at the end of the coating. Overall, the 100 µm gap was kept for the rest of this work for practical reasons.

Appendix 2: Nucleation density extracted from the microscope images.

When the substrate temperature increased in the slot-die coating process, the solvent evaporation rate and nucleation rate increased [216]. To quantify the variation of nucleation density, we extracted the crystalline domain density from optical images of the slot-die coated films by counting the number of domains on each image and dividing by the image area (**Figure A2**). The evolution of the crystalline domain density with the substrate temperature is presented in **Figure A2b**. Interestingly, the domains density did not linearly increase with the temperature, but reached a maximum for a substrate temperature of CQ_T = 60 °C. Beyond this value, the film morphology was modified and the domain density decreased. We noticed that the substrate temperature leading to the highest domain density (60 °C) is different from the one leading to the highest film coverage c (reached at CQ_T = 55 °C), underlying the need to distinguish film coverage and domain density to determine the right optimum.

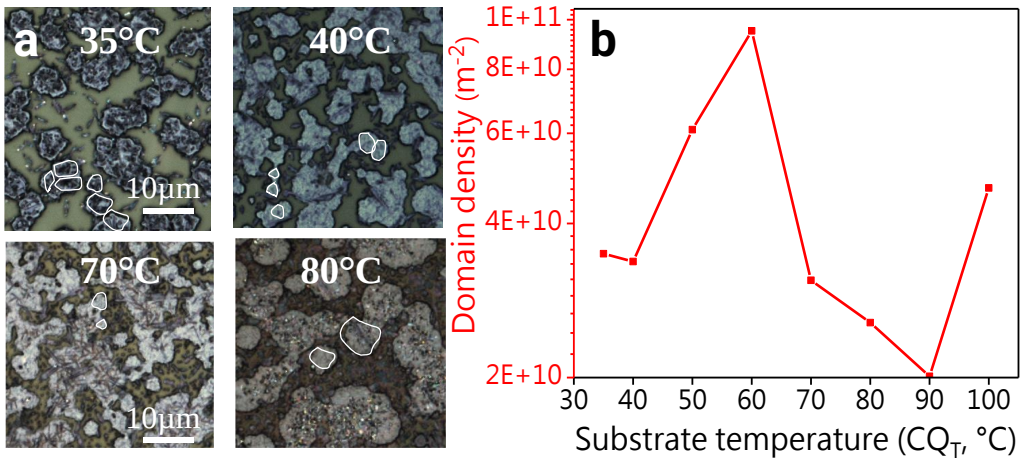

***Figure A2**: **a)** Optical images with domains highlighted in white. **b)** Extracted domain density for CQ_T = 35 °C to 100 °C.*

The reason behind this sudden change of morphology at high temperature could be the change of the precursor's solubility behaviour with the temperature. Indeed, the solubility of a salt in the solvent mixture follows the Van't Hoff equation, and can either increase with the temperature (direct solubility) or decrease with the temperature (indirect or retrograde solubility). Precursors such as PbI_2 are known for their direct solubility behaviour. A common experiment consists in cooling down a PbI_2 aqueous solution to make a golden rain appear, as the PbI_2 particles dissolved initially in the heated solution reach super saturation when the temperature decreases. In the literature, Hagfeld *et al.* [217] and Saidaminov *et al* [218]

reported the retrograde solubility behaviour of $MAPbI_3$. Later, similar behaviour for has been reported $FAPbI_3$ material in GBL solvent by Saidaminov *et al* [202].

Therefore, we propose that the CsFAPbIBr perovskite followed a retrograde solubility behaviour, whereas the PbI_2 precursor followed a direct solubility behaviour. The reactional equilibriums in the precursor solution can be described as:

$$PbI_{2\ precursor} \rightleftharpoons PbI_2\text{: DMSO} \qquad (R_1)$$

$$PbI_2\text{: DMSO} \rightleftharpoons CsFAPbIBr_{\ polytype} \qquad (R_2)$$

$$CsFAPbIBr_{\ polytype} \rightleftharpoons CsFAPbIBr_{\ perovksite} \qquad (R_3)$$

At low temperature, we observed the presence of Pb_{I2} under PbI_2 precursor form (crystalline PbI_2) or under PbI_2-solvent complex (low angle peaks in the XRD pattern), but not under the perovskite intermediate form. We propose that the PbI_2 having a poor solubility at low temperatures could undergo (R_1) reaction but not (R_2) reaction.

At 60 °C, we detected a limited crystalline PbI_2 or PbI_2-DMSO complex presence and increased perovskite material formation. We propose that when the temperature increases, the PbI_2 precursor solubility increases so that enough PbI_2:DMSO is formed to contribute to the perovskite intermediate formation (R_2) significantly. On the other hand, at this temperature, the limit of solubility of CsFAPbIBr material is reached and it can nucleate to form perovskite crystals via (R_3) equation.

For temperatures higher than 60 °C, we observed the presence of both perovskite and PbI_2-DMSO intermediate. We propose that at higher temperature, the high PbI2 solubility increases the content of PbI2:DMSO specie in solution (R_1). As the (R_3) should also be favoured due to the retrograde solubility behaviour of CsFAPbIBr, the limiting reaction could be the formation fi the CsFAPbIBr intermediate (R_2).

A perspective of this work is the experimental measure of the solubility of the precursor ink and of inks containing the precursors in function of the temperature to determine the quantitative values and identify the right process window to selectively form the α-CsFAPbIBr material.

Appendix 3: Evolution of the **absorption curves with the film coverage.**

During the gas flow rate (Q_f) optimization, we observed that the slot-die coated films absorbance curves became steeper in the 400-700 nm wavelength range. This phenomenon has been linked to light scattering effect by Tian and Scheblykin [187], though the formula exposed below (**Figure A4**). We used the scattering coefficient β to fit the experimental absorbance curves (in dotted lines). We found that this effect explained well the variation between 550 nm and 800 nm, but that other effects may influence the slope in the 300-550 nm range. In the slot-die coated films, the presence of crystalline PbI_2 or other by products that absorb within this wavelength range [41]. In conclusion, the absorbance curve slope was depending on both the light scattering due to the incomplete film coverage and to the presence of absorbent species in the film.

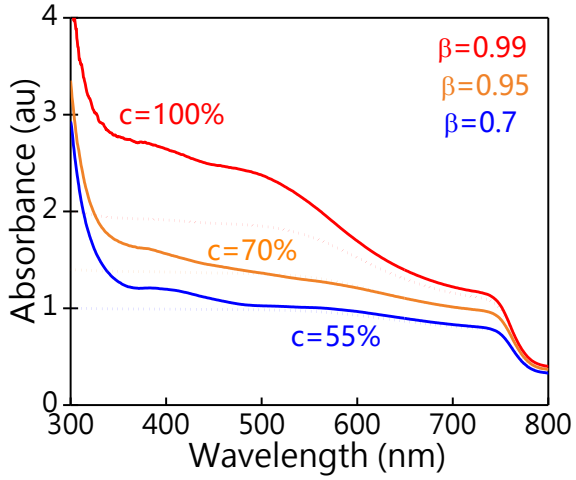

$$A_{\text{measured}} = -\log[\beta(1-\gamma(\lambda))10^{-\text{OD}(\lambda)} + (1-\beta)]$$

***Figure A3**: Absorbance curves from the slot-die coated layers fabricated at various gas flow rate Q_f. The dotted lines correspond to the simulated curves from the formula below that was extracted from the literature [187].*

Appendix 4: Gas flow-induced precursor wet film deformation.

A possible explanation of the wet film inhomogeneities observed in III-2.2 could be the mechanical deformation of the wet film by the gas-knife. In this study, we fixed the slot-die coating parameters (C_s, C_g, C_f) similarly to previous experiment to form a similar wet precursor film (**Table A4**). We decorrelated the coating speed (C_s) and the quenching speed (Q_s) by not turning on the gas-knife flow rate during the coating.

Coating		Quenching		Post-Annealing	
C_g	100 µm	Q_g	3 mm	A_T	100 °C
C_s	28 mm.s^{-1}	Q_s	0 mm.s^{-1}		
C_f	100 µL.min^{-1}	Q_f	100 L.min^{-1}	A_t	5 min
CQ_T	100 °C	CQ_T	100 °C		

***Table A4**: Process parameters used for the static quenching experiment.*

The experiment set up was the following: we first performed the precursor wet film coating step, and then placed the gas-knife on top of the precursor wet film without blowing nitrogen. We finally opened the nitrogen gas-knife it in a static position (Q_s = 0 mm.s^{-1}) on top of freshly-coated precursor wet film and maintained it open until complete drying of the film (about 5 seconds). We recorded the sample picture, optical image and profilometry mapping of the resulting dried perovskite film (**Figure A4-1**).

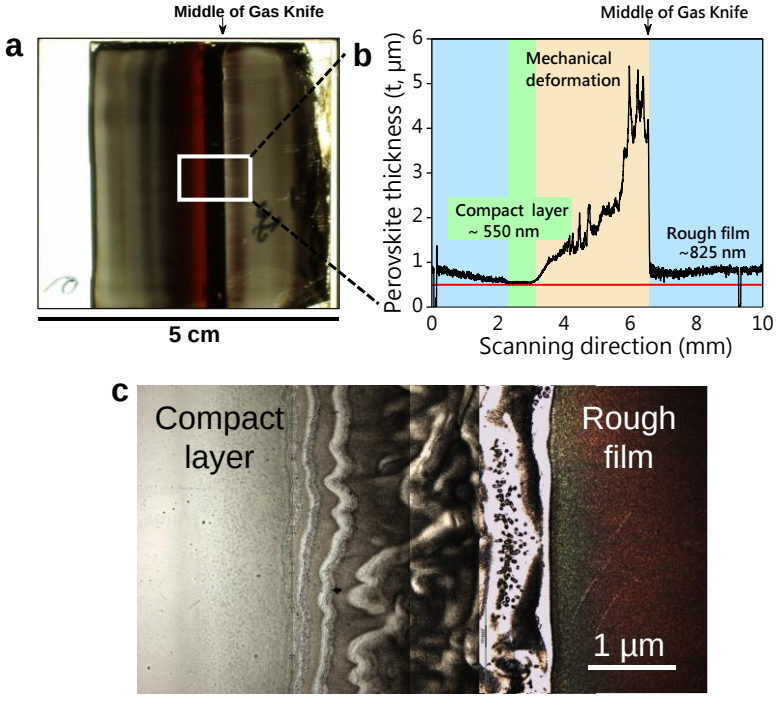

***Figure A4-1**: **a)** Picture of the sample after static quenching, the gas-knife position is indicated by the arrow. **b)** Profilometry profile performed from left to right in the white box indicated in panel a. **c)** Optical microscopy image in the white box.*

We observed that the perovskite film was deformed 1 cm around the gas-knife impact, forming three different areas: a compact area with reduced film thickness (t = 550 nm), a rough area with intermediate film thickness (t = 825 nm) and a deflagrated area with a high film thickness (t=5 µm). We extrapolated the dried perovskite thickness to determine the wet film thicknesses, taking the spin-coated layer as a reference. The rough area corresponded to a precursor wet film thickness of 2 µm (**Figure A4-2)**. The compact area with brown reflects on the sample picture was desirable to achieve. After interpolation, we confirmed the contraction of the wet film from 2 µm (rough area) to 1.2 µm in this location. The thicker area could result from the displacement of precursor solution from the contracted area. The mechanical deformation was not symmetric around the gas-knife impact, in line with the non-symmetrical geometry of the gas-knife (see **Methods**).

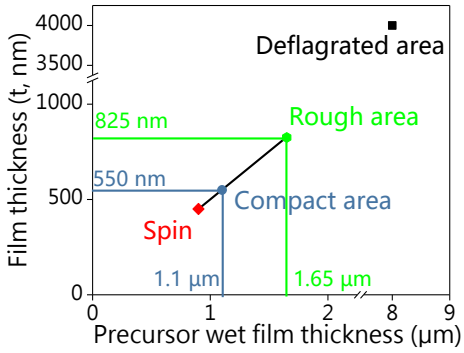

	Wet film thickness (µm)	t (nm)
Spin (reference)	0.9 µm	450 nm
Slot-die (compact area)	1.1 µm	550 nm
Slot-die (rough area)	1.65 µm	825 nm
Slot-die (deflagrated area)	8 µm	4000 nm

***Figure A4-2**: Interpolation of the wet film thicknesses from the spin-coated layer values in the three areas of interest in the static quenching experiment.*

This simple experiment confirmed that the wet film was mechanically deformed by the gas-knife which created high and low wet film levels that resulted in thick and thin dried perovskite layers respectively. In summary, the precursor wet film thickness was estimated to 1.1 µm in the strongly contracted area (brown area), to 2 µm in an intermediate rough area and to 8 µm in the deflagrated area. Therefore, in the rest of this work, we will estimate the slot-die coated precursor wet film thickness to 1.1 µm.

This experiment differed from real processing conditions, as the gas-knife was static and the nitrogen line open when placed on the substrate. In the slot-die coating process, the gas-knife was opened prior to coating and was moving at the process speed ($Q_s = CQ_s$). A perspective to this work could be the study of this phenomenon in real conditions including the dynamic effects on the mechanical deformation when the gas-knife is in movement.

Appendix 5: Reference spin-coated device and shelf life study

The first step of the J-V methodology was to determine for which day the reference spin-coated device measurement results should be reported. Indeed, perovskite solar devices can reach a maximum performance after few hours or days of storage. There is a so called maturation phenomenon whose chemical or electrical mechanisms are still unclear and which depend on the perovskite formulation [219], the solar cells architecture [220] and the storage conditions used. To adjust our own storage protocol, we compared the device J-V measurement results obtained right after device fabrication (after top electrode evaporation or day 0), after 1 day and after 4 days of storage in the dark at 30% humidity. This storage condition was the simplest in the ISOS guidelines [208], it was used to quantify the shelf life of the perovskite devices.

We observed that the best performances were reached after 1 day of storage (**Figure A2**a). After 4 days, the performances start to drop, mainly due to the FF (**Figure A2b**). The corresponding J-V curves of t = 0 and 1 day are plotted in **Figure A2c.** We observed that the J-V curve did have higher open-circuit voltage (V_{oc}) and fill factor (FF) after 1 day of storage. For the reference spin-coated device (measured after 1 day), we obtained an average power conversion efficiency (PCE) of 17.14%, an open-circuit voltage (V_{oc}) of 1.090 V, a current density (J_{sc}) of 21.9 mA.cm^{-2} and a fill factor (FF) of 71.7%. **Figure A2d** summarizes the average device parameters over six devices. Based on the maturation kinetic observed for the spin-coated devices, for the future experiments, we chose to compare performances of devices measured after 1 day, at their highest performance.

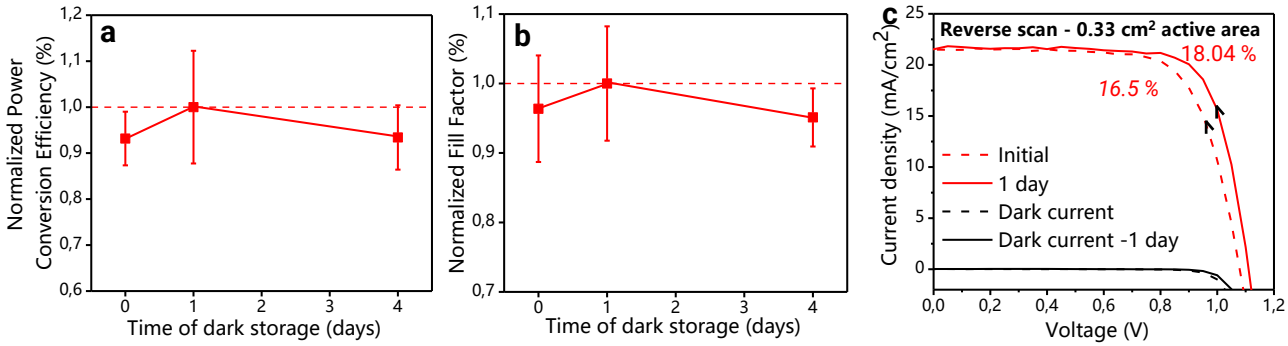

d	V_{oc} (V)	J_{sc} (mA/cm^2)	FF (%)	PCE (%)
Initial	1.075 ± 0.024	21.5 ± 0.4	69.1 ± 5.5	15.9 ± 1.0
1 day	1.090 ± 0.033	21.9 ± 0.8	71.7 ± 5.9	17.1 ± 2.1
4 days	1.078 ± 0.024	21.8 ± 0.7	68.2 ± 3.0	16.0 ± 1.2

Figure A2*: Summary of the device* ***a)*** *power conversion efficiencies and* ***b)*** *fill factor initially, after 1 day and 4 days respectively.* ***c)*** *JV curve from a reference device measured initially and after 1 day (dashed lines).* ***d)*** *Summary of average J-V parameters over 6 devices.*

Appendix 6: Device data summary.

Spin coated reference devices: shelf life study.

day 0	V_{oc} (V)	J_{sc} (mA.cm^{-2})	FF (%)	PCE (%)
1	1.071	21.9	70.4	16.51
2	1.052	21.34	70.9	15.92
3	1.078	21.5	71.1	16.52
4	1.099	21.4	63.5	14.95
5	1.073	21.3	66.7	15.28
6	1.075	21.7	71.3	16.65
	1.075 ± 0.024	**21.5 ± 0.36**	**69.1 ± 5.5**	**15.97 ± 1.02**
day 1				
1	1.099	22.3	73.2	17.94
2	1.097	21.7	73.8	17.60
3	1.108	21.8	74.9	18.04
4	1.078	21.9	68.3	16.10
5	1.067	22.1	66.5	15.66
6	1.090	21.9	73.2	17.51
	1.090 ± 0.033	**21.9 ± 0.75**	**71.7 ± 5.9**	**17.14 ± 2.1**
day 4				
1	1.069	21.3	69.7	15.90
2	1.059	21.5	67.5	15.38
3	1.082	21.6	65.9	15.38
4	1.099	21.9	66.2	15.96
5	1.064	21.9	69.9	16.32
6	1.095	22.3	70.2	17.13
	1.078 ± 0.024	**21.8 ± 0.73**	**68.2 ± 3.0**	**16.01 ± 1.2**

*The yellow highlighted data are the one corresponding to the **Appendix A5** plot.*

Spin and slot-die coated devices : process comparison.

day 0- spin	**V_{oc} (V)**	**J_{sc} (mA.cm^{-2})**	**FF (%)**	**PCE (%)**
1	1.071	21.90	70.4	16.51
2	1.052	21.3	70.9	15.92
3	1.078	21.5	71.1	16.52
4	1.099	21.4	63.5	14.95
5	1.073	21.3	66.7	15.28
6	1.076	21.7	71.3	16.65
	1.075 ± 0.024	**21.5 ± 0.36**	**69.1 ± 5.5**	**15.97 ± 1.02**
day 0- slot-die				
1	1.000	20.7	54.8	11.36
2	1.022	20.7	60.0	12.71
3	0.997	20.47	58.1	11.85
4	1.017	20.4	59.3	12.32
5	0.979	19.6	61.1	11.72
6	1.011	19.6	62.4	12.34
7	1.001	19.6	62.3	12.23
8	0.996	20.1	55.9	11.20
9	1.024	20.1	57.9	11.94
10	1.002	20.1	57.7	11.61
11	0.992	20.8	61.6	12.71
12	1.013	20.7	63.4	13.31
13	1.001	20.6	63.0	13.01
14*	0.881	21.8	56.1	10.76
	0.995 ± 0.028	**20.4 ± 0.81**	**59.5 ± 4.8**	**12.07 ± 1.2**

*The yellow highlighted data are the one corresponding to the **Figure 22** plot.*

Spin coated devices: concentration study.

day 1 - 0.9 M	V_{oc} (V)	J_{sc} (mA.cm^{-2})	FF (%)	PCE (%)
1	1.056	20.2	68.4	14.62
2	1.086	19.2	66.1	13.80
3	1.059	19.2	68.5	13.95
4	1.068	18.8	65.5	13.17
5	1.053	19.1	69.8	14.07
	1.064± 0.022	**19.3 ± 0.90**	**67.7 ± 5.5**	**13.92 ± 0.7**
day 1 - 1.2 M (ref)				
1	1.099	22.3	73.2	17.94
2	1.097	21.7	73.8	17.60
3	1.108	21.8	74.9	18.04
4	1.078	21.9	68.3	16.10
5	1.067	22.1	66.5	15.66
6	1.090	21.9	73.2	17.51
	1.090 ± 0.033	**21.9 ± 0.75**	**71.7 ± 5.9**	**17.14 ± 2.1**
day 1 - 1.5 M				
1	1.070	22.5	69.7	16.77
2	1.071	22.0	65.2	15.37
3	1.056	22.0	70.8	16.46
4	1.072	22.4	69.9	16.81
5	1.102	21.9	73.9	17.87
6	1.100	22.4	71.2	17.58
	1.080 ± 0.038	**22.1 ± 3.1**	**70.2 ± 6.2**	**16.81 ± 3.9**

*The yellow highlighted data are the one corresponding to the **Figure 26a** plot.*

Slot-die coated devices : concentration study.

day 0- slot-die 1.2 M	V_{oc} (V)	J_{sc} (mA.cm^{-2})	FF (%)	PCE (%)
1	1.000	20.7	54.8	11.36
2	1.022	20.7	60.0	12.71
3	0.997	20.47	58.1	11.85
4	1.017	20.4	59.3	12.32
5	0.979	19.6	61.1	11.72
6	1.011	19.6	62.4	12.34
7	1.001	19.6	62.3	12.23
8	0.996	20.1	55.9	11.20
9	1.024	20.1	57.9	11.94
10	1.002	20.1	57.7	11.61
11	0.992	20.8	61.6	12.71
12	1.013	20.7	63.4	13.31
13	1.001	20.6	63.0	13.01
14*	0.881	21.8	56.1	10.76
	0.995 ± 0.028	**20.4 ± 0.81**	**59.5 ± 4.8**	**12.07 ± 1.2**
day 0- slot-die 0.9 M				
1	0.983	18.8	63.7	11.78
2	1.018	18.7	63.1	12.02
3	0.981	20.2	60.4	11.98
4	1.007	19.7	60.3	11.94
5	0.921	20.0	56.5	10.42
6	0.951	20.3	55.6	10.74
7	0.959	20.2	61.4	11.87
8	0.961	20.0	60.8	11.70
9	0.869	20.1	48.9	8.52
	0.961 ± 0.091	**19.8 ± 1.04**	**59.0 ± 10**	**11.21 ± 2.7**

*The yellow highlighted data are the one corresponding to the **Figure 31a** plot.*

Chapter IV: Fine crystallization tuning via precursor ink modification

As seen in the previous chapter, the presence of the δ-$FAPbI_3$ by-product in the slot-die coated films limits the device performances. In the literature, the perovskite stoichiometry is known to strongly influence the perovskite conversion into the cubic structure. Here, we investigate the effect of tuning the CsI and FAI precursor contents in the precursor ink on the properties of slot-die coated. We present the impact of post-annealing on the perovskite layers properties fabricated from various Cs/Pb and FA/Pb ratios. We integrate slot-die coated layers fabricated from a different Cs/Pb ratio into PV devices to compare its performance with the initial devices fabricated from slot-die coated layers.

IV.1. Slot-die coated layers stoichiometry: role of CsI and FAI precursors

In the literature, the caesium cation (Cs^+) is known to favour the conversion into the perovskite cubic structure (α-CsFAPbIBr) [16] and is largely used in state-of-the-art spin-coating devices. Here, we varied the CsI precursor quantity to tune the Cs/Pb ratio in the precursor ink. We compared the reference 5% Cs/Pb to lower (0%) and higher (10, 15 and 20%) Cs/Pb ratios (**Table 1**). As the Cs^+ cation is added under the CsI form, there is a slight increased in iodide anion in the corresponding perovskite formulas (**Table 1**). We noted that these additional iodide anions did not lead to major modification of the perovskite formula as most of the iodide anions were provided by the PbI_2 and FAI precursors.

Lead concentration (M)	1.2
PbI_2 excess (%)	6
Cs/Pb molar ratio (%)	0, 5, 10, 15, 20
FA/Pb molar ratio (%)	79
Br: I molar ratio (%)	~12 : 88
DMF :DMSO volume ratio	4 : 1
Calculated perovskite formulas	$Cs_0FA_{0.79}Pb(I_{0.878}/Br_{0.122})_{2.79}$ $Cs_{0.05}FA_{0.79}Pb(I_{0.880}/Br_{0.120})_{2.84}$ * $Cs_{0.10}FA_{0.79}Pb(I_{0.882}/Br_{0.117})_{2.89}$ $Cs_{0.15}FA_{0.79}Pb(I_{0.884}/Br_{0.116})_{2.94}$ $Cs_{0.20}FA_{0.79}Pb(I_{0.886}/Br_{0.114})_{2.99}$

***Table 1**: Composition of the precursor inks used and their corresponding perovskite formulas. * reference precursor ink from **Chapter III**. The parameters studied are highlighted in green.*

IV.1.1. Precursor ink properties

In the literature, the link between the precursor ink properties, the perovskite film properties and the device performances has been studied by numerous groups [221–223]. Therefore, the first step of our methodology was to gain an understanding of the precursor ink properties (surface tension, colloids formation) when varying the Cs/Pb content.

- **Impact of CsI on the precursor ink physical properties**

First, the physical properties of the precursor ink could affect the slot-die coating process and the resulting layer morphology. Here, we measured the precursor ink surface tension to detect possible trends related to CsI addition in the precursor ink.

In **Figure 1a**, we observed that the position of the precursor ink evolved towards the side of the wettability envelop when the CsI content increased. In absolute value, the surface tension of the precursor ink was relatively constant (43 ±1 $mN.m^{-1}$). Values remain within the substrate wettability envelop for all CsI contents, indicating that the wettability of all inks should be sufficient. However, the repartition between the polar and disperse component varied. Interestingly, the higher the CsI content, the lower the polar component of the surface tension (**Figure 1b**). The polar component represents the attraction due to the polar nature of the species in solution. In our case, the DMF and DMSO solvents (polar aprotic) and the free ions in solution could contribute to this component. We suggest that a reduction of the polar component reflected the reduction of the amount of free solvent molecules and free ions in solution.

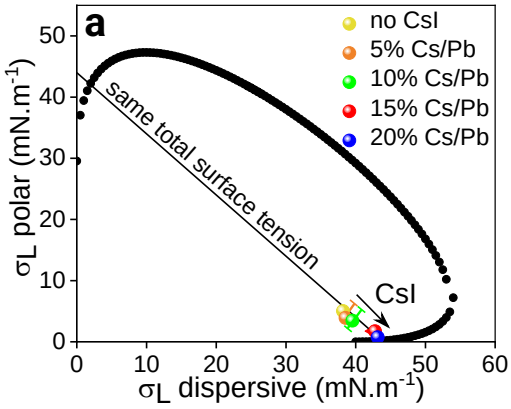

b

Cs/Pb (%)	Angle on PTFE (°)	Surface tension ($mN.m^{-1}$)	disperse composant ($mN.m^{-1}$)	polar composant ($mN.m^{-1}$)
0	78	43.2	38.2	5.0
5	76	42.5	38.6	3.9
10	76	43.1	39.6	3.4
15	76	44.5	42.8	1.7
20	74	43.9	43.2	0.7

***Figure 1**: **a)** Position of the precursor inks on the wettability envelop of SnO_2 substrate. **b)** Summary of surface tension for the different Cs/Pb content in precursor ink.*

- **Precursor ink chemistry: role of CsI precursor**

Beyond the modification of physical ink properties, the addition of CsI can impact the solute organization in solution. In the literature, dynamic light-scattering (DLS) technique can be used to determine the size distribution of colloids in solution and has been applied to perovskite solutions before [169,224,225]. Recently, in-situ characterization techniques based on in-situ X-ray diffraction [96,226,227] or optical techniques [102,133,173,174,228] were used to identify the perovskite solutions intermediate species. Indeed, some perovskite intermediates have a crystalline structure ($[PbI_6^{4-}]$ [223]) and can be detected by X-ray diffraction of the precursor semi-wet films. We decided to record the X-Ray diffraction patterns of wet films containing various Cs/Pb contents.

To decorrelate the effects of the many precursors in solution (PbI_2, $PbBr_2$, FAI, CsI), we did a preliminary study of inks containing each precursor in the DMF:DMSO mixture. This study is reported in **Appendix 1** and enabled us to identify primary cluster contributing species: PbI_2 and DMSO, and secondary contributing species: CsI and $PbBr_2$. In brief, as previously reported in the literature, the PbI_2 precursor formed [PbI_6^{4-}] complexes in presence of DMSO (detected at $2\theta = 9.5°$). Once the [PbI_6^{4-}] complex formed, Cs^+ and Br^- ions seem to be incorporated into the intermediate structure while FAI preferred to form the δ-$FAPbI_3$ phase. We also noted that CsI addition to the complex can lead to crystalline PbI_2 formation.

After the PbI_2:DMSO intermediate formation, more complex intermediates can form in the precursor solution. In the literature, Gratia *et al.* have identified the sequential formation of hexagonal polytypes, named '2H', '4H' and '6H', and whose complexity varies with the perovskite stoichiometry [41]. They observed that the addition of caesium cation in the precursor ink shortens the polytypes sequence to '2H-4H', leading to complete perovskite crystallization into α-CsFAPbIBr phase when 3% CsI was incorporated in the precursor solution. To confirm the mechanism proposed in the literature by Gratia *et al.*, we recorded the XRD patterns of the semi-dried films of precursor ink containing 5 to 20% Cs/Pb.

Figure 2 shows the resulting XRD patterns with the attributions of the various phases, according to the literature [41]. In this semi-dried film XRD experiment, it was important to define a measurement window where the inks were is a similar drying stage to be able to compare them fairly. We defined the semi-wet film window as a film which is still containing the PbI_2:DMSO intermediate (X:DMSO on **Figure 2**), visible at $2\theta = 9.5°$, and started to form the α-CsFAPbIBr perovskite ((001) on **Figure 2**), visible around $2\theta = 15°$. If the ink was too wet or too dried, the sample fabrication or the measurement were repeated until the appropriate process window was reached.

Regarding the polytypes formation, we observed the gradual diminution of the '6H' polytype ($2\theta = 13.8°$) with the increased CsI content. This is in accordance with the literature where caesium addition was found to shorter the polytype sequence from '2H-4H-6H' to '2H-4H' [41]. However, we observed this variation at a threshold value of 15% CsI which is much higher than what was observed in spin-coated layers (3% threshold value [41]]). This difference could be explained by the modification of the quenching mean from anti-solvent to gas-quenching. This result is in line with the study by Nogueira *et al.* [96] who studied using *in-situ* grazing incidence wide-angle X-Ray scattering (GIWAXS) the influence of the quenching means employed on the precursor chemistry during crystallization.

Beyond the disappearance of the '6H' polytype with the increased CsI content, we also observed the increase of the '4H' polytype at 10 and 15% CsI, and the brutal disappearance of the '4H' polytype at 20% CsI. The polytype sequence seemed to be shorten to '2H' at 20% CsI, unveiling a possibly different mechanism at that high CsI content. *In-situ* methods could be a relevant perspective to confirm the results of this experiment.

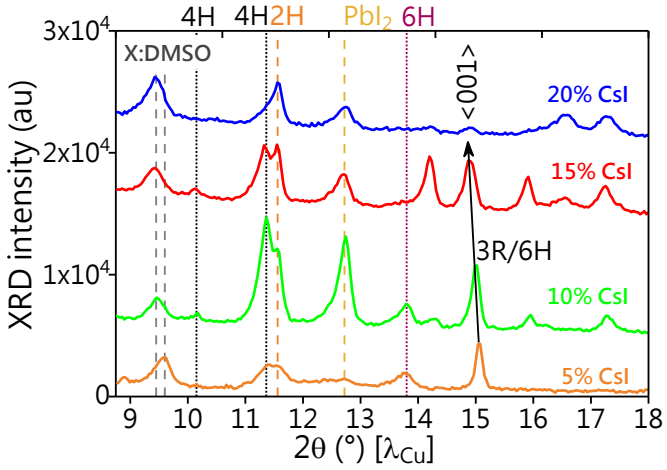

***Figure 2**: X-ray diffraction of precursor inks containing various amounts of CsI precursor.*

IV.1.2. Slot-die coated layers with various Cs/Pb ratios

Once the precursor inks characterized, we deposited perovskite layers with different Cs/Pb contents *via* slot-die coating on glass/ITO/SnO_2 substrate. To decorrelate the change of CsI content to the influence of post-annealing (**III.3.2**), we studied the "as-quenched" layers without any post-annealing first. The slot-die coating process parameters are the same as in **Chapter III** (**III.3.2.**, **Table 10**).

Monitoring of stoichiometry change

To ensure that the CsI was incorporated from the precursor ink into the slot-die coated layer, we monitored the Cs/Pb and I/Pb ratios by energy dispersive X-ray (EDX) of the slot-die coated films (**Figure 3**). We observed a gradual increase of Cs/Pb and I/Pb ratios (**Figure 3**), confirming the incorporation of the CsI precursor in the film. For both signals, we observed an experimental offset between the theoretical formula and the EDX values. Both experimental and theoretical values were well correlated from 0 to 10% Cs/Pb. The iodide ratio increased was less pronounced (from 2.70 to 2.97), in line with the previous observation that most iodide anions were provided by other iodide containing precursors (FAI and PbI_2).

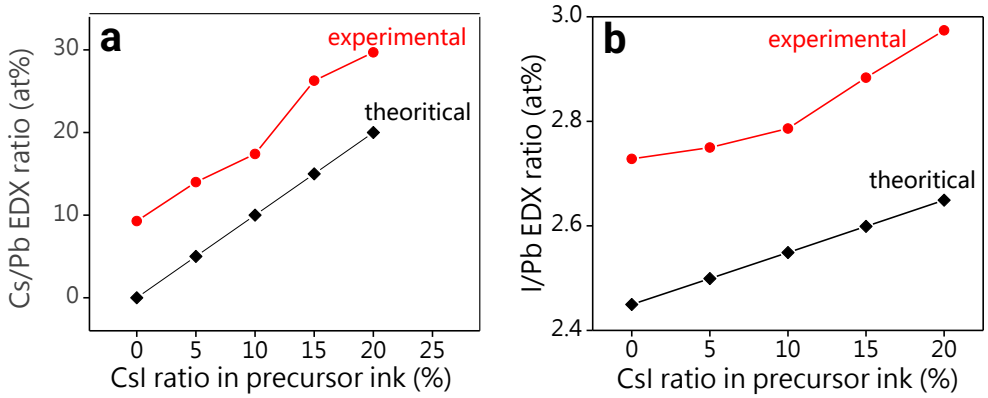

***Figure 3**: Cs/Pb and I/Pb EDX ratio showing the gradual incorporation of CsI precursor into the slot-die coated films.*

- **Crystallinity: can we limit δ-FAPbI$_3$ formation by CsI addition?**

Once the CsI incorporation confirmed in the slot-die coated layers, we measured the X-ray diffraction patterns to assess the presence of the perovskite cubic structure (α-CsFAPbIBr) and hexagonal structure (δ-FAPbI$_3$) and residual CsI (**Figure 5**).

As expected, we observed that without caesium (0% Cs/Pb), the cubic α-CsFAPbIBr structure did not form. This result was in agreement with the literature [16] and highlighted the necessary role of the caesium cation (Cs^+) for the α-CsFAPbIBr cubic structure formation. From 5 to 20% Cs/Pb, we observed a gradual increase of the perovskite peak intensity (**Figure 4a**), correlated with a decrease of the by-product (δ-FaPbI$_3$ and crystalline PbI$_2$) XRD peak ratios (**Figure 4b**). Interestingly, we did not observe any shift in the position of the XRD perovskite peaks, meaning that the Cs^+ ion incorporation was not deforming the perovskite lattice [16,229]. Turren-Cruz *et al.* observed the perovskite lattice deformation upon CsI addition at higher bromide contents, detectable by a shift of the perovskite XRD peak position. Our relative low bromide ratio (12%) could explain why we did not observe this trend here.

At 15% Cs/Pb and above, the slot-die coated films did not show any δ-FaPbI$_3$ peak in the XRD pattern. When compared to the spin-coated film, the 15% Cs/Pb slot-die coated film exhibited a significantly lower crystalline PbI$_2$ XRD area ratio (27% and 0.6% respectively). This difference can be due to the lack of post-annealing on the slot-die coated layer and will be investigated later in this section. For 15 and 20% Cs/Pb, we noticed the presence of CsI residuals ($2\theta = 27°$), which could explain the slightly larger EDX ratios observed for Cs and I in those samples (**Figure 3**). At 20% Cs/Pb, the intensity of the perovskite (011) plan increased (peak area ratio increase on **Figure 4b**), suggesting a modification of the perovskite film organization. As a change of grain orientation can be linked to a change of film morphology, we studied the morphology of the perovskite films in the next paragraph.

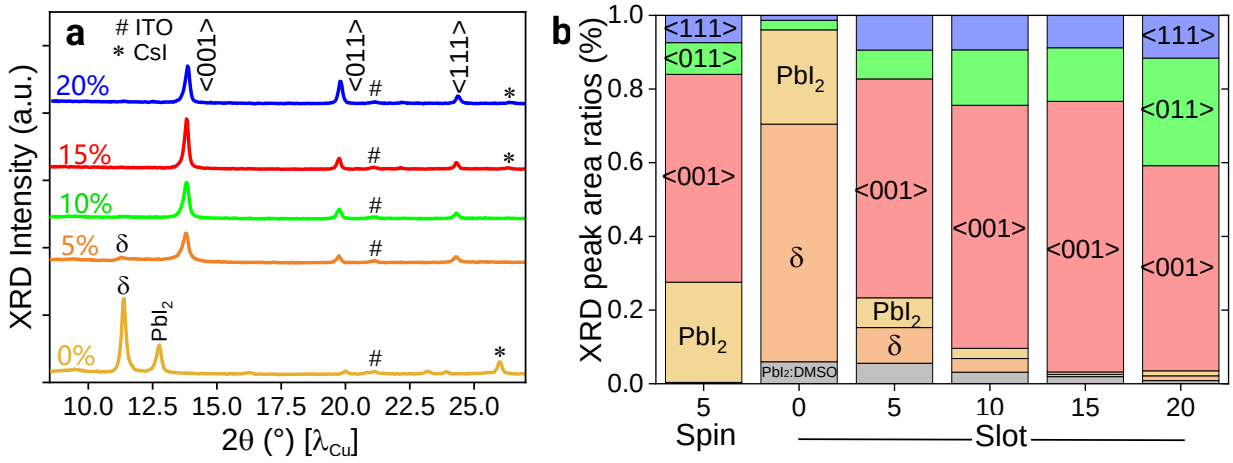

***Figure 4**: **a)** XRD patterns of slot-die coated layers with 0, 5, 10, 15, 20% CsI contents. **b)** Corresponding XRD peak area ratios. The δ-FaPbI$_3$ is in orange and the PbI$_2$:DMSO intermediate in grey.*

- **Morphology**

The slot-die coated film thickness at Cs/Pb = 5% was t = 450 nm in this batch, which was lower than the values obtained in the previous experiment (t = 575 nm, **III.2.3**). This variation could be linked to a batch-to-batch variation of the wet film thickness control. The slot-die coated films fabricated with Cs/Pb = 0 to 15% exhibited a similar perovskite thickness around 450 nm (**Figure 5a**), indicating that the CsI did not influence the film thickness in this range. Conversely, the film average roughness decreased gradually with the increased CsI content (**Figure 5b**). The CsI addition thus seems to have a beneficial effect on the surface roughness. This finding was in contradiction with a study by Braunger *et al.* [230] that observed an increase of the surface roughness with the CsI incorporation for spin-coated CsFAPbIBr films. The difference with our work could be due the lower Br ratio employed here (12%) or the difference between the anti-solvent and the gas quenching applied to crystallize the perovskite material.

At 20% Cs/Pb, the slot-die coated film was particularly thicker (t = 620 nm) than other films, beyond the batch-to-batch variation. This higher film thickness probably originated from a change in the precursor wet film properties such as a modification of the precursor ink viscosity at high CsI content. In the literature, the impact of the solvents on the precursor solution viscosity has been studied [112,113,116,231] but there are no reports on the effect of the precursor stoichiometry, in particularly for the CsFAPbIBr system. Interestingly, the thicker 20% Cs/Pb film exhibited the lowest roughness despite the thickness difference. To deepen our understanding, we investigated the perovskite layers morphology by SEM and the surface reflection by optical characterization.

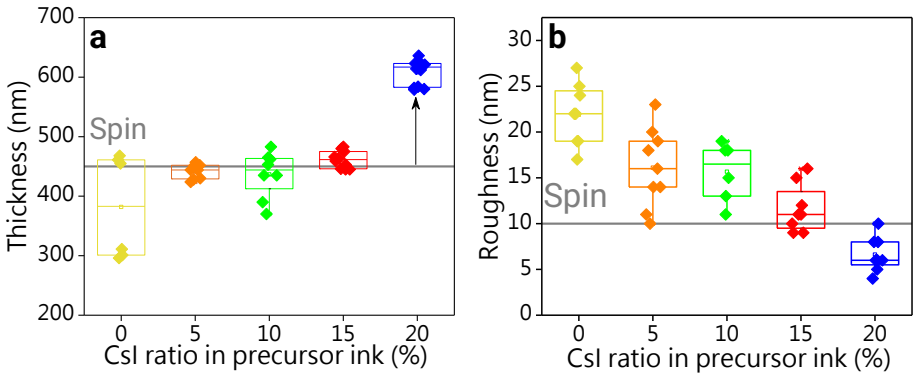

***Figure 5**: **a)** Thickness and **b)** Surface average roughness (R_a) of slot-die coated layers with 0, 5, 10, 15, 20% CsI contents.*

Smoother surfaces could originate from a change in the grain size. To investigate this hypothesis, we recorded the SEM images (**Figure 6a**) of the slot-die coated films. We observed a grain size reduction between 5% Cs/Pb (g = 215 nm) and 15 and 20% Cs/Pb (g = 160 and 155 nm respectively), in line with the roughness observations (**Figure 6b**). Surprisingly, at Cs/Pb = 10%, the perovskite grains were smaller (g ~ 95 nm). This outlier point suggests the reduction of the grain size could have contributed but was not the only reason behind the surface roughness trend observed earlier. Overall, the slot-die coated films grains were much smaller (g ~ 150 nm) than their spin-coated counterparts (g ~ 350 nm). We concluded that the quenching mean (gas- or anti-solvent) had a predominant effect on the grain size compared to other factors such as the Cs/Pb content or the precursor ink concentration (**III.4.3**).

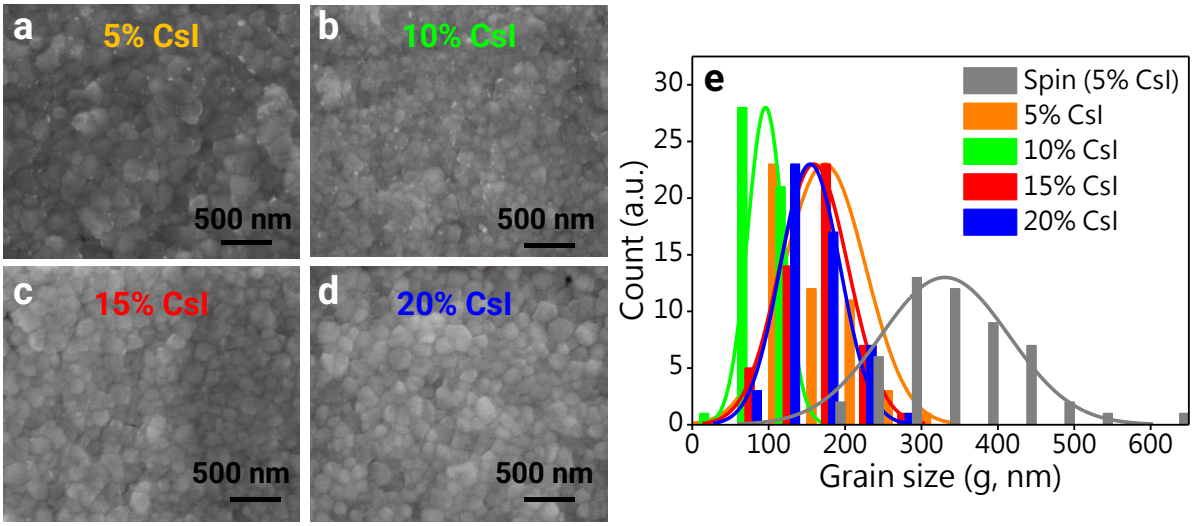

***Figure 6**: **a-d)** SEM top images of slot-die coated layers from 5, 10, 15, 20% CsI contents. **e)** Corresponding grain distributions.*

- **Optical properties**

The surface roughness decrease observed by profilometry was translated into a of the increase of the perovskite layer reflection with the CsI content (**Figure 7a**). This result confirmed that an increased perovskite formation (under α-CsFAPbIBr form) was correlated with a modification of the perovskite surface properties. Interestingly, the reflection seemed independent of the grain size, as both 15 and 20% Cs/Pb sample exhibited a similar grain size and different reflection curves (**Figure 7a**). In the literature, other grain properties such as their orientation or chemical composition are known to impact the surface properties [232,233,41,229]. Further investigations are needed to identify the causes of the surface modification in this case.

The absorption onset, visible on the Tauc plot graph (**Figure 7b**), increased with the CsI content, in line with the increase of α-CsFAPbIBr ratio in the film. In addition, we observed a reduction of the Urbach tail in the 1.55 - 1.60 eV region with the CsI addition, showing that the addition of CsI results in higher structural quality and reduced band edge defects of the perovskite material. Interestingly, the band gap of the absorber was comparable to the reference spin-coated layer band gap (E_g = 1.60 eV) for all CsI contents. In the literature, the CsI addition (in the same proportions) in spin-coated layers is known to cause a shift in the band gap when combined with a bromide content > 15% [40,229]. Our different findings could here again be explained by the lower Br content (12%) in the formulation.

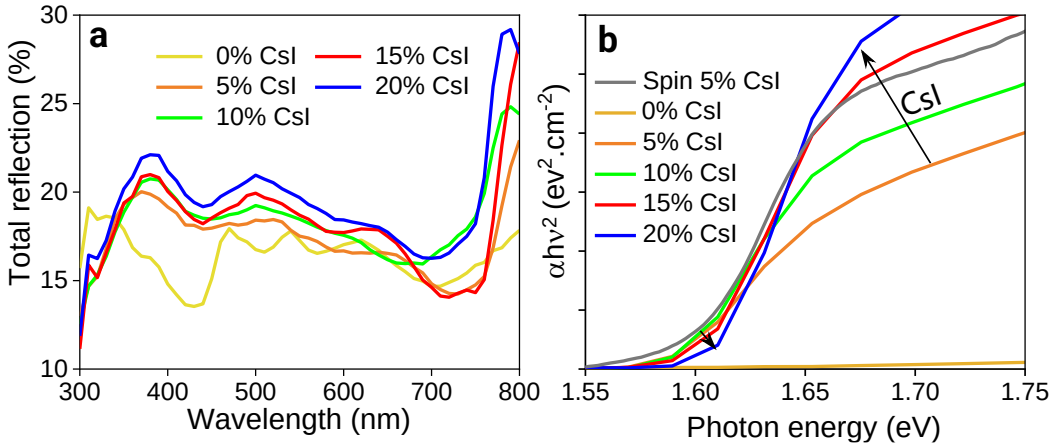

***Figure 7**: Evolution of the film optical properties at FA/Pb = 79% for various CsI contents. **a)** Total reflection and **b)** Tauc plot graphs extracted from the absorbance curves.*

We recorded the photoluminescence (PL) emission of the slot-die coated samples at an excitation wavelength of λ = 550 nm (**Figure 8a**). We observed that the CsI-free sample exhibits a wide PL peak in the 650 - 750 nm range, despite the majority δ-$FAPbI_3$ phase present ($FAPbI_3$ PL emission expected below 500 nm [234]). At 0% Cs/Pb, the XRD patterns unveiled a limited formation of α-CsFAPbIBr perovskite under the (011) and (111) orientations (**Figure 4b**). In the literature, the junction between α and δ domains has been found responsible for intense photoluminescence for emission wavelength ~ 780 nm [234,235]. We propose that the α-

CsFAPbIBr (minority) / δ-$FAPbI_3$ (majority) junctions could be responsible for the high PL intensity observed in this sample. Based on a similar PL behaviour in the 5% Cs/Pb, we suggest that the similar "junction effect" can also take place at the α-CsFAPbIBr (majority) / δ-$FAPbI_3$ (minority) interface. Furthermore, the photoluminescence peak intensity decreased drastically at 10% Cs/Pb (**Figure 8a**), in correlation with the reduction of the δ-$FAPbI_3$ XRD peak ratio (**Figure 4b**) in the film. This trend was further confirmed at 15% and 20% Cs/Pb, underlying that a minimum δ-$FAPbI_3$ material quantity was necessary to observe the PL intensity of α/δ junctions. In summary, the PL intensity was strongly correlated to the δ-$FAPbI_3$ ratio in the film.

We observed a gradual blue shift of the normalized photoluminescence emission wavelength upon addition of CsI (**Figure 8b**). In the literature, the photoluminescence blue shift has been linked to compressive strain in the perovskite lattice [236–238]. Similar gradual PL blue shift for CsI-rich samples has been observed earlier by Saliba *et al.* [16], suggesting that the Cs^+ cation is inserted in the perovskite crystalline lattice which reduces the lattice size (tuning the angle and distance between I and Pb atoms [236,238]). Notably, the photoluminescence emission wavelengths of the spin-coated or slot-die coated layers with 5% Cs/Pb were similar, suggesting that the PL emission wavelength was rather independent of the crystallization method and mainly depended on the CsI content.

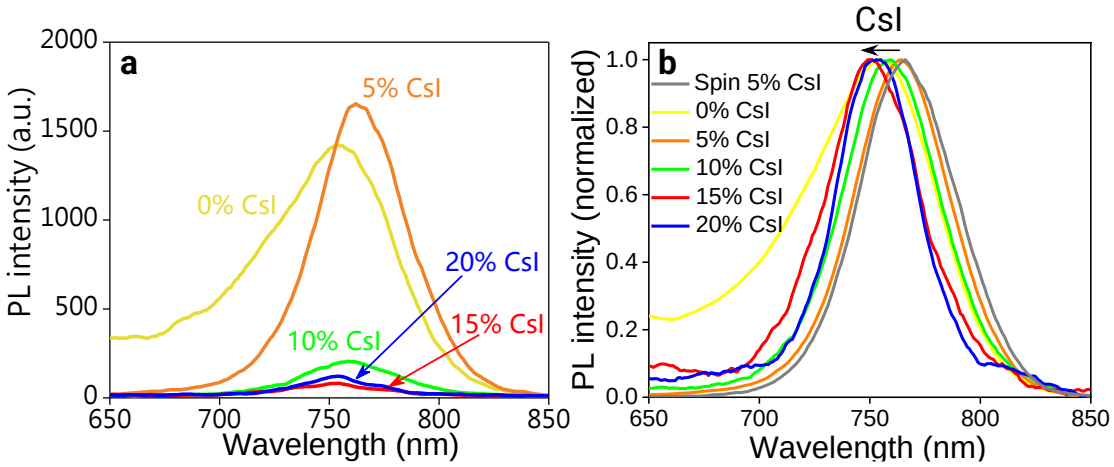

***Figure 8**: **a)** Photoluminescence of the slot-die coated layers fabricated from 0, 5, 10, 15, 20% CsI contents. **b)** Normalized photoluminescence to visualize the PL shift.*

In summary, the suppression of the '6H' polytype in the precursor ink by CsI addition appears to be a successful strategy to selectively form CsFAPbIBr perovskite under the cubic structure *via* the slot-die coating process. Beyond its effect on perovskite conversion, the CsI precursor seemed to have a gradual effect on the surface properties of the perovskite layer (surface reflection and roughness); and a more abrupt effect at higher concentration (20% Cs/Pb) on the perovskite thickness and grain orientations.

The slot-die coated layer containing 15% Cs/Pb exhibited a similar film thickness (t = 450 nm), slightly reduced grain size (g= 160 nm) and higher opto-electronic quality (reduced Urbach tail) compared to the slot-die coated layer fabricated from the 5% Cs/Pb ink (reference).

IV.1.3. Influence of annealing on the film properties

As until now, we have studied the influence of the CsI content on the "as-quenched" film (prior to the annealing step) properties to decorrelate both effects on perovskite conversion. In the reference slot-die coating process (**Chapter III**), we used a post-annealing of 5 minutes at 100 °C (nitrogen atmosphere). This section studies the evolution of the slot-die coated layers properties with 5, 15 and 20% CsI contents after the post-annealing step.

- **Impact on morphology**

In the literature, the post-annealing step has been shown to induce perovskite grain growth in mixed-cations perovskite films [239]. This technique was applied to achieve films with reduced grain boundaries that are desirable to minimize the recombination losses in the solar devices. Here, while we did not observe a grain growth phenomenon upon 5 minutes of post-annealing at 100 °C (**Figure 9**) as also discussed in **Chapter III**, we observed the formation of white particles on the surface of the perovskite layers upon annealing for the 5 and 15% Cs/Pb sample. Notably, this effect was not observed at 20% Cs/Pb. To link this observation to the perovskite material composition, we performed the XRD measurements of the annealed layers.

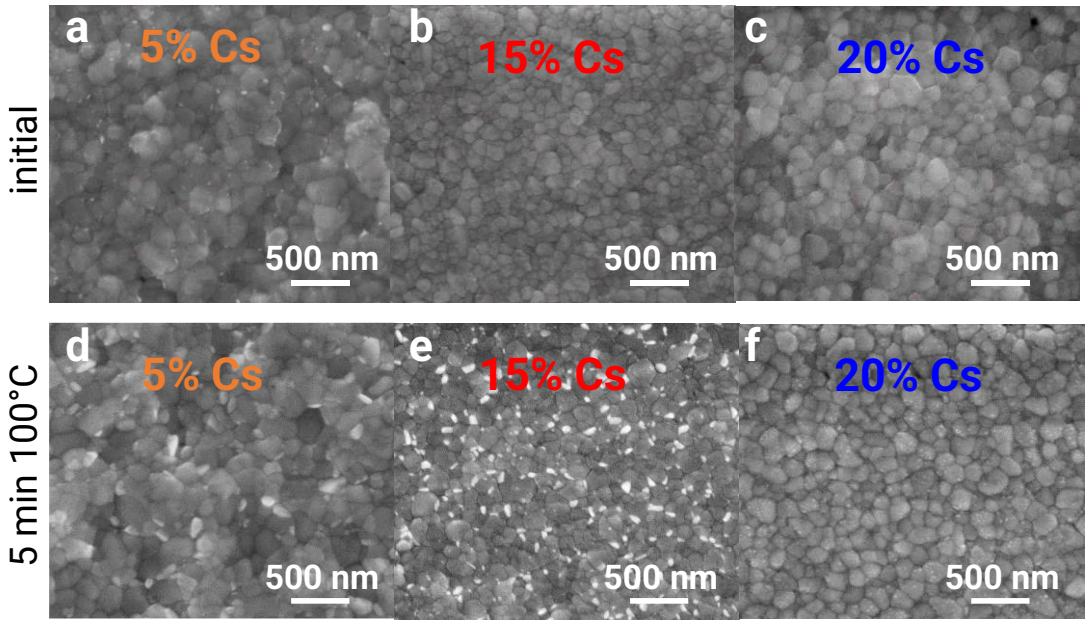

***Figure 9**: SEM top images of 'as-quenched' slot-die coated layers with **a)** 5%, **b)** 15% and **c)** 20% Cs/Pb after 5 min annealing at 100 °C with **d)** 5%, **e)** 15% and **f)** 20% Cs/Pb.*

- **Monitoring of the phase formation**

Matching the presence of the white particles on the SEM images, the crystalline PbI_2 XRD peak area ratio increased upon annealing in the 5 and 15% Cs/Pb samples and remained constant in the 20% Cs/Pb sample (**Figure 10**). Similar crystalline PbI_2 formation upon annealing of mixed-cations perovskites has been reported in the literature [107,239]. We propose that unreacted PbI_2, possible present under PbI_2:DMSO complex form and/or amorphous form, was present in the first two samples (5 and 15% Cs/Pb) due to overstoichiometric PbI_2 in the perovskite formula. Upon annealing, this unreacted PbI_2 was able to crystallize [107].

Interestingly, no additional crystalline PbI_2 was formed in the 20% Cs/Pb sample upon annealing. The addition of 20% Cs with respect to Pb could have brought the perovskite formula closer to stoichiometric proportions, by increasing the halides to lead ratio to 2.99 (against 2.94 at 15% Cs/Pb) (**IV.1.1. Table 1**). The change of stoichiometry could have suppressed the excess PbI_2 reservoir in the 20% Cs/Pb sample, resulting in the suppression of crystalline PbI_2 formation upon annealing. Regarding device integration, the reduction of crystalline PbI_2 formation in the 20% Cs/Pb sample is interesting as it could suppress the device performance loss due to crystalline PbI_2 presence. In the literature, there is a balance between the beneficial effect of PbI_2 for device performance and shelf life stability [240].

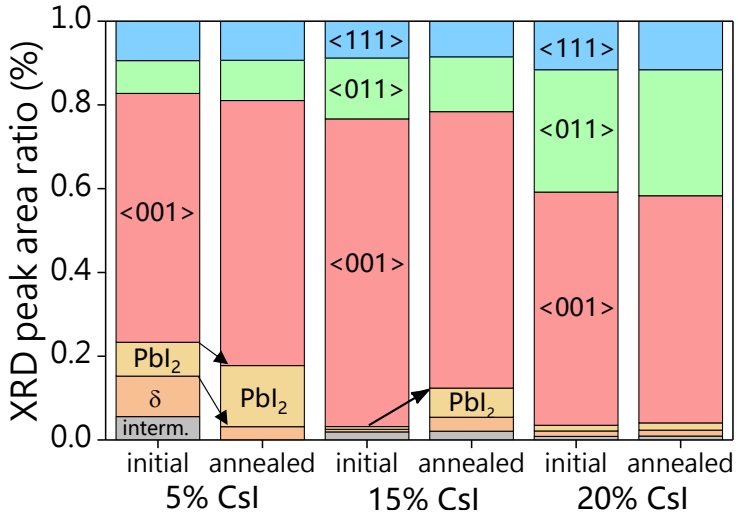

***Figure 10**: XRD peak area ratios extracted from 5, 15 and 20% Cs/Pb, as deposited and after annealing at 100 °C for 5 min.*

- **Impact on photoluminescence**

We coupled the XRD observation with PL measurement (**Figure 11a**). At 5% Cs/Pb, the decreased δ-$FAPbI_3$ peak area ratio detected by XRD led to a PL intensity decrease upon annealing, possibly linked to a diminution of the α-δ junctions in the material. The opposite situation arose at 15% Cs/Pb, where the δ-$FAPbI_3$ XRD peak area ratio increased after annealing, resulting in a PL intensity increase. Interestingly, the PL trend of 5% Cs/Pb and 15% Cs/Pb was not correlated to the formation of crystalline PbI_2 upon annealing, but rather depended on the δ-$FAPbI_3$ presence. Lastly, the PL intensity of the 20% Cs/Pb sample stayed constant after annealing, reinforcing the particularity of this perovskite composition (**Figure 11a**).

Regarding the PL emission wavelength, the PL peaks did not shift upon annealing at 5% and 20% Cs/Pb (**Figure 11b-d**), indicating that the perovskite lattice strain was probably not modified upon annealing. However, we observed a red shift and PL narrowing in the 720 - 750 nm range at 15% Cs/Pb (**Figure 11c**). The PL red shift could indicate a lattice relaxation upon annealing, leading to a less defective perovskite film [107], hence the PL intensity increase in the 15% Cs/Pb sample after annealing. As the lattice strain has been found to have a detrimental influence the device performance and stability [16,230], the 15% Cs/Pb film after annealing could be more suitable for device integration compared to the "as quenched" film.

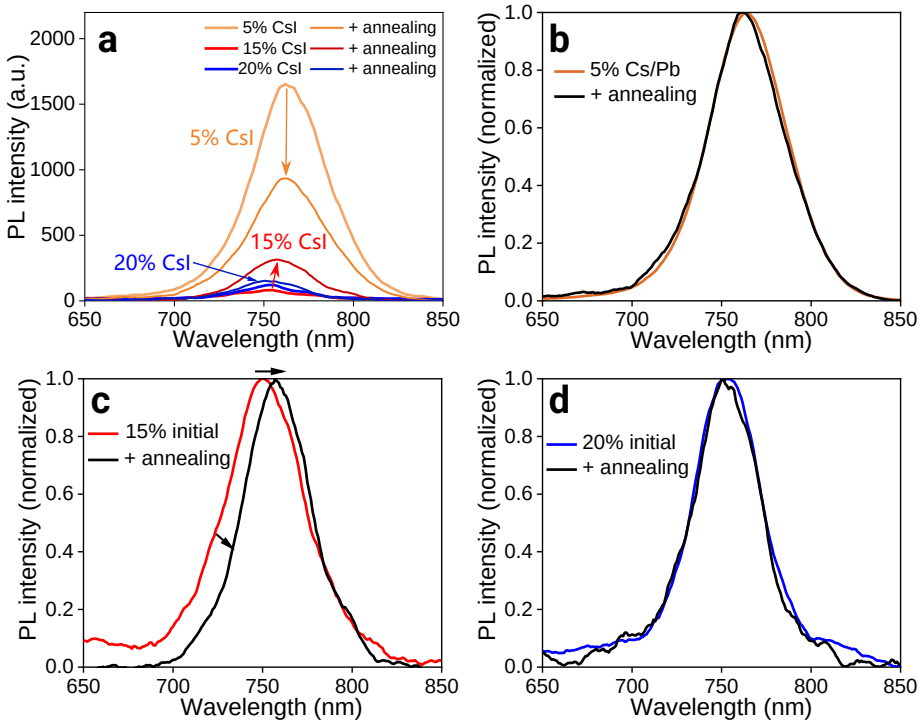

***Figure 11**: **a)** Relative and **b-c-d)** Normalized PL of the slot-die coated layer at CsI content of **b)** 5%, **c)** 15% and **d)** 20% Cs/Pb initially and after 5 minutes at 100 °C.*

IV.1.4. Slot-die coated layers with various Cs/Pb ratios at higher FA/Pb ratio

Introducing more CsI in the precursor ink seems to favour the perovskite cubic structure formation. One could argue that the CsI addition also modified the cation stoichiometry in the perovskite formula (**Table 2**), which could affect the perovskite film properties. To decorrelate both effects, we investigated the impact of varying the CsI content starting at a cation stoichiometry closer to 1 by increasing the FAI content.

We fixed this higher FA/Pb ratio to 89% to reach the cation stoichiometry of the previous 15% Cs/Pb sample (cations ratio of 2.94) at a lower CsI content (5% Cs/Pb here). In echo with the previous study, we studied the 'as-quenched' slot-die coated layers properties first, prior to investigate the effect of the post-annealing step. The corresponding perovskite formulas can be found in the **Table 2**.

Lead concentration (M)	1.2	1.2
PbI_2 excess (%)	6	6
Cs/Pb molar ratio (%)	0, 5, 10, 15, 20	5, 10, 15, 20
FA/Pb molar ratio (%)	79	89
Br: I molar ratio (%)	~12 : 88	~ 12 : 88
DMF :DMSO volume ratio	4 : 1	4 : 1
Calculated perovskite formulas	$Cs_{0.05}FA_{0.79}Pb(I_{0.880}/Br_{0.120})_{2.84}$* $Cs_{0.10}FA_{0.79}Pb(I_{0.882}/Br_{0.117})_{2.89}$ $Cs_{0.15}FA_{0.79}Pb(I_{0.884}/Br_{0.116})_{2.94}$ $Cs_{0.20}FA_{0.79}Pb(I_{0.886}/Br_{0.114})_{2.99}$	$Cs_{0.05}FA_{0.89}Pb(I_{0.884}/Br_{0.116})_{2.94}$ $Cs_{0.10}FA_{0.89}Pb(I_{0.886}/Br_{0.114})_{2.99}$ $Cs_{0.15}FA_{0.89}Pb(I_{0.888}/Br_{0.112})_{3.04}$ $Cs_{0.20}FA_{0.89}Pb(I_{0.890}/Br_{0.110})_{3.09}$

***Table 2**: Composition of the reference precursor ink to form various perovskite formulas. The pivoting halide to lead ratio is indicated in red. * Reference precursor ink (**Chapter III**).*

- **Monitoring of stoichiometry change**

Following the methodology developed earlier, we monitored the Cs/Pb and I/Pb ratios by energy dispersive X-Ray (EDX). The Cs/Pb ratio increased gradually with the CsI content in the precursor ink (**Figure 12**), following the theoretical values with an experimental offset. This result confirmed that the CsI was progressively incorporated in the slot-die coated layers at the higher FA/Pb ratio. Interestingly, a slope increase was noticed in the Cs/Pb ratio at 20% CsI, similarly to the one observed at 15% Cs/Pb with the previous FA/Pb content (79%). Regarding the I/Pb EDX ratio, a noticeable decrease was observed at 15% Cs/Pb. The other points were following the theoretical values with an experimental offset.

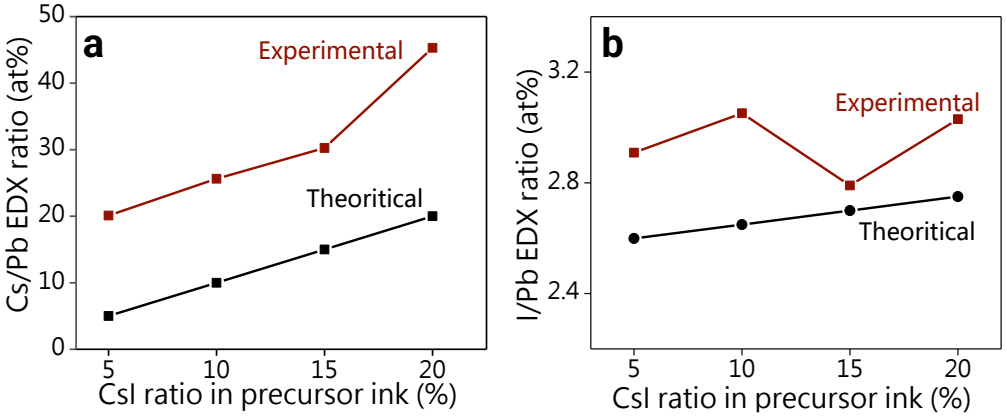

***Figure 12**: Cs/Pb EDX ratio showing the gradual incorporation of CsI in the perovskite layers at higher FA/Pb ratio (89%).*

- **Morphology**

To compare the perovskite layer fabricated from both FA/Pb ratios, we recorded the perovskite films thickness t and average surface roughness R_a (**Figure 13**). We observed a quasi-constant perovskite film thickness t ~ 500 nm from 5 to 15% Cs/Pb, and a significant film thickness increase to t = 650 nm at 20% Cs/Pb (**Figure 13a**). The slight perovskite film increase from 450 nm to 500 nm (5 - 10 -15% Cs/Pb) between the initial (79%) and the higher (89%) FA/Pb ratio could be explained by a batch-to-batch standard deviation of the wet film thickness in slot-die coating process. However, the film thickness increase observed at 20% Cs/Pb for both FA/Pb contents confirmed the particularity of the 20% Cs/Pb sample, independently of the FA/Pb ratio.

Regarding the average surface roughness (R_a), we observed a gradual decrease from 5 to 15% Cs/Pb, similarly to what was observed for the initial FA/Pb ratio (**Figure 13b**). We concluded that the Cs/Pb addition had smothering effects on the film surface in this range. To generalize, this smothering effect was observed for a stoichiometry with a theoretical cation to lead ratio (CsI+FAI /Pb) lower than 1.04.

Beyond this value (20% Cs/Pb sample with higher FA/Pb ratio), the surface roughness was hard to measure due to an irregular surface morphology. A profilometry mapping of the 20% Cs/Pb film unveiled the presence of an alveoli structure (**Figure 13d**) compared to the sample at 15% Cs/Pb (**Figure 13c**). A similar morphology has been described in the literature as a result of film wrinkling [230,241,242]. The wrinkling effect is due to compressive strains inside the wet film during crystallization. Those strains have been observed for specific perovskite stoichiometry, solvent mixtures, and process conditions (wet film thickness and temperature notably). Here, we observed this effect for a theoretical cation to lead ratio of 1.09.

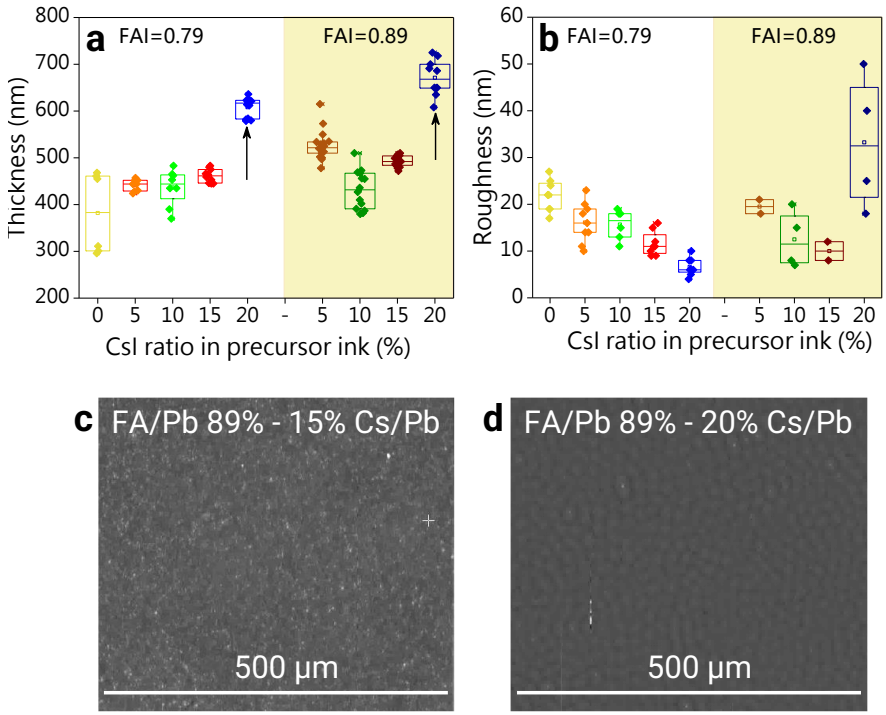

***Figure 13**: **a)** Thickness and **b)** Roughness of slot-die coated layers from 5, 10, 15, 20% Cs/Pb with higher FA content. Profilometry mappings of the perovskite layers at **c)** 15% and **d)** 20% Cs/Pb sample (FA/Pb = 89%).*

To assess whether the perovskite grain size was modified at this higher FA/Pb ratios, we recorded the SEM images (**Figure 14**) of the slot-die coated layers. We found that the 10% Cs/Pb (FA/Pb = 89%) had similar average grain size (g ~ 215 nm) compared to the previous batch 5% Cs/Pb (FA/Pb 79%). With this higher FAI content (89% FA/Pb), the 5% Cs/Pb sample exhibited larger grains size of g = 250 nm, while the 15% and 20% Cs/Pb exhibited smaller grain size (g= 180 and 160 nm respectively). We noted that those grains were still smaller than the spin-coated layer grains (g = 350 nm).

As large grains are desirable to achieve high device performance, the 5% Cs/Pb sample with 89% FA/Pb ratio may appear as a promising candidate for device integration. However, we could wonder if the grain size increase did happen at the cost of the perovskite material quality in respect to the δ-$FAPbI_3$ formation. The next paragraph reports the crystalline properties of those layers.

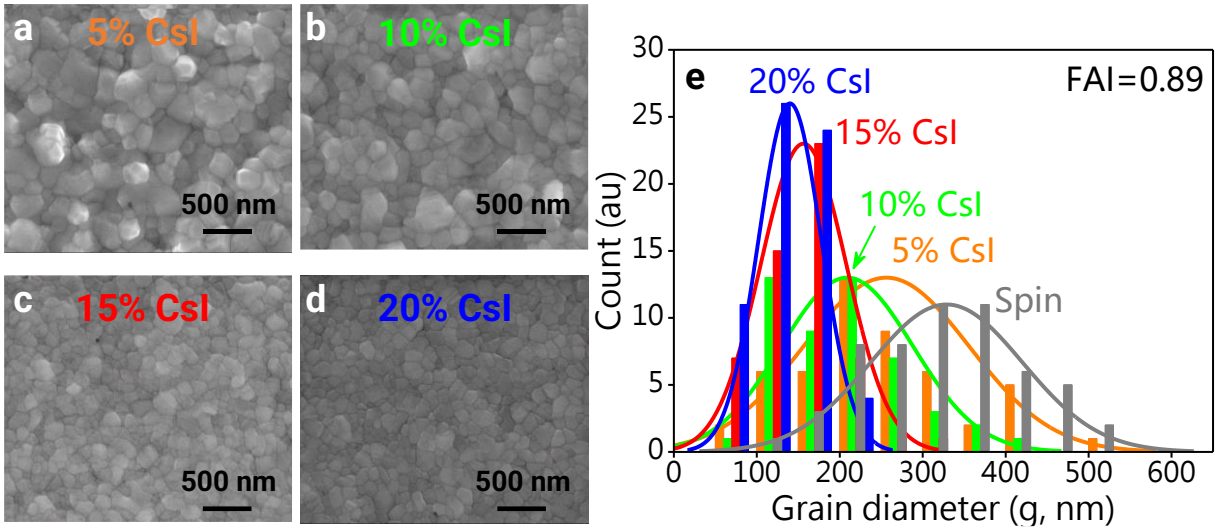

***Figure 14**: **a-d)** SEM top images of slot-die coated layers from 5, 10, 15, 20% Cs/Pb with higher FA/Pb content (89%). **e)** Corresponding grain distributions.*

- **Crystallinity of the perovskite layers**

As previously done, XRD was used to monitor the phase formation and the XRD peak area ratios extracted for the four CsI contents (5, 10, 15 and 20%) at the higher FA/Pb ratio (89%) (**Figure 15b**). We provided in **Figure 15a** the graph obtained at the initial FA/Pb (79%) ratio for direct comparison. As observed previously, the higher the CsI content in the precursor ink, the lower the δ-$FAPbI_3$ XRD peak area ratio in the films at this higher FA/Pb ratio (**Figure 15b**), confirming the predominant role of CsI precursor over the cation stoichiometry to impede the δ-$FAPbI_3$ phase formation in the gas-quenching process. Interestingly, the 5% Cs/Pb sample exhibited reduced PbI_2 and δ-$FAPbI_3$ proportions at 89% FA/Pb, suggesting that the grain size increase was not detrimental to the film crystallinity (**Figure 15b**).

Despite the enhanced perovskite conversion at 5% Cs/Pb, the CsI addition at the higher FA/Pb content was less efficient to supress the δ-$FAPbI_3$ formation, which was still visible in the 10%, 15% and 20% Cs/Pb films in the FAI-rich films (**Figure 15b**). This study shows that the CsI efficiency to impede the δ-$FAPbI_3$ formation depends on the FAI content, unveiling a synergetic effect of both cations during the perovskite crystallization. It also suggests that a FAI rich environment does not favour the selective cubic structure formation. Moreover, larger proportions of crystalline PbI_2 were observed in the FAI-rich films. We concluded that the initial FA/Pb ratio of 79% was preferable to limit the by-products formation.

Regarding the perovskite grains orientation, we observed larger proportion of the (011)-oriented grains in the 20% Cs/Pb sample at higher FA/Pb content (**Figure 15b**), in line with the previous experiment. Interestingly, the (011)-oriented perovskite grains seemed to depend on the CsI content predominantly, whereas the (001)-oriented perovskite grains depended on both CsI and FAI contents. These results suggested that the formation mechanism of the (011)-oriented grains could rely on a minimum CsI concentration in the precursor solution, while the

(001)-oriented grains depend on the respective CsI and FAI proportions during the crystallization.

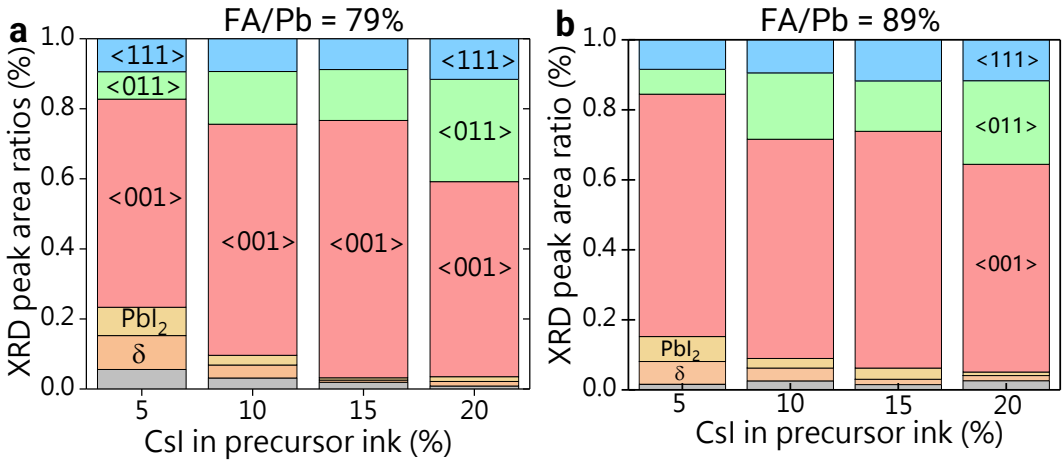

***Figure 15**: Improvement of the perovskite cubic structure formation with the increased Cs/Pb ratio for both FAI ratios: **a)** FA/Pb = 79% (copy from previous experiment) **b)** FA/Pb = 89%.*

- **Optical properties**

Regarding the optical properties, the CsI incorporation at higher FA/Pb ratio led to a similar increase of the surface reflection compared to the previous experiment at lower FAI content (**Figure 16a**). The reflection value achieved at 15% Cs/Pb (~ 20%) was similar to the one obtained at 15% Cs/Pb in the previous study, suggesting that the phenomenon behind the higher surface reflection depended mainly on the CsI content. As expected, the absorption onset increased gradually for the films with 5%, 10% and 15% Cs/Pb, in line with the enhanced conversion of the perovskite material (**Figure 16b**). It further increases at 20% Cs/Pb, possibly due to the larger film thickness (**Figure 16b**). The 5 and 20% Cs/Pb samples exhibited a slight band gap shift (~ 0.2 eV) at this higher FA/Pb ratio (89%), which could be related to their deviation to stoichiometry (cations ratio of 0.94 and 1.09, see **Table 2**).

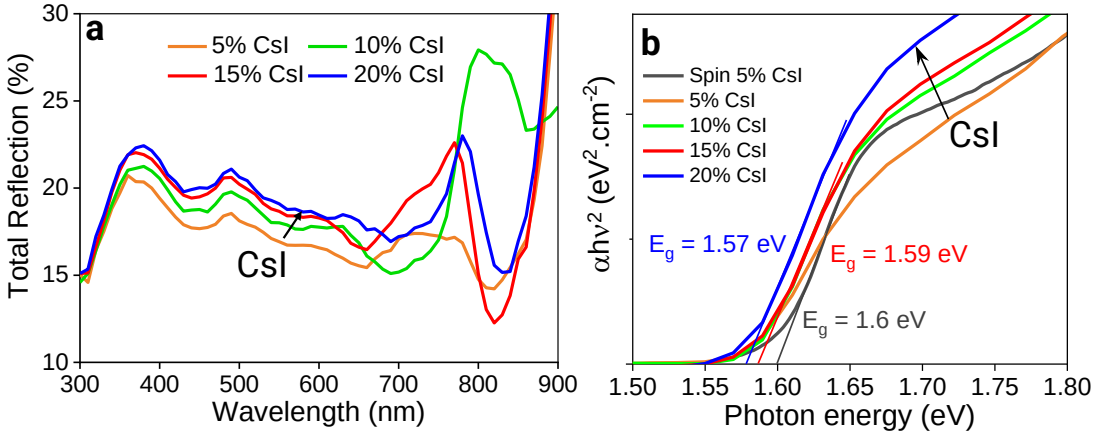

***Figure 16**: Evolution of the film optical properties at FA/Pb = 89% for various CsI contents. **a)** Total reflection and **b)** Tauc plot graph extracted from the absorbance curves.*

To further study the difference between 5% & 20% Cs/Pb and the rest of the samples, we performed photoluminescence measurements (**Figure 17**). As mentioned earlier, we interpreted the PL intensity trend by the presence of α/δ junctions in the perovskite film, responsible for a PL emission at ~ 780 nm [234]. The PL intensity at 5% Cs/Pb was significantly lower at higher FAI content compared to the previous study (**Figure 17a**), unveiling a smaller quantity of α/δ junctions in the material, which corroborates with the decrease of δ-$FAPbI_3$ proportions in this sample (**Figure 15b**). The minimum PL intensity was reached at 15% Cs/Pb, similarly to the previous study, highlighting that the CsI content determines the sample with minimal δ-$FAPbI_3$ formation at a fixed FAI content.

Contrarily to the previous experience, the 20% Cs/Pb ratio led to the highest PL intensity which cannot be solely explained by the modest δ-$FAPbI_3$ proportions detected by XRD or by the slightly higher absorption in this sample (**Figure 16b**). We rather attributed the higher PL intensity to the different morphology (presence of alveoli) of this sample which could have affected the characteristics of the α/δ junctions. Further material characterisation is needed to conclude on the PL mechanism.

Upon CsI addition, we observed a gradual blue shift of the PL emission wavelength from 5% Cs/Pb to 15% Cs/Pb with reduced amplitude compared to the previous experiment (**Figure 17c**). This result suggests that the effect of the CsI precursor on the lattice strain is limited at larger FAI content. Overall, the PL emission wavelengths of slot-die coated films at higher FAI ratio (89%) were higher (red-shifted) compared to the reference spin-coated reference (79% FA/Pb – 5% Cs), indicating an overall reduced lattice strain in the FAI-rich environment (**Figure 17 b-c**). At the 20% Cs/Pb, the emission wavelength shifted back to the PL emission wavelength of the 5% Cs/Pb sample, in line with the slight band gap variation observed in these samples (**Figure 16b**).

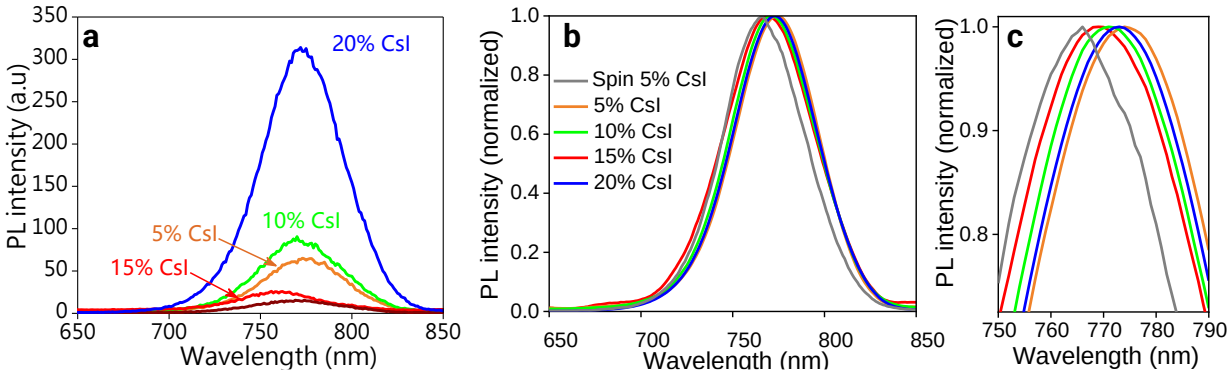

***Figure 17**: Photoluminescence evolution for different CsI ratios. **a)** Photoluminescence intensity and **b)** Normalized PL intensity of slot-die coated layers fabricated at FA/Pb=89% for various CsI contents. **c)** Zoom of plot b to visualize the shift in emission wavelength.*

In summary, the effect of the CsI content on the perovskite phase conversion, perovskite film surface properties and morphology was observed for both FAI contents, highlighting its major role during the perovskite crystallization. However, the CsI "conversion power" can be reduced in FAI rich environments, suggesting a synergetic effect of FAI and CsI precursors to achieve δ-$FAPbI_3$-free perovskite in the slot-die coating process. We concluded that the cation stoichiometry is not a sufficient condition to permit the perovskite conversion, which relies rather on the combination of the Cs/Pb and FA/Pb ratios.

IV.1.5. Influence of annealing on the perovskite film properties

- **Impact on morphology**

To complete the above study of the "as-quenched" films, we performed the post-annealing step (5 min at 100°C) on the slot-die coated layers. On the SEM images (**Figure 18**), we did not see any grain size modification for 5 and 15% Cs/Pb samples upon annealing, similarly to the lower FA/Pb ratio. However, at 20% Cs/Pb, we observed an average grain size increase from 150 to 200 nm. This increase in grain size upon annealing could be due to Ostwald ripening phenomenon that has been reported for perovskite layers, generally happening during post growth treatment such as MABr or solvent vapours exposure [243,244]. Here, the change in grain size observed in the 20% Cs/Pb sample could be attributed to its largest cations ratio of 1.09 in respect to lead, which could have provided excess FAI precursor to induce the Ostwald ripening process. As the 15% Cs/Pb sample was also overstoichiometric and did not undergo the grain increase, further experiments are needed to confirm whether there would be a link between over-stoichiometry and grain size increase.

Upon annealing, we noticed the formation of white particle's only in the 5% Cs/Pb sample, possibly due to its cation under stoichiometry (cations ratio of 0.94). Interestingly, no white particles were visible upon annealing in the 15 and 20% Cs/Pb samples, where the cation were introduced in overstoichiometric proportions (cations ratio of 1.04 and 1.09). This trend confirmed that the lack of white particles previously observed at 20% Cs/Pb (FA/Pb = 79%) was not a consequence of the perovskite morphology but rather of the perovskite stoichiometry. Furthermore, this observation reinforced the hypothesis that crystalline PbI_2 originated from a precursor excess "reservoir" at under stoichiometric compositions that was able to crystallize during the post-annealing step.

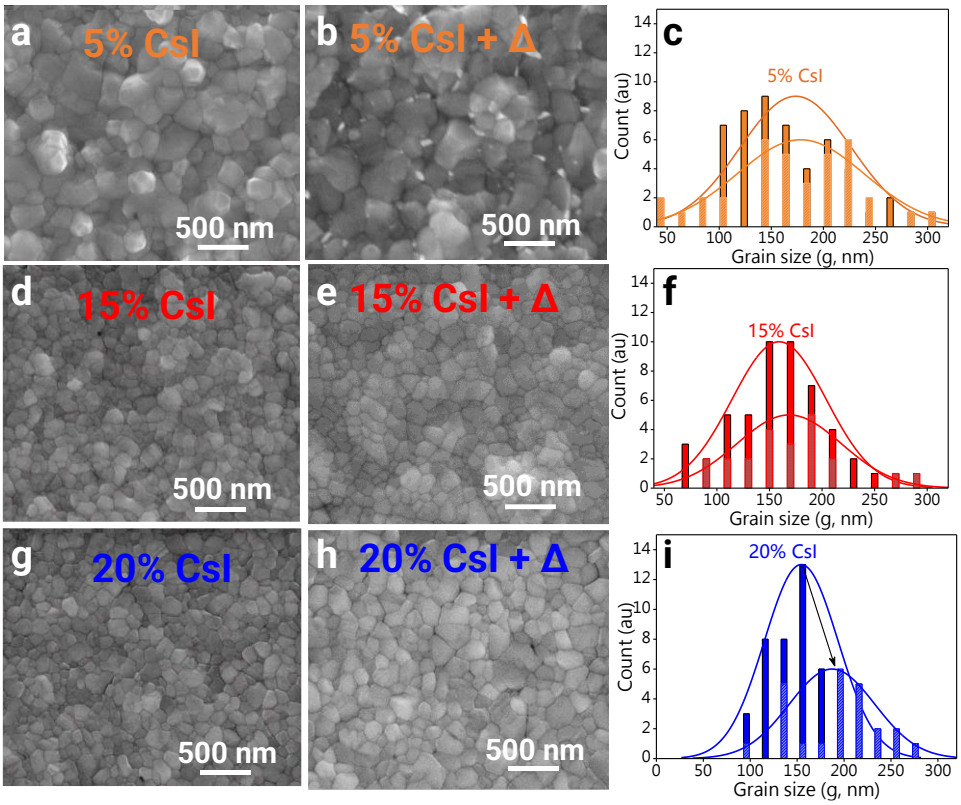

***Figure 18**: SEM top images of slot-die coated layers from before and after 5 min annealing at 100 °C with **a-b)** 5%, **d-e)** 15% and **g-f)** 20% Cs/Pb (FAI content is 89%). **c-f-i)** Corresponding grain distributions extracted from the images.*

- **Monitoring of the phase formation**

The XRD measurements confirmed that no crystalline PbI_2 was formed upon annealing in the 15 and 20% Cs/Pb samples (**Figure 19b**), in line with the absence of white particles formation in the SEM images. However, another by-product formed upon annealing in the 5 and 15% Cs/Pb samples: δ-$FAPbI_3$. We could draw an analogy between the δ-$FAPbI_3$ formation and the crystalline PbI_2 formation observed earlier (**Figure 19a**). Indeed, the δ-$FAPbI_3$ formation could result from the crystallization of a reservoir of '2H' polytype (or δ-$FAPbI_3$) present in the "as-quenched" film. The FAI rich environment in the latter could explain the difference between the species formed in the "reservoir" (PbI_2 and '2H' polytype).

Interestingly, δ-$FAPbI_3$ did not form in the 20% Cs/Pb film after 5 minutes of annealing at 100 °C. As suggested by the SEM images, this sample underwent a grain-coarsening phenomenon. In the XRD peak area ratios (**Figure 19b**), we observed that the ratio of (001)-oriented perovskite grains increased after annealing. We concluded that the large cation excess (cations ratio of 1.09) in the 20% Cs/Pb enabled the formation of α-CsFAPbIBr from the unreacted reservoir, hence the grain coarsening observed by SEM. We could anticipate that after a certain time, all cations would be consumed, and secondary by-products could appear

(δ-$FAPbI_3$ and crystalline PbI_2). This observation was interesting as it provided a second strategy to enhance the grain size, which is desirable to increase the device performance.

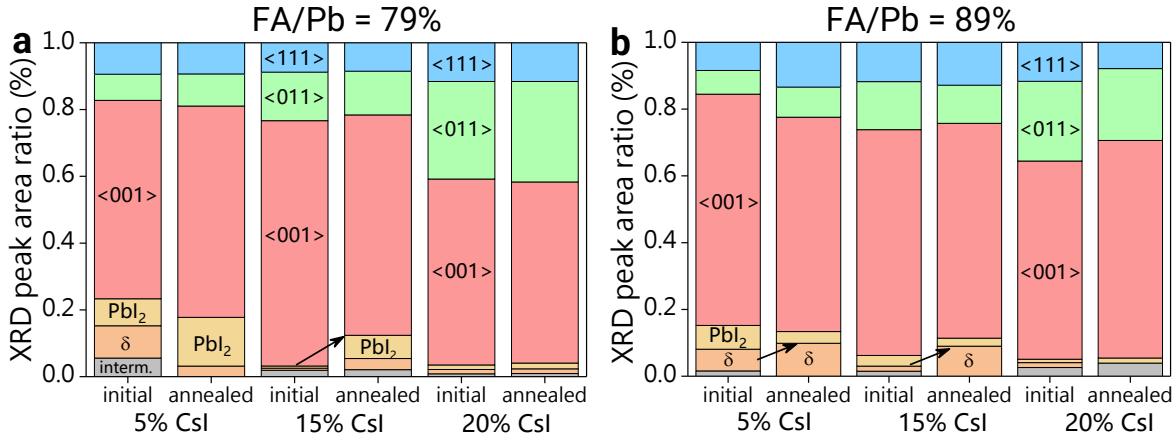

***Figure 19**: XRD ratios of slot-die coated layers from 5, 15 and 20% Cs/Pb before and after 5 min annealing at 100 °C for FA/Pb ratios of **a)** 79% (previous study) and **b)** 89% (higher FA/Pb ratio).*

- **Impact on photoluminescence**

As δ-$FAPbI_3$ was formed in the annealed slot-die coated layers (**Figure 19b**), we expected a photoluminescence increase due to the increase of α-δ junctions in the material. However, the trend in the photoluminescence peak intensity was the opposite. It increased for the 20% Cs/Pb sample, in which no δ-$FAPbI_3$ was formed upon annealing and decreased for both 5 and 15% Cs/Pb sample where δ-$FAPbI_3$ was formed upon annealing (**Figure 20a**). This suggests that the δ-$FAPbI_3$ formed upon annealing may not grow in contact with the cubic α-CsFAPbIBr, hence would not be able to form α-δ junctions. Further characterization (TEM) is needed to identify the location of δ-$FAPbI_3$ in the annealed films and confirm this hypothesis.

The PL emission wavelength behaviour upon annealing was similar as the previous experiment: the PL peaks were not modified at 5 and 20% Cs/Pb, whereas the 15% Cs/Pb peak exhibited a strong narrowing upon annealing observations (**Figure 20b**), conferring the main role to CsI over FAI or the cations stoichiometry in the level of radiative recombination. We concluded that post-annealing seemed interesting for the 15% Cs/Pb sample (narrowing of the PL peak) but not particularly for 5 and 20% Cs/Pb samples. Furthermore, at both FA/Pb ratios, the 15% Cs/Pb sample exhibited a narrower PL peak, indicating of a less defective material.

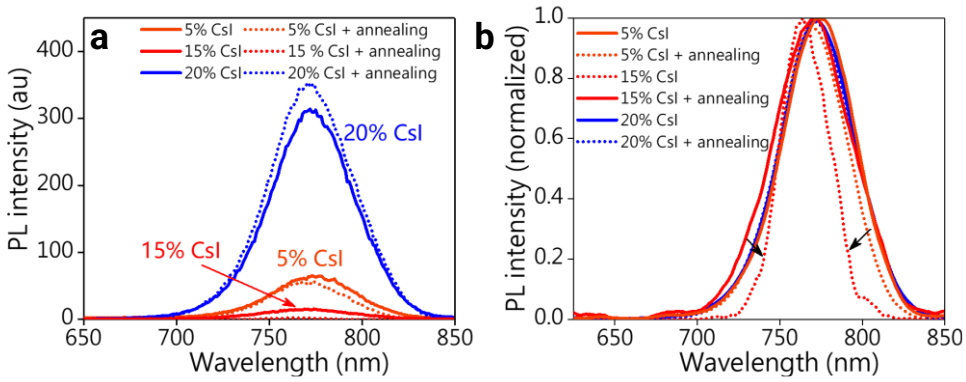

***Figure 20**: **a)** Relative and **b)** Normalized PL of the slot-die coated layers fabricated at Cs/Pb ratios of 5, 15 and 20% initially and after annealing (5 minutes at 100 °C).*

In summary, after the screening of two FAI and four CsI contents in the precursor ink, we excluded the slot-die coated layers containing δ-$FAPbI_3$ initially (1), (2) or upon annealing (5), (6), (7). Three slot-die coated layers of interest (3), (4), (8) were identified **(Table 3)**. For the first device implementation, we focused on the layer (3), where no film morphology disruptions were reported compared to the layers (4) and (8), fabricated at 20% Cs/Pb. We used the precursor ink containing 15% Cs/Pb and 79% FA/Pb for all future slot-die coated experiments.

	Precursor ink			**Before annealing**		**After annealing**	
Process	**FA/Pb**	**Cs/Pb**	**Cations ratio**	**δ-$FAPbI_3$**	**grain size (nm)**	**By-products**	**grain size (nm)**
Spin	**79%**	**5% (ref)**	**0.84**	**No**	**-**	**-**	**273**
Slot die	79%	**5% (1)**	**0.84**	Yes	**215**	crystalline PbI_2	**215**
		10% (2)	0.89	Yes	95		95
		15% (3)	0.94	No	160		160
		20% (4)	0.99	Limited	155	No	155
	89%	5% (5)	0.94	Yes	250	δ-$FAPbI_3$	250
		10% (6)	0.99	Yes	215		-
		15% (7)	1.04	Limited	160		160
		20% (8)	1.09	Limited	180	No	200

***Table 3**: Main properties of the slot-die coated layer from various CsI and FAI contents. The layers studied in **Chapter III** are highlighted in bold and provided for comparison.*

IV.2. Device performances at 15% Cs/Pb

In this section, we implemented the newly optimized slot-die coated layer into photovoltaic devices. We used the slot-die coating process parameters optimized earlier (**Chapter III-Table 10**) to perform the coating and the slot-die optimized ink, which composition is reminded in **Table 4**, as precursor ink. A post-annealing treatment of 5 minutes at 100 °C under nitrogen atmosphere was performed on the slot-die coated layers.

We performed the J-V measurements right after device fabrication (day 0), to compare them with the results presented earlier with the 5% Cs/Pb slot-die coated layer (**Chapter III-4.1**). The device fabrication was identical to the one presented in **Chapter III**.

Lead concentration (M)	1.2
PbI_2 excess (%)	6
Cs/Pb molar ratio (%)	15
FA/Pb molar ratio (%)	79
Br: I molar ratio (%)	12 : 88
DMF: DMSO volume ratio	4 : 1
Perovskite formula	$Cs_{0.15}FA_{0.79}Pb(I_{0.884}/Br_{0.116})_{2.94}$

***Table 4**: Composition of the slot-die optimized precursor ink, corresponding to layer (3) in Table 3.*

IV.2.1. Slot-die coated devices fabricated at 15% Cs/Pb

As seen in the material study, the 15% Cs/Pb precursor ink led to a well-crystallized slot-die coated perovskite under the cubic structure (no δ-$FAPbI_3$) and to a higher absorption onset. When implemented into devices, the CsI-rich perovskite layers (15% Cs/Pb) achieved higher current densities than the slot-die coated devices fabricated with the initial ink (5% Cs/Pb) (**Figure 21b**). The current density increased from 20.3 to 22.2 $mA.cm^{-2}$ in average, closing the gap towards the simulated current density curve (**Figure 21a**). We concluded that the phase purity of the perovskite material was the main cause of the shift from the model observed earlier for slot-die coated layers (**Chapter III** - **Figure 31**).

Consequently, the champion slot-die coated device yielded a power conversion efficiency (PCE) of 15.0%, open-circuit voltage (V_{oc}) of 1.003 V, current density (J_{sc}) of 21.5 $mA.cm^{-2}$ and fill factor (FF) of 69.5%. In addition, the FF was improved (+ 6 points for champion devices) by modification of the Cs/Pb ratio, which can be attributed to lower recombination in the perovskite layer thanks to its higher crystalline purity. The device performance distribution is presented in **Figure 21c-d** and the detailed device parameters are provided in **Appendix 2**.

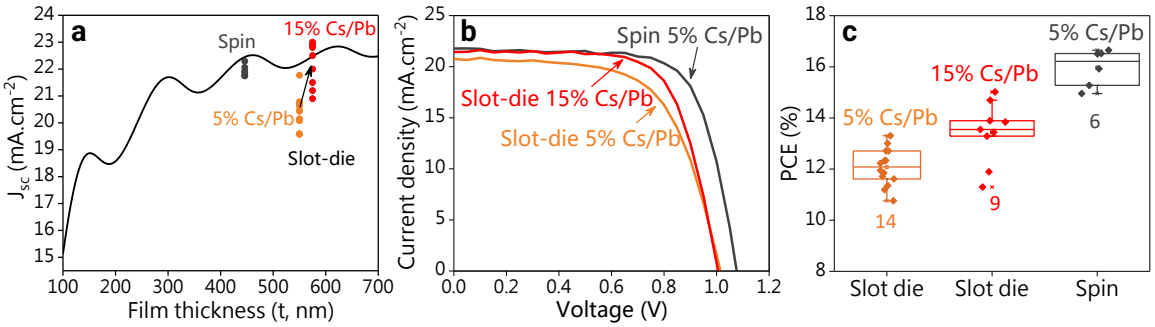

d

	V_{oc} (V)	J_{sc} (mA.cm^{-2})	FF (%)	PCE (%)
Spin (ref)	1.075 ± 0.024 *1.075*	21.5 ± 0.4 *21.7*	69.0 ± 5.5 *71.3*	15.9 ± 3.0 *16.7*
Slot-die 5% Cs/Pb	0.995 ± 0.115 *1.013*	20.3 ± 1.4 *20.7*	59.5 ± 4.7 *63.4*	12.1 ± 1.4 *13.3*
Slot-die 15% Cs/Pb	0.957 ± 0.065 *1.003*	22.2 ± 1.2 *21.5*	63.3 ± 7.5 *69.5*	13.4 ± 2.1 *15.0*

***Figure 21**: **a)** Current densities of experimental devices in respect to the theoretical line representing the optical simulation. **b)** J-V curves of the best device per batch (measured at do). **c)** Statistics of power conversion efficiencies. **d)** Summary of J-V parameters for the three conditions. The parameters of the champion devices plotted on panel b are in italic.*

Despite their higher average current density (22.2 mA.cm^{-2} compared to 21.5 mA.cm^{-2}), the 15% Cs/Pb slot-die coated devices exhibited a lower average PCE (13.4%) than their spin-coated counterpart did (15.9%). While champion devices did not suffer from large FF drop, average devices performance was still limited by the fill factor (FF). More generally, limitations of the open-circuit voltage (V_{oc}) of - 70 mV for the champion device at 15% Cs/Pb samples and - 80 mV for the champion device at 5% Cs/Pb were observed in devices with slot-die coated layers compared to the spin-coated reference ones (**Figure 21b-d**). A lower open-circuit voltage (V_{oc}) could originate from a different energy alignment or to enhanced non-radiative interfacial recombination [245,246]. As the band gaps of spin-coated and slot-die coated perovskite layers were comparable, we suggest that interfacial recombination losses could be responsible for the V_{oc} loss observed.

To assess the device interfaces, we recorded the SEM cross-section of the slot-die champion device at 15% Cs/Pb (**Figure 22**). The physical contact between the perovskite layer and the interface layers was continuous and we did not detect any particular defects. We concluded that the V_{oc} loss observed did not result from a physical cause (dewetting or presence of interfacial particles). Furthermore, as the V_{oc} deficit was not correlated with a higher crystalline PbI_2 presence, we concluded that crystalline PbI_2 presence was not the main factor behind the limited slot-die coated device performances at this stage. Therefore, we suggest that these recombination losses could be due to intrinsic properties of the slot-die coated layers such as the surface or grain boundaries properties. In the literature, the presence of surface defects such as iodide ion vacancies [25] has been found to limit the V_{oc} of perovskite solar cells [247,248].

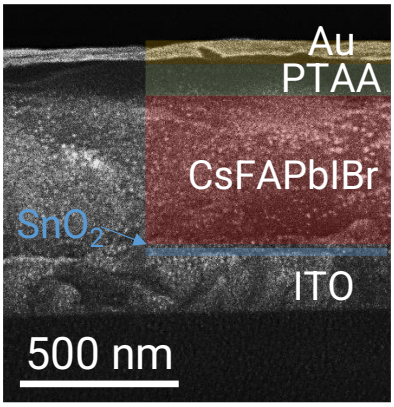

***Figure 22**: Slot-die coated device SEM cross-section. (1.2 M, 15% Cs/Pb - 79% FA/Pb)*

Before designing mitigation strategies, we investigated the effect of the 15% Cs/Pb precursor ink on spin-coated solar cells performances to determine whether these limitations are mainly linked to this precursor ink composition or if they vary with the crystallization mechanism employed.

IV.2.2. Spin-coated devices fabricated at 15% Cs/Pb

In this section, we deposited perovskite layers from both 5 and 15% Cs/Pb precursor inks *via* the reference spin-coating reference process presented in **Chapter III**. The detailed device parameters are provided in **Appendix 3**.

When spin-coated layers were implemented into PV devices, we observed a decrease of the power conversion efficiency from 17.1% to 14.5% when the Cs/Pb ratio increased from 5% to 15% (**Figure 23a**). This decrease in performance was due to a significant reduction of V_{oc} (- 82 mV in average) and FF (- 7 points) (**Figure 23b-d**). We concluded that a similar limiting phenomenon was observed when spin-coated layers fabricated from high CsI content precursor solutions were implemented into PV devices. This phenomenon was thus not specific to the gas-assisted crystallization used in the slot-die coating process but related to the precursor ink composition, more specifically to the 15% Cs/Pb ratio.

As mentioned earlier, iodide vacancies can induce recombination losses and limit the performance of perovskite solar cells. For the slot-die coated layer with 15 Cs/Pb, we monitored the iodide content in the perovskite film prior and after annealing and observed a severe iodide loss (**Appendix 4**), corroborating that the slot-die coated perovskite film could have become chemically defective due to the loss of iodide ions, either by evaporation or by diffusion to form crystalline PbI_2. Interestingly, this iodide loss was not observed at 20% Cs/Pb (**Appendix 4**). As a perspective, the device integration of the layer (4) (**Table 3**) could inform on the link between the iodide loss and device performance (open-circuit loss). To reduce the iodide ion vacancies in the 15% Cs/Pb sample, passivating post treatment steps [24,249,250] have been proven successful in the literature to mitigate the iodide loss.

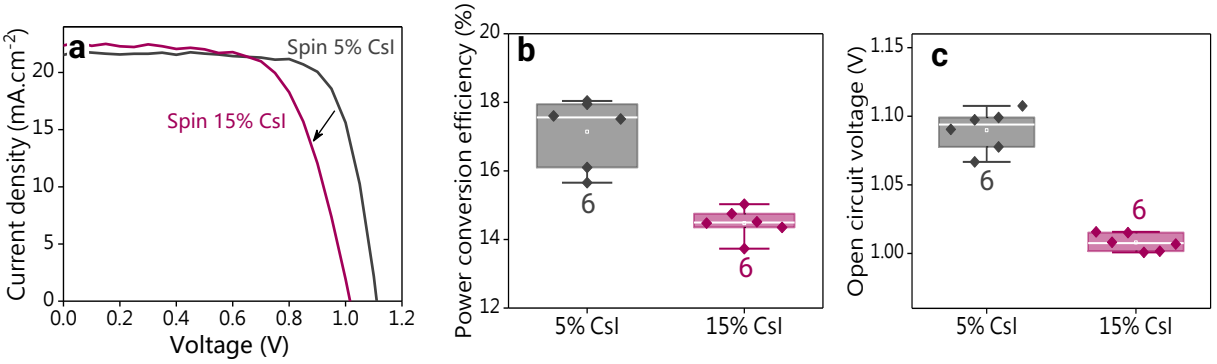

d	V_{oc} (V)	J_{sc} (mA.cm^{-2})	FF (%)	PCE (%)
Spin (ref ,d1)	1.090 ± 0.023	21.9 ± 0.4	71.7 ± 5.1	17.1 ± 1.5
Spin 15% CsI (d1)	1.008 ± 0.008	21.9 ± 0.4	65 ± 2.4	14.5 ± 0.7

***Figure 23**: Impact of CsI content on other performance parameters **a)** J-V curves of the champion devices for each condition, **b)** Power conversion efficiency and **c)** Open-circuit voltage statistics over 6 devices for each condition.*

IV.3. Removing the DMF from the precursor ink

The DMF solvent being less compatible with industrial printing, due to its higher toxicity compared to DMSO, solvent substitution strategies have been developed in the literature to reduce the ratio of DMF in the perovskite precursor inks [76,112,115,251].

Here, we investigate whether a full DMSO precursor ink could lead to the formation of perovskite layers with suitable properties for integration into photovoltaic devices. We used the same precursor stoichiometry as the slot-die optimized ink (**Table 5**) and studied the 4:1, 2:1, 1:1 and 0:1 DMF:DMSO volume ratios, aiming to gradually phase out the DMF solvent from the precursor solution.

Lead concentration (M)	1.2
PbI_2 excess (%)	6
Cs/Pb molar ratio (%)	15
FA/Pb molar ratio (%)	79
Br: I molar ratio (%)	12 : 88
DMF :DMSO volume ratio	4:1, 2:1, 1:1, 0:1 (full DMSO)
Perovskite formula	$Cs_{0.15}FA_{0.79}Pb(I_{0.884}/Br_{0.116})_{2.94}$

***Table 5**: Composition of the precursor inks studied in this section.*

We used the optimized precursor ink with Cs/Pb = 15% and the optimized slot-die coating process parameters. The detailed parameters are reminded in **Chapter III- Table 10**.

- **Precursor ink variations with DMF:DMSO ratios modification**

Prior to deposit the film via slot-die coating, we studied the variation of the ink properties containing various DMF:DMSO solvent ratios. We expect the reduction of the DMF fraction in the precursor ink to affect other parameters such as the boiling point, the density and the surface tension of the ink as those parameters vary between DMF and DMSO solvents (**Table 6**). Furthermore, as we attempt to phase out of the DMF which was the majority solvent (80% of the solvent volume) in the precursor ink, we could expect this strong modification to affect the precursors solubility or organization in solution [252].

	DMF	**DMSO**
boiling point (°C)	153	189
vapour pressure (hPa, at 20°C)	3.5	0.6
density ($g.mL^{-1}$)	0.944	1.1
surface tension ($mN.m^{-1}$)	37	43

***Table 6**: Properties of the DMF and DMSO solvents.*

As expected, gradually reducing the DMF fraction in the precursor ink had an impact on the surface tension of the precursor ink (**Figure 24a**). The precursor ink surface tension increased from 44.5 $mN.m^{-1}$ (4:1 volume ratio) to 50.1 $mN.m^{-1}$ for the 'full DMSO' ink, in accordance with the solvents relative surface tensions (**Table 6**).

Both inks were situated within the substrate wettability envelop (**Figure 24b**), indicating a full wettability on the ITO/SnO_2 substrate. The 'full DMSO' ink has an increased polar component of the surface tension, in line with the larger polarity of DMSO solvent compared to DMF. By gradually decreasing the DMF fraction in the precursor ink, the DMSO solvent was able to solubilize the PbI_2 precursor for the perovskite precursors concentration used (1.2 M).

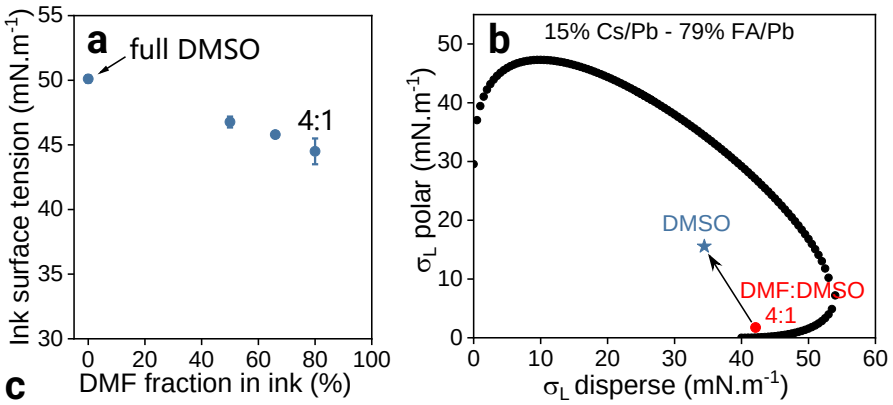

c

DMF fraction (%)	Angle on PTFE (°)	Surface tension ($mN.m^{-1}$)	polar composant ($mN.m^{-1}$)	disperse composant ($mN.m^{-1}$)
80 (4:1 ratio)	76	44.5	42.8	1.7
0 (0:1 ratio)	86.2	50.1	34.5	15.6

***Figure 24**: **a)** Ink surface tension for various DMF:DMSO solvent mixtures containing the perovskite precursors (15% Cs/Pb – 79% FA/Pb). **b)** Wettability envelope of the ITO/SnO_2 substrate with position of the reference DMF:DMSO ink (4:1 volume ratio) and of a full DMSO precursor ink. **c)** Summary of the position of the two inks on the wettability envelope.*

- **Slot-die coated layer from full DMSO precursor ink**

In this section, we used the 'full DMSO' precursor ink to deposit perovskite films via slot-die coating. We included a post-annealing step of 5 min at 100 °C. The process parameters are the one optimized in the **Chapter III** (**Table 10**).

Coating		**Quenching**		**Post-Annealing**	
C_g	100 µm	**Q_g**	3 mm	**A_T**	100 °C
CQ_s	28 $mm.s^{-1}$	**CQ_s**	28 $mm.s^{-1}$		
C_f	100 $\mu L.min^{-1}$	**Q_f**	100 $L.min^{-1}$	**A_t**	5 min
CQ_T	60 °C	**CQ_T**	60 °C		

***III-Table 10:** Optimized process parameters used in slot-die coating process.*

During the quenching step, we observed that the precursor wet film did not start evaporating at the substrate temperature of CQ_T = 60 °C. This observation was explained by the difference in boiling point between DMF (153 °C) and DMSO (189 °C) (**Table 6** above). Besides the boiling point, the solvent vapour pressure was impacted by the solvent modification. The DMSO lower vapour pressure (0.6 hPa compared to 3.5 hPa for DMF) conferred a larger volatility to the 'full DMSO' ink compared to DMF-containing inks.

We could thus expect a different drying behaviour when using the 'full DMSO' ink. The use of the same substrate temperature (CQ_T = 60 °C) on the full DMSO ink with higher boiling point resulted in a lack of wet precursor film evaporation. To solve this issue, we increased the substrate temperature until CQ_T = 80°C, substrate temperature at which the precursor wet film started to evaporate.

The new deposition parameters are summarized in the **Table 7** below.

Coating		Quenching		Post-Annealing	
C_g	100 µm	**Q_g**	3 mm	**A_T**	100 °C
CQ_s	28 mm.s^{-1}	**CQ_s**	28 mm.s^{-1}		
C_f	100 µL.min^{-1}	**Q_f**	100 L.min^{-1}	**A_t**	5 min
CQ_T	80 °C	**CQ_T**	80 °C		

***Table 7**: Optimized process parameters used for the full DMSO ink. The modified parameter is highlighted in green.*

The resulting perovskite layer had a relatively good substrate homogeneity (**Figure 25a**). The thickness of the DMSO only perovskite layer was t = 380 nm, thinner than the 575 nm slot-die coated film obtained from a mixed solvents system (**Figure 25b**). This thickness variation could be explained by the modification of the wet precursor ink properties (density, surface tension) that could affect the wet film coating and resulting precursor wet film thickness.

The optical properties of the 'full DMSO' ink sample were close to the slot-die coated layer fabricated from a DMF:DMSO solvent mixture. The perovskite material exhibited a similar band gap E_g = 1.60 eV (**Figure 25d**). However, the absorbance curve was flatter in the 300-600 nm range (**Figure 25c**), possibly due a light scattering effect [253]. The absorption onset was less pronounced in the full DMSO ink (blue curve in **Figure 25d**), revealing a larger Urbach tail and possibly a more defective layer. Prior to study the layer morphology, we monitored the perovskite conversion by recording the X6Ray diffraction patterns.

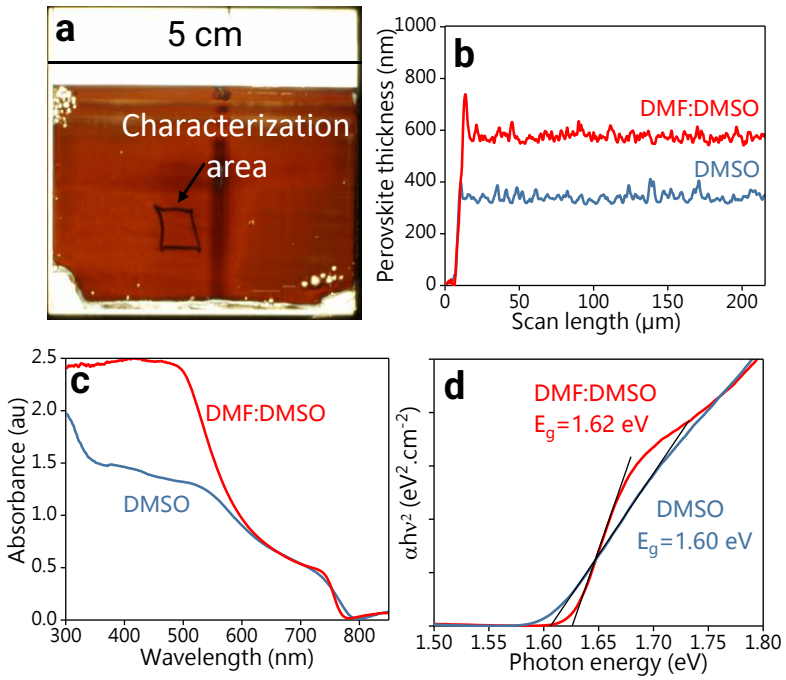

***Figure 25**: **a)** Picture of the slot-die coated layer fabricated from the 'full DMSO' precursor ink. **b)** Profilometry scan, **c)** Absorbance curves and **d)** Corresponding Tauc plot of the slot-die coated layers fabricated from 'full DMSO' and 4:1 solvent mixture containing precursor inks.*

We confirmed the formation of α-CsFAPbIBr material in the slot-die coated sample fabricated from the 'full DMSO' ink by the presence of its signature peaks corresponding to the various orientations ((001), (011) and (111)) (**Figure 26a**). We noted the presence of the δ-$FAPbI_3$ phase (3% XRD peak area ratio) and a lower (001) perovskite XRD peak intensity in the 'full DMSO' sample (**Figure 26b**), suggesting that this layer had a lower crystallinity compared to the one fabricated from the mixed solvents precursor ink.

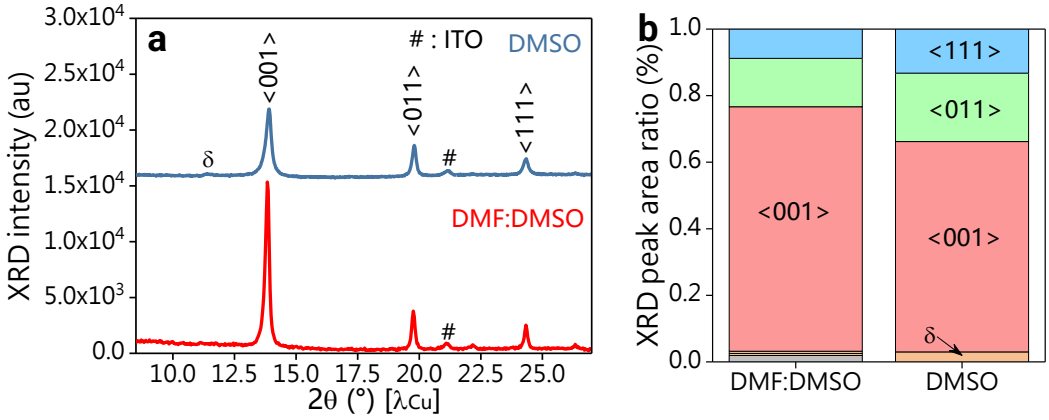

***Figure 26**: **a)** X-ray diffraction patterns from the slot-die coated layers fabricated from DMF:DMSO and full DMSO precursor inks. **b)** Corresponding XRD peak area ratios.*

- **Interfacial limitations with the 'full DMSO' precursor ink**

We observed a flatter absorption curve for the slot-die coated layer fabricated from the 'full DMSO' ink, similar to the light scattering effect observed in poor substrate coverage samples (**Chapter III.2.2-Figure 15**). As the film was compact in this case (see profilometry scan on **Figure 25b**), another material property seemed to influence the light scattering. To further assess the perovskite layer quality, we recorded the SEM cross-section of the 'full DMSO' sample (**Figure 27**).

In the cross-section image (**Figure 27**), we observed the presence of voids at the SnO_2/perovskite interface. This phenomenon has been observed before in the literature and could be attributed to an vertical evaporation gradient forming an imbalance during the quenching of the precursor wet film [90,254,255]. For solvents with higher volatility (DMSO has lower vapour pressure than DMF), the efficient solvent evaporation will contribute to the fast crystallization from the top of the precursor wet film. If this crystallization is too fast, part of the solvent can be trapped underneath the crystallized layer, resulting in the creation of voids upon drying. The interfacial voids presence can induce light scattering effects, hence flatter absorbance curves reported earlier.

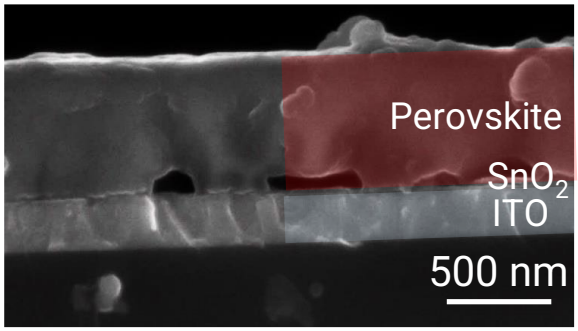

***Figure 27**: SEM cross-section of the slot-die coated perovskite layer deposited on ITO/SnO_2 substrate from the 'full DMSO' precursor ink.*

Conclusion

In this chapter, we investigated the properties of slot-die coated films deposited from precursor inks with various CsI and FAI ratios. More specifically, we increased the CsI content in the precursor ink to supress the formation of the δ-$FAPbI_3$ material in the slot-die coated films, while retaining a similar band gap and morphology. The maximum conversion into the cubic structure was achieved for Cs/Pb = 15%, independently of the FAI content. This value was notably higher than the 5% Cs/Pb needed to convert the CsFAPbIBr into the cubic structure using the spin-coating process and highlights the critical role of CsI precursor in the gas-assisted crystallization.

The perovskite grains of the slot-die coated layers were smaller than the spin-coated reference layers ones for all compositions, reinforcing that the gas-quenching crystallization was limited in terms of grain size (~150-250 nm). Notably, the post-annealing step did not help to increase the grain size but rather resulted in by-product formations: crystalline PbI_2 or δ-$FAPbI_3$, depending on the FAI ratio.

When implemented into photovoltaic devices, the slot-die coated layer with 15% Cs/Pb ratio exhibited an increased current density compared to the slot-die coated layer with 5% Cs/Pb ratio (**Chapter III**), reaching similar current densities as reference devices based on spin-coated perovskite layers. To further close the performance gap with the reference devices, further V_{oc} and FF improvement are needed. These electrical parameters are possibly limited by the intrinsic quality of the perovskite layer (grain boundaries, iodide content) or by the ETL/Perovskite interface quality. The latter will be further studied in **Chapter V**.

Finally, the modification of the precursor ink solvent from DMF:DMSO to full DMSO required additional process optimization due to the different solvent evaporation kinetics, and resulted in the formation of voids at the ETL/Perovskite interface which was not suitable for device integration.

Appendixes

Appendix 1: Formation of Intermediate clusters in the precursor ink.

To study the composition of the intermediate clusters, we decided to apply a combinatory approach. First, each precursor was added in the solvent mixture to determine which one was forming the intermediate cluster with the solvent mixture. The idea was to build up a library of interactions from which we can progressively add the other precursors to sort out their interactions.

Figure A1-1 presents the XRD patterns of the precursors in the DMF:DMSO solvent mixture. We observed that some precursors (FAI and $PbBr_2$) did not form any crystalline product. We see that FAI did not dissolve very well in the mixture and did not exhibit other crystalline peaks than the ones corresponding to FAI. Solely the PbI_2 XRD pattern was showing a low angle intermediate cluster (2θ = 9-10°), in addition to the PbI_2 peaks. This signature has been attributed to the PbI_2:DMSO complex in the literature [256]. We propose that the CsI and FAI compounds were dissociated in solution (when soluble) under the Cs^+, FA^+ and I^- ions form. Regarding the $PbBr_2$, the binding energy to form polytypes being smaller than in PbI_2, it was also dissociated into Pb^{2+} and 2 Br^- ions.

As a result, the first precursor to form an intermediate was PbI_2. To confirm that PbI_2 was principally binding with DMSO solvent in the system, we repeated the PbI_2 sample and removed the DMF. We observed the intermediate signature peaks at 2θ = 9 - 10° (**Figure A1-1b**), validating the PbI_2:DMSO cluster hypothesis. To go further, we added the other precursors to the PbI_2 (DMF:DMSO) cluster (**Figure A1-1b**). The XRD patterns resulting from $PbBr_2$ addition (in green on **Figure A1-1**) showed a slight shift in the peaks position, sign of the incorporation of the smaller Br^- anion into the [PbI_6^{4-}] polytypes.

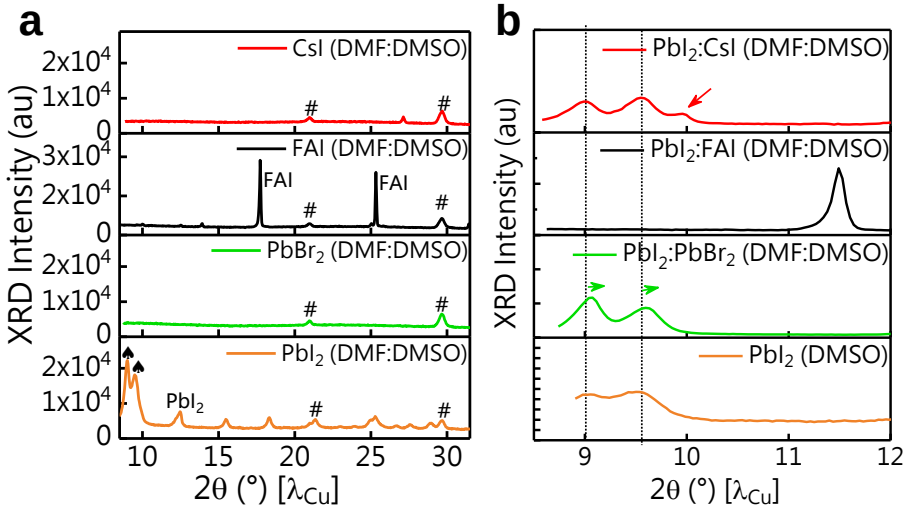

***Figure A1-1**: **a)** X-Ray diffraction of semi-wet films containing the precursors in the DMF:DMSO solvent mixture. **b)** X-Ray diffraction of semi wet films containing PbI_2 to study its interactions with DMSO and other precursors.*

When FAI was added to the PbI_2 (DMF:DMSO) mixture, we observed the formation of the δ-$FAPbI_3$ perovskite at 2θ = 11.4° (in black on **Figure A1-1**). Finally, when we added CsI to the PbI_2 (DMF:DMSO) cluster, we observed the presence of an additional peak at low angles, at 2θ = 10°, corresponding to the incorporation of CsI in the cluster. We noticed that the presence of this third peak was difficult to detect and disappeared when longer acquisition times were used, possibly indicating that the CsI intermediate cluster is thermodynamically less stable than the PbI2:DMSO intermediate.

Based on the observations, we proposed the following mechanism of the role of the various precursors in solution (**Figure A1-2**).

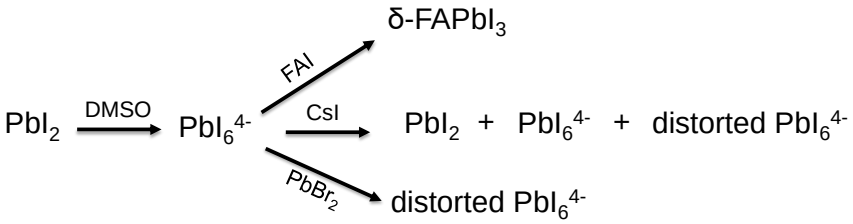

***Figure A1-2**: Proposition of mechanism for precursor organization in solution.*

Appendix 2: Device performance summary.

- Spin-coating- Reference- measured at day 0

	V_{oc} (mV)	J_{sc} (mA.cm^{-2})	FF (%)	PCE (%)
1	1.071	21.9	70.4	16.5
2	1.052	21.3	70.9	15.9
3	1.078	21.5	71.1	16.5
4	1.099	21.4	63.5	15.0
5	1.073	21.3	66.7	15.3
6	1.076	21.7	71.3	16.7
	1.075 ± 0.024	**21.5 ± 0.4**	**69.0 ± 5.5**	**15.9 ± 3**

- Slot-die coating- 5% CsI- measured at day 0

1	1.000	20.7	54.8	11.4
2	1.022	20.7	60.0	12.7
3	0.997	20.5	58.1	11.9
4	1.017	20.4	59.3	12.3
5	0.979	19.6	61.1	11.7
6	1.011	19.6	62.4	12.3
7	1.001	19.6	62.3	12.2
8	0.996	20.1	55.9	11.2
9	1.024	20.1	57.9	11.9
10	1.002	20.1	57.7	11.6
11	0.992	20.8	61.6	12.7
12	1.013	20.7	63.4	13.3
13	1.001	20.6	63.0	13.0
14	0.881	21.8	56.1	10.8
	0.995 ± 0.115	**20.34 ± 1.4**	**59.5 ± 4.7**	**12.1 ± 1.3**

- Slot-die coating- 15% CsI- measured at day 0

1	0.929	22.9	62.5	13.3
2	0.932	23.0	63.3	13.5
3	0.933	22.8	65.0	13.8
4	0.919	22.9	63.9	13.4
5	0.901	22.5	55.8	11.3
6	1.023	20.9	68.6	14.7
7	1.004	21.5	69.5	15.0
8	0.996	21.2	65.7	13.9
9	0.975	22.0	55.4	11.9
	0.957 ± 0.065	**22.2 ± 1.2**	**63.3 ± 7.5**	**13.4 ± 2.1**

*The lines highlighted in yellow correspond to the device plotted on **Figure 21**.*

Appendix 3: Device performance summary.

- Spin-coating – Reference (5% CsI)- measured at day 1

	V_{oc} (mV)	J_{sc} (mA.cm^{-2})	FF (%)	PCE (%)
1	1.099	22.3	73.2	17.9
2	1.097	21.7	73.8	17.6
3	1.108	21.8	74.9	18.0
4	1.078	21.9	68.3	16.1
5	1.067	22.1	66.5	15.7
6	1.090	21.9	73.2	17.5
	1.090 ± 0.023	**21.9 ± 0.4**	**71.7 ± 5.1**	**17.1 ± 1.5**

- Spin-coating – 15% CsI- measured at day 1

	V_{oc} (mV)	J_{sc} (mA.cm^{-2})	FF (%)	PCE (%)
1	1.001	22.2	65.3	14.5
2	1.015	22.1	66.8	15.0
3	1.002	21.7	68.0	14.8
4	1.008	22.0	64.8	14.4
5	1.007	21.6	63.3	13.7
6	1.016	21.9	65.2	14.5
	1.008 ± 0.008	**21.9 ± 0.4**	**65 ± 2.4**	**14.5 ± 0.7**

*The lines highlighted in yellow correspond to the device plotted on **Figure 23**.*

Appendix 4: Monitoring of iodide content in the slot-die coated layers for various Cs/Pb ratios (FA/Pb = 79%)

A factor that can impede the device performance is the perovskite material modification upon annealing. In particular, iodide loss due to the evaporation of volatile compounds such as I_2 [257] has been reported in the literature. To quantify the iodine content in the films, we performed electron dispersive X-Ray (EDX) measurements on the "as-quenched" and annealed samples at all CsI contents for FA/Pb = 79% (**Figure A4**) and defined the I/Pb intensity ratio as a monitoring parameter. The objective was to see how the post-annealing step affected the iodide loss in the films fabricated with various CsI contents.

Prior to annealing, the iodide content of the "as-quenched" films increased proportionally with the CsI content in the solution. Upon annealing, we observed a pronounced iodide loss at 5, 10 and 15% Cs/Pb, which was correlated with the formation of crystalline PbI_2 in larger quantities in the film (**Chapter III - Figure 11**), and the apparition of white particles on the SEM image. One could suggest that this reorganization of the iodide in the perovskite films upon annealing could have led to the formation of iodide vacancies at the grain boundaries and/or interfaces with the extraction layers. The device integration of the "as-quenched" slot-die coated layer compared to the annealed slot-die coated layers could provide additional insights on the relationship between this iodide loss and perovskite solar cells performance.

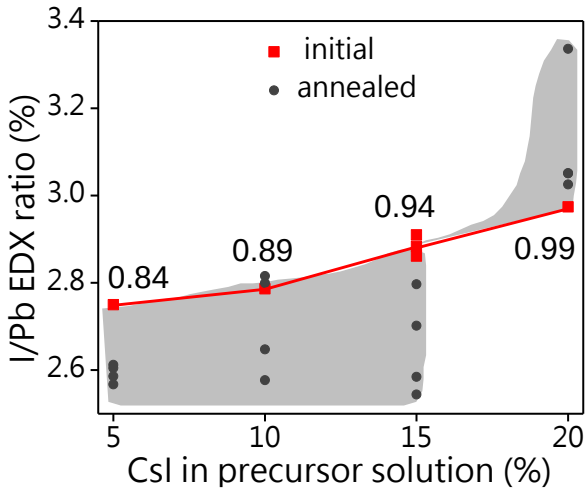

***Figure A4**: EDX ratios of I/Pb before and after 5 min annealing at 100 °C for the various Cs/Pb ratios. The superposed number corresponds to the cations (Cs^+ and FA^+) to lead (Pb) ratio.*

Chapter V: Influence of the ETL on the perovskite film properties and device performances.

In this final chapter, we present the work carried out in NTU laboratory where the slot-die coating process was adapted using the optimized precursor ink (15% Cs/Pb) developed in ***Chapter IV****. We investigate the properties of slot-die coated layers deposited on three state-of-the-art electron transporting layers (ETLs) with various chemical natures (SnO_2 and TiO_2) and morphologies (planar and mesoporous). We integrate those layers into photovoltaic devices to study the relationship between the ETL/Perovskite interface and the device performances. We studied the performance distribution of devices fabricated on large-area substrates and assessed the effect of the slot-die coated layer spatial homogeneity on device performances. Finally, we fabricate a 'proof of concept' photovoltaic module.*

V.1. Practical considerations

In the literature, a variety of architectures are available for perovskite-based photovoltaic devices fabrication (**Chapter I**) [258,259,58]. Here, we focused on the (n-i-p) device architecture in which the perovskite layer is coated on top of the electron transporting layer (ETL). In general, the device structures can be categorized into planar and mesoporous structures, defined by the morphology of the ETL employed. State-of-the-art ETL materials include TiO_2 (historically inherited from dye-sensitized devices [18]) and SnO_2 [260]. In this chapter, we aimed to assess the versatility of the slot-die coating process with the state-of-the-art ETLs used in the literature: planar SnO_2, planar TiO_2 and mesoporous TiO_2 (**Figure 1**).

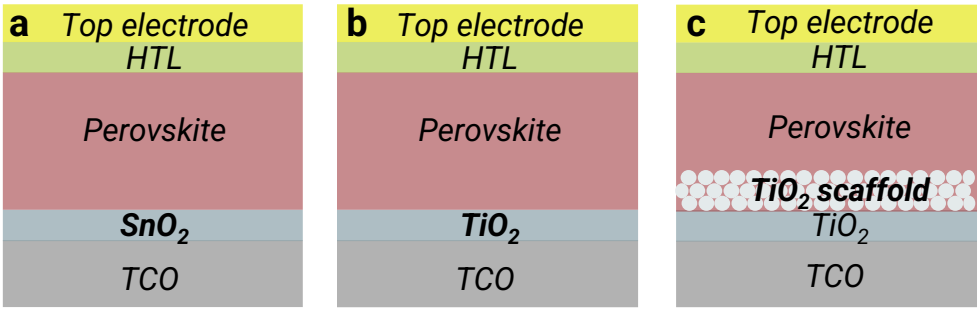

***Figure 1**: (n-i-p) device architectures investigated with various electron transporting layers (ETLs): **a)** planar SnO_2, **b)** planar TiO_2, and **c)** mesoporous TiO_2. TCO is the transparent conductive oxide electrode and HTL the hole transporting layer.*

V.1.1. ETLs investigated

In this study, the three substrates investigated were planar SnO_2, planar TiO_2 and mesoporous TiO_2. Fluorine doped tin oxide (FTO) was used as the transporting conductive oxide (TCO) for its compatibility with the high temperatures (500 °C) [261] required to sinter TiO_2 materials. The means to fabricate the ETLs varied (**Table 1**): a sol-gel approach was used to form planar SnO_2 and TiO_2 layers (later named 'sg-SnO_2' and 'sg-TiO_2' with sg = sol-gel), while a nanoparticles solution was used to form the mesoporous TiO_2 screen (named 'm-TiO_2' with m = mesoporous). We used the spin-coating process to deposit the planar SnO_2 and TiO_2 layers and the screen-printing process to deposit the mesoporous TiO_2 layer (experimental details can be found in **Chapter II**). We note that a high temperature post-annealing step (1 h at 500 °C) was required to sinter the TiO_2 materials.

We note that the planar SnO_2 fabrication via sol-gel approach differs from the nanoparticle SnO_2 solution employed earlier (in **Chapter III-IV**). To differentiate them, the previously investigated SnO_2 ETL was named 'np-SnO_2' (np = nanoparticles). The planar SnO_2 substrate ('sg-SnO_2') was defined as the reference substrate (highlighted in grey in **Table 1**). Here, we report the comparison between this reference substrate and the previous planar SnO_2 substrate ('np-SnO_2') and the intra batch comparison between the reference and planar TiO_2 ('sg-TiO_2') and mesoporous TiO_2 ('m-TiO_2') substrates.

Chapter	***III-IV***	**V**		
ETL designation	***np-SnO₂***	**sg -SnO₂ (ref)**	**sg-TiO₂** (anatase)	**m-TiO₂** (anatase)
TCO	*ITO*	FTO		
morphology	*planar*	planar	planar	mesoporous
fabrication method	*nanoparticles (SnO₂ in H₂O)*	sol-gel ($SnCl_2$ in EtOH)	sol-gel ($Ti(OBu)_4$ in EtOH)	Nanoparticles (TiO_2 in terpineol)
deposition process	*Spin-coating*	Spin-coating	Spin-coating	Screen-printing
post-annealing (in air)	*80 °C – 1 min*	180 °C – 1 h	500 °C – 1 h	500 °C – 1 h

***Table 1**: Substrates investigated in this work. The reference substrate in this chapter is highlighted in grey.*

During the slot-die coating process, the precursor wet film is deposited onto the ETL surface. Therefore, the ETL properties such as its thickness and surface roughness can affect the perovskite layer coating [262]. The main properties of the ETL-coated substrates are summarized in **Table 2.** We can distinguish the planar and mesoporous ETLs. For planar ETLs, their thickness (30-40 nm range, **Table 2**) was negligeable in comparison to the slot-die coated precursor wet film thickness (~ 4 µm). The mesoporous ETLs, however, presented larger thicknesses up to 250 nm which could affect the perovskite coating, in particularly because of their porosity.

The planar SnO_2 ETL fabricated by sol-gel method had a similar thickness (sg-SnO_2, 30 nm) compared to the SnO_2 ETL from SnO_2 nanoparticle's solution (np-SnO_2, 40 nm) and to the TiO_2 ETL fabricated by the sol-gel method (sg-TiO_2, 40 nm). This thickness has been optimized prior to this work to balance the charge selectivity properties (that require a minimum thickness to selectively extract electrons), and the light management and ETL conductivity (that are limited at high ETL thicknesses). In the literature, optimal ETLs exhibit full TCO coverage and minimal thickness [62]. Here, each layer of the stack was adjusted with respect to the nature of the TCO and perovskite as made by spin-coating to maximize the device efficiency in such configuration.

ETL designation	***np-SnO₂***	**sg-SnO₂**	**sg-TiO₂**	**m-TiO₂**
average roughness (nm)	*10* ± 1	15 ± 1	15 ± 5	-
ETL thickness (nm)	*40* ± 2	30 ± 5	40 ± 10	100, 150 and 250 ± 10
nanoparticle size* (nm)	*10 - 15*	-	-	30

***Table 2**: Main properties of the substrates investigated in this chapter. The properties of the ITO/np-SnO₂ substrates are provided for direct comparison to previous work. *This information was extracted from the specifications of the supplier.*

In the (n-i-p) device structure, the incoming light will go through the TCO and the ETL layers before reaching the perovskite absorber. Therefore, to maximize the current generation in the perovskite, the TCO/ETL stack must have a maximum transparency. Due to the presence of a scaffold in the mesoporous ETL sample, lower transparency has been reported in the literature compared to planar TiO_2 films [263]. Therefore, we focused on the comparison between the planar ETLs. We measured the optical transmission of the TCO/ETL stacks for ITO/np-SnO_2, FTO/sg-SnO_2 and FTO/sg-TiO_2 (**Figure 2**). The transmission onset was shifted of $\Delta\lambda = 15$ nm when the ETL material was modified from SnO_2 to TiO_2, in line with the literature [147]. Moreover, the ETL coated on the FTO substrates had a larger transmission in the 500 – 800 nm range (+ 5%), where the perovskite material absorbs, compared to the ETL coated on ITO. We concluded that FTO/sg-SnO_2 was the substrate maximizing the transparency among the planar samples. We will later link the substrate transparency to experimental device current density values.

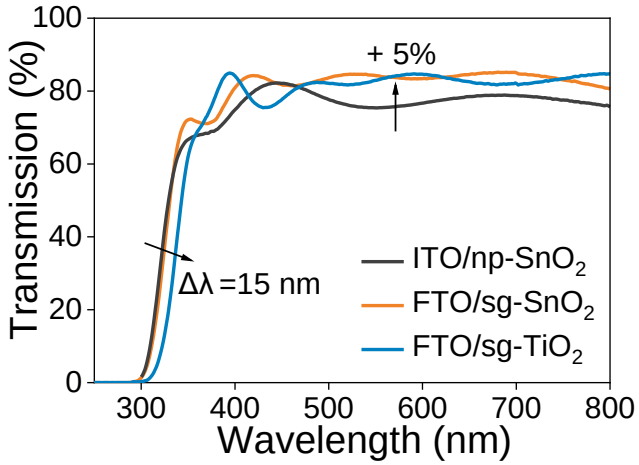

***Figure 2**: Transmission of the various TCO/ETL stacks employed here in the wavelength range where the perovskite layer absorbs (300- 780 nm).*

V.1.2. Perovskite layer deposition

As this study was performed using a different slot-die coating equipment and larger substrates (10 x 10 cm^2) (**Chapter II**), we optimized the deposition parameters to form compact perovskite layers, following the iterative optimization methodology used in **Chapter III**. The substrate temperature (CQ_T), the coating gap (C_g) and post-annealing temperature and time were directly transferred from the previous process parameters whereas the process speed (CQ_s) was adjusted from 28 $mm.s^{-1}$ to 25 $mm.s^{-1}$ and the coating flow rate (C_f) from 100 to 60 $\mu L.min^{-1}$. Those slight variations are attributed to the different ink dispense system used. The quenching flow rate (Q_f) was increased from 100 $L.min^{-1}$ to 140 $L.min^{-1}$, due to the change of nitrogen source (nitrogen cylinder with higher pressure) and the variation in gas-knife geometry. The process parameters optimized for the second slot-die coater are summarized in the **Table 3**. The annealing conditions were kept similar to the one performed in previous chapters (5 min at 100 °C) but the post-annealing step was performed in air.

Coating		Quenching		Post-Annealing	
Coating gap **(C_g)**	100 µm	Quenching gap **(Q_g)**	300 µm	Annealing temperature **(A_T)**	100°C
Coating speed **(CQ_s)**	25 mm.s^{-1}	Quenching speed **(CQ_s)**	25 mm.s^{-1}		
Coating flow rate **(C_f)**	60 µL.min^{-1}	Quenching flow rate **(Q_f)**	140 L.min^{-1}	Annealing time **(A_t)**	5 min
Substrate temperature **(CQ)**	60 °C	Substrate temperature **(CQ_T)**	60 °C		

***Table 3**: Optimized process parameters used on the second slot-die coater. The adjusted parameters are highlighted in green.*

The quenching gap (Q_g) was significantly reduced from 3 mm to 300 µm to permit lateral homogeneity of the crystallization over the 10 cm wide substrate as illustrated below (**Figure 3**).

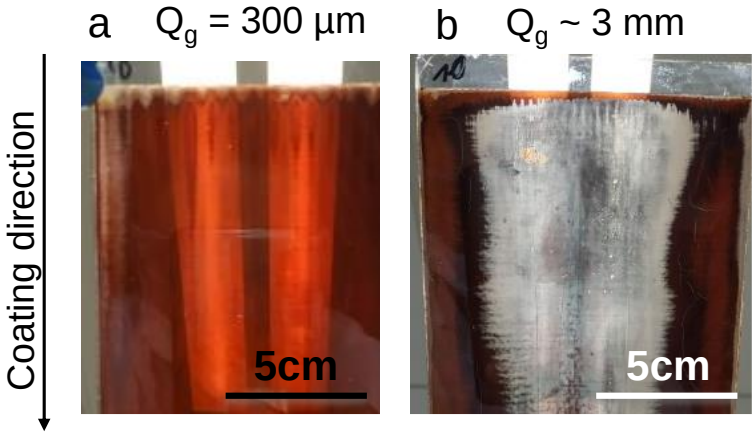

***Figure 3**: Pictures of 10 x 10 cm² slot-die coated samples obtained for various quenching gaps. **a)** Q_g = 300 µm and **b)** Q_g = 3 mm with the second slot-die coater.*

For all studies made in this chapter, we used the optimized precursor ink with 15% Cs/Pb developed in **Chapter IV**. The composition is reminded in **Table 4**.

Lead concentration (M)	1.2
PbI_2 excess (%)	6
Cs/Pb molar ratio (%)	15
FA/Pb molar ratio (%)	79
Br:I molar ratio (%)	12 : 88
DMF : DMSO volume ratio	4 : 1

***Table 4**: Composition of the optimized precursor ink to form $Cs_{0.15}FA_{0.79}Pb(I_{0.88}/Br_{0.12})_{2.84}$.*

V.2. Comparison of planar np-SnO_2 and sg-SnO_2 ETLs

The first investigation focused on the two planar SnO_2 ETLs. Indeed, the new reference substrate (FTO/sg-SnO_2) differed from the one studied in **Chapters III-IV** (ITO/np-SnO_2).

V.2.1. Perovskite layer properties on np-SnO_2 and sg-SnO_2

Following the characterization matrix presented in **Chapter III**, we compared the properties of perovskite layers slot-die coated onto the reference np-SnO_2/Perovskite (Slot-die process 1, **Chapter III-IV**) and the new reference sg-SnO_2/Perovskite (Slot-die process 2, **Chapter V**) substrates. We note that besides the change of ETL, both samples were fabricated using different slot-die coating processes. The aim of this comparison is to identify the possible changes in perovskite material properties and to link them to device performances. Further ETL layers investigations using the same slot-die coating process will be performed later to decorrelate the effects of the process and the substrate on both perovskite film properties and device performances (**V.3.3** and **V.4.3.**).

- **Morphology**

The FTO glass substrate size used in this work was 10 x 10 cm^2, as depicted in **Figure 4a**. We used the first centimetre of substrate (top of the picture) to deposit the meniscus during the slot-die coating process. The perovskite coating area was then A = 90 cm^2. We can see from the sample picture (**Figure 4a**) that a brown perovskite film was deposited homogeneously on the substrate. On the optical image (**Figure 4b**), we observed a compact morphology without any pinholes (c = 100%). The profilometry scan showed a film thickness of t = 550 nm on FTO/sg-SnO_2 with a surface average roughness R_a = 15 nm, similar to the one on ITO/np-SnO_2 (t = 575 nm and R_a = 10 nm).

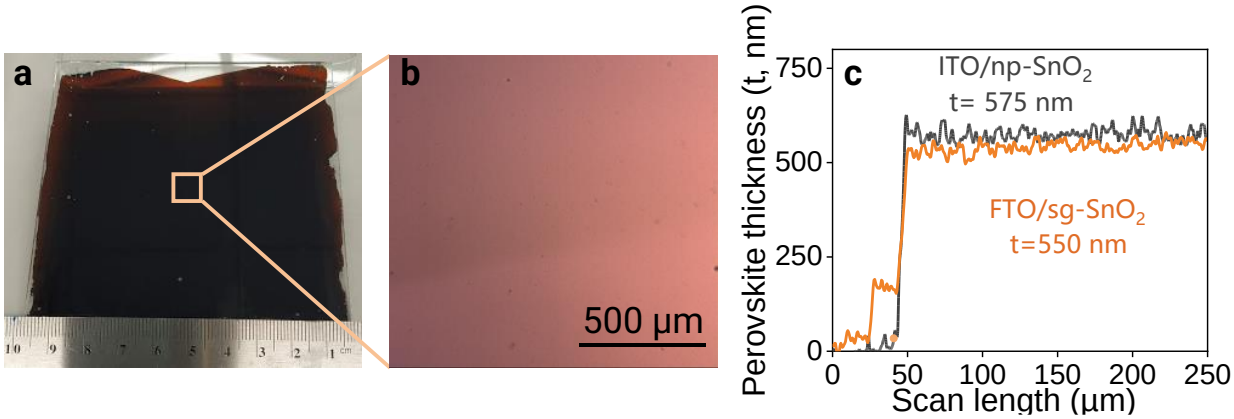

***Figure 4**: **a)** Picture of the slot-die coated perovskite layer on a sg-SnO_2/FTO substrate over 10 x 10 cm^2. **b)** Optical microscopy image of the surface of the perovskite layer. **c)** Profilometry scan of the perovskite layer slot-die coated on FTO/sg-SnO_2 and ITO/np-SnO_2.*

The SEM images confirmed the presence of a compact grain-like morphology in the perovskite film (**Figure 5b**), similarly to what was observed on the np-SnO_2-coated ITO substrate (**Figure 5a**). We noticed an increase of the perovskite grain size from g = 250 nm on ITO/np-SnO_2 to g = 400 nm on the FTO/sg-SnO_2 substrate. This grain size increase was correlated with a wider grain distribution (twice as wide), with the addition of a second populations (grain size ~ 500 nm) to the first population (grain size ~ 250 nm). This uneven grain size distribution reflects an inhomogeneous crystal nucleation: small grains formed in high nucleation density areas and larger grains in the lower nucleation density areas.

Overall, the nucleation on the sg-SnO_2 sample was less dense than on the np-SnO_2 sample. This difference could be due to many parameters such as the change of processing conditions, substrate or processing environment at this stage. Despite the origin uncertainty, this was an interesting result, as the average grain size of the slot-die coated layer deposited on FTO/sg-SnO_2 substrate (g = 400 nm) was higher than the spin-coated perovskite layer average grain size (g = 273 nm, see **Chapter III**) on ITO/np-SnO_2, which could be desirable for device integration.

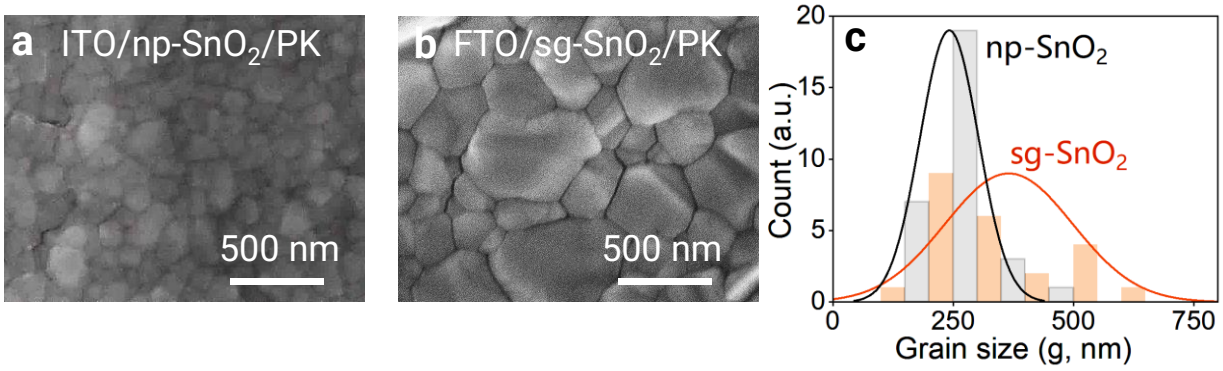

***Figure 5**: SEM image of the perovskite layer slot-die coated on **a)** ITO/np-SnO_2 and **b)** FTO/sg-SnO_2 substrates. **c)** Corresponding grain size distributions.*

- **Optical properties**

In line with the slight film thickness decrease, the absorption onset (**Figure 6a**) of the layer on FTO/sg-SnO_2 (t = 500 nm) was smaller compared to the thicker perovskite film on ITO/np-SnO_2 (t = 575 nm). Both films exhibited a similar band gap at E_g = 1.62 eV (**Figure 6b**). Regarding the photoluminescence intensity, we observed an identical PL emission wavelength for both samples (**Figure 6c**), reinforcing the fact that a material with similar electronic properties (and possibly with a similar stoichiometry) was formed on this new substrate and with this adapted process.

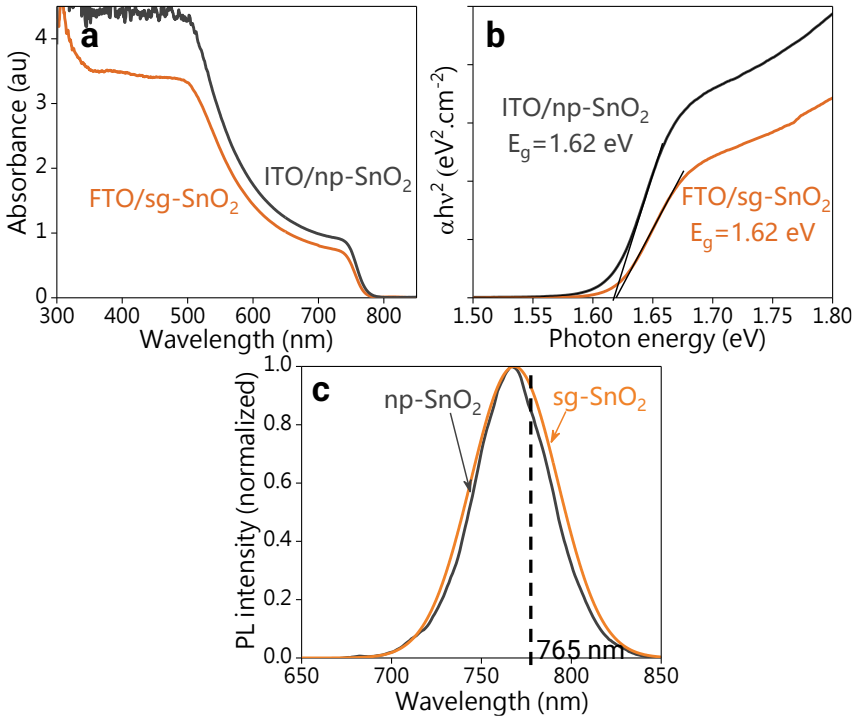

***Figure 6**: **a)** Absorbance curves, **b)** Corresponding Tauc plots (see **Chapter II**) and **c)** Normalized photoluminescence intensity (excitation wavelength: 550 nm) of slot-die coated perovskite layers deposited onto ITO/np-SnO_2 and FTO/sg-SnO_2 substrates.*

- **Crystallinity**

We monitored the X-Ray diffraction (XRD) pattern of the slot-die coated films on both FTO/sg-SnO_2 and ITO/np-SnO_2 substrates (**Figure 7a**). The presence of the α-CsFAPbIBr phase on the FTO/sg-SnO_2 substrate was confirmed by the presence of diffraction peaks at $2\theta = 13.8°$, 19.7° and 24.3° corresponding to the (001), (011) and (111) plans respectively. Regarding the by-products, we did not detect the δ-$FAPbI_3$ phase, indicating a selective perovskite conversion into the cubic structure. The presence of crystalline PbI_2 peak was, however, more pronounced in the perovskite layer coated on the FTO/sg-SnO_2 substrate (**Figure 7a**). The XRD peak area ratio of crystalline PbI_2 increases from 6 to 23% (**Figure 7b**).

Moreover, the film coated onto the FTO/sg-SnO_2 substrate exhibited a preferential orientation along the (011) plan, which was distinct from the (001) plan observed earlier. Despite the difference of measurement set-ups used to measure the XRD patterns (discussion in **Chapter II**), we attributed the change of preferential grain orientation observed by XRD to a change in the organization of the perovskite crystals. This change of organization could originate from a difference in the crystallization mechanism and be correlated with the presence of larger grains and more crystalline PbI_2 in this sample.

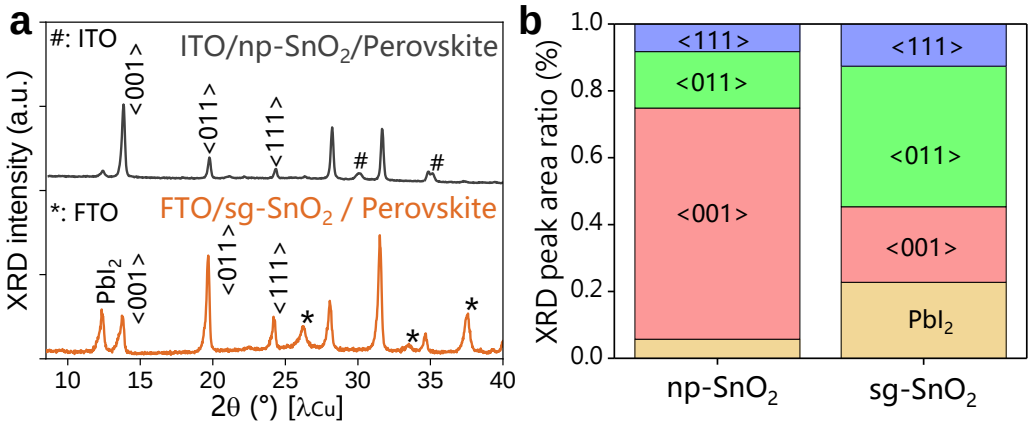

Figure 7: a) *X-Ray diffraction patterns and* ***b)*** *Corresponding XRD peak area ratio of slot-die coated layers on ITO/np-SnO_2 and FTO/sg-SnO_2.*

In summary, a perovskite layer with similar thickness, absorption properties, and selective cubic CsFAPbIBr structure was deposited on the FTO/sg-SnO_2 substrate with the adapted slot-die coating process. **Appendix 2A** summarizes the characterization matrix with the same methodology used in **Chapter III**. We have identified three main differences with the reference slot-die coated layer: the larger grain size (average value and width of distribution), the change of the preferential perovskite grain size and orientation ((011) plan was preferred on FTO/sg-SnO_2) and the larger proportion of crystalline PbI_2 observed by XRD on FTO/sg-TiO_2.

V.2.2. Performances of devices with np-SnO_2 and sg-SnO_2 ETLs

Once the main properties of the slot-die coated perovskite layer characterized, we can study the effect of those changes on the device performance. Here, we compared the performances of devices fabricated with the FTO/sg-SnO_2/Perovskite/Spiro-OMeTAD/Au structure (new reference structure) to the performance of the slot-die coated devices fabricated in **Chapter IV** with the ITO/np-SnO_2/Perovskite/PTAA/Au structure (initial structure).

- **Device architecture**

This device architecture differed from the one studied earlier (**Chapters III & IV**) as we used fluorine doped tin oxide (FTO) as transparent conductive oxide (TCO) layer instead of ITO, deposited the SnO_2 ETL via sol-gel method (nanoparticles formulation earlier) and used Spiro-OMeTAD as hole transporting layer (HTL) instead of PTAA.

We present the energy band diagram with values extracted from the literature [205–207] (**Figure 8b**). The modification of the TCO material did shift the work function of the transparent electrode from - 4.8 eV (ITO) to - 4.5 eV (FTO), but still permits the extraction of electrons from SnO_2 (conduction band of - 4.4 eV) to the TCO material. The modification of the HTL material did not affect the device energy alignment, as the valence band level was

similar (- 5.2 eV) for both PTAA and Spiro-OMeTAD. Experimentally, we could expect variations of the ETL/Perovskite energy alignment due to a variation of the ETL deposition process [264] (sol-gel, colloid, atomic layer deposition (ALD)) or surface properties [62,265] (pH, chemical groups, oxygen vacancies).

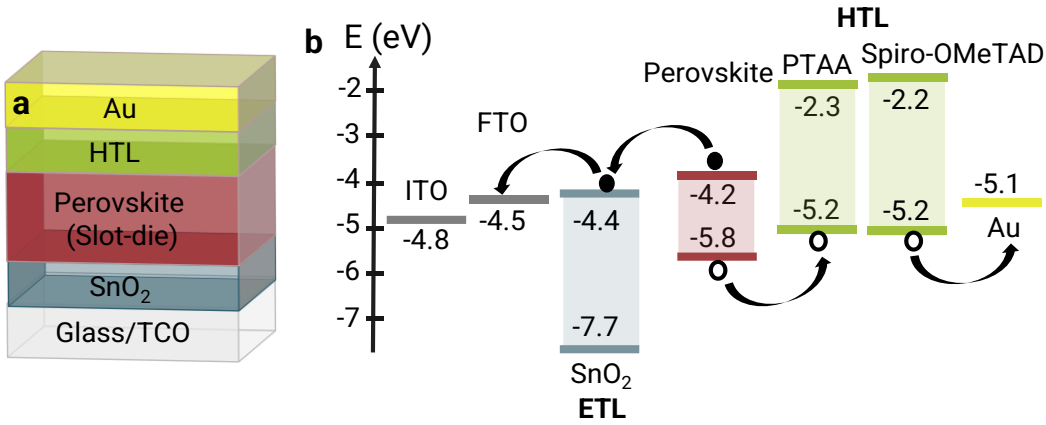

***Figure 8**: **a)** Device stack used in this chapter. **b)** Energy alignment diagram with values from the literature [205–207].*

- **Device performance classification**

We applied the same device measurement protocol as before (see **Chapter II**) and observed a more pronounced dispersion in the device performances (**Figure 9a**) compared to the one observed in **Chapter III** with the other device architecture. The high dispersion could be explained by a lower homogeneity over relatively large substrate area (100 cm^2 compared to 25 cm^2 in **Chapter III-IV**) that could have led to larger performance variations. This dispersion could be formalized into three categories of devices: defective, average and champions with power conversion efficiencies (PCE) ranging 2-8%, 8-14% and > 14% respectively (**Figure 9a**). We present the typical J-V curves under illumination (**Figure 9b**) and in the dark (**Figure 9c**) of one representative device for each category.

In the dark J-V curves, the curve of the average device (blue) is the translation of the curve of the defective device (black) towards lower dark current, possibly due to the reduction of the shunt resistance [266] (**Figure 9c**). The difference between the average and champion device is the ideality factor or the dark J-V curve, which value tends towards 1, indicative of less intra-band (Shockley Read Hall, SRH) recombination [267]. We concluded that the defective devices were limited by shunts and that the average device was limited by recombination in the absorber material. Both limiting factors encountered could have been caused by inhomogeneities of the underlying ETL (shunt resistance) and/or by the inhomogeneity of the slot-die coated perovskite layer (recombination).

When measuring the J-V curves under illumination, these dark current observations were translated into lower V_{oc} and FF (shunts) in the defective device and lower J_{sc} and V_{oc} (defective perovskite layer) in the average device (**Figure 9b**). To differentiate those device categories, we used the shunt resistance extracted from the J-V curves under illumination (**Figure 9d**). The device V_{oc} and the device shunt resistance were correlated, confirming the relevance of the shunt resistance as a threshold parameter to differentiate the various device categories.

Consequently, in the rest of the work, we filtered the device data with a shunt resistance threshold of 1 000 Ω.cm² (**Figure 9d**) to differentiate the device suffering from reduced shunt resistance. This device filtering allowed us to specifically investigate the impact of the slot-die coated layer quality on the device performance for the remaining devices (average and champion categories).

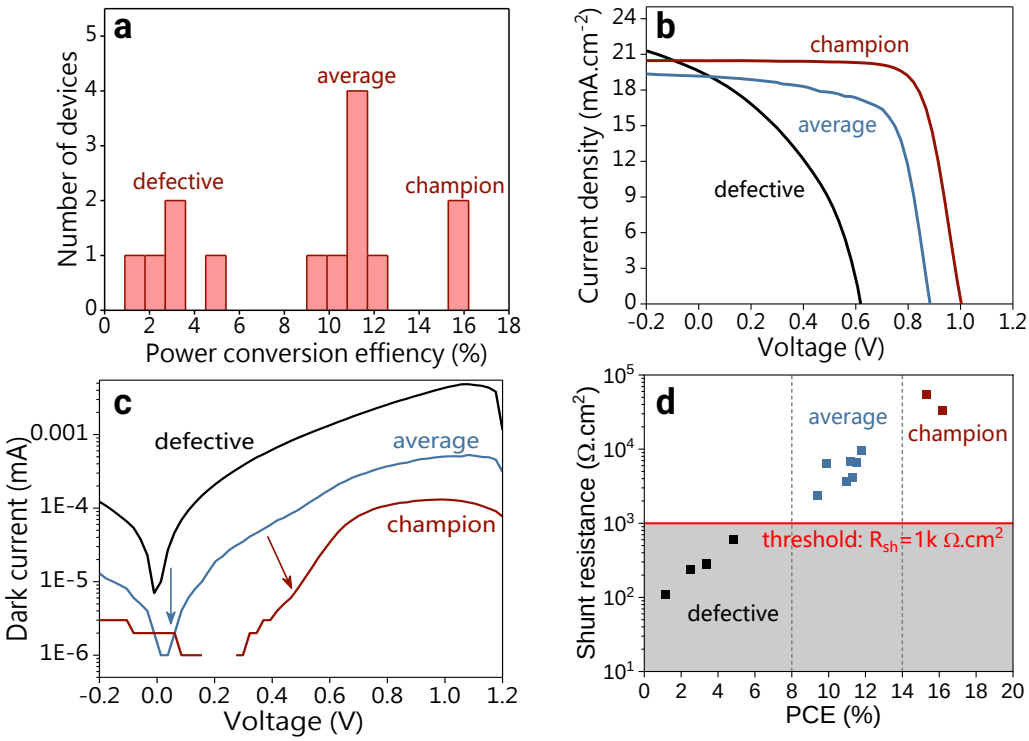

***Figure 9**: **a)** Device power conversion efficiency distribution. **b)** J-V curves under illumination. **c)** J-V curves in the dark of one representative devices for each population (defective, average and champion). **d)** Correlation between shunt resistance and power conversion efficiency.*

With the change of device structure (FTO/**sg-SnO_2**/Perovskite/**Spiro-OMeTAD**/Au), we could expect a different device aging behaviour. The next paragraph will introduce the evolution of the device performances with a storage in the dark at a relative humidity of 50%, using the methodology introduced earlier (**III.4.1**).

- **Aging behaviour and day of performance reporting**

In the literature, the evolution of the device performances over time has been reported to depend on the device structure [268]. To investigate aging behaviour of devices fabricated with the new reference device stack (FTO/sg-SnO_2/Perovskite/Spiro-OMeTAD/Au), we measured the J-V curves initially (d0) and after 1, 5 and 9 days of storage in the dark (**Figure 10**).

The day of highest power conversion efficiency (PCE) was dependant of the device category. The champion devices reached the maximum PCE after 1 day of storage, mainly correlated with the V_{oc} and FF maxima (**Figure 10b-d**); while the average devices achieved the highest performance after 5 days of storage, due to a V_{oc} local maximum (**Figure 10b**). The current density increased for both populations in the first day and remained constant until 9 days of storage (**Figure 10c**). The V_{oc} was quite constant upon dark storage for the champion devices but deteriorated after 5 days for the average devices (**Figure 10b**). The fill factor (FF) deteriorated over time for all devices (**Figure 10d**).

On SnO_2 ETL, using the triple cation perovskite (MA, FA, Cs), Praetzold *et al.* observed a power conversion efficiency increase after 10 days of storage, mainly due to a constant increase of V_{oc} and FF with storage time [268]. Our performance improvement kinetics was shorter and the FF evolution opposite to their observations. As they also demonstrated that the aging behaviour was related to the perovskite formulation, the different result could come from the different perovskite employed in this work (CsFAPbIBr).

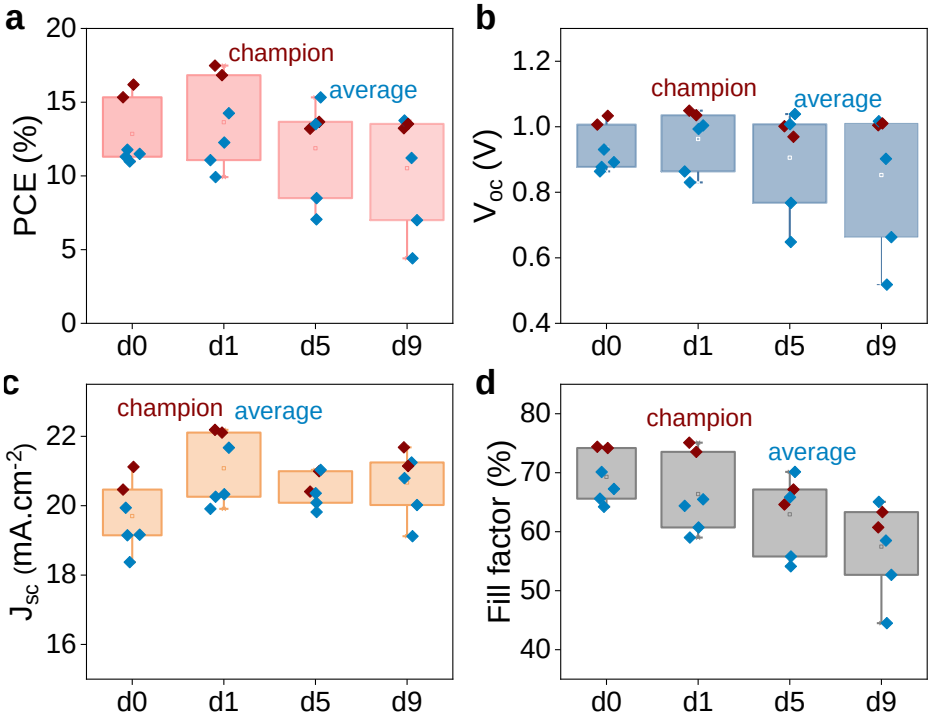

***Figure 10**: **a)** Power conversion efficiency (PCE), **b)** Fill factor (FF), **c)** Current density (J_{sc}) and **d)** Open-circuit voltage (V_{oc}) of six FTO/sg-SnO_2/Perovskite/Spiro-OMeTAD/Au devices measured*

initially (d0) and after 1, 5 and 9 days of storage in the dark under 50% relative humidity. The defective devices (shunt resistance ≥ 1000 Ω.cm²) were excluded from the representation.

In summary, the highest device performances with the new device structure were reached after one day of storage for the champion devices. We will therefore report the performance measured on that day (d1) for further comparisons.

- **Device performance: comparison of np-SnO_2 and sg-SnO_2 ETLs**

Under illumination, the J-V curves of the champion device on FTO/sg-SnO_2 substrate (**Figure 11a**) exhibited higher J_{sc} (22.2 mA.cm^{-2}), V_{oc} (1.049 V) and FF (75.1%) compared to the device fabricated on the ITO/np-SnO_2 device structure. These parameters resulted in a champion power conversion efficiency of 17.5%, closing the gap to the spin-coated device efficiency of 18%. In average, however, the power conversion efficiency on FTO/sg-SnO_2 was 13.6%, far from the 17.5% champion efficiency and rather in the range of the 13.4% average efficiency obtained for ITO/np-SnO_2 devices (**Figure 11d**). The detailed device data is available in **Appendix 3**.

If we compare the average values, both slot-die coated devices (on ITO/np-SnO_2 or FTO/sg-SnO_2) exhibited similar average V_{oc} (0.957 V and 0.963 V respectively), significantly lower than the spin-coated device average V_{oc} (1.090 V) (**Figure11d**). This suggests that the V_{oc} deficit compared to the spin-coated devices was mostly due to the perovskite layer quality that depends on the deposition process used and not on the device architecture employed.

The average fill factor of slot-die coated devices increased slightly from 63.3% for the ITO/np-SnO_2 sample to 66.4% for the FTO/sg-SnO_2 sample. As this FF increase was correlated with a change of the grain size (from 250 nm to 500 nm) in the perovskite absorber, this could be explained by the reduction of grain boundaries density, hence on the amount of recombination centres in the perovskite absorber. This FF increase could also be due to lower recombination rates at the ETL/Perovskite interface.

For slot-die coated devices, the average short-circuit current density decreased from 22.2 mA.cm^{-2} on ITO/np-SnO_2 to 21.1 mA.cm^{-2} on FTO/sg-SnO_2 (**Figure 11d**). While average J_{sc} were lower, interestingly the highest values achieved for champion devices were slightly higher on FTO/sg-SnO_2 (**Figure 11c**). This could be due either to the better transparency of the sg-SnO_2 layer when compared to the np-SnO_2 (**Figure 2**) or to a better index matching increasing charge generation.

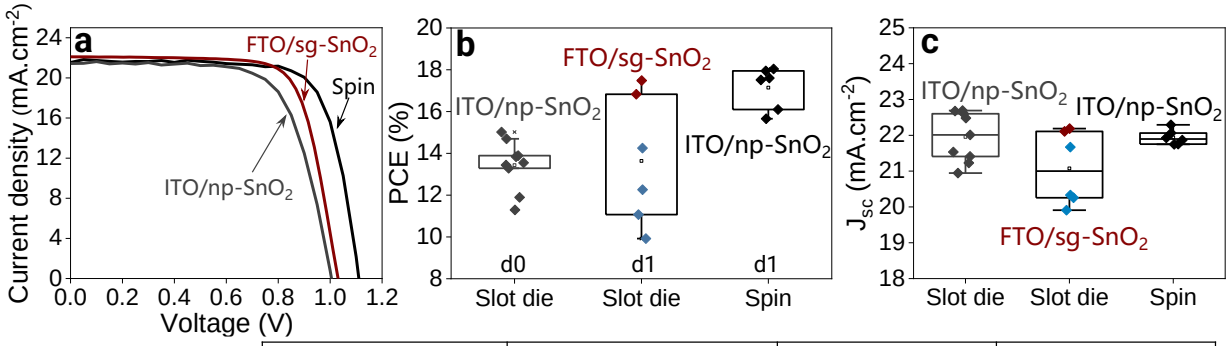

d *Perovskite process and substrate used*	V_{oc} (V)	J_{sc} (mA.cm^{-2})	FF (%)	PCE (%)
Spin ITO/np-SnO_2 (d1)	1.090 ± 0.023 *1.108*	21.9 ± 0.4 *21.8*	71.7 ± 5.1 *74.9*	17.1 ± 1.5 *18.0*
Slot-die ITO/np-SnO_2 (d0)	0.957 ± 0.065 *1.003*	22.2 ± 1.2 *21.5*	63.3 ± 7.5 *69.5*	13.4 ± 2.1 *15.0*
Slot-die FTO/sg-SnO_2 (d1)	0.963 ± 0.132 *1.049*	21.1 ± 1.2 *22.2*	66.4 ± 8.7 *75.1*	13.6 ± 3.8 *17.5*

***Figure 11**: **a)** J-V curves of the best device per batch (measured at do or d1). **b)** Statistics of power conversion efficiencies. **c)** Statistics of short-circuit current densities. **d)** Summary of J-V parameters for the three conditions. The parameters of the champion devices plotted on panel b are in italic.*

In summary, high quality perovskite absorbers were obtained via different processes on various SnO_2 ETLs, reinforcing the versatility of this deposition technique. The device performance on the FTO/sg-SnO_2 substrate reached a champion 17.5% and average PCE of 13.6%. Those devices exhibited a fill factor increase compared to the previous slot-die coated devices, possibly due to the increased perovskite grains size and reduced grain boundaries in these films.

Nevertheless, the dispersed device performances observed in this first study suggest that challenges remain regarding the homogeneous fabrication of a high-quality perovskite layer (with low recombination and ideality factor close to 1) across the substrate on which the various devices were fabricated. This aspect will be discussed in the end of the chapter (**V.5.**).

Now that the properties of the slot-die coated layers on planar SnO_2 ETLs have been studied, other electron transporting layers can be investigated. From this study onwards, the slot-die coating process conditions were not modified (**Table 3**) to focus on the influence of the ETL on the slot-die coated layer properties. These performances will serve as the reference for the new device structure and will be used as a comparison point for subsequent studies in this chapter.

V.3. Comparison of planar sg-SnO_2 and sg-TiO_2 ETLs

Besides the SnO_2 material, the TiO_2 material has largely been used as a planar ETL in perovskite solar cells since the early years of this field [47]. Here, we compared the properties of perovskite layers slot-die coated on planar TiO_2 to the reference slot-die coated layers on planar SnO_2.

V.3.1. ETL layers properties: sg-SnO_2 and sg-TiO_2

We deposited the TiO_2 ETL using the same sol-gel approach than the planar SnO_2 ETL using the spin-coating process on a FTO substrate (**Chapter II**). The main difference was the higher post-annealing temperature of 500 °C (**Table 1&2**) required to convert the tetrabutyl-titanate ($Ti(OBu)_4$) precursor into TiO_2 thin film. The concentration of the $Ti(OBu)_4$ precursor employed determines the sg-TiO_2 layer thickness. Here, we used a state-of-the-art recipe [154] resulting in a ~ 40 nm thick sg-TiO_2 thin film with an average surface roughness (R_a = 15 nm). Those properties were comparable with the reference sg-SnO_2 ETL (t= 30 nm and R_a = 15 nm).

In the literature, studies on the influence of the ETL nature on the perovskite crystallization are scarce when a slot-die coating process is used. This could be explained by the absence of significant effect of the ETLs on the perovskite crystallization for spin-coated perovskite layers. For instance, Yu *et al.* demonstrated the fabrication of $MAPbI_3$ perovskite layers with similar properties on planar SnO_2 and TiO_2 ETLs using the spin-coating process [269]. This result was confirmed by Jiang *et al.* [270]. As the crystallization process may differ between spin-coating and slot-die coating, we aim to study whether these observations are applicable when the perovskite film is slot-die coated.

V.3.2. Perovskite layer properties on sg-SnO_2 and sg-TiO_2

A direct comparison is permitted between the two substrates as the perovskite deposition process used was identical. The only modification was the ETL material deposited. Here, we report the perovskite layer properties using the characterization methodology used earlier, enriched by scanning electron microscopy cross-sections and time-resolved photoluminescence which are relevant techniques to study the ETL/Perovskite interface.

- **Morphology**

The slot-die coated layers on both ETLs exhibited a similar film thickness t = 550 nm and roughness (Ra = 15 nm). The slot-die coated layers had a similar morphology when deposited on FTO/sg-TiO_2, with full substrate coverage, compared to the reference FTO/sg-SnO_2 substrate (**Figure 12a-b**).

The grain size distribution ranged from g = 300 to 600 nm on both substrates, showing similar average grain size on FTO/sg-TiO_2 (g = 450 nm) and on FTO/sg-SnO_2 (g = 400 nm) (**Figure 12c**). Those morphologies were different from the np-SnO_2 sample and its significantly smaller grain size (g = 273 nm), suggesting that the perovskite process conditions could be the factor determining the grain size rather than the underlying substrate type (when planar ETLs are investigated).

To assess the vertical perovskite grains organization, we recorded the SEM cross-sections of the slot-die coated layers on FTO/sg-TiO_2 and FTO/np-SnO_2 (**Figure 12d-e**). We observed that the grains were stacked on top of each other similarly in both samples. Based on the SEM images, the underlying ETL nature did not seem to influence the perovskite growth.

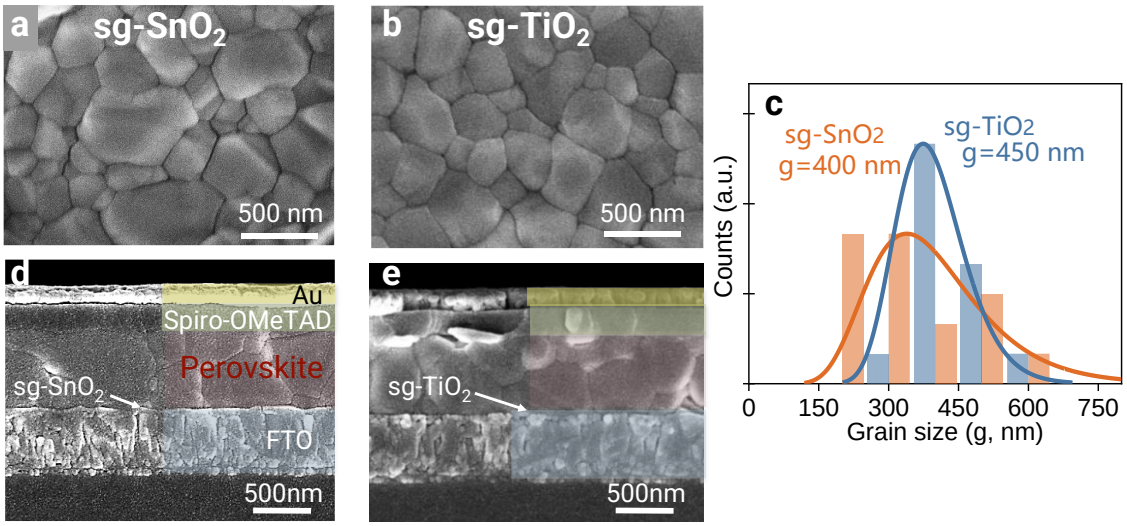

***Figure 12**: SEM surface and cross-section images of the perovskite layer slot-die coated on the **a-d)** sg-SnO_2 coated and **b-e)** sg-TiO_2 coated FTO substrate. **c)** Corresponding grain size distribution.*

- **Optical properties**

The absorption of both slot-die coated films were similar (**Figure 13a**), in accordance with the similar film morphologies observed earlier. Both materials exhibited a band gap E_g = 1.62 eV (extracted via the Tauc plot method, **Figure 13b**). The photoluminescence peak intensities of both slot-die coated layers were comparable (**Figure 13c**), indicating a similar level of radiative recombination in both films. We observed a narrowing of the PL peak in the 800 nm wavelength range on the FTO/sg-TiO_2 substrate. As discussed earlier (**Chapter IV-1-2**), the change in grain distribution was not likely to be responsible for this PL narrowing. Here, we suggest that the perovskite intrinsic quality or the ETL/Perovskite interface could have been modified in the FTO/sg-TiO_2 sample. We will assess the crystalline perovskite properties in the next paragraph.

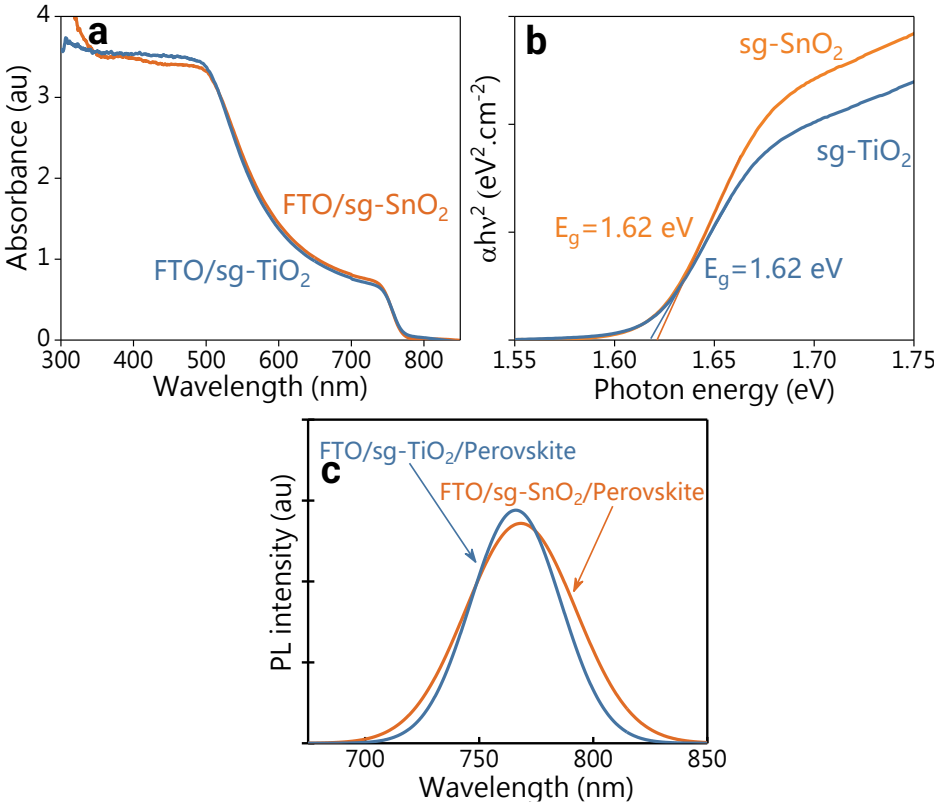

***Figure 13**: **a)** Absorbance spectra of slot-die coated perovskite layers deposited onto FTO/sg-SnO_2 and FTO/sg-TiO_2 substrates. **b)** Extraction of corresponding optical band gaps via Tauc plot method. **c)** Photoluminescence spectra with an excitation wavelength of 550 nm for both slot-die coated layers.*

- **Crystallinity**

We compared the XRD patterns of the slot-die coated layers deposited on FTO/sg-SnO_2 and FTO/sg-TiO_2 substrates (**Figure 14a**). The formation of α-CsFAPbIBr perovskite was confirmed in both samples with a difference in the grain orientation. In the film coated on the reference substrate (FTO/sg-SnO_2), the (011) plan was predominant (XRD peak area ratio of 42%, **Figure 14b**), whereas the (001) plan was the most represented in the slot-die coated film on FTO/sg-TiO_2 (XRD peak area ratio of 40%).

We could wonder whether the perovskite grain preferential orientation depends on the underlying ETL. Indeed, the perovskite grain orientation observed in FTO/sg-TiO_2 sample was closer to the one in the ITO/np-SnO_2 substrate than to the one observed in FTO/sg-SnO_2 sample. We concluded that no direct correlation can be confirmed between the ETL material (SnO_2 or TiO_2) or the ETL deposition process (sol-gel or nanoparticles) used and the perovskite grain orientation. To further probe the ETL/Perovskite interface, we later used time-resolved photoluminescence to compare the charge carriers recombination in the perovskite absorber for both FTO/sg-SnO_2 and FTO/sg-TiO_2 samples.

Regarding the by-products, the absence of δ-$FAPbI_3$ confirmed the selective formation of the cubic structure. The formation of crystalline PbI_2 was observed in both sg-SnO_2 and sg-TiO_2 samples with XRD peak area ratios of 23 and 18% respectively. As crystalline PbI_2 XRD peak area ratios were significantly higher in those two substrates compared to the ITO/np-SnO_2 substrate studied earlier (XRD peak area ratio of 6%), we attributed the change in crystalline PbI_2 formation to the slot-die coating process rather than to the substrate nature.

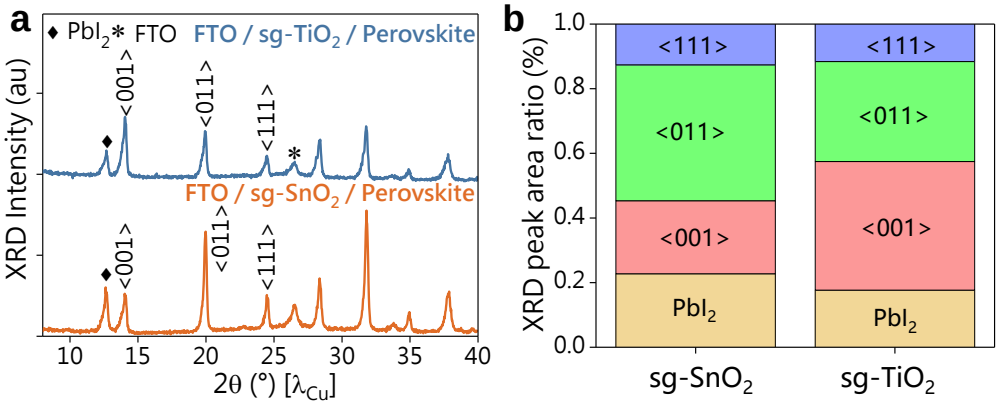

***Figure 14**: **a)** X-Ray diffraction patterns and **b)** Corresponding XRD peak area ratio of slot-die coated layers on FTO/sg-SnO_2 and FTO/sg-TiO_2.*

- **Time-resolved photoluminescence**

To further assess the quality of the perovskite layer deposited on both ETLs, we extracted the charge carriers lifetime from a time-resolved photoluminescence (TRPL) measurement. The monitoring of the PL signal over time provides insights on the recombination mechanisms in the perovskite material or at the substrate/perovskite interface [271]. In the literature, the experimental decay profiles can be fitted using a bi-exponential model:

$$y = y_0 + A_1 e^{-(x-xo)/t1} + A_2 e^{-(x-xo)/t2},$$

where the first decay (short decay t_1) is rather related to charge extraction or recombination at the interface while the second (longer decay t_2) is related to charge recombination in the bulk [271,272]. Typical values for the charge carrier lifetime in the perovskite bulk for spin-coated perovskite films span a wide range from 100 ns to 8 µs, depending on the perovskite composition, processing and potential post-treatments [273,274,50].

Here, we recorded the TRPL decays of perovskite layers coated on sg-SnO_2 and sg-TiO_2 and extracted the average decay lifetimes of 147 ± 10 ns and 124 ± 10 ns respectively (**Figure 15**). The 'bulk' recombination decay (t_2 ~ 210 ± 5 ns) was similar on both ETLs, indicating a similar charge recombination behaviour in both absorbers. The initial decay (t_1) was slightly shorter (t_1 = 4.8 ± 1 ns) on FTO/sg-TiO_2 compared to FTO/sg-SnO_2 (t_1 = 5.6 ± 1 ns).

In the literature, a shorter t1 value can either be attributed to enhanced charge extraction or to enhanced recombination at the ETL/Perovskite interface (due to a change in the perovskite quality in this region) [272]. Here, the values being overall very close, we suggest that the charge extraction properties were comparable for both ETLs. More generally, those values are comparable with the literature for slot-die coated methylammonium-free perovskite such as Yang *et al.* who demonstrated TRPL lifetimes between 100 and 200 ns [91].

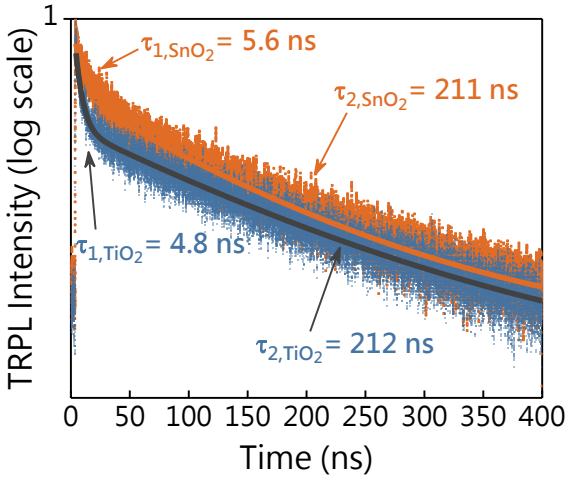

***Figure 15**: Time-resolved photoluminescence (TRPL) of slot-die coated layers on FTO/sg-SnO_2 and FTO/sg-TiO_2.*

In summary, the perovskite layer deposited on the FTO/sg-TiO_2 substrate had similar film thickness, grain size and absorption properties compared to the sg-SnO_2 reference sample and exhibited a selective formation of the α-CsFAPbIBr cubic structure (detailed matrix available in **Appendix 2B**). The similarity of the slot-die coated layers properties, when deposited on both ETLs, was in line with existing literature for spin-coated layers [15,18].

The only difference in the sg-TiO_2 sample was the change of the perovskite grains preferential orientation ((001) plan was preferred on FTO/sg-TiO_2), resembling more the ITO/np-SnO_2 sample studied earlier than the FTO/sg-SnO_2 sample prepared in the same conditions. Despite this variation, similar charge carriers lifetimes were observed in the bulk of both perovskite layers (t_2 ~ 210 ns). In the literature, the effect of the perovskite orientation on the perovskite opto-electronic properties is not well studied for mixed-cations formulations. Yang *et al.* recently deposited $FA_{0.83}Cs_{0.17}PbI_{2.83}Br_{0.17}$ slot-die coated films on SnO_2 substrate with a preferential (001) orientation and similar charge carriers' lifetimes (100 - 200 ns) [91]. Therefore, we would suggest that the grain orientation does not particularly affect the charge mobility in the absorber (at a similar grain size).

Furthermore, the grain orientation seems linked to a combination of parameters including the the perovskite ink composition and coating conditions, relying less on the substrate nature. These observations suggest that the gas-quenching assisted crystallization

would rather follow a homogeneous nucleation. The precise nucleation mechanism (*e.g.* the growth direction upwards or downwards) is still under discussion in the literature [275].

V.3.3. Performances of devices with sg-SnO_2 and sg-TiO_2

In this study, we fabricated photovoltaic devices using either sg-SnO_2 (reference) or sg-TiO_2 as ETL material, both deposited by spin-coating.

- **Device architecture**

The only modification compared to the reference device structure (sg-SnO_2) is the use of sg-TiO_2 as electron transporting layer (**Figure16**). The SnO_2 and TiO_2 materials conduction band (CB) and valence band (VB) energy levels differ (**Figure 16**), resulting in a different energy alignment with the perovskite absorber. The deeper CB level of SnO_2 favours the electrons extraction and its deeper VB level results in enhanced holes blocking properties, hence SnO_2 has a better electron selectivity compared to TiO_2 [150,270]. This result has been demonstrated for both sol-gel [269] and nanoparticles based [270] process route for planar SnO_2 ETLs.

Further studies showed that the TiO_2 crystalline form (rutile or anatase) can affect the energy band alignment between perovskite and TiO_2. The band alignment between perovskite and rutile TiO_2 is more favourable compared to the perovskite/anatase TiO_2 contact [276]. However, the electron transport is 100 times slower in rutile compared to anatase TiO_2 [277]. Therefore, most TiO_2 materials used as ETL for perovskite solar cells are under the anatase form [155], with few exceptions such as Luo *et al.* who selectively formed rutile TiO_2 at the surface of anatase TiO_2 particles [278]. This hybrid approach took advantage of the two crystalline forms properties to appropriately match the two ETL roles in a solar device: electrons extraction and transport. The formation of the rutile phase depends on the sintering temperature used in the sol-gel process [279]. In our case (sintering at 500 °C), we were likely to form a planar TiO_2 layer predominantly under the anatase structure.

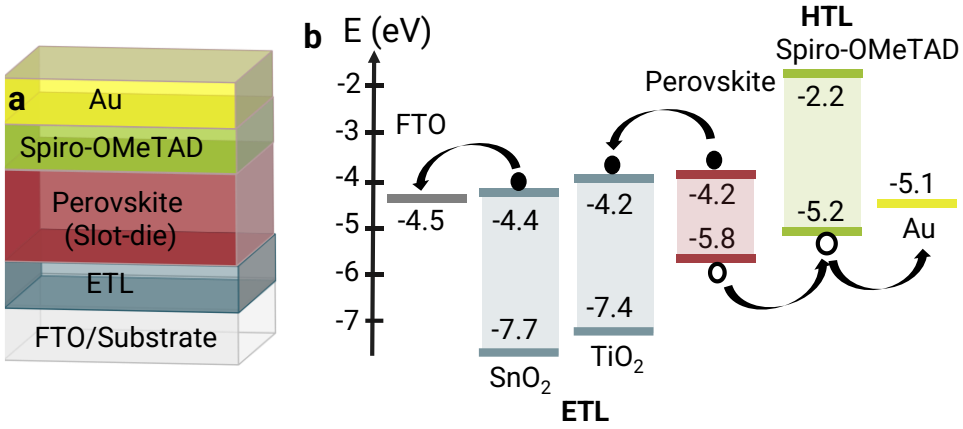

***Figure 16**: **a)** Device stack used in this chapter. **b)** Energy alignment diagram with values from the literature [205–207].*

- **Aging behaviour and day of performance reporting**

Regarding the maturation effect, we observed that sg-TiO_2 based device performances decreased after one day of storage in the dark at 50% relative humidity (**Appendix 4**). Consequently, the J-V curves and parameters are reported for a measurement at d0, right after device fabrication for these samples (**Figure 17**).

- **Device performance: comparison of sg-SnO_2 and sg-TiO_2 ETLs**

In the J-V curves under illumination (**Figure 17a**), the champion device of sg-TiO_2 yielded a power conversion efficiency of 15.9%, lower than the champion device on sg-SnO_2 (PCE = 17.5%). In average, the device performances of sg-TiO_2 based devices were comparable (13.5%) to the one obtained on sg-SnO_2 (13.6%).

The average V_{oc} values of the sg-TiO_2 devices were slightly lower (0.933 V) compared to the reference sg-SnO_2 devices (0.963 V) (**Figure 17d**). Similarly, the champion device V_{oc} was reduced on sg-TiO_2 (1.017 V compared to 1.049 V). The different band energy alignment of TiO_2 material could be responsible for this voltage loss, in respect to the sg-SnO_2 devices. This voltage loss adds on to V_{oc} limitation that was already observed for slot-die coated devices when compared to the spin-coated devices. In brief, two phenomena due to the perovskite quality and the ETL energy alignment limit the V_{oc} in the sg-TiO_2 devices.

The average fill factor of sg-TiO_2-based devices was similar (67.3%) compared to the sg-SnO_2 devices (66.4%). The best fill factor, however, was lower on sg-TiO_2 (72.4%) compared to sg-SnO_2 (75.1%). As the grain size was similar between both samples, we suggest that the charge extraction or the ETL/Perovskite quality could have differed in presence of TiO_2 compared to SnO_2.

For both ETLs, the average short-circuit current density was 21.1 $mA.cm^{-2}$ (**Figure 17d**). The current density of the best sg-TiO_2 based device (21.5 $mA.cm^{-2}$) was lower than on sg-SnO_2 (22.2 $mA.cm^{-2}$). This could be partially explained by the substrate transmission loss observed for the FTO/sg-TiO_2 substrate (shift at $\lambda \sim 320$ nm, **Figure 2**). Moreover, the crystalline PbI_2 peak area ratios were similar on sg-SnO_2 and sg-TiO_2 (18 and 23% respectively) and lower than the crystalline PbI_2 ratio present in the spin-coated layer (27%, see **Chapter III**). Consequently, the PbI_2 presence cannot be responsible for the lower current density. As comparable charge carriers lifetime as been measured on sg-SnO_2 and sg-TiO_2, the transport properties in the absorber should not be responsible for the J_{sc} loss. However, a slight variation of the TRPL first decay value on sg-TiO_2 could indicate a more defective ETL/perovskite interface, in line with the lower FF observed. Thus, we suggest that the charge recombination at the ETL/Perovskite interface was limiting the J_{sc} of sg-TiO_2 based devices.

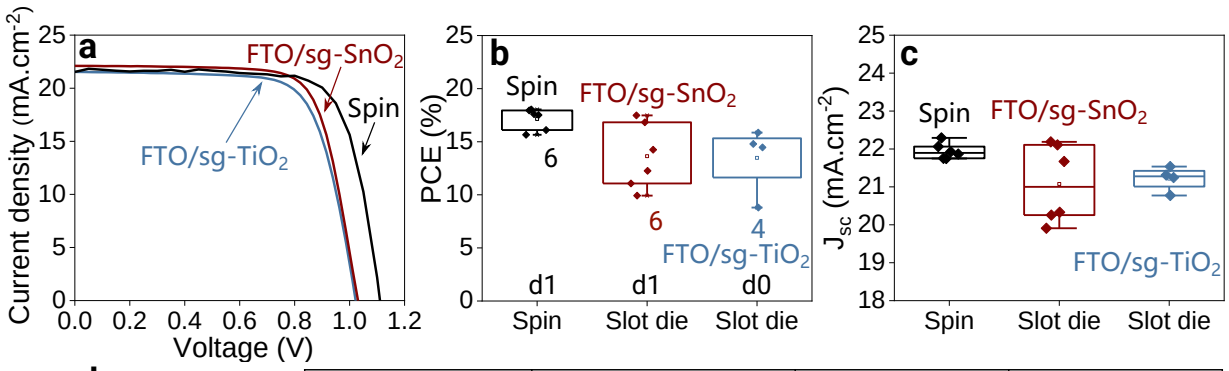

d

	V_{oc} (V)	J_{sc} (mA.cm^{-2})	FF (%)	PCE (%)
Spin ITO/np-SnO_2 (d1)	1.090 ± 0.023 *1.108*	21.9 ± 0.4 *21.8*	71.7 ± 5.1 *74.9*	17.1 ± 1.5 *18.0*
Slot-die FTO/sg-SnO_2 (d1)	0.963 ± 0.132 *1.049*	21.1 ± 1.2 *22.2*	66.4 ± 8.7 *75.1*	13.6 ± 3.8 *17.5*
Slot-die FTO/sg-TiO_2 (d0)	0.933 ± 0.218 *1.017*	21.1 ± 0.4 *21.5*	67.3 ± 8.0 *72.4*	13.5 ± 4.7 *15.9*

***Figure 17**: **a)** J-V curves of the best device per batch (measured at do or d1). **b)** Statistics of power conversion efficiencies. **c)** Statistics of short-circuit current densities. **d)** Summary of J-V parameters for the three conditions. The parameters of the champion devices plotted on panel a) are in italic.*

Besides the planar ETLs, mesoporous ETLs have been successfully implemented to fabricated efficiency perovskite photovoltaic devices [58]. The advantage of a mesoporous ETL is the increased surface contact between the ETL and the perovskite layer, resulting in enhanced charge extraction at that device interface and better photovoltaic performances [139,145]. In the next section, we will investigate a state-of-the-art mesoporous TiO_2 (m-TiO_2) layer as electron transport layer and its compatibility with the slot-die coating process.

V.4. Comparison of planar and mesoporous TiO_2 ETLs

In contrary to planar ETLs, mesoporous ETLs can affect the meniscus coating of the precursor wet film as a competition happens between the precursor ink infiltration and crystallization at the surface of the ETL [280]. In this work, we aim is to assess whether the as-developed slot-die coating process is compatible with mesoporous ETLs substrates and to determine the TiO_2 scaffold thickness maximizing device performance.

First, we will introduce the mesoporous layer properties, then the properties of the perovskite layer deposited on top of m-TiO_2 with various thicknesses and the corresponding device performances. We will compare those results to reference devices using the planar TiO_2 ETL (sg-TiO_2).

V.4.1. ETL layers properties: sg-TiO_2 and m-TiO_2

The mesoporous TiO_2 layers were deposited by screen-printing using a commercial TiO_2 paste (see **Chapter II**), with TiO_2 nanoparticles with a diameter of 30 nm. This stock solution was diluted with terpineol to reach the 1 : 5.5, 1 : 4.5 and 1 : 3.5 volume ratios to obtain mesoporous TiO_2 layer thicknesses of 100, 150 and 250 nm respectively (**Table 5**). We used the same post-annealing step as sg-TiO_2 to transform the precursor into TiO_2 layer (500 °C for 1 h in air). In the literature, Zhang *et al.* reported the formation of the TiO_2 anatase using both spin-coated and screen-printed methods [281]. Here, both TiO_2 materials (Dyesol paste or sol-gel approach [279]) were expected to form anatase TiO_2.

The surface roughness of m-TiO_2 layers was slightly higher (R_a ~ 30 nm) compared to sg-TiO_2 substrate (R_a ~ 15 nm) but both were still negligeable in relation to the precursor wet film thickness (~1 µm). The mesoporous TiO_2 scaffolds thicknesses (100 - 250 nm), however, approached the precursor wet film thickness range and could be expected to interfere in the perovskite crystallization. In the literature, the mesoporous scaffold porosity and thickness is well known to influence the perovskite infiltration, the 'capping layer' crystallization (see **Chapter I**) and the resulting device performance [262].

ETL designation	**sg-TiO_2** (anatase)	**m-TiO_2** (anatase)		
TCO	FTO			
morphology	planar	mesoporous		
fabrication method	sol-gel ($Ti(OBu)_4$ in EtOH)	TiO_2 paste in terpineol		
dilution volume ratio	-	1 : 5.5	1 : 4.5	1 : 3.5
deposition process	Spin-coating	Screen-printing		
post-annealing (atmosphere)	500 °C – 1 h (in air)			
average roughness	15 nm	30 nm		
ETL thickness	30 nm	100 nm	150 nm	250 nm

***Table 5**: Substrates compared in this section.*

V.4.2. Perovskite layer properties on sg-TiO_2 and m-TiO_2

- **Morphology**

The slot-die coated layers deposited on the various m-TiO_2 substrates were all compact and exhibited a perovskite capping layer thickness comprised between 470 nm and 500 nm (**Figure 18a**). We noticed that for some m-TiO_2 scaffold thicknesses (150 and 250 nm), the grain size of the perovskite capping layer increased (**Figure 18b**) from g = 450 nm (sg-TiO_2) to 500 nm in average. Grains as large as of 700 nm are visible in the SEM top image (**Figure 19c-d**). For the thinner m-TiO_2 scaffold (100 nm), the grain size decreased to g = 300 nm (**Figure 18b**). Those observations confirmed the interaction between the infiltration into the mesoporous scaffold and the morphology of the capping layer, which has been previously reported in the literature [262].

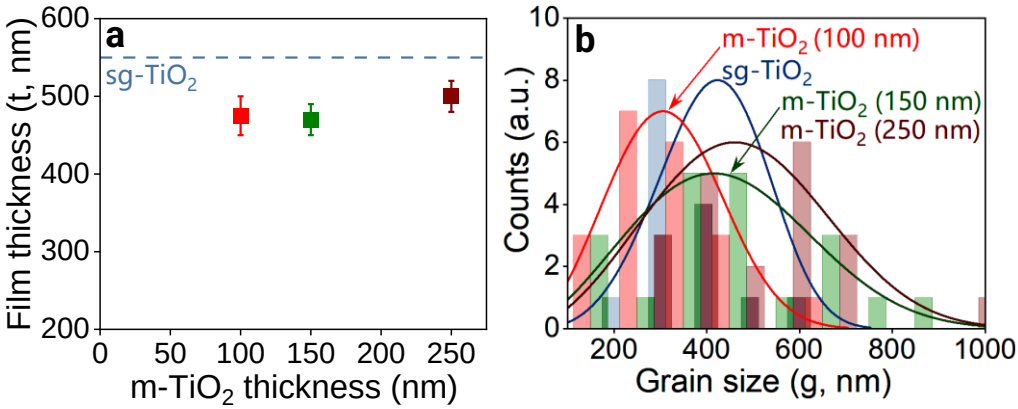

***Figure 18**: **a)** Thicknesses of the slot-die coated layers on the m-TiO_2 ETLs. **b)** Grain distributions of the slot-die coated layers coated on sg-TiO_2 (planar) and m-TiO_2 layers with various thicknesses.*

The SEM cross-section images of the devices fabricated with the various ETLs informed us on the capping layer vertical morphology and TiO_2 scaffold infiltration. Here, we observed that the grain size increase was linked to the presence of a monolithic perovskite capping layer (**Figure 19c-d**). This observation suggested that the presence of mesoporous TiO_2 did influence the crystallization, leading to larger perovskite grain for TiO_2 scaffolds thicker than 150 nm. In the literature, similar observations of the influence of the mesoporous scaffold thickness on the perovskite capping layer morphology were reported [262,280].

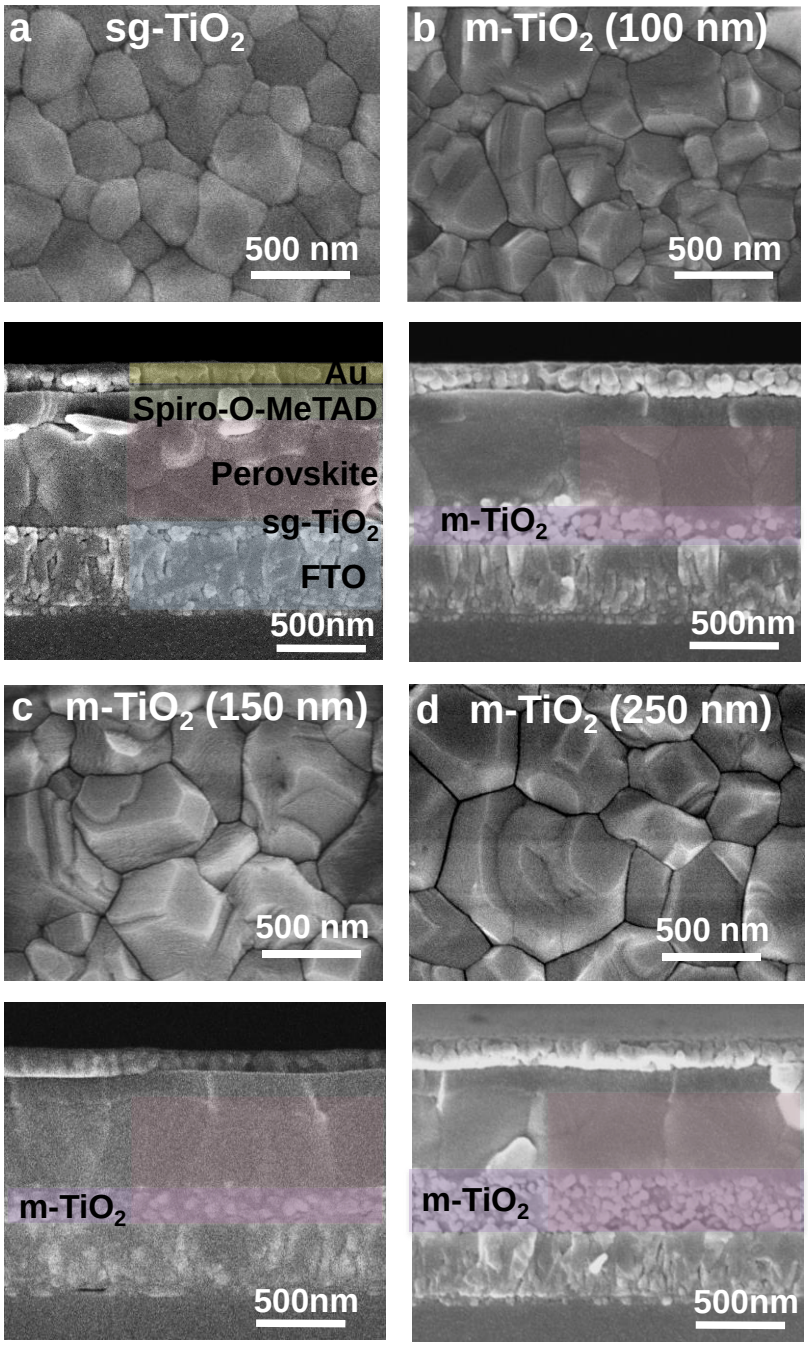

***Figure 19**: Slot-die coated layer top and cross-section SEM images on various ETLs substrates. **a)** sg-TiO_2, **b)** m-TiO_2 (100 nm), **c)** m-TiO_2 (150 nm) and **d)** m-TiO_2 (250 nm).*

We performed additional cross-section images with a lower magnification to assess the homogeneity of the perovskite infiltration in the mesoporous TiO_2 scaffold over larger areas (10 µm, **Figure 20**). The infiltration homogeneity varied with the TiO_2 scaffold thickness: the 100 and 150 nm thick m-TiO_2 scaffolds were fully infiltrated (**Figure 20a**), whereas partially infiltrated areas were detected in the 250 nm thick TiO_2 scaffold (**Figure 20b**) with the presence of micrometric voids (500 nm – 1 µm).

Here, we observed a threshold m-TiO_2 scaffold thickness (150 nm) under which the scaffold was homogeneously infiltrated using the slot-die coating process. This value probably depended on the delay time (~ 3.6 s) between the coating and gas-quenching steps, during which the precursor ink can infiltrate the scaffold before being crystallized by the gas-knife. Overall, the TiO_2 scaffold thickness maximizing the capping layer grain size while retaining a good infiltration by the precursor solution had a scaffold thickness of 150 nm.

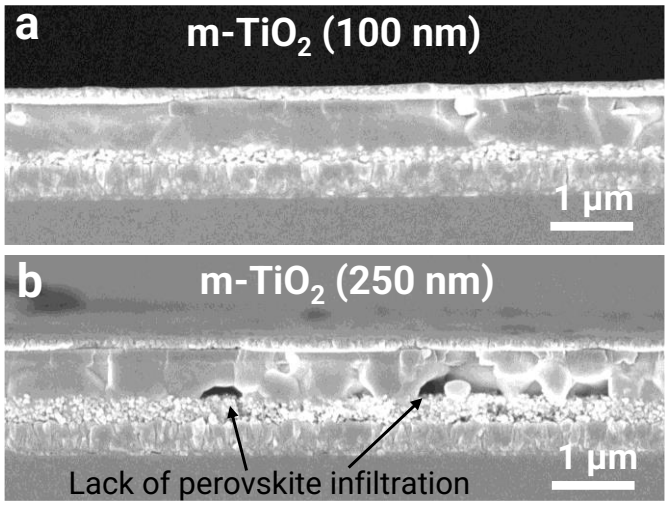

***Figure 20**: SEM cross-section of **a)** FTO/m-TiO_2 (**100 nm**)/Perovskite/Spiro/Au and **b)** FTO/m-TiO_2 (**250 nm**)/Perovskite/Spiro/Au.*

- **Optical properties**

We recorded the absorption of the slot-die coated layers deposited on m-TiO_2 with TiO_2 scaffold thicknesses of 100, 150 and 250 nm (**Figure 21a**). The film deposited on m-TiO_2 (250 nm) showed a higher absorption onset, in line with its larger perovskite thicknesses (250 nm of partially infiltrated scaffold and 500 nm of perovskite capping layer). The band gap extracted by the Tauc plot method was E_g = 1.62 eV for all the slot-die coated layers (**Figure 21b**), confirming that the substrate morphology did not affect the absorber band gap.

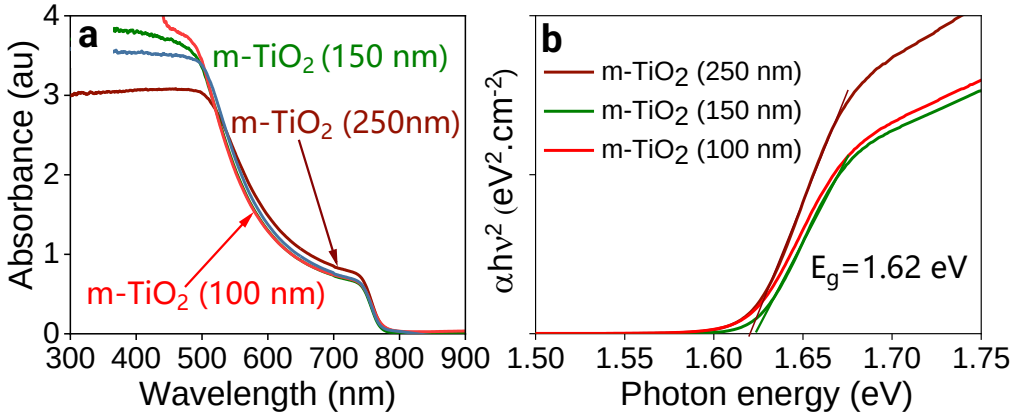

***Figure 21**: **a)** Absorbance curves. **b)** Corresponding band gap extraction via Tauc plot method.*

To decorrelate the presence of a mesoporous ETL and the change of grain size in the capping layer, we focused on the comparison between m-TiO_2 (100 nm) and sg-TiO_2 samples.

- **Crystallinity**

The formation of the α-CsFAPbIBr perovskite was confirmed on sg-TiO_2 and m-TiO_2 (100 nm) by the presence of its signature peaks at 2θ = 13.8°, 19.7° and 24.3°, corresponding respectively to the (001), (011) and (111) plans (**Figure 22a**). We noticed the reduced relative intensity of the (001) and (111) perovskite peaks at 2θ = 13.8° and 24.3°, suggesting that the presence of the m-TiO_2 scaffold favours the (011) orientation over the others (**Figure 22b**).

In the same proportions than the (001) perovskite peak, the crystalline PbI_2 peak intensity decreased (**Figure 22a**), suggesting that the presence of the mesoporous scaffold also affects this by-product formation (XRD peak area ratio decrease from 18 to 10%, **Figure 22b**). This could indicate that the crystallization of the infiltrated solution follows a different mechanism than the capping layer crystallization, leading to a variation of crystalline PbI_2 content in the final film and a preferential orientation of the perovskite crystals.

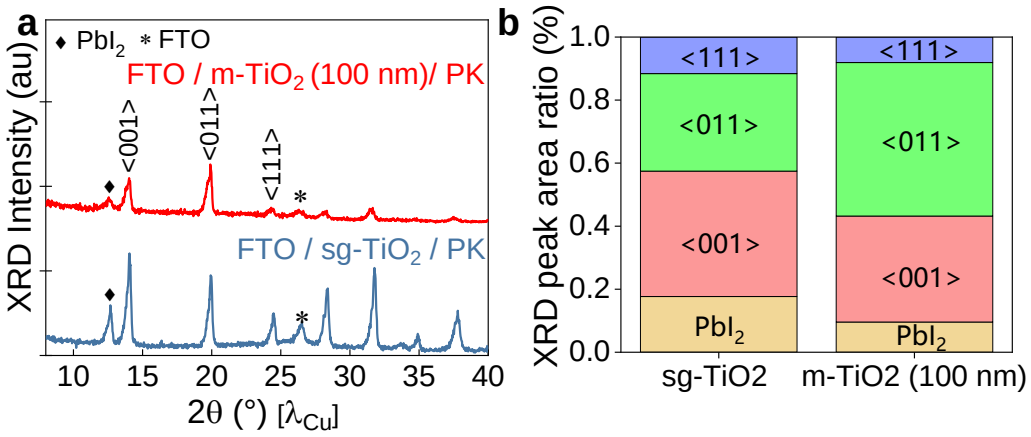

***Figure 22**: **a)** X-Ray diffraction patterns and **b)** Corresponding XRD peak area ratio of slot-die coated layers on FTO/sg-TiO_2, FTO/c-TiO_2 and FTO/c/m-TiO_2 (100 nm).*

- **Time-resolved photoluminescence**

We performed the time-resolved photoluminescence (TRPL) measurement of the perovskite film coated on m-TiO_2 (100 nm) to confirm our steady-state PL observations (**Figure 23**). When the structure was modified from planar to mesoporous, both time constants (t_1 and t_2) varied. The t_1 value slightly increased from 4.8 ns to 6.4 ns, indicating of a less defective ETL/Perovskite interface or of a slower charge extraction at that interface. The t_2 value, however, decreased from 212 ns (sg-TiO_2) to 155 ns in the m-TiO_2 (100 nm) sample. Both values are comprised in the range of the literature [91]. The lower t_2 value could reflect a lower perovskite absorber quality, in line with the lower perovskite XRD peaks intensity observed for this sample.

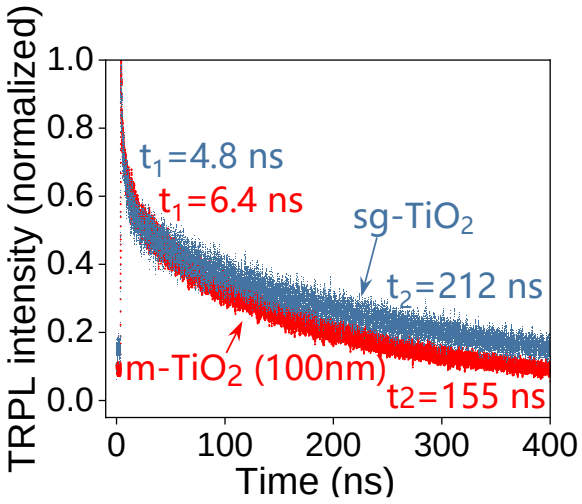

***Figure 23**: Time-resolved photoluminescence of slot-die coated layers on sg-TiO_2 and m-TiO_2 (scaffold thickness of 100 nm).*

In summary, the m-TiO_2 scaffold thickness influenced the capping layer morphology, with enhanced grain size for TiO_2 thicknesses of 150 and 250 nm. However, the quality of the perovskite absorber (crystallinity, charge carriers' lifetimes in the absorber - t_2) seemed lower on the mesoporous TiO_2 layer compared to planar TiO_2 ETL. The full characterization matrix is available in **Appendix 2C**. The 150 nm thick m-TiO_2 showed both a good perovskite ink infiltration inside the scaffold and a capping layer with enhanced grain size. The next section will present the implementation of those layers into photovoltaic devices.

V.4.3. Performances of devices with sg-TiO_2 and m-TiO_2

In this study, we fabricated photovoltaic devices with either a mesoporous (m-TiO_2) or a planar (sg-TiO_2) TiO_2 ETL. We reported the device performances with the same methodology than sg-TiO_2 (**Figure 17**). In particular, the J-V measurements of m-TiO_2 devices were performed right after device fabrication (d0), when the highest performance was measured for sg-TiO_2 devices. The detailed device data is provided in **Appendix 5**.

The integration of a mesoporous TiO_2 layer led to functioning devices with average power conversion efficiency of 12.7%, 10.7% and 7.9% for the TiO_2 scaffold thicknesses of 100, 150 and 250 nm respectively (**Figure 24d**). The best champion efficiencies were 13.4%, 13.2% and 7.9% respectively. These device performances are lower than the average PCE of 13.5% and the champion PCE of 15.9% obtained on planar TiO_2 (sg-TiO_2), mainly due to lower J_{sc} and FF values.

We found that the V_{oc} of devices with an inhomogeneous perovskite infiltration (250 nm of m-TiO_2) was reduced (0.879 V) compared to devices with good perovskite infiltration (100 and 150 nm of m-TiO_2) (0.980 V in average). The average V_{oc} values of infiltrated devices, however, were the highest achieved so far, larger than the planar TiO_2 (0.933V average V_{oc}) and planar SnO_2 (0.963 V). The higher open-circuit voltages achieved in a mesoporous configuration can be explained by the larger surface contact between the ETL and the perovskite absorber when good infiltration is achieved.

The device fill factor (FF) was limited in the thick TiO_2 scaffold sample (47%), possibly due to the incomplete perovskite infiltration. For fully infiltrated devices, we could have expected an increase of the device fill factor with the perovskite capping layer grain size. However, the device with larger capping layer grain size did not lead to a better fill factor (60.4% in average, 65.8% for champion) compared to the small capping layer grain size sample (64.5% in average, 68.0 for champion). We concluded that the mesoporous ETL presence controls the device FF: the thinner the m-TiO_2 layer, the higher the FF, independently of the capping layer grain size observed.

The current density was inversely related to the m-TiO_2 scaffold thickness (**Figure 24c**). Despite its higher absorption, the 250 nm sample current density was limited, most likely due to the poor perovskite ink infiltration in this sample that limited the current extraction to the ETL. For both infiltrated devices, the current density increased from 18.0 mA.cm^{-2} to 20.1 mA.cm^{-2} in average when the scaffold thickness decreased from 150 to 100 nm. The best J_{sc} of 19.7 mA.cm^{-2} (achieved at 100 and 150 nm) was limited compared to the planar sg-TiO_2 sample (best J_{sc} = 21.5 mA.cm^{-2}), possibly due a lower light transmission in the mesoporous TiO_2 layers [ ]. Furthermore, the thinner the m-TiO_2 thickness, the narrower the current density distribution. Which is desirable to fabricate large-area devices with a high fabrication yield and device performance consistency.

Overall, the performance of m-TiO_2-based devices was limited by the current density (- 1 mA.cm^{-2}) and the fill factor (- 5 points for champion device) compared to planar sg-TiO_2 (**Figure 24d**). Mesoporous ETLs, if optimized in terms of infiltration, exhibited higher average open-circuit voltage compared to the planar ETLs studied earlier, suggesting a better ETL/Perovskite interface in this device structure.

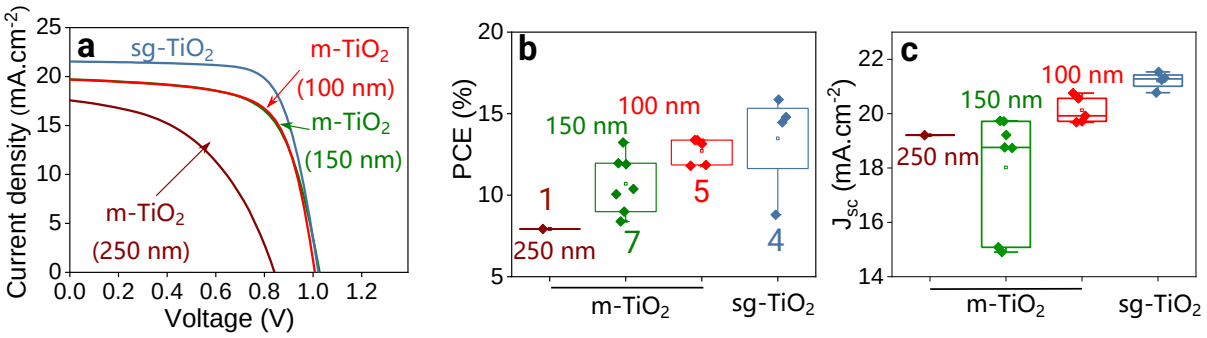

d

	V_{oc} (V)	J_{sc} (mA.cm^{-2})	FF (%)	PCE (%)
Slot-die sg-TiO_2 (d0)	0.933 ± 0.218 *1.017*	21.1 ± 0.4 *21.5*	67.3 ± 8.0 *72.4*	13.5 ± 4.7 *15.9*
Slot-die m-TiO_2 (250 nm, d0)	0.879	19.2	47.0	7.9
Slot-die m-TiO_2 (150 nm, d0)	0.981 ± 0.109 *1.020*	18.0 ± 3.1 *19.7*	60.4 ± 5.5 *65.8*	10.7± 2.5 *13.2*
Slot-die m-TiO_2 (100 nm, d0)	0.980 ± 0.020 *1.000*	20.1 ± 0.6 *19.7*	64.5 ± 6.0 *68.0*	12.7 ± 0.9 *13.4*

***Figure 24**: **a)** J-V curves of the best device per batch (measured at d0 or d1). **b)** Statistics of power conversion efficiencies. **c)** Statistics of short-circuit current densities. **d)** Summary of J-V parameters for the four ETLs studied. The parameters of the champion devices plotted on panel a) are in italic.*

In conclusion of this extensive study of the ETL influence on the perovskite layer properties and device performance, we identified (sg-SnO_2) as the ETL providing the highest power conversion efficiency. The next section will present the developments made towards large-area devices fabricated on the sg-SnO_2 ETL.

V.5. Towards large-area devices

In the section **V.2.2**., we presented the performance distribution for the sg-SnO_2 devices with power conversion efficiencies (PCE) ranging from 9 to 17% (average and champion devices). In the literature, Di Giacomo *et al.* fabricated 32 devices at various locations of a slot-die coated film deposited on a 6 x 6 inches substrate yielded similar PCEs ranging from 4 to 17% [75]. Device performance reproducibility of perovskite solar cells is a major concern [16,282] and can be interpreted as spatial performance inhomogeneities when the devices are fabricated from large-area substrates. Consequently, our first aim towards large-area devices was to improve the consistency of our devices performances on the FTO/sg-SnO_2 substrate.

V.5.1. Reduction of the device performance distribution

In the literature, the treatment of large-area electron transporting layers has been proven successful to improve the substrate homogeneity and, consequently, the perovskite solar cells performance consistency. For instance, Anaraki *et al.* introduced a chemical bath deposition step (CBD) to improve the SnO_2 ETL layer homogeneity over large areas [148]. The CBD is a chemical process during which a thin conformal SnO_2 layer is deposited on top of the spin-coated SnO_2 layer to improve its coverage and ensure the continuity of the ETL selectivity over large areas. Here, we applied the same CBD method prior to the perovskite deposition to improve the ETL/Perovskite interface. The device performance showed an average power conversion efficiency of 16.9%, open-circuit voltage of 0.999 V, fill factor of 76.5% and short-circuit current density of 21.8 $mA.cm^{-2}$ (**Figure 25**). The champion device exhibited a PCE of 18.03%, V_{oc} of 1.020V, fill factor of 78% and J_{sc} of 22.4 $mA.cm^{-2}$.

The champion device obtained in this batch exhibited a higher PCE (18.03%) compared to the previous champion device fabricated from the sg-SnO_2 ETL (PCE = 17.5%). In particular, the average device fill factors in the CBD treated batch were significantly higher (FF = 76.2%) compared to the batch without CBD (FF = 66.4%), and even higher than the champion spin-coated device (FF = 71.7%). The tremendous fill factor increase upon SnO_2 treatment indicates that the ETL/Perovskite interface was limiting the performances in the initial sg-SnO_2 samples.

We noticed, nonetheless, that the slot-die coated devices open-circuit voltages remained lower (0.986 V in average), independently of the CBD step, compared to the spin-coated devices V_{oc} (1.090 V in average). This V_{oc} limitation appeared independent of the ETL/Perovskite interface quality, suggesting that other factors such as the slot-die coated perovskite intrinsic properties are responsible for the open-circuit voltage limitation in those devices.

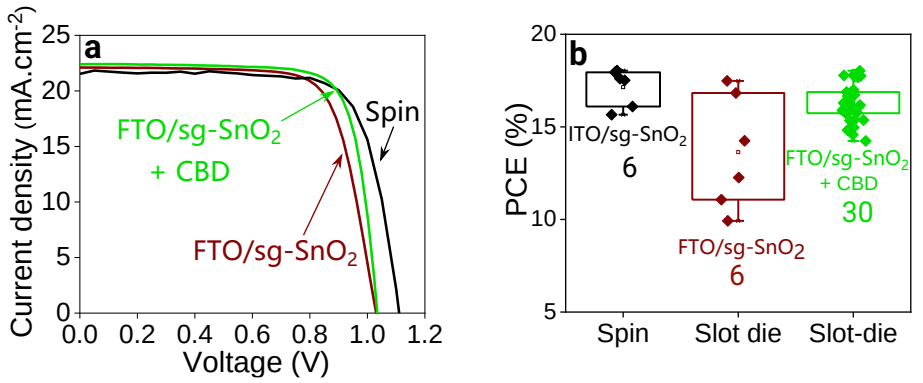

c	V_{oc} (V)	J_{sc} (mA.cm^{-2})	FF (%)	PCE (%)
Spin ITO/np-SnO_2 (d1)	1.090 ± 0.023 *1.108*	21.9 ± 0.4 *21.8*	71.7 ± 5.1 *74.9*	17.1 ± 1.5 *18.0*
Slot-die FTO/sg-SnO_2 (d1)	0.963 ± 0.132 *1.049*	21.1 ± 1.2 *22.2*	66.4 ± 8.7 *75.1*	13.6 ± 3.8 *17.5*
Slot-die (d1) FTO/sg-SnO_2 + CBD	0.986 ± 0.056 *1.024*	21.45 ± 1.1 *22.4*	76.2 ± 9.2 *78.6*	16.3 ± 2.1 *18.0*

***Figure 25**: **a)** J-V curves of the best device per batch (measured at d1). **b)** Statistics of power conversion efficiencies. **c)** Summary of J-V parameters for the four ETLs studied. The parameters of the champion devices plotted on panel a) are in italic.*

In the literature, Liu *et al.* identified the pH of the SnO_2 surface as a factor influencing the ETL/Perovskite interface [283]. Following their methodology, we quantified the pH of the substrate surface by rinsing it with a fixed volume of deionized water (1 mL), and subsequently measuring the pH of the rinsing solution (**Figure 26**). Interestingly, we found that the pH of the rinsing solution increased from 3 – 4 (sg-SnO_2 initial) to 5 - 6 (CBD-treated sg-SnO_2), suggesting that this treatment contributed to the neutralization of the substrate surface. In their work, Liu *et al.* reported a similar neutralization effect after the CBD treatment, which was favorable to the device performances. Here, this neutralization effect could explain the gain in performance compared to the previous batch. Further characterization of the perovskite layer on the CBD-treated sg-SnO_2 are a perspective of this work to elucidate the origin of this FF increase.

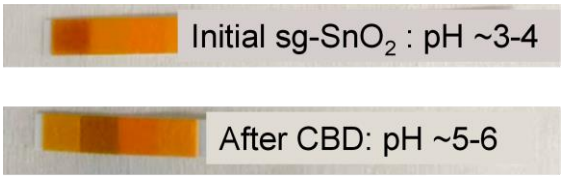

***Figure 26**: pH of a rinsing aqueous solution from the sg-SnO_2 substrate initially (top) and after the CBD treatment (bottom).*

As the champion device was obtained in this batch, we recorded additional measurements (i.e. forward bias JV curves, electron quantum efficiency and maximum power point tracking) that are typical for perovskite solar cells devices (**Figure 27**).

We observed a slight hysteresis between the J-V curves measured in forward bias compare to the ones measured via the reverse bias (reference) (**Figure 27a**). Both devices fabricated from slot-die coated and spin-coated absorbers exhibit a comparable behaviour (see **Appendix 6**) in the first device structure (ITO/SnO_2/Perovskite/PTAA/Au). The hysteresis occurs as a variation of open circuit voltage (~ 70 mV) between JV curves measured in the forward compared to the reverse bias. A change of V_{oc} could be due to a variation of the charge transfer mechanisms with the scanning direction [284].

Hysteresis in JV curves of perovskite solar cells is known in the literature [285] and can be caused by interfacial or to transient phenomena including ion migration at the device interfaces. At the ETL/Perovskite interface, ethylenediamine tetraacetic acid (EDTA) post-treatment [286], or the addition of self-assembled monolayer (SAMs) molecules [287] or of a phenyl-C61-butyricacid methyl ester (PCBM) layer [288] between the SnO_2 and the perovskite are successful strategies to reduce the perovskite solar cells hysteresis. In this work, we observed a less pronounced hysteresis behaviour when SnO2 (with CBD step) was used as an ETL (**Figure 27a**). We therefore propose that the modification of the ETL/Perovskite interface (by modification of the SnO_2 properties) did reduce the hysteresis phenomenon by improving the charge extraction at the SnO2/Perovskite interface.

In summary, the presence of hysteresis behaviours in the JV curves of the perovskite solar cells presented in the frame of this work was not significantly influenced by the deposition technique used to coat the perovskite layer, but rather depended on the device structure employed.

The internal quantum efficiency of the solar cell span homogeneously in the 300 - 780 nm wavelength range with values over 80% (**Figure 27b**). The integrated current (21.24 $mA.cm^{-2}$) was slightly lower than the current measured from the J-V curves (22.4 $mA.cm^{-2}$), showing a current mismatch (~1 $mA.cm^{-2}$) within the range of the literature [289].

Lastly, the maximum power point tracking of the device under nitrogen atmosphere for 120 minutes under illumination showed a constant performance over 120 minutes under illumination at ambient temperature (**Figure 27c**). The stabilized power conversion efficiency was 16.8% for the cell shown in **Figure 27c**.

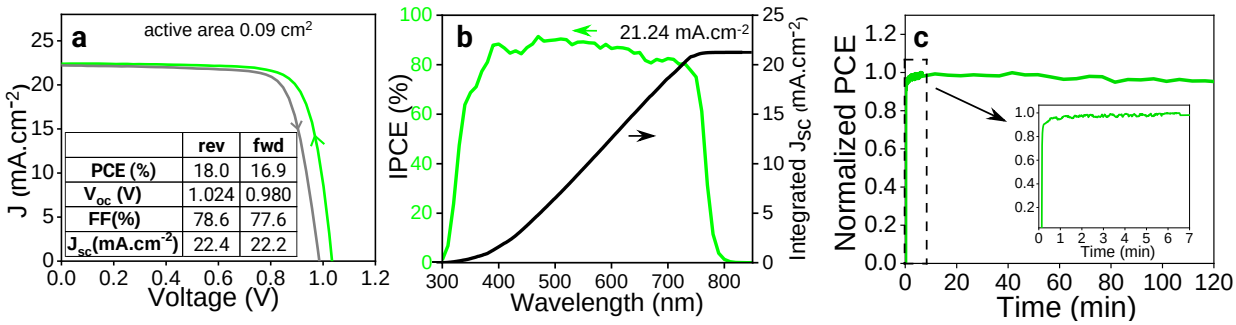

***Figure 27**: **a)** J-V curves of the best device per batch (measured in both forward and revers biais). **b)** Internal quantum efficiency (IQE) measurement and. **c)** Maximum power point tracking under nitrogen at ambient temperature for the champion device with FTO/sg-SnO_2/CBD-SnO_2/Perovskite/Spiro-OMeTAD/Au architecture.*

Now that consistent device performances were obtained for laboratory scale devices (active area 0.09 cm²), with to the SnO_2 ETL post-treatment, we assessed the perovskite layer homogeneity over the 10 x 10 cm² substrate.

V.5.2. Spatial perovskite layer homogeneity

To study the perovskite layer homogeneity with a high spatial resolution, we took a picture of the sample using a backlit light (**Chapter II**). On the sample picture, the perovskite layer became lighter in the direction of coating (**Figure 28a**). We used a purpose-develop algorithm (PerovskiteVision, **Chapter II**) to extract a thickness map from the sample image (**Figure 28b**). The perovskite film thickness decreased from 600 nm to 450 nm (- 25%) between the beginning and the end of coating. This thickness variation can explain the modification of the perovskite layer absorption at the end of the coating (**Figure 28c**) and was obviously not desirable for large area devices fabrication.

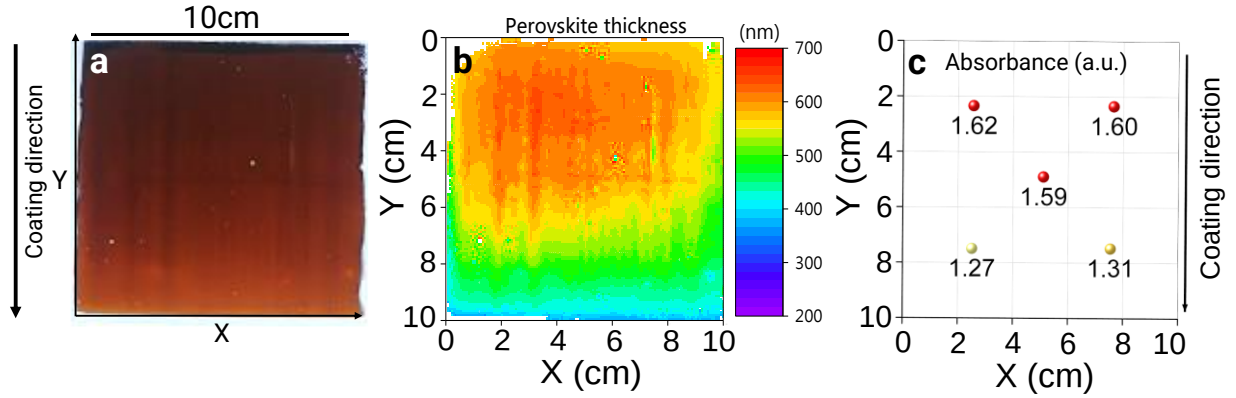

***Figure 28**: **a)** Picture of a 10 x 10 cm² slot-die coated perovskite layer using a backlit light. **b)** Perovskite thickness mapping (resolution 10 x 10 µm²) extracted from the sample image using PerovskiteVision. **c)** Film absorption at 600 nm. The standard deviation is ± 0.2 a.u.*

V.5.3. Spatial performance homogeneity

To assess the device performance spatial homogeneity, we fabricated devices at nine various locations on a 10 x 10 cm² substrate, resulting in the fabrication of 18 devices (2 devices per piece, see **Chapter II**) with the following structure: FTO/sg-SnO_2/CBD-SnO_2/Perovskite(slot-die)/Spiro-OMeTAD/Au (**Figure 29a**). The average power conversion efficiency for this batch was 16.9% and the champion PCE was 18.03%. Overall, the performance distribution was quite homogeneous, due to consistent V_{oc} and FF values, but we noticed a slight PCE decrease (- 10% or 1.7 point) between the beginning and the end of the coating (**Figure 29a**).

This PCE decrease was correlated with a current density decrease along the coating direction (**Figure 29e**). Based on the previous data on the perovskite layer homogeneity, we concluded that the perovskite film thickness variation reduced the absorption of light at the end of coating and hence the device current density. Here, a perovskite layer variation of – 150 nm (- 25%) was translated into a J_{sc} variation of - 1 mA.cm^{-2} (- 5%). This perovskite layer thickness inhomogeneity could be a limiting factor for the fabrication of efficient large-scale photovoltaic modules and its homogeneity improvement is a perspective of this work.

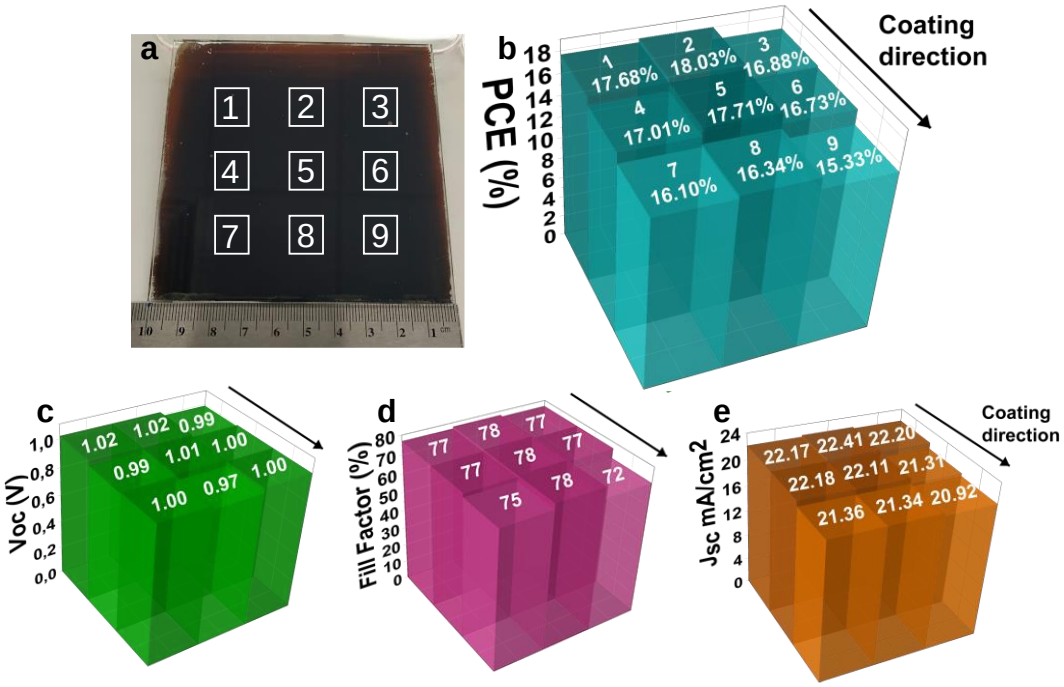

***Figure 29**: **a)** Picture of a 10 x 10 cm² slot-die coated layer, the device positions are indicated in white. **b)** Power conversion efficiency map, **c)** Open-circuit voltage map, **d)** Fill factor map and **e)** Current density map for the 18 devices in function of their location on the 10 x 10 cm² substrate.*

V.5.4. Large-area photovoltaic device on sg-SnO_2

Finally, we upscaled the as-developed process to investigate the processing of larger area devices using the same device structure (FTO/sg-SnO_2/CBD-SnO_2/Perovskite(slot-die)/Spiro-

OMeTAD/Au). The as-processed module design consisted in 13 stripes connected in series and had an active area of 52 cm² (**Figure 30a**). The module yielded a power conversion efficiency of 11.5%, with an open-circuit voltage of 12.36 V, a fill factor of 53.8% and a short-circuit current of 90 mA (**Figure 30b**).

Each stripe performance parameters can be extrapolated from the module parameters. The V_{oc} of the hypothetical stripe is defined as the total module V_{oc} divided by the number of stripes (series connection) and J_{sc} of the hypothetical stripe is defined as the total current flowing in the module divided by the hypothetical stripe area (equal to the active area divided by the number of stripes). The extracted V_{oc} and J_{sc} were 0.951 V and 22.51 mA.cm^{-2} respectively (**Figure 30c**). We then compared the device parameters obtained on the small devices fabricated with the same structure to the hypothetical stripe parameters. The loss in performance (- 36%) between the small device (PCE = 18%) and the module (PCE = 11.5%) was mainly due to a FF loss (- 30%) and a V_{oc} loss (- 6%).

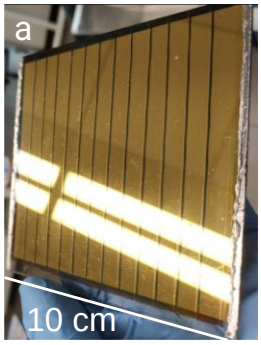

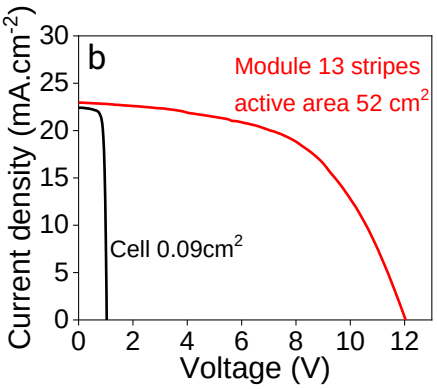

c	Lab device	Module (13 cells)	*hypothetical cell in module*
active area (cm^2)	0.09	52.0	*4.0*
PCE (%)	**18.0**	**11.5**	
V_{oc} (V)	1.024	12.36	*0.951*
J_{sc} (mA.cm^{-2}) or I_{sc} (A)*	22.4	0.090*	*22.5*
FF (%)	78.6	53.8	

***Figure 30**: **a)** Picture of the photovoltaic module fabricated over 52 cm² active area with 13 stripes with the FTO/sg-SnO_2/CBD-SnO_2/Perovskite (slot-die)/Spiro-OMeTAD/Au device structure. **b)** J-V curves of a 0.09 cm² device and of the module (measured in reverse bias). **c)** Comparison of the device electrical parameters and extraction of an hypothetical stripe electrical parameters from the module.*

The V_{oc} of the hypothetical stripe (0.951 V) was significantly lower than the champion device V_{oc} (V_{oc} = 1.024 V), and from the V_{oc} average (0.999 V) of laboratory scale devices. In the module, we noticed the presence of some pinholes in the perovskite layer. We therefore suggest that those pinholes could have created local shunts pathways and limit the V_{oc} in the module.

Furthermore, we observed a sharp decrease of the fill factor (FF = 53.8%) in the module compared to the small devices (FF = 76% in average). On the J-V curve of the module (**Figure 31b**), the lower fill factor value was due to significantly higher series resistance in this device. The high series resistance could for instance be due to interconnections losses between the stripes of the module. Thinner stripes are also desirable (actual stripe width ~ 7 mm) as the charge transport in the TCO can be limited over large areas [290].

Lastly, the extracted current density (J_{sc}) for one hypothetical stripe was 22.6 mA.cm^{-2}, in accordance with the champion small device value (J_{sc} = 22.41 mA.cm^{-2}). This result was surprising as we identified the current density as the factor limiting large-area device performance homogeneity. Further investigation on the current density prediction in large-area devices is a perspective of this work. Besides the J_{sc}, the perovskite thickness variation could affect the ETL/Perovskite interface and hence the device V_{oc}. Another perspective of this work would be to elucidate the cause of the V_{oc} loss in the module and its eventual link to the perovskite layer thickness variations.

Conclusion

In this chapter, we studied the properties of slot-die coated perovskite layers on three state-of-the-art electron transporting layers (ETLs): planar SnO_2, planar TiO_2 and mesoporous TiO_2. Slot-die coating appears as a versatile method yielding a compact morphology, similar band gap and selective perovskite conversion into the cubic structure on all three substrates. In presence of mesoporous ETL, the mesoporous thickness affected both the degree of infiltration (incomplete infiltration for thick m-TiO_2 layers) and the capping layer morphology (grain size increase for thicker m-TiO_2 layer).

We integrated the various ETLs into photovoltaic devices, yielding performances of 17.5% on planar SnO_2 (sg-SnO_2), 15.9% on planar TiO_2 (sg-TiO_2) and 13.4% on mesoporous TiO_2 (100 nm thick scaffold). The comparison of SnO_2 and TiO_2 materials confirmed that the energy alignment of the ETL affects the device performance (mainly V_{oc} and FF). On planar ETLs, the perovskite grain orientation and crystalline PbI_2 ratios did not significantly impact the device performances. The larger grain size observed in the second slot-die coating process, however, led to higher device fill factors. On mesoporous ETLs, relatively high V_{oc} were obtained, due to the enhanced ETL/Perovskite contact. Despite the higher V_{oc}, the TiO_2 scaffold limited the device FF and J_{sc} and its thickness had to be minimized. As the scaffold effect was predominant, the capping layer morphology (grain size) had limited effect on the performance.

Compared to spin-coated devices, the slot-die coated devices were limited in terms of FF and V_{oc} on planar ETLs, and of the J_{sc} and FF on mesoporous ETLs. One the one hand, the device fill factor was improved by adding a SnO_2 surface treatment via chemical bath deposition (CBD). This strategy could be applied to m-TiO_2 devices to improve their FF. On the other hand, the V_{oc} loss seemed due the lower intrinsic quality slot-die coated perovskite films related to the crystallization mean employed (gas-quenching).

Prior to large-area device fabrication, we used a chemical bath deposition (CBD) treatment to increase the SnO_2 ETL homogeneity, resulting in a narrower device performances distribution and higher device fill factors. We reported the contribution of the perovskite layer thickness inhomogeneity along the coating direction on the J_{sc} inhomogeneity (~1 $mA.cm^{-2}$). Despite this J_{sc} inhomogeneity, we fabricated a large-area module of 52 cm^2 active area with PCE of 11.5% with a correct current density. The FF and V_{oc} limitations observed in the module could be mitigated by further module design optimization (FF) and slot-die coated perovskite layers quality enhancement (V_{oc}).

Appendixes

Appendix 1: Maturation phenomenon of the champion devices.

Upon storage in the dark at controlled humidity, a maturation phenomenon happens in perovskite solar cells. This effect depends on the device architectures, the perovskite composition and the storage environment [ ]. In the literature, the underlying mechanisms behind the maturation phenomena are still unclear. Ho Baillie *et al.* observed that storage under limited humidity, can reduce the traps density in the perovskite film itself, shifting the HTL/perovskite energy alignment favourably and resulting in better V_{oc} and FF in the aged devices [291].

To illustrate this phenomenon, we plotted the J-V curves of the devices measured at d0 and d1 for the spin-coated and slot-die coated reference devices (**Chapters III-IV**, on ITO/np-SnO_2) and for the new device structure (on FTO/sg-SnO_2) (**Figure A1**). We observed that the maturation phenomenon was beneficial for the spin-coated device that encountered a V_{oc} gain upon 1 day of storage (**Figure A1a**). The slot-die coated layer in the initial device structure, however, exhibited an inverse maturation phenomenon, during which the V_{oc} decreased slightly after 1 day (**Figure A1b**). The slot-die coated device with the new device structure showed both J_{sc} and V_{oc} improvements upon storage (**Figure A1c**). In the new device structure, the high storage humidity (50% relative humidity compared to 30% initially) could have contributed to the larger J_{sc} change upon storage.

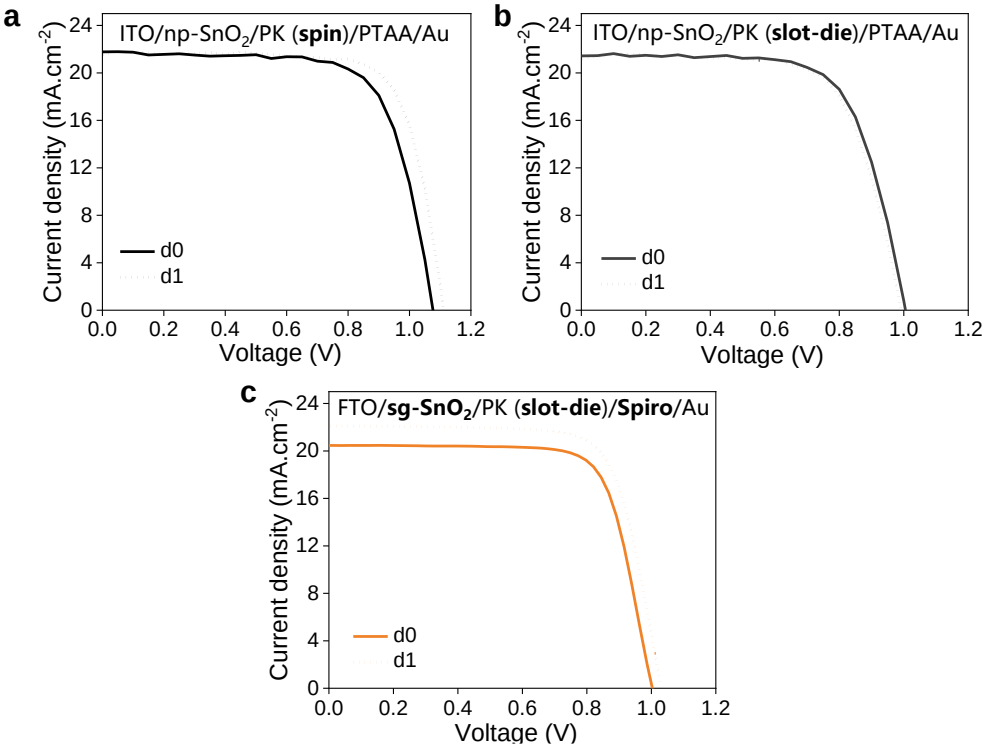

***Figure A1**: J-V curves at day 0 and day 1 for the champion device with a perovskite layer: **a)** Spin-coated on ITO/np-SnO_2, **b)** Slot-die coated on ITO/np-SnO_2 and **c)** Slot-die coated on FTO/sg-SnO_2.*

Appendix 2: Detailed perovskite layer properties comparisons.

- 2A: ITO/np-SnO_2 vs FTO/sg-SnO_2

	Slot-die coated films	ITO/np-SnO_2	FTO/sg-SnO_2
Morphology	coated area	A' = 18 cm^2	A' = 90 cm^2
	film coverage	c = 100%	c = 100%
	perovskite thickness	t = 575 nm	t = 550 nm
	film roughness	R_a = 10 nm	R_a = 15 nm
Zoom in	film compacity	c' = 100%	c' = 100%
	grain size	g = 273 nm	g = 400 nm
Optical	band gap	E_g = 1.62 eV	E_g = 1.62 eV
Crystallization	α-CsFAPbIBr	Yes	Yes
	Preferential orientation	(001)	(011)
	δ-$FAPbI_3$	No	No
	crystalline PbI_2	Yes (6%)	Yes (23%)

***Table A2-A**: Properties of slot-die coated layer deposited on np-SnO_2 and sg-SnO_2 ETLs.*

- 2B: FTO/sg-SnO_2 vs FTO/sg-TiO_2

	Slot-die coated films	FTO/sg-SnO_2	FTO/sg-TiO_2
Morphology	coated area	A' = 90 cm^2	A' = 90 cm^2
	film coverage	c = 100%	c = 100%
	perovskite thickness	t = 550 nm	t = 550 nm
	film roughness	R_a = 100 nm	R_a = 100 nm
Zoom in	film compacity	c' = 100%	c' = 100%
	grain size	g = 400 nm	g = 450 nm
Optical	band gap	E_g = 1.62 eV	E_g = 1.62 eV
	TRPL	t_1 = 5.6 ns	t_1 = 4.8 ns
		t_2 = 211 ns	t_2 = 212 ns
Crystallization	α-CsFAPbIBr	Yes	Yes
	Preferential orientation	(011)	(001)
	δ-$FAPbI_3$	No	No
	crystalline PbI_2	Yes (23%)	Yes (18%)

***Table A2-B**: Properties of slot-die coated layer deposited on sg-SnO_2 and sg-TiO_2 ETLs.*

- 2C: FTO/sg-TiO_2 vs m-TiO_2 (100, 150 and 250 nm scaffolds)

	Slot-die coated films	**FTO/c-TiO_2**	**FTO/c/m-TiO_2 (100 nm)**	**FTO/c/m-TiO_2 (150 nm)**	**FTO/c/m-TiO_2 (250 nm)**
Morphology	coated area	A' = 90 cm^2	A' = 90 cm^2	A' = 90 cm^2	A' = 90 cm^2
	film coverage	c = 100%	c = 100%	c = 100%	c = 100%
	perovskite thickness	t = 550 nm	t = 480 nm (capping layer)	t = 470 nm (capping layer)	t = 500 nm (capping layer)
	film roughness	R_a = 15 nm	R_a = 30 nm	R_a = 30 nm	R_a = 30 nm
Zoom in	film compacity	c' = 100%	c' = 100%	c' = 100%	c' = 100%
	grain size	g = 450 nm	g = 300 nm	**g = 500 nm**	**g = 500 nm**
	Infiltration	NA	**Complete**	**Complete**	Partial
Optical	band gap	E_g = 1.62 eV	E_g = 1.62 eV	E_g = 1.62 eV	E_g = 1.62 eV
	TRPL	τ_1 = 6 ns	τ_1 = 6.4 ns		
		τ_2 = 219 ns	**τ_2 = 155 ns**		
Crystallization	α-CsFAPbIBr	Yes	Yes		
	Preferential orientation	(001)	(011)		
	δ-$FAPbI_3$	No	No		
	crystalline PbI_2	Yes (18%)	Yes (10%)		

***Table A2-C**: Properties of slot-die coated layer deposited on sg-TiO_2 and m-TiO_2 ETLs.*

Appendix 3: Device performance summary on ITO/np-SnO_2 and FTO/sg-SnO_2.

- Spin-coated reference devices on ITO/np-SnO_2

day 1	V_{oc} (V)	J_{sc} (mA.cm^{-2})	FF (%)	PCE (%)
1	1.099	22.3	73.2	17.9
2	1.097	21.7	73.8	17.6
3	1.108	21.8	74.9	18.0
4	1.078	21.9	68.3	16.1
5	1.067	22.1	66.5	15.7
6	1.090	21.9	73.2	17.5
	1.090 ± 0.033	**21.9 ± 0.75**	**71.7 ± 5.9**	**17.1 ± 2.1**

- Slot-die coated devices on ITO/np-SnO_2

day 0

1	0.929	22.9	62.5	13.3
2	0.932	23.0	63.3	13.5
3	0.933	22.8	65.0	13.8
4	0.919	22.9	63.9	13.4
5	0.901	22.5	55.8	11.3
6	1.023	20.9	68.6	14.7
7	1.004	21.5	69.5	15.0
8	0.996	21.2	65.7	13.9
9	0.975	22.0	55.4	11.9
	0.957 ± 0.065	**22.2 ± 1.2**	**63.3 ± 7.5**	**13.4 ± 2.1**

- Slot-die coated devices on FTO/sg-SnO_2

day 1

1	1.035	22.1	73.5	16.8
2	1.049	22.2	75.1	17.5
3	0.993	20.3	60.7	12.3
4	1.004	21.7	65.5	14.3
5	0.830	20.3	59.0	9.9
6	0.864	19.9	64.4	11.1
	0.963 ± 0.132	**21.1 ± 1.17**	**66.4 ± 8.7**	**13.6 ± 3.8**

*The yellow highlighted data are the one corresponding to the **Figure 11b** J-V curves.*

Appendix 4: Device performance summary on FTO/sg-TiO_2.

- Maturation effect:

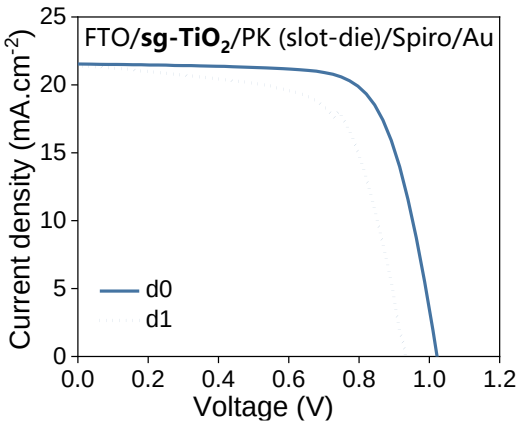

***Figure A4**: Comparison of J-V curves measured at d0 and d1.*

- Slot-die coated devices on FTO/sg-TiO_2

day 0	**V_{oc} (V)**	**J_{sc} (mA.cm^{-2})**	**FF (%)**	**PCE (%)**
1	0.715	20.8	59.2	8.8
2	1.017	21.5	72.4	15.9
3	0.997	21.2	68.3	14.5
4	1.004	21.3	69.1	14.8
	0.933 ± 0.218	**21.2 ± 0.4**	**67.3 ± 8.0**	**13.5 ± 4.7**

*The yellow highlighted data are the one corresponding to the **Figure 17a** J-V curves.*

Appendix 5: Device performance summary on FTO/m-TiO_2.

- Slot-die coated devices on FTO/m-TiO_2 (250 nm)

day 0	V_{oc} (V)	J_{sc} (mA.cm^{-2})	FF (%)	PCE (%)
1	0.879	19.21	46.99	7.93

- Slot-die coated devices on FTO/m-TiO_2 (150 nm)

day 0	V_{oc} (V)	J_{sc} (mA.cm^{-2})	FF (%)	PCE (%)
1	1.020	19.7	65.8	13.2
2	0.991	14.9	56.8	8.4
3	0.946	18.7	58.5	10.4
4	1.039	15.1	64.2	10.1
5	0.872	18.8	55.0	9.0
6	0.996	19.7	60.8	12.0
7	1.001	19.2	61.9	11.9
	0.981 ± 0.109	**18.0 ± 3.1**	**60.4 ± 5.5**	**10.7 ± 2.5**

- Slot-die coated devices on FTO/m-TiO_2 (100 nm)

day 0	V_{oc} (V)	J_{sc} (mA.cm^{-2})	FF (%)	PCE (%)
1	0.963	19.9	61.8	11.9
2	1.000	19.7	68.0	13.4
3	0.973	20.8	58.4	11.8
4	0.989	20.6	65.8	13.4
5	0.976	19.7	68.4	13.1
	0.980 ± 0.020	**20.1 ± 0.6**	**64.5 ± 6.0**	**12.7 ± 0.9**

*The yellow highlighted data are the one corresponding to the **Figure 24a** J-V curves.*

Appendix 6: Hysteresis behaviour in the perovskite solar cells.

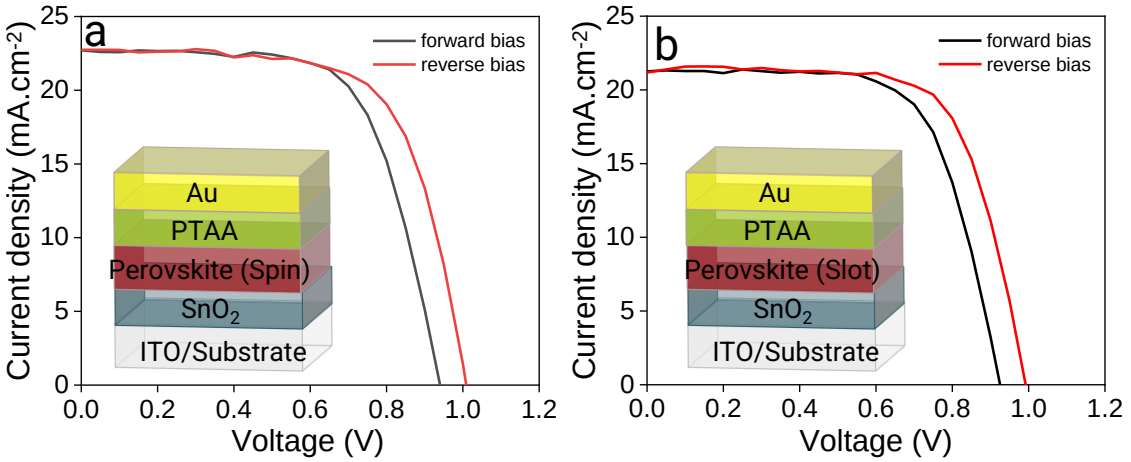

	V_{oc} (mV)	J_{sc} (mA/cm^2)	FF (%)	PCE (%)
(reverse)	1007	22.8	67	15.36
(forward)	941	22.6	67	14.21

	V_{oc} (mV)	J_{sc} (mA/cm^2)	FF (%)	PCE (%)
(reverse)	993	21.4	69	14.7
(forward)	925	21.3	68	13.32

*JV curves of n-i-p devices with **a.** spin-coated and **b.** slot-die coated perovskite layers. Inset: device structure. Below: Table of JV parameters measured in forward and reverse bias.*

General Conclusion

In this work, we aimed at developing a scalable method to deposit compact perovskite films over large areas. The main challenge consisted in the understanding and control of the perovskite material crystallization *via* synergetic gas-quenching and substrate heating. Here, we optimized the slot-die coating and gas-quenching process conditions to achieve compact perovskite layers over large substrates (5 x 5 cm^2 and 10 x 10 cm^2). We investigated and compared the properties of the perovskite layers deposition from spin-coating and slot-die coating processes (**Chapter III**), as well as how these variations in crystallization induced during the deposition may affect the photovoltaic device performances. To close the performance gap between both deposition processes, we investigated the role of the perovskite ink composition (**Chapter IV**) and of the underlying substrate nature (**Chapter V**) on both slot-die coated layers properties and photovoltaic device performances.

- **Achievement of compact slot-die coated layers**

We developed a **customized gas-quenching system embedded to the slot-die coating process to control CsFAPbIBr perovskite crystallization** over large areas. We optimized the gas flow rate and substrate temperature to maximize the microscopic film coverage and tuned the coating speed and quenching gap to achieve **macroscopic homogeneity over 5 x 5 cm^2 and 10 x 10 cm^2 substrates**. This was the first report of controlled large-area crystallization of CsFAPbIBr perovskite *via* this method at the time of this work.

- **Comparison between spin-coated and slot-die coated layers**

After having introduced the spin-coating and slot-die coating processes used to deposit the perovskite layer, we compared the morphological, optical and crystalline properties of the perovskite layers fabricated by both processes. We found that despite the similar thicknesses and band gap obtained, **the slot-die coated layers suffered incomplete conversion into perovskite cubic structure. We attributed this difference to the various crystallization mean used (gas-assisted quenching) compared to the conventional anti-solvent strategy used in the spin-coating process**. This effect was independent from the perovskite precursor ink concentration employed. In particular, the reduction of concentration did not seem to increase the 'conversion power' of the gas-quenching assisted crystallization.

This variation in perovskite material quality impacted the device performances, that were lower (PCE ~ 13%) when the perovskite absorber was slot-die coated compared to a spin-coated perovskite absorber (PCE ~ 16.5%). All electrical parameters: current density, fill factor and open-circuit voltage were affected. Overall, both perovskite film intrinsic properties (smaller grain size, possibly higher non-

radiative recombination) and the ETL/Perovskite and Perovskite/HTL interfaces seemed more defective when this new deposition process was used. To mitigate the first effect, we decided to focus on the slot-die coated layers conversion into cubic.

- **Role of the precursor ink composition**

A common approach employed in the spin-coating process to favour the formation of the perovskite cubic structure is to adjust the perovskite precursors stoichiometry. We found that **a larger amount of CsI precursor was required (15% Cs/Pb) to achieve complete conversion of the slot-die coated perovskite layers into the cubic structure, compared to the spin-coating process (5% Cs/Pb)**. The modification of the precursor ink stoichiometry did not impact the coatability of the precursor solution. We therefore attributed the CsI effect to the formation of various solution intermediates (polytypes) which may be needed in larger quantities during the gas-quenching assisted crystallization compared to the anti-solvent assisted crystallization. **The enhancement of the cubic structure formation was translated into an increase of the perovskite film absorption** (for a similar thickness) **and into a larger device current density** that matched the current density of reference devices fabricated from spin-coated perovskite layers.

However, the performance of devices integrating the slot-die coated perovskite layers were still limited in terms of open-circuit voltage and fill factor, which can originate from increased non-radiative recombination in the bulk (grain boundaries) or at the device interfaces. To reduce the density of grain boundaries in the slot-die coted films, we **tuned the stoichiometry to increase the grain size of the perovskite films**. Larger grains were obtained for high FA/Cs ratios initially or for highly overstoichiometric samples (Cation/Pb ratio of 1.09) after post-annealing. The stoichiometries leading to larger grains exhibited, unfortunately, an incomplete conversion into the perovskite cubic structure. We concluded that **the grain size enhancement *via* stoichiometry tuning happened at the expense of the perovskite structural quality.**

Finally, we studied the effect of the varying the precursor ink solvent ratios from 4:1 (DMF:DMSO) to 0:1 (full DMSO). We found that **the DMF free ink led to the formation of voids at the ETL/Perovskite interface, attributed to the various solvent's evaporation kinetics**. Mitigation strategies include to either re-adjust the coating parameters (substrate temperature) or the addition of cosolvents or surfactants to the precursor ink to increase the affinity between the precursor ink and the underlying substrate.

- **Role of the underlying substrate (ETL)**

To study this ETL/Perovskite interface further, we investigated various state-of-the-art electron transporting layers (ETLs): planar SnO_2, planar TiO_2 and mesoporous TiO_2. **Compact slot-die coated layers with the perovskite cubic structure were obtained on all three ETLs**, highlighting the versatility of the slot-die coating technique. It confirmed that the precursor ink formulation controls the perovskite conversion, independently of the processing conditions. The integration of the slot-die coated layers into photovoltaic devices resulted **in champion device performances of 17.5% on planar SnO_2, 15.9% on planar TiO_2 and 13.4% on mesoporous TiO_2**. These results confirmed the compatibility of the slot-die coating process with various device architectures.

For planar ETLs, we found that the chemical nature of the ETL (SnO_2 vs TiO_2) did not affect the perovskite film formation significantly. **The TiO_2 ETL led to lower device performances (lower V_{oc}) attributed to the modification of the energy band alignment between the ETL and the perovskite.** The maturation phenomenon varied between both ETLs, suggesting a different aging mechanism at the ETL/Perovskite interface.

In presence of mesoporous ETL (m-TiO_2), we found that the mesoporous thickness affected both the degree of infiltration (poor infiltration for thick m-TiO_2 layers) and the capping layer morphology (grain size increase for thicker m-TiO_2 layer). Consequently, **the TiO_2 scaffold thickness was the main factor affecting the device performance**. We found that **a very thin m-TiO_2 layer was desirable to maintain high device V_{oc} and FF and that the capping layer morphology had a limited effect on the device performance**.

For large-area devices fabrication, the device performance distribution had to be reduced. We introduced a chemical bath deposition (CBD) step prior to the perovskite deposition to improve the ETL/Perovskite interface. **The CBD-treated devices resulted in higher fill factor (up to 78%) and a champion power conversion efficiency of 18% over a device active area of 0.09 cm^2**, highlighting the importance of interface engineering on device performance. **The CBD step narrowed the PCE distribution, leading to average PCE of 16.3 ± 2%** for 30 devices fabricated on the same 10 x 10 cm^2 substrate.

Regarding the perovskite spatial homogeneity**, the perovskite film thickness decrease of 10% along the coating direction** induced a **J_{sc} decrease of 0.1 $mA.cm^{-2}$**. Despite the absorber thickness inhomogeneities, **we fabricated a large-area module over 52 cm^2 with 11.5% PCE**. The module limiting parameters were the fill factor and open-circuit voltage, possibly due to unoptimized module design and recombination losses in the slot-die coated perovskite layer itself and at the ETL/Perovskite interface.

Perspectives

- **Understanding of the crystallization mechanism**

Although we have studied the perovskite film properties after deposition in details, a more fundamental understanding of the nucleation and growth mechanisms during the perovskite crystallization is desired. Hence, in-situ characterizations (such as reflectance of GIWACS measurements) during the perovskite crystallization is recommended to validate or invalidate our hypothesis regarding the role of the CsI precursor. Furthermore, advanced material characterization of the slot-die coated films (TOF-SIMS, TEM) can be performed to get insights on the spatial distribution of the caesium cation in the perovskite film thickness or within a single perovskite grain. Such information can help to intuit whether the nucleation started from the substrate or from the top of the precursor wet film and if it was rather homogeneous or heterogenous or a combination of both.

Moreover, we observed that the slot-die coated films had enhanced charge recombination compared to their spin-coated counterparts. Further work is needed to quantify the concentration, energy and the location of these charge recombination centres. Charge carriers lifetime mapping (by time-resolved photoluminescence) or quasi-Fermi levels cartography (by hyperspectral photoluminescence imaging) are promising tools that can be used over large areas to quantify the perovskite layer quality. For instance, the evolution of the trap's properties (location, energy) depending on the CsI ratio in the film could provide indirect information on the crystallization mechanism.

- **Relationship between perovskite properties and device performances**

In this work, we studied the effect of various factors (crystallization mean, precursor solution composition and underlying substrate nature) on the slot-die coated layers properties and photovoltaic performances. The methodology developed here could be applied to various device structures to identify the substrates yielding high performance devices, while understanding the link between the substrate type and the perovskite layer properties. In particular, it can be extended to (p-i-n) device structures.

We have identified correlations between the perovskite material properties (grain size, presence of the δ-$FAPbI_3$ phase) and the device performances. However, additional studies such as the device integration of the promising perovskite stoichiometries identified in **Chapter IV.1.5. - Table 3** could contribute to decorrelate both effects (grain size enhancement or perovskite conversion into cubic structure) and to identify the main factor limiting the slot-die coated based device performances. Lastly, we could not conclude regarding impact of the crystalline PbI_2 content and of the perovskite grain orientations on the device performances. However, these material properties may be relevant when investigating the devices shelf-life stability which has not been studied in the frame of this work.

- **Improvement of the device performances**

The technological barriers to reach power conversion efficiencies over 18% are multiple. First, the open-circuit voltage (V_{oc}) was limited in our devices due to both perovskite intrinsic quality and interface management. The significant effect of the chemical bath deposition step on the device performance highlights the need for interface mitigation strategies. In the literature, SnO_2 treatment with potassium ions or its replacement with self-assembled monolayers (SAMs) are successful to reduce the defects at the ETL/Perovskite interface, resulting in higher performance and enhanced stability.

Similarly, passivation strategies could be implemented at the perovskite grain boundaries (via additive engineering) or on top of the perovskite film via a post-treatment such as phenethyl ammonium iodide (PEAI) to reduce charge recombination in the bulk and at the Perovskite/HTL interface. Finally, the device current density could be improved by reducing the band gap by removing the bromide anion from the formulation. As the latter may play a stabilizing role towards the intermediate phase during the crystallization, it could be interesting to repeat the CsI ratios experiment in a bromide free environment.

- **Towards efficient, reproducible and robust photovoltaic modules fabrication**

We demonstrated the fabrication of a 55 cm^2 module with 11.6% efficiency, far from the 18% PCE achieved on laboratory scale devices. Further design optimization work, including the implementation of a full laser patterning process for the series interconnection, could help to improve the module fill factor. Alternative module designs such as back contact interconnection or parallel interconnection could also be investigated. Furthermore, we showed that the homogeneity of all layers and interfaces was crucial to reach homogeneous performances over large-area substrates. To deposit the interfacial layers homogeneously, spin-coating could be replaced by atomic layer deposition (ALD), spray-coating or slot-die coating. Regarding the perovskite layer quality control, our tool based on the sample picture (PerovskiteVision) can help to map the perovskite film thickness non-destructively. This tool could be extended to assess the quality of ETL/Perovskite and HTL/Perovskite interfaces (using photoluminescence data fusion) and to predict the device current density from the perovskite thickness map (using an optical model linking film thickness and J_{sc}).

- **Route to phase out of toxic solvents**

Scaling up the perovskite deposition process goes hand to hand with transferring those processes outside the glovebox. This transfer in ambient conditions has two consequences: (1) the exposition of the perovskite films to ambient environment (humidity, oxygen) which can

affect the films morphological and crystalline properties and (2) the possible direct exposure of the operator to the toxic solvent and lead present in the perovskite precursor.

To limit the exposure of the perovskite films, we enclosed in this work the coating environment and controlled the humidity level with dehumidification systems. The impact of coating environment humidity level and oxygen level could, however, be studied further as both may impact the quality of the resulting slot-die coated films, hence the device performances and shelf-life stability. Similar work could be carried out to identify a most favourable post-annealing environment (atmosphere of nitrogen, argon, air, influence of the humidity level).

We noticed that the presence of those enclosures resulted in the protection of the operator direct contact with the precursor solution during the coating. To further reduce the toxicity of the precursor ink, alternative solvent mixture could be investigated. Here, we demonstrated the coating of films from a precursor ink based on DMSO solvent to phase out from the more toxic dimethylformamide (DMF) solvent. However, other approaches such as the use of low boiling point solvents such as acetonitrile (ACN) is known in the literature for slot-die coating or d-bar coating of $MAPbI_3$ perovskite. Their applicability to formamidinium-based perovskite could be investigated as a perspective of this work. In particular, the addition of ACN as cosolvent in the precursor ink based of DMSO could be a strategy to affect the wet film drying kinetics and improve the resulting perovskite film morphology.

References

1. BNEF: Developing countries add more renewables than fossil fuel generation for first time. *Institute for Energy Economics & Financial Analysis* https://ieefa.org/bnef-developing-countries-add-more-renewables-than-fossil-fuel-generation-for-first-time/ (2018).
2. Global Energy Review 2021 – Analysis. *IEA* https://www.iea.org/reports/global-energy-review-2021.
3. Levelized Costs of New Generation Resources in the Annual Energy Outlook 2021. 25 (2021).
4. Life Cycle Assessment Harmonization. https://www.nrel.gov/analysis/life-cycle-assessment.html.
5. Water Use in the Semiconductor Manufacturing Industry. *The Engineered Environment* https://engineeredenvironment.tumblr.com/post/30464844411/water-use-in-the-semiconductor-manufacturing.
6. Solar cell efficiency tables (version 57). doi:10.1002/pip.3371.
7. Powalla, M. *et al.* Thin-film solar cells exceeding 22% solar cell efficiency: An overview on CdTe-, Cu(In,Ga)Se2-, and perovskite-based materials. *Applied Physics Reviews* **5**, 041602 (2018).
8. Gong, J., Darling, S. B. & You, F. Perovskite photovoltaics: life-cycle assessment of energy and environmental impacts. *Energy Environ. Sci.* **8**, 1953–1968 (2015).
9. Sundaram, S., Shanks, K. & Upadhyaya, H. 18 - Thin Film Photovoltaics. in *A Comprehensive Guide to Solar Energy Systems* (eds. Letcher, T. M. & Fthenakis, V. M.) 361–370 (Academic Press, 2018). doi:10.1016/B978-0-12-811479-7.00018-X.
10. Best Research-Cell Efficiency Chart. https://www.nrel.gov/pv/cell-efficiency.html.
11. B. Whitaker, J. *et al.* Scalable slot-die coating of high performance perovskite solar cells. *Sustainable Energy & Fuels* **2**, 2442–2449 (2018).
12. Galagan, Y. *et al.* Roll-to-Roll Slot Die Coated Perovskite for Efficient Flexible Solar Cells. *Advanced Energy Materials* **8**, 1801935 (2018).
13. Conings, B. *et al.* A Universal Deposition Protocol for Planar Heterojunction Solar Cells with High Efficiency Based on Hybrid Lead Halide Perovskite Families. *Advanced Materials* **28**, 10701–10709 (2016).
14. Rolston, N. *et al.* Rapid Open-Air Fabrication of Perovskite Solar Modules. *Joule* **4**, 2675–2692 (2020).
15. Li, X. *et al.* A vacuum flash-assisted solution process for high-efficiency large-area perovskite solar cells. *Science* **353**, 58–62 (2016).
16. Saliba, M. *et al.* Cesium-containing triple cation perovskite solar cells: improved stability, reproducibility and high efficiency. *Energy & Environmental Science* **9**, 1989–1997 (2016).
17. Kojima, A., Teshima, K., Shirai, Y. & Miyasaka, T. Organometal Halide Perovskites as Visible-Light Sensitizers for Photovoltaic Cells. *J. Am. Chem. Soc.* **131**, 6050–6051 (2009).

18. Im, J.-H., Lee, C.-R., Lee, J.-W., Park, S.-W. & Park, N.-G. 6.5% efficient perovskite quantum-dot-sensitized solar cell. *Nanoscale* **3**, 4088–4093 (2011).

19. Lee, M. M., Teuscher, J., Miyasaka, T., Murakami, T. N. & Snaith, H. J. Efficient Hybrid Solar Cells Based on Meso-Superstructured Organometal Halide Perovskites. *Science* **338**, 643–647 (2012).

20. Liu, M., Johnston, M. B. & Snaith, H. J. Efficient planar heterojunction perovskite solar cells by vapour deposition. *Nature* **501**, 395–398 (2013).

21. Jeon, N. J. *et al.* o-Methoxy Substituents in Spiro-OMeTAD for Efficient Inorganic–Organic Hybrid Perovskite Solar Cells. *J. Am. Chem. Soc.* **136**, 7837–7840 (2014).

22. Zhou, H. *et al.* Interface engineering of highly efficient perovskite solar cells. *Science* **345**, 542–546 (2014).

23. Saliba, M. *et al.* A molecularly engineered hole-transporting material for efficient perovskite solar cells. *Nature Energy* **1**, 1–7 (2016).

24. Jiang, Q. *et al.* Surface passivation of perovskite film for efficient solar cells. *Nat. Photonics* **13**, 460–466 (2019).

25. Yang, W. S. *et al.* Iodide management in formamidinium-lead-halide–based perovskite layers for efficient solar cells. *Science* **356**, 1376–1379 (2017).

26. Grätzel, M. The light and shade of perovskite solar cells. *Nature Materials* **13**, 838–842 (2014).

27. Goldschmidt, V. M. Die Gesetze der Krystallochemie. *Naturwissenschaften* **14**, 477–485 (1926).

28. Kieslich, G., Sun, S. & Cheetham, A. K. Solid-state principles applied to organic–inorganic perovskites: new tricks for an old dog. *Chem. Sci.* **5**, 4712–4715 (2014).

29. Filip, M. R., Eperon, G. E., Snaith, H. J. & Giustino, F. Steric engineering of metal-halide perovskites with tunable optical band gaps. *Nature Communications* **5**, 5757 (2014).

30. Motta, C. *et al.* Revealing the role of organic cations in hybrid halide perovskite CH 3 NH 3 PbI 3. *Nature Communications* **6**, 7026 (2015).

31. Grånäs, O., Vinichenko, D. & Kaxiras, E. Establishing the limits of efficiency of perovskite solar cells from first principles modeling. *Scientific Reports* **6**, 36108 (2016).

32. Koh, T. M. *et al.* Formamidinium-Containing Metal-Halide: An Alternative Material for Near-IR Absorption Perovskite Solar Cells. *J. Phys. Chem. C* **118**, 16458–16462 (2014).

33. Eperon, G. E. *et al.* Formamidinium lead trihalide: a broadly tunable perovskite for efficient planar heterojunction solar cells. *Energy Environ. Sci.* **7**, 982–988 (2014).

34. Noh, J. H., Im, S. H., Heo, J. H., Mandal, T. N. & Seok, S. I. Chemical Management for Colorful, Efficient, and Stable Inorganic–Organic Hybrid Nanostructured Solar Cells. *Nano Lett.* **13**, 1764–1769 (2013).

35. Wu, Y. *et al.* The Impact of Hybrid Compositional Film/Structure on Organic–Inorganic Perovskite Solar Cells. *Nanomaterials* **8**, 356 (2018).

36. Li, Z. *et al.* Stabilizing Perovskite Structures by Tuning Tolerance Factor: Formation of Formamidinium and Cesium Lead Iodide Solid-State Alloys. *Chem. Mater.* **28**, 284–292 (2016).

37. Kim, T. W. *et al.* Self-Organized Superlattice and Phase Coexistence inside Thin Film Organometal Halide Perovskite. *Advanced Materials* **30**, 1705230 (2018).

38. Stoumpos, C. C., Malliakas, C. D. & Kanatzidis, M. G. Semiconducting Tin and Lead Iodide Perovskites with Organic Cations: Phase Transitions, High Mobilities, and Near-Infrared Photoluminescent Properties. *Inorg. Chem.* **52**, 9019–9038 (2013).

39. Jeon, N. J. *et al.* Compositional engineering of perovskite materials for high-performance solar cells. *Nature* **517**, 476–480 (2015).

40. Yi, C. *et al.* Entropic stabilization of mixed A-cation ABX $_3$ metal halide perovskites for high performance perovskite solar cells. *Energy & Environmental Science* **9**, 656–662 (2016).

41. Gratia, P. *et al.* The Many Faces of Mixed Ion Perovskites: Unraveling and Understanding the Crystallization Process. *ACS Energy Lett.* **2**, 2686–2693 (2017).

42. Han, Q. *et al.* Single Crystal Formamidinium Lead Iodide (FAPbI3): Insight into the Structural, Optical, and Electrical Properties. *Advanced Materials* **28**, 2253–2258 (2016).

43. McMeekin, D. P. *et al.* A mixed-cation lead mixed-halide perovskite absorber for tandem solar cells. *Science* **351**, 151–155 (2016).

44. Chi, W. & Banerjee, S. K. Progress in Materials Development for the Rapid Efficiency Advancement of Perovskite Solar Cells. *Small* **16**, 1907531 (2020).

45. Park, N.-G. Perovskite solar cells: an emerging photovoltaic technology. *Materials Today* **18**, 65–72 (2015).

46. Stranks, S. D. *et al.* Electron-Hole Diffusion Lengths Exceeding 1 Micrometer in an Organometal Trihalide Perovskite Absorber. *Science* **342**, 341–344 (2013).

47. M. Ball, J., M. Lee, M., Hey, A. & J. Snaith, H. Low-temperature processed meso-superstructured to thin-film perovskite solar cells. *Energy & Environmental Science* **6**, 1739–1743 (2013).

48. Yun, J. S. *et al.* Critical Role of Grain Boundaries for Ion Migration in Formamidinium and Methylammonium Lead Halide Perovskite Solar Cells. *Advanced Energy Materials* **6**, 1600330 (2016).

49. Yan, Y. *et al.* Physics of grain boundaries in polycrystalline photovoltaic semiconductors. *Journal of Applied Physics* **117**, 112807 (2015).

50. Egger, D. A. *et al.* What Remains Unexplained about the Properties of Halide Perovskites? *Advanced Materials* **30**, 1800691 (2018).

51. Thin Film Photovoltaics. *A Comprehensive Guide to Solar Energy Systems* 361–370 (2018) doi:10.1016/B978-0-12-811479-7.00018-X.

52. First Solar's CdTe module technology – performance, life cycle, health and safety impact assessment. 41.

53. Kovalenko, M. V., Protesescu, L. & Bodnarchuk, M. I. Properties and potential optoelectronic applications of lead halide perovskite nanocrystals. *Science* **358**, 745–750 (2017).

54. Brenes, R. *et al.* Metal Halide Perovskite Polycrystalline Films Exhibiting Properties of Single Crystals. *Joule* **1**, 155–167 (2017).

55. Sutherland, B. R. Tailoring Perovskite Thin Films to Rival Single Crystals. *Joule* **1**, 23–25 (2017).

56. Jin, H. *et al.* It's a trap! On the nature of localised states and charge trapping in lead halide perovskites. *Mater. Horiz.* **7**, 397–410 (2020).

57. Wehrenfennig, C., Eperon, G. E., Johnston, M. B., Snaith, H. J. & Herz, L. M. High Charge Carrier Mobilities and Lifetimes in Organolead Trihalide Perovskites. *Advanced Materials* **26**, 1584–1589 (2014).

58. Saliba, M. *et al.* How to Make over 20% Efficient Perovskite Solar Cells in Regular (n–i–p) and Inverted (p–i–n) Architectures. *Chem. Mater.* **30**, 4193–4201 (2018).

59. Jena, A. K., Kulkarni, A. & Miyasaka, T. Halide Perovskite Photovoltaics: Background, Status, and Future Prospects. *Chem. Rev.* **119**, 3036–3103 (2019).

60. Shockley, W. & Queisser, H. J. Detailed Balance Limit of Efficiency of p-n Junction Solar Cells. *Journal of Applied Physics* **32**, 510–519 (1961).

61. Ehrler, B. *et al.* Photovoltaics Reaching for the Shockley–Queisser Limit. *ACS Energy Lett.* **5**, 3029–3033 (2020).

62. Yoo, J. J. *et al.* Efficient perovskite solar cells via improved carrier management. *Nature* **590**, 587–593 (2021).

63. Research Areas. *QPV Research Group* https://www.qpvgroup.org/research-areas.

64. Polman, A., Knight, M., Garnett, E. C., Ehrler, B. & Sinke, W. C. Photovoltaic materials: Present efficiencies and future challenges. *Science* **352**, (2016).

65. S-Q Charts – LMPV. https://www.lmpv.nl/sq/.

66. Swartwout, R., Hoerantner, M. T. & Bulović, V. Scalable Deposition Methods for Large-area Production of Perovskite Thin Films. *ENERGY & ENVIRONMENTAL MATERIALS* **2**, 119–145 (2019).

67. Park, N.-G. & Zhu, K. Scalable fabrication and coating methods for perovskite solar cells and solar modules. *Nature Reviews Materials* **5**, 333–350 (2020).

68. Cho, K. T. *et al.* Highly efficient perovskite solar cells with a compositionally engineered perovskite/hole transporting material interface. *Energy Environ. Sci.* **10**, 621–627 (2017).

69. Emslie, A. G., Bonner, F. T. & Peck, L. G. Flow of a Viscous Liquid on a Rotating Disk. *Journal of Applied Physics* **29**, 858–862 (1958).

70. Li, Z. *et al.* Scalable fabrication of perovskite solar cells. *Nat Rev Mater* **3**, 1–20 (2018).

71. Verma, A., Martineau, D., Abdolhosseinzadeh, S., Heier, J. & Nüesch, F. Inkjet printed mesoscopic perovskite solar cells with custom design capability. *Mater. Adv.* **1**, 153–160 (2020).

72. Kim, Y. Y. *et al.* Gravure-Printed Flexible Perovskite Solar Cells: Toward Roll-to-Roll Manufacturing. *Advanced Science* **6**, 1802094 (2019).

73. Deng, Y. *et al.* Surfactant-controlled ink drying enables high-speed deposition of perovskite films for efficient photovoltaic modules. *Nat Energy* **3**, 560–566 (2018).

74. Jeong, D.-N. *et al.* Perovskite Cluster-Containing Solution for Scalable D-Bar Coating toward High-Throughput Perovskite Solar Cells. *ACS Energy Lett.* **4**, 1189–1195 (2019).

75. Di Giacomo, F. *et al.* Up-scalable sheet-to-sheet production of high efficiency perovskite module and solar cells on 6-in. substrate using slot die coating. *Solar Energy Materials and Solar Cells* **181**, 53–59 (2018).

76. Burkitt, D. *et al.* Acetonitrile based single step slot-die compatible perovskite ink for flexible photovoltaics. *RSC Advances* **9**, 37415–37423 (2019).

77. Li, J. *et al.* 20.8% Slot-Die Coated MAPbI3 Perovskite Solar Cells by Optimal DMSO-Content and Age of 2-ME Based Precursor Inks. *Advanced Energy Materials* **11**, 2003460 (2021).

78. Tang, S. *et al.* Composition Engineering in Doctor-Blading of Perovskite Solar Cells. *Advanced Energy Materials* **7**, 1700302 (2017).

79. Patidar, R., Burkitt, D., Hooper, K., Richards, D. & Watson, T. Slot-die coating of perovskite solar cells: An overview. *Materials Today Communications* **22**, 100808 (2020).

80. A Fast Deposition-Crystallization Procedure for Highly Efficient Lead Iodide Perovskite Thin-Film Solar Cells - Xiao - 2014 - Angewandte Chemie - Wiley Online Library. https://onlinelibrary.wiley.com/doi/full/10.1002/ange.201405334.

81. Howard, I. A. *et al.* Coated and Printed Perovskites for Photovoltaic Applications. *Advanced Materials* **31**, 1806702 (2019).

82. Yang, M. *et al.* Highly Efficient Perovskite Solar Modules by Scalable Fabrication and Interconnection Optimization. *ACS Energy Lett.* **3**, 322–328 (2018).

83. Uličná, S. *et al.* Scalable Deposition of High-Efficiency Perovskite Solar Cells by Spray-Coating. *ACS Appl. Energy Mater.* **1**, 1853–1857 (2018).

84. Parvazian, E., Abdollah-zadeh, A., Akbari, H. R. & Taghavinia, N. Fabrication of perovskite solar cells based on vacuum-assisted linear meniscus printing of MAPbI3. *Solar Energy Materials and Solar Cells* **191**, 148–156 (2019).

85. Cotella, G. *et al.* One-step deposition by slot-die coating of mixed lead halide perovskite for photovoltaic applications. *Solar Energy Materials and Solar Cells* **159**, 362–369 (2017).

86. Kim, J.-E. *et al.* Slot die coated planar perovskite solar cells via blowing and heating assisted one step deposition. *Solar Energy Materials and Solar Cells* **179**, 80–86 (2018).

87. Troughton, J. *et al.* Rapid processing of perovskite solar cells in under 2.5 seconds. *J. Mater. Chem. A* **3**, 9123–9127 (2015).

88. Sanchez, S., Hua, X., Phung, N., Steiner, U. & Abate, A. Flash Infrared Annealing for Antisolvent-Free Highly Efficient Perovskite Solar Cells. *Advanced Energy Materials* **8**, 1702915 (2018).

89. Huang, F. *et al.* Gas-assisted preparation of lead iodide perovskite films consisting of a monolayer of single crystalline grains for high efficiency planar solar cells. *Nano Energy* **10**, 10–18 (2014).

90. Chen, B. *et al.* Blade-Coated Perovskites on Textured Silicon for 26%-Efficient Monolithic Perovskite/Silicon Tandem Solar Cells. *Joule* (2020) doi:10.1016/j.joule.2020.01.008.

91. Yang, Z. *et al.* Slot-die coating large-area formamidinium-cesium perovskite film for efficient and stable parallel solar module. *Science Advances* **7**, eabg3749 (2021).

92. Gao, L.-L., Li, C.-X., Li, C.-J. & Yang, G.-J. Large-area high-efficiency perovskite solar cells based on perovskite films dried by the multi-flow air knife method in air. *J. Mater. Chem. A* **5**, 1548–1557 (2017).

93. Gao, L.-L., Zhang, K.-J., Chen, N. & Yang, G.-J. Boundary layer tuning induced fast and high performance perovskite film precipitation by facile one-step solution engineering. *J. Mater. Chem. A* **5**, 18120–18127 (2017).

94. Chu, D. B. K., Owen, J. S. & Peters, B. Nucleation and Growth Kinetics from LaMer Burst Data. *J. Phys. Chem. A* **121**, 7511–7517 (2017).

95. Hu, H. *et al.* Room-Temperature Meniscus Coating of >20% Perovskite Solar Cells: A Film Formation Mechanism Investigation. *Advanced Functional Materials* **29**, 1900092 (2019).

96. Szostak, R. *et al.* Revealing the Perovskite Film Formation Using the Gas Quenching Method by In Situ GIWAXS: Morphology, Properties, and Device Performance. *Advanced Functional Materials* **31**, 2007473 (2021).

97. Rai, M., Wong, L. H. & Etgar, L. Effect of Perovskite Thickness on Electroluminescence and Solar Cell Conversion Efficiency. *J. Phys. Chem. Lett.* **11**, 8189–8194 (2020).

98. Kim, B. G., Jang, W., Cho, J. S. & Wang, D. H. Tailoring solubility of methylammonium lead halide with non-stoichiometry molar ratio in perovskite solar cells: Morphological and electrical relationships for high current generation. *Solar Energy Materials and Solar Cells* **192**, 24–35 (2019).

99. Heo, J. H. *et al.* Stable semi-transparent CH3NH3PbI3 planar sandwich solar cells. *Energy Environ. Sci.* **8**, 2922–2927 (2015).

100. Habibi, M., Ahmadian-Yazdi, M.-R. & Eslamian, M. Optimization of spray coating for the fabrication of sequentially deposited planar perovskite solar cells. *JPE* **7**, 022003 (2017).

101. Saliba, M. *et al.* Incorporation of rubidium cations into perovskite solar cells improves photovoltaic performance. *Science* **354**, 206–209 (2016).

102. Hu, Q. *et al.* In situ dynamic observations of perovskite crystallisation and microstructure evolution intermediated from [PbI 6] 4− cage nanoparticles. *Nature Communications* **8**, 15688 (2017).

103. Xu, X. *et al.* Air-processed mixed-cation Cs0.15FA0.85PbI3 planar perovskite solar cells derived from a PbI2–CsI–FAI intermediate complex. *J. Mater. Chem. A* **6**, 7731–7740 (2018).

104. Ramsdell, L. S. Studies on silicon carbide. *American Mineralogist* **32**, 64–82 (1947).

105. Park, N.-G. Nonstoichiometric Adduct Approach for High-Efficiency Perovskite Solar Cells. *Inorg. Chem.* **56**, 3–10 (2017).

106. Roose, B., Dey, K., Chiang, Y.-H., Friend, R. H. & Stranks, S. D. Critical Assessment of the Use of Excess Lead Iodide in Lead Halide Perovskite Solar Cells. *J. Phys. Chem. Lett.* **11**, 6505–6512 (2020).

107. Jacobsson, T. J. *et al.* Unreacted PbI2 as a Double-Edged Sword for Enhancing the Performance of Perovskite Solar Cells. *J. Am. Chem. Soc.* **138**, 10331–10343 (2016).

108. Chen, Q. *et al.* Controllable Self-Induced Passivation of Hybrid Lead Iodide Perovskites toward High Performance Solar Cells. *Nano Letters* **14**, 4158–4163 (2014).

109. Cao, X. *et al.* A Review of the Role of Solvents in Formation of High-Quality Solution-Processed Perovskite Films. *ACS Appl. Mater. Interfaces* **11**, 7639–7654 (2019).

110. Jeon, Y.-J. *et al.* Planar heterojunction perovskite solar cells with superior reproducibility. *Scientific Reports* **4**, 6953 (2014).

111. Ahn, N. *et al.* Highly Reproducible Perovskite Solar Cells with Average Efficiency of 18.3% and Best Efficiency of 19.7% Fabricated via Lewis Base Adduct of Lead(II) Iodide. *J. Am. Chem. Soc.* **137**, 8696–8699 (2015).

112. Deng, Y. *et al.* Tailoring solvent coordination for high-speed, room-temperature blading of perovskite photovoltaic films. *Science Advances* **5**, eaax7537 (2019).

113. Arain, Z. *et al.* Low-Temperature Annealed Perovskite Films: A Trade-Off between Fast and Retarded Crystallization via Solvent Engineering. *ACS Appl. Mater. Interfaces* **11**, 16704–16712 (2019).

114. Noel, N. K. *et al.* A low viscosity, low boiling point, clean solvent system for the rapid crystallisation of highly specular perovskite films. *Energy Environ. Sci.* **10**, 145–152 (2017).

115. Burkitt, D. *et al.* Roll-to-roll slot-die coated P–I–N perovskite solar cells using acetonitrile based single step perovskite solvent system. *Sustainable Energy Fuels* (2020) doi:10.1039/D0SE00460J.

116. Jeon, N. J. *et al.* Solvent engineering for high-performance inorganic–organic hybrid perovskite solar cells. *Nature Materials* **13**, 897–903 (2014).

117. Yang, W. S. *et al.* High-performance photovoltaic perovskite layers fabricated through intramolecular exchange. *Science* **348**, 1234–1237 (2015).

118. Zhao, Y. *et al.* Perovskite seeding growth of formamidinium-lead-iodide-based perovskites for efficient and stable solar cells. *Nature Communications* **9**, 1607 (2018).

119. Abdi-Jalebi, M. *et al.* Potassium- and Rubidium-Passivated Alloyed Perovskite Films: Optoelectronic Properties and Moisture Stability. *ACS Energy Lett.* **3**, 2671–2678 (2018).

120. Lin, C.-Y. *et al.* Unveiling the Nanoparticle-Seeded Catalytic Nucleation Kinetics of Perovskite Solar Cells by Time-Resolved GIXS. *Advanced Functional Materials* **29**, 1902582 (2019).

121. Kosmatos, K. O. *et al.* Methylammonium Chloride: A Key Additive for Highly Efficient, Stable, and Up-Scalable Perovskite Solar Cells. *ENERGY & ENVIRONMENTAL MATERIALS* **2**, 79–92 (2019).

122. Zuo, C. & Ding, L. An 80.11% FF record achieved for perovskite solar cells by using the NH4Cl additive. *Nanoscale* **6**, 9935–9938 (2014).

123. Han, Q. *et al.* Additive engineering for high-performance room-temperature-processed perovskite absorbers with micron-size grains and microsecond-range carrier lifetimes. *Energy Environ. Sci.* **10**, 2365–2371 (2017).

124. Xia, Y. *et al.* Management of perovskite intermediates for highly efficient inverted planar heterojunction perovskite solar cells. *J. Mater. Chem. A* **5**, 3193–3202 (2017).

125. Zhao, Y. & Zhu, K. CH3NH3Cl-Assisted One-Step Solution Growth of CH3NH3PbI3: Structure, Charge-Carrier Dynamics, and Photovoltaic Properties of Perovskite Solar Cells. *J. Phys. Chem. C* **118**, 9412–9418 (2014).

126. Kim, M. *et al.* Methylammonium Chloride Induces Intermediate Phase Stabilization for Efficient Perovskite Solar Cells. *Joule* **3**, 2179–2192 (2019).

127. De Marco, N. *et al.* Guanidinium: A Route to Enhanced Carrier Lifetime and Open-Circuit Voltage in Hybrid Perovskite Solar Cells. *Nano Lett.* **16**, 1009–1016 (2016).

128. Li, X. *et al.* In-situ cross-linking strategy for efficient and operationally stable methylammoniun lead iodide solar cells. *Nature Communications* **9**, 3806 (2018).

129. Han, T.-H. *et al.* Perovskite-polymer composite cross-linker approach for highly-stable and efficient perovskite solar cells. *Nature Communications* **10**, 520 (2019).

130. Liao, K. *et al.* Hot-Casting Large-Grain Perovskite Film for Efficient Solar Cells: Film Formation and Device Performance. *Nano-Micro Lett.* **12**, 156 (2020).

131. Chang, C.-Y., Huang, Y.-C., Tsao, C.-S. & Su, W.-F. Formation Mechanism and Control of Perovskite Films from Solution to Crystalline Phase Studied by in Situ Synchrotron Scattering. *ACS Appl. Mater. Interfaces* **8**, 26712–26721 (2016).

132. Nie, W. *et al.* High-efficiency solution-processed perovskite solar cells with millimeter-scale grains. *Science* **347**, 522–525 (2015).

133. Tang, M.-C. *et al.* Ambient blade coating of mixed cation, mixed halide perovskites without dripping: in situ investigation and highly efficient solar cells. *J. Mater. Chem. A* **8**, 1095–1104 (2020).

134. Brice, J. C. & Rudolph, P. Crystal Growth. in *Ullmann's Encyclopedia of Industrial Chemistry* (American Cancer Society, 2007). doi:10.1002/14356007.a08_099.pub2.

135. Husain, S. B. & Hasan, M. Epitaxial Lattice Matching and the Growth Techniques of Compound Semiconductors for their Potential Photovoltaic Applications. *J. Mod. Mater.* **5**, 34–42 (2018).

136. Roy, P., Kumar Sinha, N., Tiwari, S. & Khare, A. A review on perovskite solar cells: Evolution of architecture, fabrication techniques, commercialization issues and status. *Solar Energy* **198**, 665–688 (2020).

137. Aharon, S., Gamliel, S., Cohen, B. E. & Etgar, L. Depletion region effect of highly efficient hole conductor free CH3NH3PbI3 perovskite solar cells. *Phys. Chem. Chem. Phys.* **16**, 10512–10518 (2014).

138. Heo, J. H. *et al.* Efficient inorganic–organic hybrid heterojunction solar cells containing perovskite compound and polymeric hole conductors. *Nature Photonics* **7**, 486–491 (2013).

139. Chen, W. *et al.* A comparative study of planar and mesoporous perovskite solar cells with printable carbon electrodes. *Journal of Power Sources* **412**, 118–124 (2019).

140. Choi, J., Song, S., Hörantner, M. T., Snaith, H. J. & Park, T. Well-Defined Nanostructured, Single-Crystalline TiO2 Electron Transport Layer for Efficient Planar Perovskite Solar Cells. *ACS Nano* **10**, 6029–6036 (2016).

141. Cojocaru, L. *et al.* Surface Treatment of the Compact TiO2 Layer for Efficient Planar Heterojunction Perovskite Solar Cells. *Chem. Lett.* **44**, 674–676 (2015).

142. Paik, M. J. *et al.* TiO2 Colloid-Spray Coated Electron-Transporting Layers for Efficient Perovskite Solar Cells. *Advanced Energy Materials* **10**, 2001799 (2020).

143. Zardetto, V. *et al.* Plasma-assisted atomic layer deposition of TiO2 compact layers for flexible mesostructured perovskite solar cells. *Solar Energy* **150**, 447–453 (2017).

144. Shalan, A. E. *et al.* Optimization of a compact layer of TiO ₂ via atomic-layer deposition for high-performance perovskite solar cells. *Sustainable Energy Fuels* **1**, 1533–1540 (2017).

145. Ye, W., Xiang, J., Huang, F. & Zhong, D. Towards large-area perovskite solar cells: the influence of compact and mesoporous TiO ₂ electron transport layers. *Mater. Res. Express* **5**, 085506 (2018).

146. Jiang, Q., Zhang, X. & You, J. SnO2: A Wonderful Electron Transport Layer for Perovskite Solar Cells. *Small* **14**, 1801154 (2018).

147. Ke, W. *et al.* Low-Temperature Solution-Processed Tin Oxide as an Alternative Electron Transporting Layer for Efficient Perovskite Solar Cells. *J. Am. Chem. Soc.* **137**, 6730–6733 (2015).

148. Anaraki, E. H. *et al.* Highly efficient and stable planar perovskite solar cells by solution-processed tin oxide. *Energy Environ. Sci.* **9**, 3128–3134 (2016).

149. Electron Mobility and Injection Dynamics in Mesoporous ZnO, SnO2, and TiO2 Films Used in Dye-Sensitized Solar Cells | ACS Nano. https://pubs.acs.org/doi/10.1021/nn201243y.

150. Baena, J. P. C. *et al.* Highly efficient planar perovskite solar cells through band alignment engineering. *Energy Environ. Sci.* **8**, 2928–2934 (2015).

151. Ding, J. *et al.* Fully Air-Bladed High-Efficiency Perovskite Photovoltaics. *Joule* **3**, 402–416 (2019).

152. Kim, J.-E. *et al.* Humidity-Tolerant Roll-to-Roll Fabrication of Perovskite Solar Cells via Polymer-Additive-Assisted Hot Slot Die Deposition. *Advanced Functional Materials* **29**, 1809194 (2019).

153. Subbiah, A. S. *et al.* High-Performance Perovskite Single-Junction and Textured Perovskite/Silicon Tandem Solar Cells via Slot-Die-Coating. *ACS Energy Lett.* **5**, 3034–3040 (2020).

154. Li, J. *et al.* A contact study in hole conductor free perovskite solar cells with low temperature processed carbon electrodes. *RSC Advances* **7**, 20732–20737 (2017).

155. Priyadarshi, A. *et al.* A large area (70 cm 2) monolithic perovskite solar module with a high efficiency and stability. *Energy & Environmental Science* **9**, 3687–3692 (2016).

156. Surfaces and their Measurement - 1st Edition. https://www.elsevier.com/books/surfaces-and-their-measurement/whitehouse/978-1-903996-60-7.

157. Tauc, J., Grigorovici, R. & Vancu, A. Optical Properties and Electronic Structure of Amorphous Germanium. *physica status solidi (b)* **15**, 627–637 (1966).

158. Wang, T. *et al.* Indirect to direct bandgap transition in methylammonium lead halide perovskite. *Energy Environ. Sci.* **10**, 509–515 (2017).

159. Ke, J. C.-R. *et al.* In situ investigation of degradation at organometal halide perovskite surfaces by X-ray photoelectron spectroscopy at realistic water vapour pressure. *Chem. Commun.* **53**, 5231–5234 (2017).

160. Meier, T. *et al.* Impact of excess PbI2 on the structure and the temperature dependent optical properties of methylammonium lead iodide perovskites. *J. Mater. Chem. C* **6**, 7512–7519 (2018).

161. Caprioglio, P. *et al.* On the Relation between the Open-Circuit Voltage and Quasi-Fermi Level Splitting in Efficient Perovskite Solar Cells. *Advanced Energy Materials* **9**, 1901631 (2019).

162. Burkhard, G. F., Hoke, E. T. & McGehee, M. D. Accounting for Interference, Scattering, and Electrode Absorption to Make Accurate Internal Quantum Efficiency Measurements in Organic and Other Thin Solar Cells. *Advanced Materials* **22**, 3293–3297 (2010).

163. McGehee Group - Stanford Materials Science and Engineering. https://web.stanford.edu/group/mcgehee/transfermatrix/index.

164. Pettersson, L. A. A., Roman, L. S. & Inganäs, O. Modeling photocurrent action spectra of photovoltaic devices based on organic thin films. *Journal of Applied Physics* **86**, 487–496 (1999).

165. Peumans, P., Yakimov, A. & Forrest, S. R. Small molecular weight organic thin-film photodetectors and solar cells. *Journal of Applied Physics* **93**, 3693–3723 (2003).

166. Ramadan, A. J. *et al.* Revealing the Stoichiometric Tolerance of Lead Trihalide Perovskite Thin Films. *Chem. Mater.* **32**, 114–120 (2020).

167. Falk, L. M. *et al.* Effect of Precursor Stoichiometry on the Performance and Stability of MAPbBr3 Photovoltaic Devices. *Energy Technology* **8**, 1900737 (2020).

168. Lee, Y. H. *et al.* Unraveling the Reasons for Efficiency Loss in Perovskite Solar Cells. *Advanced Functional Materials* **25**, 3925–3933 (2015).

169. McMeekin, D. P. *et al.* Crystallization Kinetics and Morphology Control of Formamidinium–Cesium Mixed-Cation Lead Mixed-Halide Perovskite via Tunability of the Colloidal Precursor Solution. *Advanced Materials* **29**, 1607039 (2017).

170. Giuri, A. *et al.* Rheological Tunability of Perovskite Precursor Solutions: From Spin Coating to Inkjet Printing Process. *Nanomaterials* **9**, 582 (2019).

171. You, J. *et al.* The fabrication of homogeneous perovskite films on non-wetting interfaces enabled by physical modification. *Journal of Energy Chemistry* **38**, 192–198 (2019).

172. Lee, J.-W., Lee, D.-K., Jeong, D.-N. & Park, N.-G. Control of Crystal Growth toward Scalable Fabrication of Perovskite Solar Cells. *Advanced Functional Materials* **29**, 1807047 (2019).

173. Ternes, S. *et al.* Drying Dynamics of Solution-Processed Perovskite Thin-Film Photovoltaics: In Situ Characterization, Modeling, and Process Control. *Advanced Energy Materials* **9**, 1901581 (2019).

174. Eye in the process: Formation of “triple cation” perovskite thin films rationalized by in-situ optical monitoring. https://www.researchsquare.com (2020) doi:10.21203/rs.3.rs-102041/v1.

175. Xiao, M. *et al.* A Fast Deposition-Crystallization Procedure for Highly Efficient Lead Iodide Perovskite Thin-Film Solar Cells. *Angewandte Chemie* **126**, 10056–10061 (2014).

176. Qaid, S. M. H. *et al.* Band-gap tuning of lead halide perovskite using a single step spin-coating deposition process. *Materials Letters* **164**, 498–501 (2016).

177. Li, C. *et al.* Efficient lead acetate sourced planar heterojunction perovskite solar cells with enhanced substrate coverage via one-step spin-coating. *Organic Electronics* **33**, 194–200 (2016).

178. Wang, G. *et al.* Efficient perovskite solar cell fabricated in ambient air using one-step spin-coating. *RSC Advances* **6**, 43299–43303 (2016).

179. Cai, B., Zhang, W.-H. & Qiu, J. Solvent engineering of spin-coating solutions for planar-structured high-efficiency perovskite solar cells. *Chinese Journal of Catalysis* **36**, 1183–1190 (2015).

180. Yuan, Z. *et al.* Approximately 800-nm-Thick Pinhole-Free Perovskite Films via Facile Solvent Retarding Process for Efficient Planar Solar Cells. *ACS Appl. Mater. Interfaces* **8**, 34446–34454 (2016).

181. Wang, J.-F. *et al.* Surface engineering of perovskite films for efficient solar cells. *Scientific Reports* **7**, 14478 (2017).

182. Phung, N. *et al.* The Role of Grain Boundaries on Ionic Defect Migration in Metal Halide Perovskites. *Advanced Energy Materials* **10**, 1903735 (2020).

183. Bahrami, B. *et al.* Nanoscale spatial mapping of charge carrier dynamics in perovskite solar cells. *Nano Today* **33**, 100874 (2020).

184. Momblona, C. *et al.* Efficient methylammonium lead iodide perovskite solar cells with active layers from 300 to 900 nm. *APL Materials* **2**, 081504 (2014).

185. Yu, Y. *et al.* Improving the Performance of Formamidinium and Cesium Lead Triiodide Perovskite Solar Cells using Lead Thiocyanate Additives. *ChemSusChem* **9**, 3288–3297 (2016).

186. Li, Y. *et al.* Tuning Nucleation Sites to Enable Monolayer Perovskite Films for Highly Efficient Perovskite Solar Cells. *Coatings* **8**, 408 (2018).

187. Tian, Y. & Scheblykin, I. G. Artifacts in Absorption Measurements of Organometal Halide Perovskite Materials: What Are the Real Spectra? *J. Phys. Chem. Lett.* **6**, 3466–3470 (2015).

188. Ono, L. K., Juarez-Perez, E. J. & Qi, Y. Progress on Perovskite Materials and Solar Cells with Mixed Cations and Halide Anions. *ACS Applied Materials & Interfaces* **9**, 30197–30246 (2017).

189. Lee, J.-W. & Park, N.-G. Chemical Approaches for Stabilizing Perovskite Solar Cells. *Advanced Energy Materials* **10**, 1903249 (2020).

190. Bouchard, M. Pérovskites halogénées AMX3: synthèse, substitution cationique et étude structurale. 120.

191. Dally, P. Cellules Solaires à base de Matériaux Pérovskites : De la caractérisation des matériaux à l'amélioration des rendements et de la stabilité. (Université Grenoble Alpes (ComUE), 2019).

192. Weller, M. T., Weber, O. J., Frost, J. M. & Walsh, A. Cubic Perovskite Structure of Black Formamidinium Lead Iodide, α-[HC(NH $_2$) $_2$]PbI $_3$, at 298 K. *The Journal of Physical Chemistry Letters* **6**, 3209–3212 (2015).

193. Nguyen, V. H., Hoang, T. K. A., Kurokawa, Y. & Usami, N. The impact of highly excessive PbI2 on the correlation of MAPbI3 perovskite morphology and carrier lifetimes. *J. Mater. Chem. C* **8**, 14481–14489 (2020).

194. Gujar, T. P. *et al.* The role of PbI2 in CH3NH3PbI3 perovskite stability, solar cell parameters and device degradation. *Phys. Chem. Chem. Phys.* **20**, 605–614 (2017).

195. Pool, V. L. *et al.* Thermal engineering of FAPbI 3 perovskite material via radiative thermal annealing and in situ XRD. *Nature Communications* **8**, 14075 (2017).

196. Babayigit, A., D'Haen, J., Boyen, H.-G. & Conings, B. Gas Quenching for Perovskite Thin Film Deposition. *Joule* **2**, 1205–1209 (2018).

197. Zuo, C., Vak, D., Angmo, D., Ding, L. & Gao, M. One-step roll-to-roll air processed high efficiency perovskite solar cells. *Nano Energy* **46**, 185–192 (2018).

198. Qin, T. *et al.* Amorphous hole-transporting layer in slot-die coated perovskite solar cells. *Nano Energy* **31**, 210–217 (2017).

199. Vijayan, A. *et al.* Simple Method for Efficient Slot-Die Coating of MAPbI3 Perovskite Thin Films in Ambient Air Conditions. *ACS Appl. Energy Mater.* **3**, 4331–4337 (2020).

200. Xu, X. *et al.* Air-processed mixed-cation Cs $_{0.15}$ FA $_{0.85}$ PbI $_3$ planar perovskite solar cells derived from a PbI $_2$ –CsI–FAI intermediate complex. *Journal of Materials Chemistry A* **6**, 7731–7740 (2018).

201. Troughton, J., Hooper, K. & Watson, T. M. Humidity resistant fabrication of CH3NH3PbI3 perovskite solar cells and modules. *Nano Energy* **39**, 60–68 (2017).

202. Saidaminov, M. I., Abdelhady, A. L., Maculan, G. & Bakr, O. M. Retrograde solubility of formamidinium and methylammonium lead halide perovskites enabling rapid single crystal growth. *Chem. Commun.* **51**, 17658–17661 (2015).

203. Riedel et Karato - 1996 - Microstructural Development During Nucleation and .pdf.

204. Wang, F., Bai, S., Tress, W., Hagfeldt, A. & Gao, F. Defects engineering for high-performance perovskite solar cells. *npj Flexible Electronics* **2**, 1–14 (2018).

205. Yang, D. *et al.* Achieving 20% Efficiency for Low-Temperature-Processed Inverted Perovskite Solar Cells. *Advanced Functional Materials* **29**, 1807556 (2019).

206. Zardetto, V. *et al.* Atomic layer deposition for perovskite solar cells: research status, opportunities and challenges. *Sustainable Energy Fuels* **1**, 30–55 (2017).

207. Amratisha, K. *et al.* Layer-by-layer spray coating of a stacked perovskite absorber for perovskite solar cells with better performance and stability under a humid environment. *Opt. Mater. Express, OME* **10**, 1497–1508 (2020).

208. Khenkin, M. V. *et al.* Consensus statement for stability assessment and reporting for perovskite photovoltaics based on ISOS procedures. *Nature Energy* **5**, 35–49 (2020).

209. Schubert, M. C., Mundt, L. E., Walter, D., Fell, A. & Glunz, S. W. Spatially Resolved Performance Analysis for Perovskite Solar Cells. *Advanced Energy Materials* **10**, 1904001 (2020).

210. Le Berre, M., Chen, Y. & Baigl, D. From Convective Assembly to Landau–Levich Deposition of Multilayered Phospholipid Films of Controlled Thickness. *Langmuir* **25**, 2554–2557 (2009).

211. 48 - DRAGGING OF A LIQUID BY A MOVING PLATE. in *Collected Papers of L.D. Landau* (ed. Ter haar, D.) 355–364 (Pergamon, 1965). doi:10.1016/B978-0-08-010586-4.50053-5.

212. Ding, X., Liu, J. & Harris, T. A. L. A review of the operating limits in slot die coating processes. *AIChE Journal* **62**, 2508–2524 (2016).

213. Ruschak, K. J. Limiting flow in a pre-metered coating device. *Chemical Engineering Science* **31**, 1057–1060 (1976).

214. Romero, O. J., Scriven, L. E. & Carvalho, M. S. Slot coating of mildly viscoelastic liquids. *Journal of Non-Newtonian Fluid Mechanics* **138**, 63–75 (2006).

215. Verma, A. *et al.* Towards industrialization of perovskite solar cells using slot die coating. *J. Mater. Chem. C* **8**, 6124–6135 (2020).

216. Srivastava, P., Parhi, A. P., Ranjan, R., Satapathi, S. & Bag, M. Temperature Assisted Nucleation and Growth To Optimize Perovskite Morphology at Liquid Interface: A Study by Electrochemical Impedance Spectroscopy. *ACS Appl. Energy Mater.* **1**, 4420–4425 (2018).

217. Kadro, J. M., Nonomura, K., Gachet, D., Grätzel, M. & Hagfeldt, A. Facile route to freestanding CH 3 NH 3 PbI 3 crystals using inverse solubility. *Scientific Reports* **5**, 11654 (2015).

218. Saidaminov, M. I. *et al.* High-quality bulk hybrid perovskite single crystals within minutes by inverse temperature crystallization. *Nature Communications* **6**, 7586 (2015).

219. Hwang, T. *et al.* Electronic Traps and Their Correlations to Perovskite Solar Cell Performance via Compositional and Thermal Annealing Controls. *ACS Appl. Mater. Interfaces* **11**, 6907–6917 (2019).

220. Correa-Baena, J.-P. *et al.* Promises and challenges of perovskite solar cells. *Science* **358**, 739–744 (2017).

221. Kim, J. *et al.* Unveiling the Relationship between the Perovskite Precursor Solution and the Resulting Device Performance. *J. Am. Chem. Soc.* **142**, 6251–6260 (2020).

222. Petrov, A. A. *et al.* Crystal Structure of DMF-Intermediate Phases Uncovers the Link Between CH3NH3PbI3 Morphology and Precursor Stoichiometry. *J. Phys. Chem. C* **121**, 20739–20743 (2017).

223. Yan, K. *et al.* Hybrid Halide Perovskite Solar Cell Precursors: Colloidal Chemistry and Coordination Engineering behind Device Processing for High Efficiency. *J. Am. Chem. Soc.* **137**, 4460–4468 (2015).

224. Li, B., Li, M., Fei, C., Cao, G. & Tian, J. Colloidal engineering for monolayer $CH_3NH_3PbI_3$ films toward high performance perovskite solar cells. *J. Mater. Chem. A* **5**, 24168–24177 (2017).

225. Boonmongkolras, P., Kim, D., Alhabshi, E. M., Gereige, I. & Shin, B. Understanding effects of precursor solution aging in triple cation lead perovskite. *RSC Adv.* **8**, 21551–21557 (2018).

226. Rossander, L. H. *et al.* In situ X-ray scattering of perovskite solar cell active layers roll-to-roll coated on flexible substrates. *CrystEngComm* **18**, 5083–5088 (2016).

227. Gu, X. *et al.* Compact Roll-to-Roll Coater for in Situ X-ray Diffraction Characterization of Organic Electronics Printing. *ACS Applied Materials & Interfaces* **8**, 1687–1694 (2016).

228. Suchan, K., Just, J., Becker, P., Unger, E. L. & Unold, T. Optical in situ monitoring during the synthesis of halide perovskite solar cells reveals formation kinetics and evolution of optoelectronic properties. *J. Mater. Chem. A* **8**, 10439–10449 (2020).

229. Turren-Cruz, S.-H., Hagfeldt, A. & Saliba, M. Methylammonium-free, high-performance, and stable perovskite solar cells on a planar architecture. *Science* **362**, 449–453 (2018).

230. Braunger, S. *et al.* CsxFA1–xPb(I1–yBry)3 Perovskite Compositions: the Appearance of Wrinkled Morphology and its Impact on Solar Cell Performance. *J. Phys. Chem. C* **122**, 17123–17135 (2018).

231. Huang, S.-H. *et al.* Controlling Morphology and Interface of Perovskite Layer for Scalable High-Efficiency Solar Cell Fabricated by Using Green Solvents and Blade Coating in Ambient Environment. *ACS Applied Materials & Interfaces* (2020) doi:10.1021/acsami.0c06211.

232. Szostak, R. *et al.* Nanoscale mapping of chemical composition in organic-inorganic hybrid perovskite films. *Science Advances* **5**, eaaw6619 (2019).

233. Saidaminov, M. I. *et al.* Multi-cation perovskites prevent carrier reflection from grain surfaces. *Nature Materials* **19**, 412–418 (2020).

234. Ma, F. *et al.* Stable α/δ phase junction of formamidinium lead iodide perovskites for enhanced near-infrared emission. *Chem. Sci.* **8**, 800–805 (2016).

235. Zhang, Y., Kim, S.-G., Lee, D.-K. & Park, N.-G. CH3NH3PbI3 and HC(NH2)2PbI3 Powders Synthesized from Low-Grade PbI2: Single Precursor for High-Efficiency Perovskite Solar Cells. *ChemSusChem* **11**, 1813–1823 (2018).

236. Cao, Y. *et al.* Pressure-Tailored Band Gap Engineering and Structure Evolution of Cubic Cesium Lead Iodide Perovskite Nanocrystals. *J. Phys. Chem. C* **122**, 9332–9338 (2018).

237. Xue, D.-J. *et al.* Regulating strain in perovskite thin films through charge-transport layers. *Nature Communications* **11**, 1514 (2020).

238. Zhu, C. *et al.* Strain engineering in perovskite solar cells and its impacts on carrier dynamics. *Nature Communications* **10**, 815 (2019).

239. Tian, L. *et al.* Effects of Annealing Time on Triple Cation Perovskite Films and Their Solar Cells. *ACS Appl. Mater. Interfaces* **12**, 29344–29356 (2020).

240. Shukla, S. *et al.* Effect of Formamidinium/Cesium Substitution and PbI2 on the Long-Term Stability of Triple-Cation Perovskites. *ChemSusChem* **10**, 3804–3809 (2017).

241. Bush, K. A. *et al.* Controlling Thin-Film Stress and Wrinkling during Perovskite Film Formation. *ACS Energy Lett.* **3**, 1225–1232 (2018).

242. Beal, R. E. *et al.* Cesium Lead Halide Perovskites with Improved Stability for Tandem Solar Cells. *J. Phys. Chem. Lett.* **7**, 746–751 (2016).

243. Zhu, W. *et al.* Coarsening of one-step deposited organolead triiodide perovskite films via Ostwald ripening for high efficiency planar-heterojunction solar cells. *Dalton Trans.* **45**, 7856–7865 (2016).

244. Cao, X. *et al.* Fabrication of Perovskite Films with Large Columnar Grains via Solvent-Mediated Ostwald Ripening for Efficient Inverted Perovskite Solar Cells. *ACS Appl. Energy Mater.* **1**, 868–875 (2018).

245. Stolterfoht, M. *et al.* The impact of energy alignment and interfacial recombination on the internal and external open-circuit voltage of perovskite solar cells. *Energy & Environmental Science* **12**, 2778–2788 (2019).

246. Mahesh, S. *et al.* Revealing the origin of voltage loss in mixed-halide perovskite solar cells. *Energy Environ. Sci.* **13**, 258–267 (2020).

247. Meggiolaro, D. *et al.* Iodine chemistry determines the defect tolerance of lead-halide perovskites. *Energy Environ. Sci.* **11**, 702–713 (2018).

248. Wu, W.-Q. *et al.* Reducing Surface Halide Deficiency for Efficient and Stable Iodide-Based Perovskite Solar Cells. *J. Am. Chem. Soc.* **142**, 3989–3996 (2020).

249. Germino, J. C. *et al.* Postpassivation of Multication Perovskite with Rubidium Butyrate. *ACS Photonics* **7**, 2282–2291 (2020).

250. Liu, X. *et al.* Comprehensive insights into defect passivation and charge dynamics for FA0.8MA0.15Cs0.05PbI2.8Br0.2 perovskite solar cells. *Appl. Phys. Lett.* **117**, 013503 (2020).

251. Cheng, F. *et al.* N-Methyl-2-pyrrolidone as an excellent coordinative additive with a wide operating range for fabricating high-quality perovskite films. *Inorg. Chem. Front.* **6**, 2458–2463 (2019).

252. Jung, M., Ji, S.-G., Kim, G. & Seok, S. I. Perovskite precursor solution chemistry: from fundamentals to photovoltaic applications. *Chem. Soc. Rev.* **48**, 2011–2038 (2019).

253. De Wolf, S. *et al.* Organometallic Halide Perovskites: Sharp Optical Absorption Edge and Its Relation to Photovoltaic Performance. *The Journal of Physical Chemistry Letters* **5**, 1035–1039 (2014).

254. Lee, D. *et al.* Slot-Die Coated Perovskite Films Using Mixed Lead Precursors for Highly Reproducible and Large-Area Solar Cells. *ACS Appl. Mater. Interfaces* **10**, 16133–16139 (2018).

255. Dai, X. *et al.* Scalable Fabrication of Efficient Perovskite Solar Modules on Flexible Glass Substrates. *Advanced Energy Materials* **10**, 1903108 (2020).

256. Manser, J. S., Saidaminov, M. I., Christians, J. A., Bakr, O. M. & Kamat, P. V. Making and Breaking of Lead Halide Perovskites. *Acc. Chem. Res.* **49**, 330–338 (2016).

257. Fu, F. *et al.* I_2 vapor-induced degradation of formamidinium lead iodide based perovskite solar cells under heat–light soaking conditions. *Energy Environ. Sci.* **12**, 3074–3088 (2019).

258. Rong, Y. *et al.* Challenges for commercializing perovskite solar cells. *Science* **361**, (2018).

259. Ansari, M. I. H., Qurashi, A. & Nazeeruddin, M. K. Frontiers, opportunities, and challenges in perovskite solar cells: A critical review. *Journal of Photochemistry and Photobiology C: Photochemistry Reviews* **35**, 1–24 (2018).

260. Dewi, H. A. *et al.* Highly Efficient Semitransparent Perovskite Solar Cells for Four Terminal Perovskite-Silicon Tandems. *ACS Appl. Mater. Interfaces* **11**, 34178–34187 (2019).

261. Gong, J., Liang, J. & Sumathy, K. Review on dye-sensitized solar cells (DSSCs): Fundamental concepts and novel materials. *Renewable and Sustainable Energy Reviews* **16**, 5848–5860 (2012).

262. Salado, M. *et al.* Understanding the Influence of Interface Morphology on the Performance of Perovskite Solar Cells. *Materials (Basel)* **11**, (2018).

263. Abdellatif, S. *et al.* Refractive index and scattering of porous TiO2 films. *Microporous and Mesoporous Materials* **264**, 84–91 (2018).

264. Jiang, Q. *et al.* Planar-Structure Perovskite Solar Cells with Efficiency beyond 21%. *Advanced Materials* **29**, 1703852 (2017).

265. Yang, D. *et al.* High efficiency planar-type perovskite solar cells with negligible hysteresis using EDTA-complexed SnO 2. *Nature Communications* **9**, 3239 (2018).

266. Michels, J. J., Oostra, A. J. & Blom, P. W. M. Short-circuit prevention strategies in organic light-emitting diodes and solar cells. *Smart Mater. Struct.* **25**, 084015 (2016).

267. Tress, W. *et al.* Interpretation and evolution of open-circuit voltage, recombination, ideality factor and subgap defect states during reversible light-soaking and irreversible degradation of perovskite solar cells. *Energy Environ. Sci.* **11**, 151–165 (2018).

268. Moghadamzadeh, S. *et al.* Spontaneous enhancement of the stable power conversion efficiency in perovskite solar cells. *Journal of Materials Chemistry A* **8**, 670–682 (2020).

269. Yu, M. *et al.* The influence of the electron transport layer on charge dynamics and trap-state properties in planar perovskite solar cells. *RSC Adv.* **10**, 12347–12353 (2020).

270. Jiang, Q. *et al.* Enhanced electron extraction using SnO 2 for high-efficiency planar-structure HC(NH 2) 2 PbI 3 -based perovskite solar cells. *Nat Energy* **2**, 1–7 (2016).

271. Shi, D. *et al.* Low trap-state density and long carrier diffusion in organolead trihalide perovskite single crystals. *Science* **347**, 519–522 (2015).

272. Stolterfoht, M. *et al.* Visualization and suppression of interfacial recombination for high-efficiency large-area pin perovskite solar cells. *Nature Energy* **3**, 847–854 (2018).

273. Han, G. *et al.* Additive Selection Strategy for High Performance Perovskite Photovoltaics. *J. Phys. Chem. C* **122**, 13884–13893 (2018).

274. deQuilettes, D. W. *et al.* Photoluminescence Lifetimes Exceeding 8 μs and Quantum Yields Exceeding 30% in Hybrid Perovskite Thin Films by Ligand Passivation. *ACS Energy Lett.* **1**, 438–444 (2016).

275. Chen, S. *et al.* Crystallization in one-step solution deposition of perovskite films: Upward or downward? *Science Advances* **7**, eabb2412 (2021).

276. Geng, W. *et al.* Structures and Electronic Properties of Different CH 3 NH 3 PbI 3 /TiO 2 Interface: A First-Principles Study. *Scientific Reports* **6**, 20131 (2016).

277. Sarkar, T. *et al.* Electron Transport at the TiO2 Surfaces of Rutile, Anatase, and Strontium Titanate: The Influence of Orbital Corrugation. *ACS Appl. Mater. Interfaces* **7**, 24616–24621 (2015).

278. Luo, J. *et al.* Surface Rutilization of Anatase TiO2 for Efficient Electron Extraction and Stable Pmax Output of Perovskite Solar Cells. *Chem* **4**, 911–923 (2018).

279. Liang, Y. *et al.* The Preparation of TiO2 Film by the Sol-Gel Method and Evaluation of Its Self-Cleaning Property. *Materials* **11**, 450 (2018).

280. Li, N. *et al.* Multifunctional perovskite capping layers in hybrid solar cells. *J. Mater. Chem. A* **2**, 14973–14978 (2014).

281. Zhang, C. *et al.* Influence of different TiO2 blocking films on the photovoltaic performance of perovskite solar cells. *Applied Surface Science* **388**, 82–88 (2016).

282. Zhang, Y. *et al.* Achieving Reproducible and High-Efficiency (>21%) Perovskite Solar Cells with a Presynthesized FAPbI3 Powder. *ACS Energy Lett.* **5**, 360–366 (2020).

283. Liu, Z. *et al.* A holistic approach to interface stabilization for efficient perovskite solar modules with over 2,000-hour operational stability. *Nature Energy* **5**, 596–604 (2020).

284. Ravishankar, S. *et al.* Influence of Charge Transport Layers on Open-Circuit Voltage and Hysteresis in Perovskite Solar Cells. *Joule* **2**, 788–798 (2018).

285. Chen, B., Yang, M., Priya, S. & Zhu, K. Origin of J–V Hysteresis in Perovskite Solar Cells. *J. Phys. Chem. Lett.* **7**, 905–917 (2016).

286. Yang, D. *et al.* High efficiency planar-type perovskite solar cells with negligible hysteresis using EDTA-complexed SnO2. *Nat Commun* **9**, 3239 (2018).

287. Zuo, L. *et al.* Tailoring the Interfacial Chemical Interaction for High-Efficiency Perovskite Solar Cells. *Nano Lett* **17**, 269–275 (2017).

288. Ke, W. *et al.* Cooperative tin oxide fullerene electron selective layers for high-performance planar perovskite solar cells. *J. Mater. Chem. A* **4**, 14276–14283 (2016).

289. Saliba, M. & Etgar, L. Current Density Mismatch in Perovskite Solar Cells. *ACS Energy Lett.* **5**, 2886–2888 (2020).

290. Meredith, P. & Armin, A. Scaling of next generation solution processed organic and perovskite solar cells. *Nature Communications* **9**, 5261 (2018).

291. Cho, Y. *et al.* Elucidating Mechanisms behind Ambient Storage-Induced Efficiency Improvements in Perovskite Solar Cells. *ACS Energy Lett.* **6**, 925–933 (2021).

Dépôt de pérovskite hybride par procédé slot-die: étude matériau et intégration en dispositifs photovoltaïques.

Résumé : Depuis une décennie, les pérovskites halogénées ont émergé comme matériaux alternatifs aux cellules solaires classiques en silicium en se distinguant par leur rapidité et facilité d'élaboration. Cette technologie très performante (25% de rendement) a l'avantage de réduire le budget énergétique en plus de minimiser les ressources nécessaires à sa fabrication ce qui la rend très compétitive et en phase avec les objectifs environnementaux. Ce travail a pour but de rendre industrialisable le dépôt de la couche pérovskite pour permettre la fabrication de modules photovoltaïques à faible empreinte carbone. La solution retenue pour sa compatibilité industrielle est le 'slot-die coating', procédé au cours duquel un film humide d'encre pérovskite est étalé par le déplacement d'un ménisque du fluide au contact du substrat, puis cristallisé par un flux d'air. Ces travaux de thèse ont permis d'obtenir des couches pérovskites homogènes sur des substrats de plus en plus grands (jusqu'à 10 x 10 cm^2). L'intégration de cette couche dans des dispositifs photovoltaïques a conduit à un rendement de 18% à l'échelle laboratoire (0.09 cm^2) et de 11.5% à l'échelle mini-module (52 cm^2), démontrant le potentiel de cette technologie pour une production durable de l'énergie solaire disponible partout et pour tous.

Mots clés : Pérovskite double cation, Slot-die, Couteau d'air, Larges surfaces.

Slot-die coating of hybrid perovskite: material study and integration into photovoltaic devices.

Abstract: In the last decade, metal halide perovskite photovoltaics have emerged as an innovative thin film photovoltaic technology that contrasts with current technologies due to its solution processability that could significantly reduce its manufacturing environmental footprint. In 2021, perovskite solar cells at laboratory scale reach 25.5% power conversion efficiency, closing the gap to silicon based solar cells performances. This work aims at making existing deposition processes compatible with industrial standards to permit the fabrication of efficient solar panels with reduced environmental footprint. The technical solution presented here is the slot-die coating process, where a wet film is deposited by the movement of a precursor fluid meniscus onto a substrate and subsequently crystallized by the combined action of a gas flow and substrate heating. This work demonstrates the formation of homogeneous perovskite films over large-area substrates (up to 10 x 10 cm^2). The perovskite layers were implemented into solar cells, yielding power conversion efficiency of 18% at laboratory scale and 11.6% at mini-module scale. These results highlight the potential of this technology for a sustainable production of solar energy available to everyone and everywhere.

Keywords: Methylammonium-free perovskite, Slot-die coating, Gas-quenching, Large areas.